Porous silicon-based electrochemical biosensors

Keying Guo

Bachelor of Material Science and Engineering
Master of Material Science and Engineering

Supervisors: Dr. Beatriz Prieto-Simón; Prof. Nicolas H. Voelcker

A thesis submitted for the degree of **Doctor of Philosophy** at

Monash University in 2019

Drug Delivery, Disposition and Dynamics

Monash Institute of Pharmaceutical Sciences

February 2019

Contents

Copyright notice

Declaration

In accordance with Monash University Doctorate Regulation 17.2 Doctor of Philosophy and Research Master's regulations the following declarations are made:

I hereby declare that this thesis contains no material which has been accepted for the award of any other degree or diploma at any university or equivalent institution and that, to the best of my knowledge and belief, this thesis contains no material previously published or written by another person, except where due reference is made in the text of the thesis.

This thesis includes texts and figures from 1 submitted publication in peer reviewed journals and at least 4 unpublished publications. Work from submitted papers may have been modified and altered to improve consistency and readability of the thesis.

The core theme of the thesis is "Porous silicon-based electrochemical biosensors". The ideas, development and writing up of all the papers in the thesis were the principal responsibility of myself, the student, working within the Drug Delivery, Disposition and Dynamics theme under the supervision of Dr. Beatriz Prieto-Simón and Professor Nicolas H. Voelcker.

The inclusion of co-authors reflects the fact that the work came from active collaboration between researchers and acknowledges input into team-based research. In the case of the submitted papers, my contribution to the work involved the following:

Thesis Chapter	Publication Title	Status	Nature and % of student contribution	Co-author name(s) Nature and % of Co-author's contribution*	Monash student Y/N*
Chapter 3	Porous silicon nanostructures as effective Faradaic electrochemical sensing platforms	submitted	81%. Concept and collecting data and wrote the manuscript	1%-Apoorva Sharma, data collecting	No
				2%-Rou Jun Toh, data collecting	No
				2%- Eva Alvárez de Eulate, data collecting, input to the manuscript	No
				1% -Thomas R. Gengenbach, XPS data analysis	No
				1% -Xavier Cetó, manuscript preparation	No
				3% -Nicolas H. Voelcker, concept and manuscript preparation	No
				9%- Beatriz Prieto-Simón, concept and manuscript preparation	No

I have renumbered sections of submitted or published papers in order to generate a consistent presentation within the thesis.

Student signature: [redacted] Date: 11.02.2019

The undersigned hereby certify that the above declaration correctly reflects the nature and extent of the student's and co-authors' contributions to this work. In instances where I am not the responsible author I have consulted with the responsible author to agree on the respective contributions of the authors.

Main Supervisor signature: [redacted] **Date:** 15/02/2019

Publications

Keying Guo, Apoorva Sharma, Rou Jun Toh, Eva Alvárez de Eulate, Thomas R. Gengenbach, Xavier Cetó, Nicolas H. Voelcker*, Beatriz Prieto-Simón*. Porous silicon nanostructures as effective Faradaic electrochemical sensing platforms. *Advanced Functional Materials,* 2019, 1809206.

Manuscript in preparation

Keying Guo, Maria Alba, Grace Pei Chin, Bin Guan, Ziqiu Tong, Michael Sailor*, Nicolas H. Voelcker*, Beatriz, Prieto-Simón*. Designing versatile biosensing platforms using layered carbon-stabilized porous silicon nanostructures. Intended for submission to the journal: *The Journal of American Chemical Society*.

Keying Guo, Maria Alba, Nicolas H. Voelcker*, Beatriz, Prieto-Simón*. Porous silicon based electrochemical biosensors: a review. Intended for submission to the journal: *ACS Sensors*.

Keying Guo, Grace Pei Chin, Maria Alba, Rajpreet S. Minhas, Nicolas H. Voelcker*, Beatriz Prieto-Simón*. Rapid and label-free detection of *Escherichia coli* 16S rRNA using carbon-stabilized porous silicon nanochannels-based voltammetric biosensor. Intended for submission to the journal: *ACS Nano*.

Keying Guo, Maria Alba, Hashim Alhmoud, Nicolas H. Voelcker*, Beatriz Prieto-Simón*. Uniform gold-porous silicon (Au-pSi) composite nanochannel arrays controllably engineered by metal-assisted chemical etching (MACE) and their electrochemical properties. Intended for submission to the journal: *Advanced Functional Materials*.

Conference

Keying Guo, Maria Alba, Nicolas H. Voelcker*, Beatriz, Prieto-Simón*. Towards versatile porous silicon nanochannel-based electrochemical biosensing platforms. *ARC Centre of Excellence in Bio-Nano Science & Technology (CBNS) Annual Research Workshop 2016*, Adelaide, Australia.

Keying Guo, Maria Alba, Nicolas H. Voelcker*, Beatriz, Prieto-Simón*. Layering carbon-stabilized porous silicon nanostructures via electrochemical anodization to design versatile biosensing platforms. *3rd International Symposium on Anodizing Science and Technology 2019*, Hyogo, Japan (abstract accepted).

Publication unrelated to the thesis:

Ziqiu Tong, Angela Ivask, Keying Guo, Scott McCormick, Enzo Lombi, Craig Priest, Nicolas H. Voelcker. Crossed flow microfluidics for high throughput screening of bioactive chemical-cell interactions. *Lab on a Chip*, 2017 (3), 501-510.

Tong, Ziqiu, Gayathri Rajeev, Keying Guo, Angela Ivask, Scott McCormick, Enzo Lombi, Craig Priest, Nicolas H. Voelcker. Microfluidic cell microarray platform for high throughput analysis of particle-cell interactions. *Analytical Chemistry*, 2018, 90 (7), 4338-4347.

Acknowledgements

First and foremost, I would like to express my sincere gratitude and appreciation to my supervisors Dr. Beatriz Prieto-Simón and Professor Nicolas H. Voelcker. I am very grateful to both of them for giving me such an amazing opportunity to be involved in this PhD project. I would like to thank them for the leadership in directing the projects and providing enough resources and intellectual support through this work, your contribution cannot be overstated. Thank you both for giving me numerous opportunities during my PhD years to expand my skill sets and to improve myself, and also for constantly guiding my growth as an independent researcher. You both are good role model as highly enthusiastic, professional and successful scientists. An extra special thanks to Dr. Beatriz Prieto-Simón in particular, a great mentor I have had over the years.

Special thanks should be given to Dr. Maria Alba for her priceless assistance all the way through this journey starting from my first PhD experiment I conducted in the lab, without your help I could not have got this far.

I would like to specially thank Dr. Tommy Tong, Dr. Bin Guan, Dr. Hashim Alhmoud and Dr. Roshan Vasani and Dr. Bo Peng for their recommendations and suggestions, which have been invaluable for my PhD life. I would like to acknowledge to Dr. Steven McInnes, Dr. Martin Sweetman, Dr. Anna Cifuentes-Rius, Dr. Bahaman Delatat, Raj Minhas, Stella Aslanoglou, Dexiang Zhang, Terence Tieu and all the other group members not mentioned here who gave me a lot advices and great support all the time.

I also wish to extend my gratitude to Professor Michael Sailor and his group members, for these guidance and support during my PhD replacement in his lab in California.

Also I would like to express my gratitude to my friends for their unconditional friendship, my beloved parents for their unconditional support.

And finally, the most special thanks to Vicky my dearest, you carried me for so far along the way. For so long you straightened out my soul and made me into the best version of myself that I could be. I am endlessly grateful for your sacrifice and support to our family over all these years. Thanks to my lovely kids, Camilla and Kevin, for these most wonderful moments I have ever had in my life.

Abstract

Electrochemical biosensors have emerged as very powerful and profitable analytical tools, due to their striking features such as fast detection, high efficiency, portability to resolve central issues in many challenging areas including water and food quality control, biomedical diagnostics, and environmental monitoring. As an established porous material with desired properties to be used as sensing platform, such as the extensively tunable structure, versatile surface chemistry and large surface area (up to 800 m^2/g), porous silicon (pSi) offers ample opportunities for biosensor design. However, the use of pSi to develop electrochemical biosensors has been limited because the unavoidable growth of the insulating SiO_2 layer at the surface. Consequently, this thesis aims to understand the potential to utilize carbon-stabilized pSi nanostructures directly as electrochemical transducer in the effort to develop a novel biosensing system.

In Chapter 3, the electrochemical performance of carbon-stabilized pSi is firstly investigated. PSi undergoes two thermal treatments via decomposition of acetylene gas at either 525 or 800 °C, which results in hydrogen-terminated thermally hydrocarbonized pSi (THCpSi) and hydroxyl-terminated thermally carbonized pSi (TCpSi), respectively. Electrochemical characterization using cyclic voltammetry, chronocoulometry and electrochemical impedance spectroscopy (EIS) in the presence of several redox pairs, $[Fe(CN)_6]^{3-/4-}$, $[Ru(NH_3)_6]^{2+/3+}$ and hydroquinone/quinone (HQ/Q), is used to demonstrate the versatility and high stability to degradation of carbon-stabilized pSi nanostructures and their excellent electrochemical performance. Added to the large surface area, adjustable pore morphology and tailorable surface chemistry of both THCpSi and TCpSi, these nanostructures demonstrate fast electron-transfer kinetics, providing key advantages over conventional electrodes (i.e. glassy carbon electrodes, carbon-based screen-printed electrodes). The versatile surface chemistry of both THCpSi and TCpSi offers various possibilities to introduce multiple functional groups

depending on the nature of the bioreceptor to be immobilized. For proof of principle, the possibility to covalently immobilize anti-MS2 bacteriophage antibodies on a THCpSi surface previously hydrosilylated with undecylenic acid was demonstrated. This platform was then used to detect MS2 bacteriophage by means of EIS. The normalized charge-transfer resistance obtained with the MS2 immunosensor linearly increases with increasing concentration of MS2 bacteriophage, and shows a detection limit (LOD) of 4.9 pfu mL^{-1}.

In Chapter 4, a robust and highly sensitive THCpSi single layer based voltammetric sensing platform for the detection of a specific bacterial biomarker, 16S rRNA from *Escherichia coli*, is successfully developed. A fast analysis time of 15 min and a LOD of 0.183 pM target 16S rRNA were achieved in buffer. The developed 16S rRNA sensor used carbon-stabilized pSi (i.e. THCpSi) as the electrochemical transducer to interpret the hybridization event between ssDNA probes and the target 16S rRNA. Various parameters involved in the fabrication and modification of the 16S rRNA sensor (e.g. nanochannel diameter, thickness of the porous layer, concentration of ssDNA probe, etc) were firstly optimized for the detection of the ssDNA sequence equivalent to the target 16S rRNA, achieving an excellent LOD of 2 fM in buffer.

In Chapter 5, the potential for biosensing purposes of a unique and versatile carbon-stabilized pSi double-layer nanostructure is further explored. Carbon-stabilized surface chemistries were applied to pSi layers via stepwise thermal decomposition of acetylene gas under controllable reaction temperature. Specifically, a double layer nanostructure combining a top layer of TCpSi and a bottom layer of THCpSi was implemented. The hydrophilic TCpSi top layer featured -OH termination that could be further functionalized via silanization. In contrast, the hydrophobic THCpSi bottom layer enabled further functionalization via hydrosilylation with alkenes. The TCpSi-THCpSi double layer platform retained the open pore structure, tunable pore size, large available surface area and the Fabry-Pérot fringe patterns, and in addition

featured excellent electrochemical properties such as fast electron-transfer kinetics. These properties were exploited here to generate a high performance DNA sensor with a LOD of 0.4 pM based on a TCpSi-THCpSi double layer structure, showing two orders of magnitude lower LOD than those achieved by any pSi-based electrochemical DNA sensor previously reported. Compared to the LOD of 2 fM obtained using an optimized THCpSi-based DNA sensor, this LOD could be improved by proper optimization of the physical features of the double layer nanostructure (e.g. the combination of pore diameters, thickness of each porous layer, deposition of an external insulating layer, etc.) as well as the sensor working conditions (e.g. target incubation temperature and time, etc.).

In Chapter 6, uniform gold-pSi (Au-pSi) composite nanochannel arrays were developed using metal-assisted chemical etching (MACE) combined with colloidal lithography and controlled deep reactive ion etching (DRIE). This fabrication process provides the ability to tune the pore dimensions and density of ordered Au-pSi composite nanochannel arrays. Straight and highly uniform channel arrays in silicon, ranging from 100 nm to several μm in diameter, with flat gold discs at the bottom were produced. The depth and density of nanochannel arrays were well controlled by selecting the proper template size and etching time. The excellent control of the dimensions of the Au-pSi composite nanochannel arrays, and the high uniformity and regularity featured by the channel arrays, could be exploited in the future to suit the use of these platforms for electrochemical biosensing.

Finally, Chapter 7 concluded this thesis by summarizing the main findings of this research and providing an outlook of the promising development of such carbon-stabilized pSi working as electrochemical biosensors.

List of abbreviations

Au-pSi	gold-porous silicon
ATR-FTIR	attenuated total reflectance Fourier transform infrared spectroscopy
CC	chronocoulometry
CV	cyclic voltammetry
C-V	capacitance-voltage
C_{dl}	double layer capacitance
Cy5	Cyanine5
DRIE	deep reactive ion etching
DPV	differential pulse voltammetry
DNA	deoxyribonucleic acid
EDC	1-ethyl-3-(3-dimethylaminopropyl) carbodiimide hydrochloride
EIS	electrochemical impedance spectroscopy
EISC	electrolyte-insulator-semiconductor capacitor
ELISA	enzyme-linked immunosorbent assay
EM	electron microscopy
FTIR	Fourier transform infrared spectroscopy
GCE	glassy carbon electrode

h^+	holes
h	hour
HF	hydrofluoric acid
H_2O_2	hydrogen peroxide
HRP	horseradish peroxidase
HQ/Q	hydroquinone/quinone
LOD	limit of detection
MACE	metal-assisted chemical etching
min	minute
MES	2-(N-morpholino)-ethanesulfonic acid
MPTMS	mercaptopropyltrimethoxysilane
NHS	N-hydroxysuccinimide
NH_2-ssDNA	amine-conjugated single-stranded DNA
OCP	open circuit potential
PCR	polymerase chain reaction
PBS	phosphate buffered saline
PECVD	plasma enhanced chemical vapor deposition
PS	polystyrene spheres

pSi	porous silicon
R_{ct}	charge transfer resistance
R_s	solution resistance
RSD	relative standard deviation
s	second
SD	standard deviation
SEM	scanning electron microscopy
Si	silicon
SiO_2	silicon dioxide
SPE	screen printed electrode
ssDNA	single-stranded DNA
THC	thermal hydrocarbonization
THCpSi	thermally hydrocarbonized porous silicon
TC	thermal carbonization
TCpSi	thermally carbonized porous silicon
W	Warburg impedance
XPS	X-ray photoelectron microscopy
ΔEp	peak-to-peak potential difference

Δi	normalized current change

Chapter 1. Introduction

1.1 Introduction

Food and water are both essential resources for human life, but they are also a potential source of harmful microbes and chemicals.[1-2] Food and water contaminated with harmful chemical compounds, bacteria, viruses or toxins, lead to numerous diseases. Viruses are small acellular microorganisms with diameters of 20 to 300 nm, each containing only one type of nucleic acid.[3-4] They can produce a wide range of diseases in plants, animals or humans. Every year, an estimated 4.7 million cases of viral infections occur in Australia.[5] As an example, the common Norovirus is reported to be responsible for 1.6 million cases, corresponding to 18% of the foodborne illnesses.[5] Foodborne or waterborne viruses cannot replicate by themselves in food or water, so they are always present in very low numbers. Viruses have a very low infective dose, just a few infectious food particles or a little volume of infectious water is sufficient to produce illness.[6] Besides, it is difficult to detect viruses in food and water because the current culture systems are not suitable for all virus types. Conventional methods for virus detection in food and water are culture and colony counting methods, immunology-based methods and polymerase chain reaction (PCR).[6] The culture and colony counting methods involve counting of viruses via electron microscopy (EM). The immunology-based methods rely on antigen–antibody interactions and the PCR method involves nucleic acid analysis. While these techniques can provide qualitative as well as quantitative results of the tested microbes, most of them are greatly restricted by the assay time, high cost, initial enrichment of the sample with cell culture systems or intensive labor. Moreover, many viruses have a low infectious dose, rendering the accurate determination of whether or not a food item or water sample poses a health risk challenging.[7] Therefore, fast, reliable and highly sensitive diagnostic methods are necessary to ascertain and implement proper treatment of virus infections.

Medical diagnostics is the most common and necessary process to recognize patient's symptoms and signs so that a medical practitioner can make accurate medical decisions in relation to the appropriate treatment.[8-9] However, diagnostic errors such as inaccurate or delayed diagnosis are hampering the treatment and recovery of an unacceptable number of patients (**Figure 1.1**).[10] There is an increasing demand of highly efficient compact devices for improving medical diagnosis as getting the right diagnostic procedure is a key aspect of healthcare. Biomarkers in medicine have gained an increasing research interest. As biological indicators of disease, biomarkers produced by the diseased organ or by the body in response to disease provide a powerful approach to obtain vital information in medical diagnosis.[11-15] A biomarker can be specific cells, molecules, enzymes, genes or gene products, etc..[11] The biomarkers are often present in very low concentrations and also complexed with proteins or other molecules which make difficult to identify and detect them.[16] Different biomarker detection methods have been applied to diagnose many infectious diseases as well as cancer, such as enzyme-linked immunosorbent assay (ELISA), immunofluorescence, immunodiffusion, PCR, flow cytometry and many other techniques.[17-20] Most of these techniques are time consuming, labor intensive, complex, expensive or consume large volumes of samples. To overcome limitations of biomarker detection in medical diagnostics, there is an immediate need for simple, rapid, low-cost and portable diagnostic systems and methods.

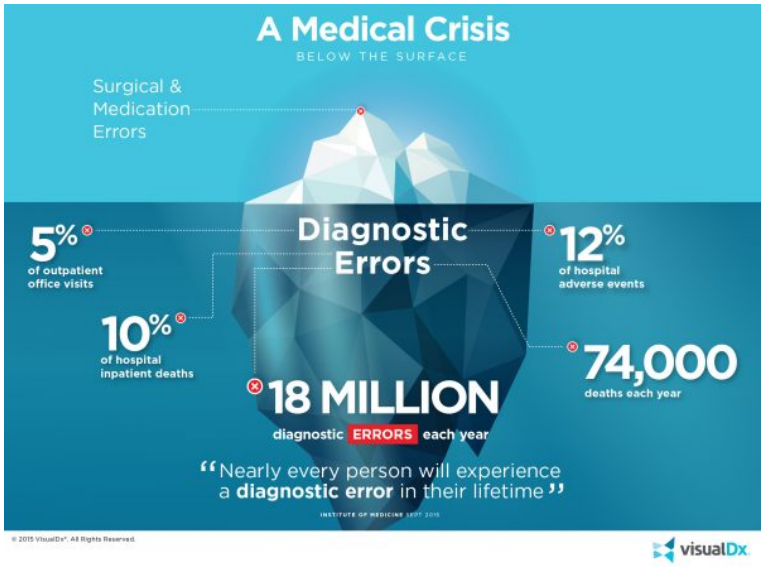

Figure 1.1 Diagnostic errors in medical diagnostics. Picture source: VisualDx (https://medcitynews.com/2016/05/diagnostic-errors-infographic/)

Biosensors have emerged as a very powerful and profitable analytical technique due to their striking features such as fast detection, high efficiency, and potential portability to resolve considerable number of central issues in many challenging areas including the quality control of food and water, and medical diagnostics.[21-23] From the global view, the significance of biosensors has been reflected by the dramatic increase in biosensor global market from the value of US$14.8 billion in 2015 to a remarkable expected value of US $ 22.6 billion in 2020.[24] In the development of biosensors, the sensitivity, selectivity, linear and dynamic ranges, limit of detection (LOD) and reproducibility are key parameters on account of the essential requirement for the practical applications to effectively recognize and quantify the target analyte.[23, 25-26]

Electrochemical biosensors have attracted a growing attention and have been widely recognized as promising candidates for portable, easy-to-use detection devices in view of the high sensitivity, fast response, high signal-to-noise ratio and relative simplicity.[27] Apart from the high sensitivity of electrochemical transduction, electrochemical biosensors also provide

the specificity of biological recognition reactions. As an integrated sensing system, electrochemical biosensors harness the affinity of a biological recognition species (such as enzymes, antibodies, DNA) to react selectively with specific targets.[28] Consequently the interaction or binding event is transduced to an electrical signal, which is in line with the concentration of the target analyte.[29]

As for commercial applications, in order to fabricate biosensors with sufficient sensitivity and specificity, fast detection speed, simplicity of operation, portability and low cost, intensive attention has been primarily paid to two directions: (i) improvement of the biorecognition elements [30]; (ii) exploitation of new nanostructured materials as electrochemical transducers (such as nanowires[31-32], carbon nanotubes[33-35], graphene[36-39], metal nanoparticles[31, 40], porous materials[41-42]). Among these candidate materials being developed for various applications in bionanotechnology, porous silicon (pSi) is a very promising one, due to its potential integration with silicon technologies, the extensive tailoring of its structural properties (pore diameter and depth), high surface area, easy and cheap fabrication and biocompatibility.[43] Not surprisingly, pSi has attracted widespread interest not only in optical sensing but also in electrochemical sensing. Especially, the combination of advantages of electrochemical techniques and the promising properties of pSi enables the design of novel sensing platforms with high selectivity and sensitivity for a wide range of practical applications.

1.2 Porous silicon (pSi)

1.2.1 Fabrication

PSi is an inorganic semiconductor that can be generated by etching crystalline silicon in aqueous or non-aqueous etchant in the presence of hydrofluoric acid (HF). In order to controllably fabricate nanostructured architectures, a wide range of approaches have been explored such as electrochemical etching[43-44], MACE[45-46], stain and galvanostatic etching[47].

One of the most common and popular pSi fabrication methods is electrochemical etching. This anodic process comprises of an etching cell, silicon wafer (anode), a constant current source, platinum wire (cathode) and an electrolyte (**Figure 1.2**).[44] The etching solution generally consists of aqueous HF as an etchant and a surfactant or wetting agent like ethanol, which lowers the surface tension of the etching solution and helps HF to access to the surface. It is possible to control the pore size, porosity, pSi layer geometrical features as well as the number of layers by fine-tuning properly selected variables (such as the current density, HF concentration, the ratio of HF to surfactant, the type of silicon, the dopant and the doping level).

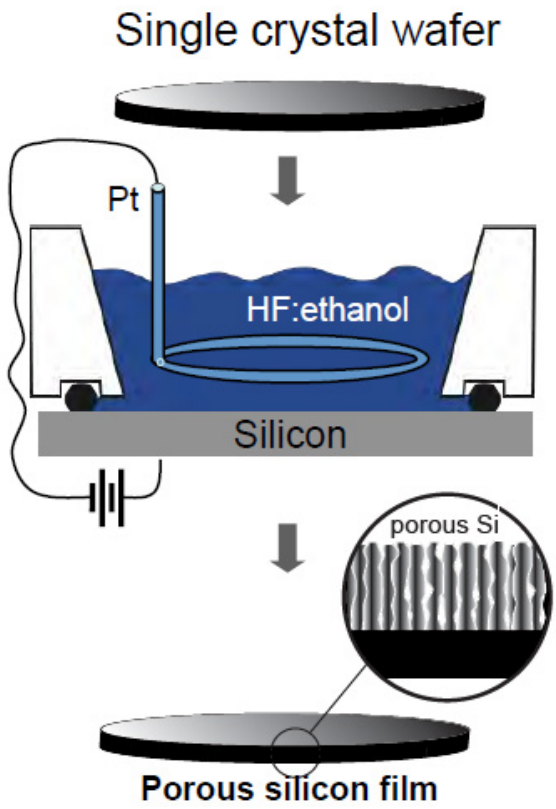

Figure 1.2 Schematic of a two-electrode electrochemical cell used to fabricate pSi.[48] The silicon chip is the working electrode. In this case, the silicon is an anode as an oxidation reaction occurs at its surface. The cathode counter-electrode is a platinum electrode.

MACE is another intriguing and controllable way to develop pSi nanostructures without the requirement of electrical bias. By proper metal-induced chemical etching, silicon substrates are

able to be etched into not only pillar arrays but also ordered pore arrays.[49] Depending on the catalytic ability of the noble metal, the final morphology of the pSi nanostructures is usually defined by the pattern of the metal catalyst used because the silicon under the metal catalyst is etched much faster by HF than the silicon without metal coverage. Instead of electrical bias, the reduction of an oxidant such as hydrogen peroxide (H_2O_2) catalyzed at the surface of the noble metal is the power supply.[45] The holes generated from the reduction are injected into the surface of silicon which is specifically oxidized and partially dissolved at the silicon-metal interface by HF.

In a typical MACE process, silicon partly coated with a noble metal is subjected to an etchant that contains HF and an oxidative agent, H_2O_2.[45-46] Depending on the catalytic activity of the noble metal, the noble metal-coated area is etched much faster than the uncoated area. After a certain time of etching, the noble metal sinks into the bottom of the substrate and relevant morphology is formed according to the initial morphologies of noble metal coverage. The processes in MACE are described in **Figure 1.3**: (1) The oxidant is preferred to be reduced at the surface of the metal catalyst and holes (h^+) are generated as a result of oxidant reduction. (2) The injection of holes takes place subsequently from the metal surface to the silicon beneath the metal. (3) The noble metal-coated silicon has a high local hole concentration and is preferentially oxidized and dissolved at the silicon-metal interface by HF. At the same time, generated byproducts, such as SiF_6^{2-}, diffuse along the silicon-metal interface as well. (4) With an increasing concentration of holes at the interface between silicon and noble metal, the noble metal-coated silicon is etched in a much faster speed by HF than the bare silicon surface. (5) The diffusion of holes occurs from the metal-coating area to bare silicon area or to the wall of the pore when the rate of hole consumption at the silicon-metal interface becomes lower compared to the rate of hole injection.

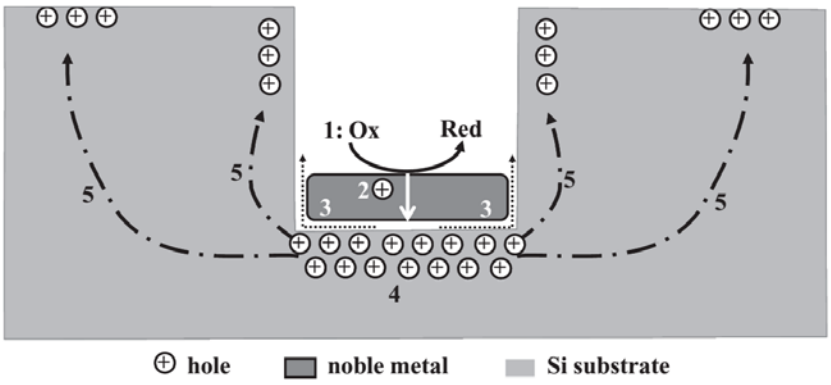

Figure 1.3 Scheme of processes involved in MACE.[45]

1.2.2 Surface stabilization

The freshly etched surface of pSi is terminated primarily with hydride species, which are highly reactive and prone to oxidation both in water and air.[44, 50-51] This limitation makes pSi unsuitable for biosensors with expected long-term stability in view of the fact that aqueous medium is inevitable in most biosensing applications. There have been several methods to stabilize the surface by means of either directly modifying freshly etched surface or further chemical transformations on purposely oxidized pSi. Silanization, hydrosilylation and carbon-stabilization are the most common surface modification procedures not only because their capability of surface passivation but also they allow the incorporation of desired chemical functionalities across the pSi surface and hence enable further immobilization of specific recognition biomolecules.[52-60]

Silanization reactions involve the silanol-based coupling with alkoxy or chloro silane compounds (**Figure 1.4**).[61] This type of reactions can attach various compounds with terminal functionalities including amines, thiols and polyethylene glycol to a pre-oxidized hydroxyl-terminated pSi surface.[62-64]

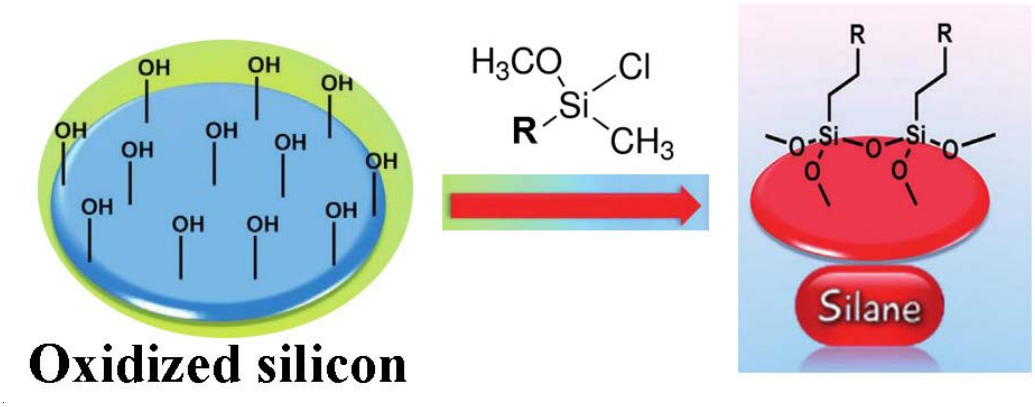

Figure 1.4 Silanization reaction on oxidized pSi surface.[65]

Hydrosilylation reactions yield stable Si-C bonded surface species by attacking a hydrogen-terminated pSi surface with an alkene or alkyne (**Figure 1.5**).[56, 59, 66-72] Hydrosilylation reactions are also able to incorporate a wide variety of chemical groups, including carboxylic acids, thiols, polyethylene glycol, alcohols and esters that then allow further chemical modification.[73-75]

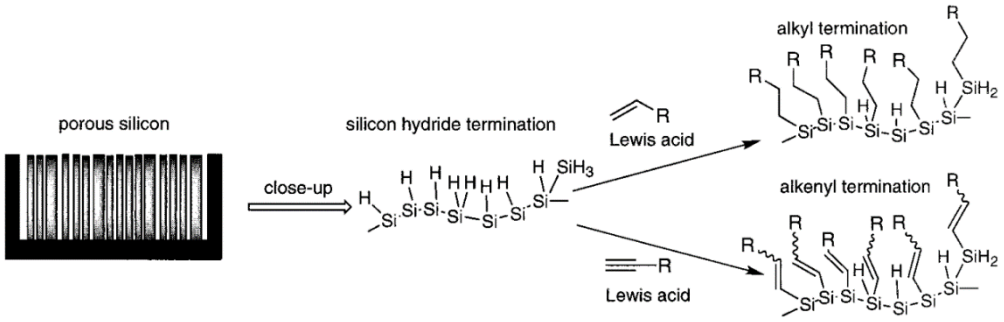

Figure 1.5 Hydrosilylation of alkenes and alkynes on freshly etched pSi surface.[66]

Carbon-stabilization via thermal decomposition of acetylene gas is another useful method to modify pSi surface, which was introduced by Salonen and coworkers.[76] This method produces a thin carbon coating on pSi surface from the reaction with gas phase acetylene at high temperature (**Figure 1.6**), which is very stable in harsh environment like in solutions with

extreme pH values such as in KOH, NaOH, HF etc..[55, 77] In detail, this carbonization reaction is based on the adsorption of acetylene molecules first onto the pSi surface and then into the nanostructures, eventually generating a nonstoichiometric SiC layer. These acetylene molecules adsorbed at room temperature undergo dissociation above 400 °C. Depending on the temperature of thermal reaction, thermal hydrocarbonization (THC) takes place at lower temperature (400-600 °C), and as an additional step, thermal carbonization (TC) is induced at a higher temperature (600-900 °C). Apart from providing carbon coverage and high chemical stability, THC and TC tune the hydrophobicity/hydrophilicity of the pSi surface, which can be used to introduce distinct chemical functionalities on the outer and inner part of the pSi structure. This carbon stabilization treatment has also been found to be non-toxic both for in vitro and in vivo applications.[78] Besides, THC and TC treatments increase the conductivity of pSi, which enables pSi to offer ample opportunities for novel electrochemical biosensors design.

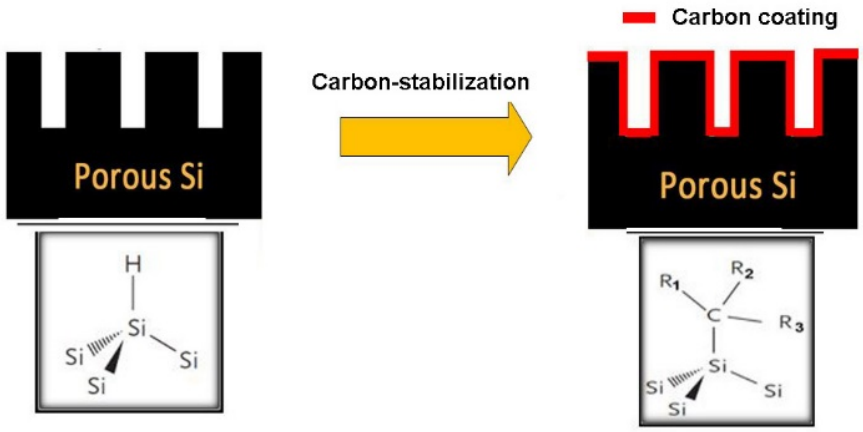

Figure 1.6 Carbon-stabilization via thermal decomposition of acetylene gas on the surface of freshly etched pSi.

1.2.3 Building a biorecognition interface

Building a biorecognition interface with a diverse range of functional groups plays a key role in the development of a highly specific biosensor, not only because its capability of providing selectivity to the biosensor towards a specific target analyte of interest but also its capability of preventing interactions with other interfering non-specific species.[27-28, 79] These non-specific binding events can either result in a false positive signal or degrade the key performance of biosensors like sensitivity and selectivity due to the fact that the reactions between pSi and interfering species change the chemical composition of pSi.[61] Numerous bioconjugation techniques to couple various specific molecules ranging from antibody,[64, 80] oligonucleotides,[81] to enzymes,[82-83] onto a functionalized surface have been well documented.[30] For instance, carbodiimide, click or maleimide chemistries can be used to build a biorecognition interface with specific bioreceptors such as antibodies and ssDNA.

1.3 Biosensors

A biosensor is an analytical device which can detect analytes and translate the biological response into a readable signal.[84] A biosensor consists of two key components, a bioreceptor and a transducer (**Figure 1.7**).[85] The bioreceptor provides selectivity through its affinity towards the analyte. The analyte binding to the bioreceptor is converted by the transducer into a measurable signal. The output can be in the form of current or a change in optical properties.[85] Biosensors have several advantages as analytical tools, such as high sensitivity and selectivity, simplicity, cost-effectiveness and short analysis time.[86] They can be easily miniaturized enabling their use as portable point-of-care devices.[86] According to their biorecognition element, biosensors can be classified as immunosensors, DNA sensors, enzymatic sensors, tissue-based sensors, etc.. According to the transducing mechanism, biosensors can be also classified as electrochemical, optical, piezoelectric, etc. biosensors.

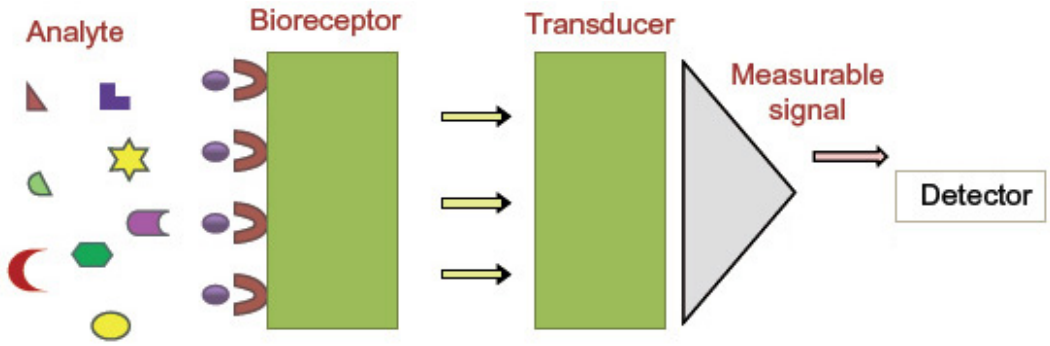

Figure 1.7 A typical representation of a biosensor.[87]

1.4 Electrochemical biosensors

As shown in **Figure 1.8**, electrochemical transduction interprets the binding events to a measurable current (amperometry), charge accumulation or potential (potentiometry), change in resistance (impedance) or in the conductive properties of the medium between electrodes (conductometry).[28, 88] According to the detection technique, electrochemical biosensors can be divided into four types: amperometric/voltammetric, potentiometric, impedimetric and conductometric.

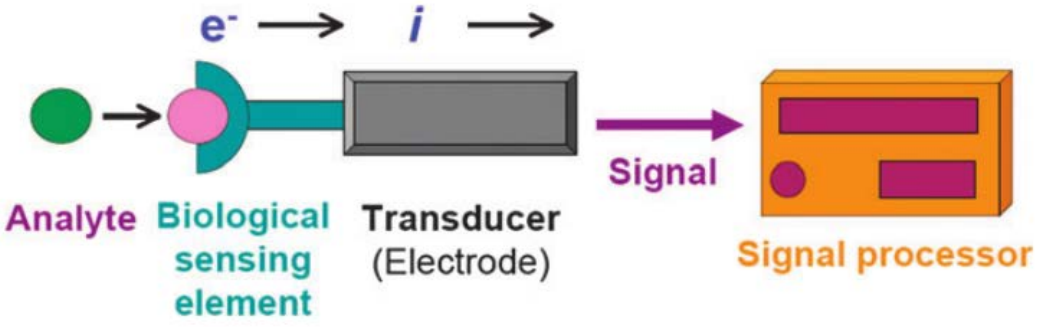

Figure 1.8. Schematic of an electrochemical biosensor.[28]

1.4.1 Amperometric and voltammetric biosensors

Amperometric and voltammetric techniques measure the current that flows between the working and auxiliary electrodes, when a potential is applied. On the one hand, if the change of current is monitored over time at a constant potential, it is termed as amperometry.[28, 89] On the other hand, if changes in current are measured during a set potential range, this is termed as voltammetry. Amperometric/voltammetric biosensors mainly focus on monitoring the changes in current due to the redox reactions at the working electrode when the target molecule is recognized by the bioreceptor. A label is usually required if the analyte of interest is not electroactive. These labels can produce electroactive products by catalytic conversion, then undergo the oxidation or reduction and result in current changes that are quantitatively related to the concentration of target analyte. Electroactive species can also be introduced into the electrochemical system, then the charge transfer takes place at the partially blocked electrode/solution interface, with a magnitude that is quantitatively proportional to the amount of bound analyte.

1.4.2 Potentiometric biosensors

The measured parameter in potentiometry is the potential difference between the working and reference electrodes in electrochemical devices with negligible current flow.[90-94] Potentiometric biosensors are promising in practical applications as many of them are commercially available such as those developed by glass electrodes and metal oxides.[95]

1.4.3 Impedimetric biosensors

Electrochemical impedance spectroscopy (EIS) is a widely utilized technique to measure resistive and capacitive properties of materials through the application of a small sinusoidally varying potential [28]. By adjusting the excitation frequency of the applied potential, the complex impedance can be calculated, including real impedance (resistance) and imaginary impedance

(capacitance and inductance). Due to the ability of directly probing the interfacial properties of a modified electrode, EIS has rapidly been developed to monitor biorecognition events at the electrode surface. EIS can work as a label-free sensing system, where changes in the electrical properties of the surface (e.g. capacitance, resistance) can be measured from the solely presence of target molecules. Besides, labels can also be introduced into impedimetric sensing systems as to increase selectivity and enhance sensitivity. A major drawback of EIS is the potential interaction of other substances at the electrode surface.[96] Due to the high sensitivity of EIS, non-specific adsorption can have an effect on the monitored signal and thus cause interference.

1.4.4 Conductometric biosensors

Conductometric biosensors monitor the changes in conductivity upon analyte detection. Conductometric biosensors often include enzymes whose charged products result in ionic strength changes, and thus increased conductivity. Conductometric biosensors have been widely used in different applications such as environmental monitoring, clinical analysis and the detection of foodborne pathogens.[28]

1.5 Thesis aims, tasks and research methodology

1.5.1 Thesis aims

PSi has demonstrated its advantages and versatility in biosensor applications since Sailor and coworkers first reported the use of oxidized pSi as optical transducer to investigate basic biological systems.[51] Its pore morphological parameters (e.g. pore size, pore depth and porosity) can be easily adjusted by simply varying the electrochemical anodization parameters (i.e. current density, etching time, HF and ethanol ratio) used to fabricate pSi.[97] The ease of controlling pore morphology has implications in its sensing capabilities and has driven advances in the detection of a large range of chemical and biological species.[81, 98-101] Other features of pSi, such as the large available internal surface area and excellent biocompatibility,

have also been harnessed to develop high performing biosensing platforms.[102-106] Of particular interest for biosensing purposes is the versatile surface chemistry of pSi, allowing a wide range of functionalization routes (e.g. hydrosilylation,[56, 59, 67-72] silanization[62-64]) to attach functional groups further used to covalently immobilize diverse biomolecules as bioreceptors (e.g. antibodies,[64, 80] oligonucleotides,[81] enzymes[82-83]). However, the use of pSi to develop electrochemical biosensors has been limited even though this type of biosensors is able to offer a promising way to detect target analytes featuring ease of use, rapid and robust detection, low cost, miniaturization potential and hence portability.[107-108] The main challenge of using pSi as electrochemical transducer is the unavoidable growth of an insulating SiO_2 layer at the surface. Additionally, the area and geometry of the porous electrode surface strongly affect the double-layer capacitance, which can cause significant capacitive effects.[109] In order to limit the growth of SiO_2 on the pSi and render pSi fit for the purpose of electrochemical sensing, researchers have reported various pSi modifications to preserve the semiconductor properties of silicon or to introduce conductive coatings (e.g. metal[110-113] or conductive polymeric layers[67, 114]) with the aim of developing pSi-based electrochemical biosensors. To indirectly overcome the limitations in using pSi for electrochemical sensing purposes, Reta and coworkers recently explored the use of hydrosilylated pSi membrane-modified gold electrodes to develop label-free immunosensors based on voltammetric detection.[115]

The aim of this thesis is to explore the potential to directly use carbon-stabilized pSi nanostructures as electrochemical transducers to create the next generation of highly sensitive, cost-effective and label-free electrochemical biosensors for target analytes of potential interest in viral detection for water quality control, and bacterial 16S rRNA detection for medical diagnosis. Specifically, this thesis aims to:

(a) Design, fabricate and characterize electrochemical transducers based on pSi nanostructures

(1) Engineer pSi nanostructures. Fabricate pSi single and double layer nanostructures via electrochemical anodization. Additionally, design and fabricate uniform Au-pSi composite nanochannel arrays using MACE combined with colloidal lithography and DRIE.

(2) Improve the conductivity and chemical stability of pSi nanostructures. Employ carbon-stabilization process via thermal decomposition of acetylene to render pSi and Au-pSi nanostructures suitable for electrochemical transduction, leaving the pore structure intact, while providing high chemical stability, controllable hydrophilicity, and versatile surface chemistry.

(3) Investigate the electrochemical performance of carbon-stabilized pSi nanostructures (including THCpSi and TCpSi single layers, TCpSi-THCpSi double layer and Au-THCpSi composite nanochannel arrays) and demonstrate their suitability for electrochemical transducer design.

(b) Develop electrochemical biosensors for label-free detection of analytes

(1) Design, fabricate and functionalize various impedimetric and voltammetric biosensors using the previously optimized carbon-stabilized pSi single and double layer nanostructures. Apply nanochannel blockage as sensing mechanism, based on measuring the partial blockage caused upon analyte binding to the immobilized bioreceptor, for the label-free detection of analytes of interest including MS2 bacteriophage, ssDNA and *Escherichia coli* 16S rRNA.

(2) Optimize the sensing performance of the developed biosensors including selectivity, sensitivity and limit of detection by properly tuning the pore dimensions of these electrochemical transducers (i.e. carbon-stabilized pSi nanostructures) and suitably choosing the functionalization strategy.

1.5.2 Tasks and research methodology

In order to achieve the aims, the project is divided into 4 tasks:

Task 1: Fabrication of pSi nanostructures. Depending on the size of the target analytes to detect, different morphological features (such as diameter, length) of the pSi nanochannels ranging from single layer to multi layers were fabricated either by electrochemical anodization or MACE.

Task 2: Carbon-stabilization of pSi surface. The freshly etched pSi nanostructures were immediately carbon-stabilized via thermal decomposition of acetylene gas.[116-117] Then SEM was used to characterize the morphology (such as diameter and depth) of carbon-stabilized pSi nanostructures. The surface chemistry and chemical composition of carbon-stabilized pSi (both THCpSi and TCpSi) was analyzed by FTIR, XPS and Raman spectroscopy. Electrochemical characterization techniques such as cyclic voltammetry (CV), chronocoulometry (CC) and EIS were used to investigate the electrochemical performance of carbon-stabilized pSi nanostructures (both THCpSi and TCpSi) directly working as electrochemical transducers. Several redox pairs, $[Fe(CN)_6]^{3-/4-}$, $[Ru(NH_3)_6]^{2+/3+}$ and hydroquinone/quinone (HQ/Q) were used during these electrochemical analyses.

Task 3: Biorecognition interface development of carbon-stabilized pSi. Different chemical functionalities (such as carboxyl groups) were further introduced onto the surface of carbon-stabilized pSi via hydrosilylation or silanization.[116, 118] Bioreceptors such as antibodies and ssDNA, were conjugated onto the surface to develop a biorecognition interface for specific detection. Conjugation methods, such as carbodiimide chemistry, were used to build the biorecognition interface.[59, 115]

Task 4: Electrochemical detection of target analytes. The bio-inspired carbon-stabilized pSi nanostructures (e.g. single and double layers) were used as electrochemical transducers to design sensors for detection of various analytes based on the sensing mechanism of nanochannel blockage.[22, 115] EIS and DPV were used as electrochemical detection techniques

to quantify the partial nanochannel blockage caused upon analyte binding.[115] The sensing mechanism based on nanochannel blockage for label-free detection of a target is shown in **Figure 1.9**. When the target is captured by the probe immobilized at the surface of the nanochannels, the specific binding event causes partial blockage of the nanochannels. And this partial nanochannel blockage hinders the diffusion of a redox species added in solution, such as $[Fe(CN)_6]^{3-/4-}$, towards the transducer surface, resulting in a decrease in the intensity of peak current monitored by DPV or an increase in the value of charge transfer resistance measured by EIS.

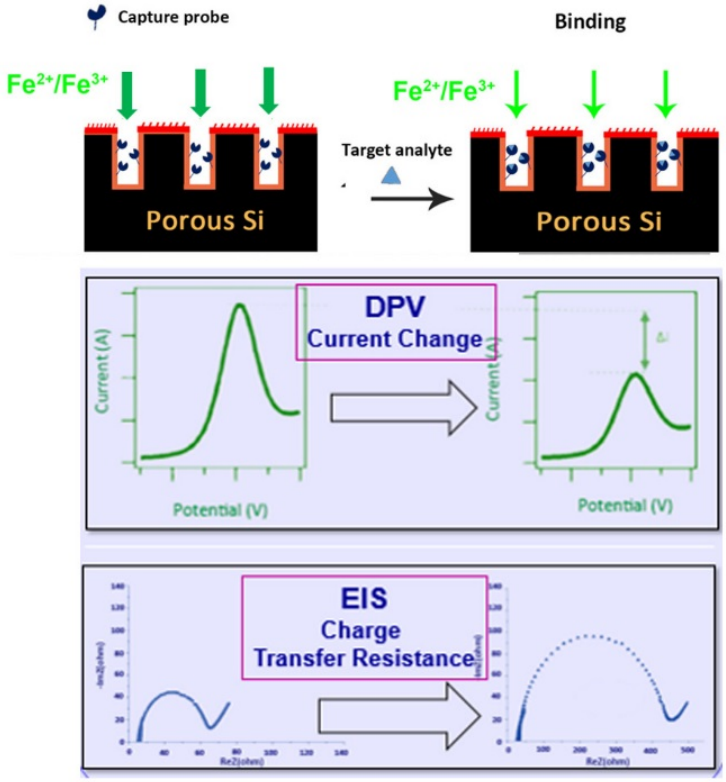

Figure 1.9 Sensing mechanism based on nanochannel blockage for label-free detection of target analytes.

1.6 References

1. Keenan, K. P.; Wallig, M. A.; Haschek, W. M., Nature Via Nurture: Effect of Diet on Health, Obesity, and Safety Assessment. *Toxicol. Pathol.* **2013,** *41* (2), 190-209.

2. Springmann, M.; Clark, M.; Mason-D'Croz, D.; Wiebe, K.; Bodirsky, B. L.; Lassaletta, L.; de Vries, W.; Vermeulen, S. J.; Herrero, M.; Carlson, K. M.; Jonell, M.; Troell, M.; DeClerck, F.; Gordon, L. J.; Zurayk, R.; Scarborough, P.; Rayner, M.; Loken, B.; Fanzo, J.; Godfray, H. C. J.; Tilman, D.; Rockström, J.; Willett, W., Options for Keeping the Food System within Environmental Limits. *Nature* **2018,** *562* (7728), 519-525.

3. Velusamy, V.; Arshak, K.; Korostynska, O.; Oliwa, K.; Adley, C., An Overview of Foodborne Pathogen Detection: In the Perspective of Biosensors. *Biotechnol. Adv.* **2010,** *28* (2), 232-254.

4. Yuan, S.; Chu, H.; Chan, J. F.-W.; Ye, Z.-W.; Wen, L.; Yan, B.; Lai, P.-M.; Tee, K.-M.; Huang, J.; Chen, D.; Li, C.; Zhao, X.; Yang, D.; Chiu, M. C.; Yip, C.; Poon, V. K.-M.; Chan, C. C.-S.; Sze, K.-H.; Zhou, J.; Chan, I. H.-Y.; Kok, K.-H.; To, K. K.-W.; Kao, R. Y.-T.; Lau, J. Y.-N.; Jin, D.-Y.; Perlman, S.; Yuen, K.-Y., Srebp-Dependent Lipidomic Reprogramming as a Broad-Spectrum Antiviral Target. *Nat. Commun.* **2019,** *10* (1), 120.

5. Fleet, G. H.; Heiskanen, P.; Reid, I.; Buckle, K. A., Foodborne Viral Illness-Status in Australia. *Int. J. Food Microbiol.* **2000,** *59* (1-2), 127-136.

6. Bosch, A.; Sánchez, G.; Abbaszadegan, M.; Carducci, A.; Guix, S.; Le Guyader, F. S.; Netshikweta, R.; Pintó, R. M.; Van Der Poel, W. H.; Rutjes, S., Analytical Methods for Virus Detection in Water and Food. *Food Anal. Methods* **2011,** *4* (1), 4-12.

7. Connelly, J. T.; Baeumner, A. J., Biosensors for the Detection of Waterborne Pathogens. *Anal. Bioanal. Chem.* **2012,** *402* (1), 117-127.

8. Damestani, Y.; Reynolds, C. L.; Szu, J.; Hsu, M. S.; Kodera, Y.; Binder, D. K.; Park, B. H.; Garay, J. E.; Rao, M. P.; Aguilar, G., Transparent Nanocrystalline Yttria-Stabilized-Zirconia Calvarium Prosthesis. *Nanomedicine-Nanotechnol.* **2013,** *9* (8), 1135-1138.

9. National Academies of Sciences, E.; Medicine, *Improving Diagnosis in Health Care*. National Academies Press: **2016**.

10. Johnson, P. E.; Duran, A. S.; Hassebrock, F.; Moller, J.; Prietula, M.; Feltovich, P. J.; Swanson, D. B., Expertise and Error in Diagnostic Reasoning. *Cogn. Sci.* **1981,** *5* (3), 235-283.

11. Fathi, E.; Mesbah-Namin, S. A.; Farahzadi, R., Biomarkers in Medicine: An Overview. *Br. J. Med. Med. Res.* **2014,** *4* (8), 1701.

12. Mosley, J. D.; Feng, Q.; Wells, Q. S.; Van driest, S. L.; Shaffer, C. M.; Edwards, T. L.; Bastarache, L.; Wei, W.-Q.; Davis, L. K.; McCarty, C. A.; Thompson, W.; Chute, C. G.; Jarvik, G. P.; Gordon, A. S.; Palmer, M. R.; Crosslin, D. R.; Larson, E. B.; Carrell, D. S.; Kullo, I. J.; Pacheco, J. A.; Peissig, P. L.; Brilliant, M. H.; Linneman, J. G.; Namjou, B.; Williams, M. S.; Ritchie, M. D.; Borthwick, K. M.; Verma, S. S.; Karnes, J. H.; Weiss, S. T.; Wang, T. J.; Stein, C. M.; Denny, J. C.; Roden, D. M., A Study Paradigm Integrating Prospective Epidemiologic Cohorts and Electronic Health Records to Identify Disease Biomarkers. *Nat. Commun.* **2018,** *9* (1), 3522.

13. Hussein, A. A.; Forouzanfar, T.; Bloemena, E.; de Visscher, J.; Brakenhoff, R. H.; Leemans, C. R.; Helder, M. N., A Review of the Most Promising Biomarkers for Early Diagnosis and Prognosis Prediction of Tongue Squamous Cell Carcinoma. *Br. J. Cancer* **2018,** *119* (6), 724-736.

14. Sina, A. A. I.; Carrascosa, L. G.; Liang, Z.; Grewal, Y. S.; Wardiana, A.; Shiddiky, M. J. A.; Gardiner, R. A.; Samaratunga, H.; Gandhi, M. K.; Scott, R. J.; Korbie, D.; Trau, M., Epigenetically Reprogrammed Methylation Landscape drives the DNA Self-Assembly and Serves as a Universal Cancer Biomarker. *Nat. Commun.* **2018,** *9* (1), 4915.

15. Teder, H.; Koel, M.; Paluoja, P.; Jatsenko, T.; Rekker, K.; Laisk-Podar, T.; Kukuškina, V.; Velthut-Meikas, A.; Fjodorova, O.; Peters, M.; Kere, J.; Salumets, A.; Palta, P.; Krjutškov,

K., Tac-Seq: Targeted DNA and Rna Sequencing for Precise Biomarker Molecule Counting. *NPJ Genom. Med.* **2018,** *3* (1), 34.

16. Rifai, N.; Gillette, M. A.; Carr, S. A., Protein Biomarker Discovery and Validation: The Long and Uncertain Path to Clinical Utility. *Nat. Biotechnol.* **2006,** *24* (8), 971.

17. Al-Harthi, L.; Marchetti, G.; Steffens, C. M.; Poulin, J.-F.; Sékaly, R.-P.; Landay, A., Detection of T Cell Receptor Circles (Trecs) as Biomarkers for De Novo T Cell Synthesis Using a Quantitative Polymerase Chain Reaction–Enzyme Linked Immunosorbent Assay (Pcr–Elisa). *J. Immunol. Methods* **2000,** *237* (1-2), 187-197.

18. Jin, X.; Jin, X.; Jung, J.-E.; Beck, S.; Kim, H., Cell Surface Nestin Is a Biomarker for Glioma Stem Cells. *Biochem. Biophys. Res. Commun.* **2013,** *433* (4), 496-501.

19. Talyzina, N. M.; Moldowan, J. M.; Johannisson, A.; Fago, F. J., Affinities of Early Cambrian Acritarchs Studied by Using Microscopy, Fluorescence Flow Cytometry and Biomarkers. *Rev. Palaeobot. Palynol.* **2000,** *108* (1-2), 37-53.

20. Boyle, D. L.; Rosengren, S.; Bugbee, W.; Kavanaugh, A.; Firestein, G. S., Quantitative Biomarker Analysis of Synovial Gene Expression by Real-Time Pcr. *Arthritis Res. Ther.* **2003,** *5* (6), R352.

21. Kilian, K. A.; Böcking, T.; Gaus, K.; Gooding, J. J., Introducing Distinctly Different Chemical Functionalities onto the Internal and External Surfaces of Mesoporous Materials. *Angew. Chem. Int. Ed.* **2008,** *47* (14), 2697-2699.

22. Reta, N.; Saint, C. P.; Michelmore, A.; Prieto-Simón, B.; Voelcker, N. H., Nanostructured Electrochemical Biosensors for Label-Free Detection of Water-and Food-Borne Pathogens. *ACS Appl. Mater. Interfaces* **2018**.

23. Jane, A.; dronov, R.; Hodges, A.; Voelcker, N. H., Porous Silicon Biosensors on the Advance. *Trends Biotechnol.* **2009,** *27* (4), 230-239.

24. Global Market Study on Biosensor: Asia-Pacific to Witness Highest Growth by 2020. **2014**.

25. Eggins, B. R., *Chemical Sensors and Biosensors*. John Wiley & Sons: **2008**; Vol. 28.

26. Yeom, S.-J.; Kim, M.; Kwon, K. K.; Fu, Y.; Rha, E.; Park, S.-H.; Lee, H.; Kim, H.; Lee, D.-H.; Kim, D.-M.; Lee, S.-G., A Synthetic Microbial Biosensor for High-Throughput Screening of Lactam Biocatalysts. *Nat. Commun.* **2018,** *9* (1), 5053.

27. Kirsch, J.; Siltanen, C.; Zhou, Q.; Revzin, A.; Simonian, A., Biosensor Technology: Recent Advances in Threat Agent Detection and Medicine. *Chem. Soc. Rev.* **2013,** *42* (22), 8733-8768.

28. Ronkainen, N. J.; Halsall, H. B.; Heineman, W. R., Electrochemical Biosensors. *Chem. Soc. Rev.* **2010,** *39* (5), 1747-1763.

29. Bakker, E.; Telting-Diaz, M., Electrochemical Sensors. *Anal. Chem.* **2002,** *74* (12), 2781-2800.

30. Hermanson, G. T., *Bioconjugate Techniques*. Academic press: **2013**.

31. Guo, S.; Wen, D.; Dong, S.; Wang, E., Gold Nanowire Assembling Architecture for H 2 O 2 Electrochemical Sensor. *Talanta* **2009,** *77* (4), 1510-1517.

32. Xia, C.; Ning, W., A Novel Non-Enzymatic Electrochemical Glucose Sensor Modified with Feooh Nanowire. *Electrochem. Commun.* **2010,** *12* (11), 1581-1584.

33. Ramnani, P.; Saucedo, N. M.; Mulchandani, A., Carbon Nanomaterial-Based Electrochemical Biosensors for Label-Free Sensing of Environmental Pollutants. *Chemosphere* **2016,** *143*, 85-98.

34. Zhao, Q.; Gan, Z.; Zhuang, Q., Electrochemical Sensors Based on Carbon Nanotubes. *Electroanalysis* **2002,** *14* (23), 1609-1613.

35. Zhang, M.; Smith, A.; Gorski, W., Carbon Nanotube− Chitosan System for Electrochemical Sensing Based on Dehydrogenase Enzymes. *Anal. Chem.* **2004,** *76* (17), 5045-5050.

36. Pumera, M.; Ambrosi, A.; Bonanni, A.; Chng, E. L. K.; Poh, H. L., Graphene for Electrochemical Sensing and Biosensing. *Trends Anal. Chem.* **2010,** *29* (9), 954-965.

37. Guo, S.; Wen, D.; Zhai, Y.; Dong, S.; Wang, E., Platinum Nanoparticle Ensemble-on-Graphene Hybrid Nanosheet: One-Pot, Rapid Synthesis, and Used as New Electrode Material for Electrochemical Sensing. *ACS Nano* **2010,** *4* (7), 3959-3968.

38. Zhang, Y.; Sun, X.; Zhu, L.; Shen, H.; Jia, N., Electrochemical Sensing Based on Graphene Oxide/Prussian Blue Hybrid Film Modified Electrode. *Electrochim. Acta* **2011,** *56* (3), 1239-1245.

39. Zeng, Q.; Cheng, J.; Tang, L.; Liu, X.; Liu, Y.; Li, J.; Jiang, J., Self-Assembled Graphene–Enzyme Hierarchical Nanostructures for Electrochemical Biosensing. *Adv. Func. Mater.* **2010,** *20* (19), 3366-3372.

40. Hrapovic, S.; Liu, Y.; Male, K. B.; Luong, J. H., Electrochemical Biosensing Platforms Using Platinum Nanoparticles and Carbon Nanotubes. *Anal. Chem.* **2004,** *76* (4), 1083-1088.

41. Rai, V.; Deng, J.; Toh, C.-S., Electrochemical Nanoporous Alumina Membrane-Based Label-Free DNA Biosensor for the Detection of Legionella Sp. *Talanta* **2012,** *98*, 112-117.

42. Ye, W.; Xu, Y.; Zheng, L.; Zhang, Y.; Yang, M.; Sun, P., A Nanoporous Alumina Membrane Based Electrochemical Biosensor for Histamine Determination with Biofunctionalized Magnetic Nanoparticles Concentration and Signal Amplification. *Sensors* **2016,** *16* (10), 1767.

43. Lin, V. S.; Motesharei, K.; Dancil, K. P.; Sailor, M. J.; Ghadiri, M. R., A Porous Silicon-Based Optical Interferometric Biosensor. *Science* **1997,** *278* (5339), 840-843.

44. Sailor, M. J., *Porous Silicon in Practice*. John Wiley & Sons: **2012**.

45. Huang, Z.; Geyer, N.; Werner, P.; De Boor, J.; Gösele, U., Metal-Assisted Chemical Etching of Silicon: A Review. *Adv. Mater.* **2011,** *23* (2), 285-308.

46. Han, H.; Huang, Z.; Lee, W., Metal-Assisted Chemical Etching of Silicon and Nanotechnology Applications. *Nano Today* **2014,** *9* (3), 271-304.

47. Canham, L. T. In *Properties of Porous Silicon*, Institution of Electrical Engineers: 1997.

48. Sailor, M. J., Fundamentals of Porous Silicon Preparation. *Porous Silicon in Practice: Preparation, Characterization and Applications* **2012**, 1-42.

49. Hochbaum, A. I.; Gargas, D.; Hwang, Y. J.; Yang, P., Single Crystalline Mesoporous Silicon Nanowires. *Nano. Lett.* **2009,** *9* (10), 3550-3554.

50. Dhanekar, S.; Jain, S., Porous Silicon Biosensor: Current Status. *Biosens. Bioelectron.* **2013,** *41*, 54-64.

51. Lin, V. S.-Y.; Motesharei, K.; Dancil, K.-P. S.; Sailor, M. J.; Ghadiri, M. R., A Porous Silicon-Based Optical Interferometric Biosensor. *Science* **1997,** *278* (5339), 840-843.

52. Buriak, J. M., Silicon-Carbon Bonds on Porous Silicon Surfaces. *Adv. Mater.* **1999,** *11* (3), 265-267.

53. Schwartz, M. P.; Cunin, F.; Cheung, R. W.; Sailor, M. J., Chemical Modification of Silicon Surfaces for Biological Applications. *Phys. Satatus Solidi A* **2005,** *202* (8), 1380-1384.

54. Sweetman, M. J.; Ronci, M.; Ghaemi, S. R.; Craig, J. E.; Voelcker, N. H., Porous Silicon Films Micropatterned with Bioelements as Supports for Mammalian Cells. *Adv. Func. Mater.* **2012,** *22* (6), 1158-1166.

55. Salonen, J.; Björkqvist, M.; Laine, E.; Niinistö, L., Stabilization of Porous Silicon Surface by Thermal Decomposition of Acetylene. *Appl. Surf. Sci.* **2004,** *225* (1), 389-394.

56. Langner, A.; Panarello, A.; Rivillon, S.; Vassylyev, O.; Khinast, J. G.; Chabal, Y. J., Controlled Silicon Surface Functionalization by Alkene Hydrosilylation. *J. Am. Chem. Soc.* **2005,** *127* (37), 12798-12799.

57. Scheres, L.; Giesbers, M.; Zuilhof, H., Organic Monolayers onto Oxide-Free Silicon with Improved Surface Coverage: Alkynes Versus Alkenes. *Langmuir* **2010,** *26* (7), 4790-4795.

58. Tsang, C. K.; Kelly, T. L.; Sailor, M. J.; Li, Y. Y., Highly Stable Porous Silicon–Carbon Composites as Label-Free Optical Biosensors. *ACS Nano* **2012,** *6* (12), 10546-10554.

59. Sweetman, M. J.; McInnes, S. J. P.; Vasani, R. B.; Guinan, T.; Blencowe, A.; Voelcker, N. H., Rapid, Metal-Free Hydrosilanisation Chemistry for Porous Silicon Surface Modification. *Chem. Commun.* **2015,** *51* (53), 10640-10643.

60. Pujari, S. P.; Scheres, L.; Marcelis, A. T.; Zuilhof, H., Covalent Surface Modification of Oxide Surfaces. *Angew. Chem. Int. Ed.* **2014,** *53* (25), 6322-6356.

61. Kilian, K. A.; Bocking, T.; Gooding, J. J., The Importance of Surface Chemistry in Mesoporous Materials: Lessons from Porous Silicon Biosensors. *Chem Commun (Camb)* **2009,** (6), 630-640.

62. Kim, D.; Zuidema, J. M.; Kang, J.; Pan, Y.; Wu, L.; Warther, D.; Arkles, B.; Sailor, M. J., Facile Surface Modification of Hydroxylated Silicon Nanostructures Using Heterocyclic Silanes. *J. Am. Chem. Soc.* **2016,** *138* (46), 15106-15109.

63. Krueger, N. A.; Holsteen, A. L.; Kang, S.-K.; Ocier, C. R.; Zhou, W.; Mensing, G.; Rogers, J. A.; Brongersma, M. L.; Braun, P. V., Porous Silicon Gradient Refractive Index Micro-Optics. *Nano. Lett.* **2016,** *16* (12), 7402-7407.

64. Delalat, B.; Sheppard, V. C.; Rasi Ghaemi, S.; Rao, S.; Prestidge, C. A.; McPhee, G.; Rogers, M.-L.; Donoghue, J. F.; Pillay, V.; Johns, T. G.; Kröger, N.; Voelcker, N. H., Targeted drug Delivery Using Genetically Engineered Diatom Biosilica. *Nat. Commun.* **2015,** *6*, 8791.

65. Pujari, S. P.; Scheres, L.; Marcelis, A. T. M.; Zuilhof, H., Covalent Surface Modification of Oxide Surfaces. *Angew. Chem. Int. Ed.* **2014,** *53* (25), 6322-6356.

66. Sweetman, M. J.; Harding, F. J.; Graney, S. D.; Voelcker, N. H., Effect of Oligoethylene Glycol Moieties in Porous Silicon Surface Functionalisation on Protein Adsorption and Cell Attachment. *Appl. Surf. Sci.* **2011,** *257* (15), 6768-6774.

67. Islam, M. A.; Sinelnikov, R.; Howlader, M. A.; Faramus, A.; Veinot, J. G. C., Mixed Surface Chemistry: An Approach to Highly Luminescent Biocompatible Amphiphilic Silicon Nanocrystals. *Chem. Mater.* **2018,** *30* (24), 8925-8931.

68. Buriak, J. M., Illuminating Silicon Surface Hydrosilylation: An Unexpected Plurality of Mechanisms. *Chem. Mater.* **2014,** *26* (1), 763-772.

69. Buriak, J. M.; Stewart, M. P.; Geders, T. W.; Allen, M. J.; Choi, H. C.; Smith, J.; Raftery, D.; Canham, L. T., Lewis Acid Mediated Hydrosilylation on Porous Silicon Surfaces. *J. Am. Chem. Soc.* **1999,** *121* (49), 11491-11502.

70. Stewart, M. P.; Buriak, J. M., Exciton-Mediated Hydrosilylation on Photoluminescent Nanocrystalline Silicon. *J. Am. Chem. Soc.* **2001,** *123* (32), 7821-7830.

71. Escorihuela, J.; Zuilhof, H., Rapid Surface Functionalization of Hydrogen-Terminated Silicon by Alkyl Silanols. *J. Am. Chem. Soc.* **2017,** *139* (16), 5870-5876.

72. Zhukhovitskiy, A. V.; Mavros, M. G.; Queeney, K. T.; Wu, T.; Voorhis, T. V.; Johnson, J. A., Reactions of Persistent Carbenes with Hydrogen-Terminated Silicon Surfaces. *J. Am. Chem. Soc.* **2016,** *138* (27), 8639-8652.

73. Schmeltzer, J.; Porter, L. A.; Stewart, M. P.; Buriak, J. M., Hydride Abstraction Initiated Hydrosilylation of Terminal Alkenes and Alkynes on Porous Silicon. *Langmuir* **2002,** *18* (8), 2971-2974.

74. Boukherroub, R.; Petit, A.; Loupy, A.; Chazalviel, J.-N.; Ozanam, F., Microwave-Assisted Chemical Functionalization of Hydrogen-Terminated Porous Silicon Surfaces. *J. Phys. Chem. B* **2003,** *107* (48), 13459-13462.

75. Britcher, L.; Barnes, T. J.; Griesser, H. J.; Prestidge, C. A., Pegylation of Porous Silicon Using Click Chemistry. *Langmuir* **2008,** *24* (15), 7625-7627.

76. Salonen, J.; Lehto, V. P.; Björkqvist, M.; Laine, E.; Niinistö, L., Studies of Thermally-Carbonized Porous Silicon Surfaces. *Phys. Satatus Solidi A* **2000,** *182* (1), 123-126.

77. Salonen, J.; Laine, E.; Niinistö, L., Thermal Carbonization of Porous Silicon Surface by Acetylene. *J. Appl. Phys.* **2002,** *91* (1), 456-461.

78. Bimbo, L. M.; Sarparanta, M.; Santos, H. A.; Airaksinen, A. J.; Mäkilä, E.; Laaksonen, T.; Peltonen, L.; Lehto, V.-P.; Hirvonen, J.; Salonen, J., Biocompatibility of Thermally Hydrocarbonized Porous Silicon Nanoparticles and Their Biodistribution in Rats. *ACS Nano* **2010,** *4* (6), 3023-3032.

79. Pacholski, C.; Sartor, M.; Sailor, M. J.; Cunin, F.; Miskelly, G. M., Biosensing Using Porous Silicon Double-Layer Interferometers: Reflective Interferometric Fourier Transform Spectroscopy. *J. Am. Chem. Soc.* **2005,** *127* (33), 11636-11645.

80. Cunin, F.; Schmedake, T. A.; Link, J. R.; Li, Y. Y.; Koh, J.; Bhatia, S. N.; Sailor, M. J., Biomolecular Screening with Encoded Porous-Silicon Photonic Crystals. *Nat. Mater.* **2002,** *1*, 39.

81. Jenison, R.; Yang, S.; Haeberli, A.; Polisky, B., Interference-Based Detection of Nucleic Acid Targets on Optically Coated Silicon. *Nat. Biotechnol.* **2001,** *19*, 62.

82. Orosco, M. M.; Pacholski, C.; Sailor, M. J., Real-Time Monitoring of Enzyme Activity in a Mesoporous Silicon Double Layer. *Nat. Nanotechnol.* **2009,** *4*, 255.

83. Rémond, E.; Martin, C.; Martinez, J.; Cavelier, F., Silicon-Containing Amino Acids: Synthetic Aspects, Conformational Studies, and Applications to Bioactive Peptides. *Chem. Rev.* **2016,** *116* (19), 11654-11684.

84. Mehrotra, P., Biosensors and Their Applications - A Review. *J. Oral. Biol. Craniofac. Res.* **2016,** *6* (2), 153-159.

85. Ali, J.; Najeeb, J.; Asim Ali, M.; Farhan Aslam, M.; Raza, A., Biosensors: Their Fundamentals, Designs, Types and Most Recent Impactful Applications: A Review. *J. Biosens. Bioelectron.* **2017,** *08* (01).

86. Soleymani, L.; Li, F., Mechanistic Challenges and Advantages of Biosensor Miniaturization into the Nanoscale. *ACS Sens* **2017,** *2* (4), 458-467.

87. Amine, A.; Mohammadi, H.; Bourais, I.; Palleschi, G., Enzyme Inhibition-Based Biosensors for Food Safety and Environmental Monitoring. *Biosens. Bioelectron.* **2006,** *21* (8), 1405-1423.

88. Salis, A.; Setzu, S.; Monduzzi, M.; Mula, G., Porous Silicon-Based Electrochemical Biosensors. *Biosensors-Emerging Materials and Applications* **2011**, 333-352.

89. Grieshaber, D.; MacKenzie, R.; Voeroes, J.; Reimhult, E., Electrochemical Biosensors-Sensor Principles and Architectures. *Sensors* **2008,** *8* (3), 1400-1458.

90. Basu, I.; Subramanian, R. V.; Mathew, A.; Chadha, A.; Bhattacharya, E., Potentiometric Biosensors Based on Silicon and Porous Silicon. *NSTI-Nanotech*, **2004**, 224-227.

91. Thust, M.; Schöning, M. J.; Frohnhoff, S.; Arens-Fischer, R.; Kordos, P.; Lüth, H., Porous Silicon as a Substrate Material for Potentiometric Biosensors. *Meas. Sci. Technol.* **1996,** *7* (1), 26.

92. Reddy, R. R. K.; Basu, I.; Bhattacharya, E.; Chadha, A., Estimation of Triglycerides by a Porous Silicon Based Potentiometric Biosensor. *Curr. Appl. Phys.* **2003,** *3* (2), 155-161.

93. Reddy, R. R. K.; Chadha, A.; Bhattacharya, E., Porous Silicon Based Potentiometric Triglyceride Biosensor. *Biosens. Bioelectron.* **2001,** *16* (4), 313-317.

94. Setzu, S.; Salis, S.; Demontis, V.; Salis, A.; Monduzzi, M.; Mula, G., Porous Silicon-Based Potentiometric Biosensor for Triglycerides. *Phys. Satatus Solidi A* **2007,** *204* (5), 1434-1438.

95. Koncki, R., Recent Developments in Potentiometric Biosensors for Biomedical Analysis. *Anal. Chim. Acta* **2007,** *599* (1), 7-15.

96. Bonanni, A.; Del Valle, M., Use of Nanomaterials for Impedimetric DNA Sensors: A Review. *Anal. Chim. Acta* **2010,** *678* (1), 7-17.

97. Sailor, M. J., *Porous Silicon in Practice: Preparation, Characterization and Applications*. John Wiley & Sons: **2012**.

98. Jane, A.; dronov, R.; Hodges, A.; Voelcker, N. H., Porous Silicon Biosensors on the Advance. *Trends Biotechnol.* **2009,** *27* (4), 230-239.

99. Mariani, S.; Robbiano, V.; Strambini, L. M.; Debrassi, A.; Egri, G.; Dähne, L.; Barillaro, G., Layer-by-Layer Biofunctionalization of Nanostructured Porous Silicon for High-Sensitivity and High-Selectivity Label-Free Affinity Biosensing. *Nat. Commun.* **2018,** *9* (1), 5256.

100. Orosco, M. M.; Pacholski, C.; Sailor, M. J., Real-Time Monitoring of Enzyme Activity in a Mesoporous Silicon Double Layer. *Nat. Nanotechnol.* **2009,** *4* (4), 255-258.

101. Pacholski, C.; Sartor, M.; Sailor, M. J.; Cunin, F.; Miskelly, G. M., Biosensing Using Porous Silicon Double-Layer Interferometers: Reflective Interferometric Fourier Transform Spectroscopy. *J. Am. Chem. Soc.* **2005,** *127* (33), 11636-11645.

102. Zuidema, J. M.; Kumeria, T.; Kim, D.; Kang, J.; Wang, J.; Hollett, G.; Zhang, X.; Roberts, D. S.; Chan, N.; Dowling, C., Oriented Nanofibrous Polymer Scaffolds Containing Protein-Loaded Porous Silicon Generated by Spray Nebulization. *Adv. Mater.* **2018,** *30* (12), 1706785.

103. Urmann, K.; Walter, J.-G.; Scheper, T.; Segal, E., Label-Free Optical Biosensors Based on Aptamer-Functionalized Porous Silicon Scaffolds. *Anal. Chem.* **2015,** *87* (3), 1999-2006.

104. Janshoff, A.; Dancil, K.-P. S.; Steinem, C.; Greiner, D. P.; Lin, V. S. Y.; Gurtner, C.; Motesharei, K.; Sailor, M. J.; Ghadiri, M. R., Macroporous P-Type Silicon Fabry−Perot Layers.

Fabrication, Characterization, and Applications in Biosensing. *J. Am. Chem. Soc.* **1998,** *120* (46), 12108-12116.

105. Urmann, K.; Arshavsky-Graham, S.; Walter, J.-G.; Scheper, T.; Segal, E., Whole-Cell Detection of Live Lactobacillus Acidophilus on Aptamer-Decorated Porous Silicon Biosensors. *Analyst* **2016,** *141* (18), 5432-5440.

106. Vilensky, R.; Bercovici, M.; Segal, E., Oxidized Porous Silicon Nanostructures Enabling Electrokinetic Transport for Enhanced DNA Detection. *Adv. Func. Mater.* **2015,** *25* (43), 6725-6732.

107. Lugo, J.; Ocampo, M.; Kirk, A.; Plant, D.; Fauchet, P., Electrochemical Sensing of DNA with Porous Silicon Layers. *J. New. Mat. Electr. Sys.* **2007,** *10* (2), 113.

108. Melikjanyan, G.; Martirosyan, K. S., Possibility of Application of Porous Silicon as Glucose Biosensor. *Armenian Journal of Physics* **2011,** *4* (4), 225-227.

109. Díaz, D. J., Electrochemistry of Porous Materials. ACS Publications: 2010.

110. Thakur, M.; Isaacson, M.; Sinsabaugh, S. L.; Wong, M. S.; Biswal, S. L., Gold-Coated Porous Silicon Films as Anodes for Lithium Ion Batteries. *J. Power Sources* **2012,** *205*, 426-432.

111. Yu, Y.; Gu, L.; Zhu, C.; Tsukimoto, S.; van Aken, P. A.; Maier, J., Reversible Storage of Lithium in Silver-Coated Three-Dimensional Macroporous Silicon. *Adv. Mater.* **2010,** *22* (20), 2247-2250.

112. Zhang, H.; Zhu, Y.; Qu, L.; Wu, H.; Kong, H.; Yang, Z.; Chen, D.; Mäkilä, E.; Salonen, J.; Santos, H. A.; Hai, M.; Weitz, D. A., Gold Nanorods Conjugated Porous Silicon Nanoparticles Encapsulated in Calcium Alginate Nano Hydrogels Using Microemulsion Templates. *Nano. Lett.* **2018,** *18* (2), 1448-1453.

113. Lin, L.; Ma, Y.; Xie, Q.; Wang, L.; Zhang, Q.; Peng, D.-L., Copper-Nanoparticle-Induced Porous Si/Cu Composite Films as an Anode for Lithium Ion Batteries. *ACS Nano* **2017,** *11* (7), 6893-6903.

114. Yao, Y.; Liu, N.; McDowell, M. T.; Pasta, M.; Cui, Y., Improving the Cycling Stability of Silicon Nanowire Anodes with Conducting Polymer Coatings. *Energy Environ. Sci.* **2012,** *5* (7), 7927-7930.

115. Reta, N.; Michelmore, A.; Saint, C.; Prieto-Simón, B.; Voelcker, N. H., Porous Silicon Membrane-Modified Electrodes for Label-Free Voltammetric Detection of MS2 Bacteriophage. *Biosens. Bioelectron.* **2016,** *80*, 47-53.

116. Makila, E.; Bimbo, L. M.; Kaasalainen, M.; Herranz, B.; Airaksinen, A. J.; Heinonen, M.; Kukk, E.; Hirvonen, J.; Santos, H. A.; Salonen, J., Amine Modification of Thermally Carbonized Porous Silicon with Silane Coupling Chemistry. *Langmuir* **2012,** *28* (39), 14045-14054.

117. Salonen, J.; Björkqvist, M.; Paski, J., Temperature-Dependent Electrical Conductivity in Thermally Carbonized Porous Silicon. *Sens. Actuators A Phys.* **2004,** *116* (3), 438-441.

118. Sciacca, B.; Alvarez, S. D.; Geobaldo, F.; Sailor, M. J., Bioconjugate Functionalization of Thermally Carbonized Porous Silicon Using a Radical Coupling Reaction. *Dalton Trans.* **2010,** *39* (45), 10847-10853.

Chapter 2. Literature review: porous silicon-based electrochemical biosensors

2.1 Introduction

As an established porous material with desired properties to be used as sensing platform, pSi offers ample opportunities for biosensor design.[1] The pore morphological features (e.g. pore size shown as an example in **Figure 2.1**, depth and porosity) of pSi can be easily adjusted by the fast fabrication process of electrochemical anodization in the presence of HF and ethanol by simply varying etching parameters (e.g. current density, etching time, etchant ratio).[2] The easy controllability of the pSi morphology greatly enhances its sensing capabilities for a large range of chemical and biological species in various sizes.[3] Along with its good biocompatibility, the large available internal surface area of pSi permits the immobilization of a great number of biological receptors within the porous matrix. Control over surface functionalities to incorporate desired bioreceptors is of great importance in the design of biosensing systems.[4-6] Benefiting from the convenient surface chemistry of pSi, a diverse range of bioreceptors can be easily incorporated on the pSi surface upon introduction of the required functional groups via hydrosilylation or silanization.

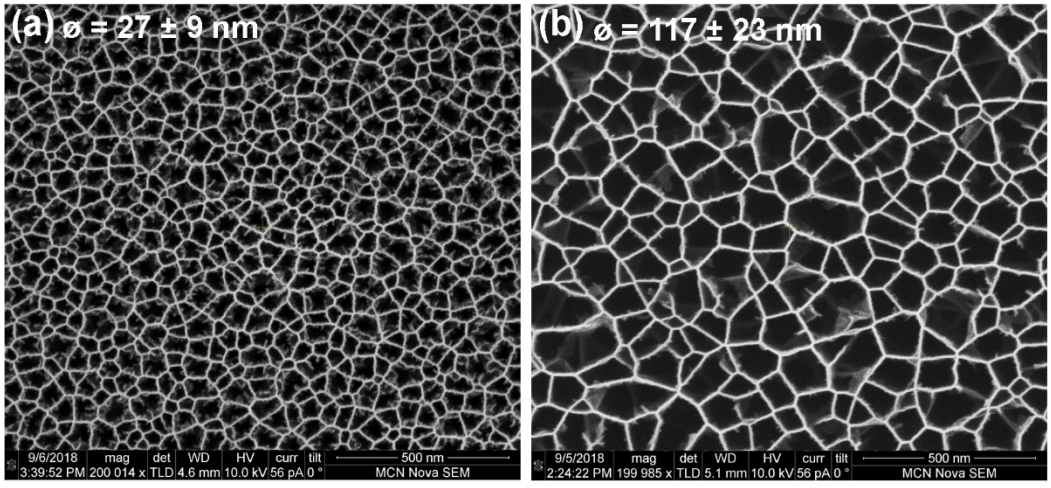

Figure 2.1 Top view SEM images of pSi with different pore diameter by varying the current density using 1:1 HF/Ethanol etchant: (a) 27 ± 9 nm and (b) 117 ± 23 nm. Current density: (a) 18.9 mA cm^{-2}, (b) 71.9 mA cm^{-2}.

The major drawback of freshly etched pSi is its unstable surface in atmospheric or biological media because of the reactive hydrogen termination, which makes pSi unsuitable for biosensing experiments in aqueous environments. Surface stabilization of pSi is crucial for improving its low chemical stability and a range of different methods have been well explored such as oxidation[7-8], silanization[9-10], hydrosilylation[3-4, 11-12] and thermal carbonization[13-15]. Thanks to these stabilization techniques and the unique properties of pSi, this material has been shown as a highly sensitive optical biosensing transducer. Indeed, pSi-based optical biosensors have been well discussed in several recent reviews.[16-17] Compared to these reports using pSi as optical transducer, it has been challenging to use pSi as electrochemical transducer due to the growth of an insulating SiO_2 layer on freshly etched pSi and the fact that the charge transfer is limited to the pore tips where the high radius of curvature is responsible of generating a region of enhanced electric field.[18]

Electrochemical biosensors offer a wide range of striking features such as high sensitivity, selectivity and robustness at low cost.[19] The combination of electrochemical biosensing strategies and pSi provides an attractive approach to design novel sensing platforms with improved selectivity and sensitivity for a range of practical applications. Specifically, the remarkable physical and chemical properties of pSi make it extremely attractive for a wide range of electrochemical biosensors ranging from enzyme sensors and immunosensors to DNA sensors. However, currently pSi-based electrochemical biosensors mainly take advantage of pSi's semiconductor characteristics and large surface area. The electrical properties of pSi are highly influenced by its morphological features (e.g. porosity) and the initial resistivity of the bulk silicon wafer used for producing pSi.[20] In order to stabilize the surface of freshly etched pSi and allow further functionalization, the surface of pSi has typically been passivated by oxidation. However, because of the insulating property of the SiO_2 layer, it has been challenging to use pSi as electrochemical transducer. Apart from preserving the semiconductor

properties of Si, researchers have reported various pSi modifications to introduce conductive coatings (e.g. metal[21-24] or conductive polymeric layers[25-26]) with the aim of developing pSi-based electrochemical biosensors. The electrochemical transduction mechanisms employed for pSi mainly focus on amperometry (monitoring current change), potentiometry (monitoring charge accumulation or potential), impedance (monitoring change in resistance) and conductometry (monitoring the conductive properties of the medium between electrodes).[19, 27] Here, pSi-based electrochemical biosensors are classified according to their bioreceptors and transduction mechanisms.

2.2 pSi-based electrochemical enzyme sensors

Electrochemical enzyme sensors combine the bioselectivity of the enzyme with the high sensitivity of the electroanalytical techniques.[19] Enzymes not only provide selectivity to biosensors but also catalyze biochemical reactions involving detectable electroactive species.

As an example of a pSi-based amperometric enzyme sensor, Song and coworkers developed an array of four sensors to detect various liver disease biomarkers: cholesterol, bilirubin and alanine and aspartate aminotransferases.[28] All the enzymes are oxidases and all related enzymatic reactions produce H_2O_2. The sensors were based on platinum electrodes modified with a pSi layer generated by electrochemical anodization of p-type Si. The enzymes used as bioreceptors were covalently immobilized onto a pSi-modified working electrode previously silanized with (3-aminopropyl)triethoxysilane (APTES). The amperometric detection of cholesterol, bilirubin and aminotransferases was carried out at a fixed potential, suitable for the electrochemical oxidation of the H_2O_2 generated when the enzymatic reaction occurs. Compared with flat platinum electrodes, the pSi-modified biosensors were able to achieve higher sensitivity for the detection of these four biomarkers. By adhering pSi to a platinum working electrode a three-dimensional structure was introduced, greatly enlarging the active surface sensing area, thus enabling high levels of sensitivity: the sensitivity of the cholesterol

sensor was 0.2656 μA/mM and that of the bilirubin sensor 0.15354 mA/mM. The measured current increased linearly with cholesterol concentrations from 1 to 50 mM and the amperometric response covered a bilirubin concentration range from 2 to 20 μM. Besides, good stability of these pSi-modified electrodes was demonstrated: the sensors remained stable without loss in enzymatic activity for at least 120 days. This can be attributed to the minimized enzyme loss and deactivation achieved by the porous environment where the enzymes were immobilized. The same authors also confirmed that the Pt-coated-pSi working electrodes present larger effective surface area (0.5054 cm^2) than that of Pt-coated-planar-Si working electrodes (0.1608 cm^2).[29] Agreeing with the larger effective surface area of the Pt-coated porous electrode, its sensitivity (0.2656 μA mM^{-1}) was over 3-fold larger than that of the planar electrode (0.08567 μA mM^{-1}).

PSi-based potentiometric enzyme sensors have also been reported. The concept of using pSi-based potentiometric biosensors to monitor the enzymatic process was first investigated by Thus and coworkers in 1996.[30] Enzymatic reactions can cause a change in the pH of the electrolyte solution because of the formation of an acid or base. These designed pSi-based potentiometric biosensors monitor the potential difference between a cathode (usually Pt) and anode (pSi electrode) caused by the enzymatic reaction in terms of capacitance-voltage (C-V) changes. The enzyme penicillinase was immobilized on an oxidized pSi surface via physical adsorption. A linear potentiometric response for penicillin G ranging from 0.5 to 20 mM was demonstrated with a sensitivity of ~40 mV per pH decade using p-type pSi. No significant degradation of the sensor output signal was observed for up to 50 days of storage. Instead of using p-type pSi, the same sensor designed from n-type pSi showed similar sensitivity of ~50 mV per pH decade. Following this work, Reddy and Setzu published a series of papers aimed at developing pSi-based potentiometric enzyme sensors for triglycerides.[31-32] Lipase enzyme, which catalyzes the hydrolysis of triglycerides, was immobilized within oxidized pSi layers

through physisorption. Enzymatic hydrolysis of triglycerides resulted in a decrease in pH due to the formation of fatty acids. pH changes were monitored during the hydrolysis process of tributyrin as a shift in the C-V characteristics, achieving a sensitivity of 30 mV per pH decade, a LOD of 6 mM, a good stability over a period of 6 months at 0-5 °C and excellent reproducibility (± 2 %).[31] Alternatively, Setzu and coworkers recorded a time evolution of the open circuit potential (OCP) value to monitor the changes in pH as a result of tributyrin hydrolysis.[33] A LOD of 0.3 mM of tributyrin was achieved and a stability over a period of 2 months was demonstrated (total 17 working h within 2 months corresponding to about 70 separate measurements).

Additionally, another type of potentiometric sensor reported by Basu and coworkers, an electrolyte-insulator-semiconductor capacitor (EISC), was designed using planar silicon or pSi as substrate and silicon nitride as the sensing dielectric to monitor triglycerides based on their enzymatic hydrolysis.[34] The change in pH of the electrolyte due to the production of acid/base from the hydrolyzed triglyceride was measured by C-V. The EISC sensor using pSi as substrate achieved a 34.5-fold larger accumulation capacitance than that of planar Si, because of the larger surface area provided by the former. The advantage of using the large surface area of pSi to design the EISC sensors was also demonstrated by Schoning and coworkers.[35] Two kinds of penicillin EISC sensors, one based on oxidized pSi and the other one on a non-porous oxidized planar silicon substrate, were designed simultaneously. An increase in hydrogen ion caused by the hydrolysis of penicillin decreased the pH value, which was detected by the C-V measurements. A sensitivity of 54 mV per pH decade was achieved by the EISC using pSi as the substrate, being 30-fold larger than that of the EISC sensor using planar silicon as the substrate.

Conductometric biosensors have also been strongly associated with enzymes whose charged products lead to ionic strength changes and increased conductivity.[19] These biosensors can monitor changes in the conductivity of the solution caused by the charged species involved in the enzyme reaction that modify the ionic strength. Alternatively, changes in conductivity can also be directly monitored when binding events happen at the electrode surface. A conductivity-based sensor for quantitative detection of catechol by physically adsorbing the enzyme tyrosinase onto oxidized p-type pSi was reported by Tembe and coworkers.[36] Conductivity measurements were initially performed for characterization purposes, to confirm the adsorption of the enzyme in the porous structure, and later for detection, to quantify the response to catechol. A LOD of 50 µM and a response time of 120 s were achieved for catechol detection, showing a linear response in the concentration range from 50 to 100 µM. The porous structure helped to retain almost 90% of the enzymatic activity of the adsorbed tyrosinase for 20 days. Moreover, as previously discussed for sensors with enzymes adsorbed on pSi, tyrosinase molecules were protected inside the pores from leaching out, contributing to a high mechanical stability.

2.3 pSi-based electrochemical immunosensors

Prabhakar and coworkers developed a pSi-based voltammetric immunosensor capable of detecting goat anti-human IgG as antigen, with a LOD of 10 ng mL^{-1} (equal to 6.7 nM).[37] Nano-pSi was prepared by electrochemical anodization using p-type silicon wafers, followed by the immobilization of the capture probe (human IgG) onto the APTES-silanized pSi surface. The detection of the antigen was done by CV, based on the effect caused on the electron transfer of the redox couple $[Fe(CN)_6]^{3-/4-}$ added in solution. The authors concluded that this sensing system could detect the antigen in the ng mL^{-1} range, supporting the high sensitivity enabled by the large surface area of pSi. However, a more thorough study should be done to accurately assess the performance of this kind of sensors, using a quantitative electrochemical detection

technique rather than the semi-quantitative CV, and testing a wider range of antigen concentrations.

Das and coworkers investigated the effect of the pore morphological features (e.g. pore depth) on the sensitivity of a pSi-based impedimetric immunosensor for bacteria (*E. coli O157*) detection.[38] The electrode was fabricated by deposition of two metallic contacts (Al and Au) onto the macroporous silicon surface, and the change in impedance caused by the antibody-antigen binding event was monitored. Three different thicknesses (3, 8 and 12 μm) of macroporous silicon with a porosity of 55% were fabricated and then thermally oxidized and silanized with mercaptopropyltrimethoxysilane (MPTMS) to allow anti-*E.coli O157* antibody immobilization. Briefly, the thiol group from MPTMS reacted with the maleimide group from the 4-maleimidobutyric acid N-succinimidyl ester, used as hetero bifunctional crosslinker, providing succinimide groups for direct binding to the amino groups of the anti-*E. coli* antibody. By incubating these biosensors with serially diluted *E.coli O157* solutions in PBS ranging from 10^3 to 10^7 colony-forming units (cfu) mL^{-1} at 37 °C for 10 min, the biosensor fabricated with the macroporous silicon with 8 μm thickness achieved a LOD of 1000 cfu mL^{-1}, because of optimum current lines confinement. Another example of impedimetric immunosensor utilizing nanoporous silicon structure with 100 nm pore diameter prepared by electrochemical etching of p-type silicon was reported by Ghosh and coworkers for the detection of aflatoxin B_1, a food toxin.[39] The nanoporous silicon structure was thermally oxidized to enable silanization and further uniform immobilization of antibodies. This immunosensor achieved a LOD of 1 fg mL^{-1} aflatoxin B_1 in buffer by monitoring the change in impedance, as well as the shift in peak frequency.

Additionally, a pSi-based conductometric immunosensor for the detection of bacterial fragments of *E.coli* was reported by Recio-Sanchez and coworkers.[40] The electrochemical

etched pSi was firstly oxidized in air, then silanization with APTES was conducted prior to attachment of the anti-*E. coli* antibody. In order to use such pSi to monitor the current-voltage change by exposing these antibody-functionalized electrodes to various concentrations of *E.coli* fragments from 10 to 100 µg/mL, metallic contacts were previously introduced by depositing Au and NiCr on the top surface and Al on the back-side of the pSi to form a Au-NiCr/pSi/Si/Al structure. An increased conductivity was observed along with the increasing concentration of the bacteria fragments in buffer. The authors didn't mention the LOD and further work is required with real samples.

In 2016, Reta et al. reported an immunosensor using pSi membranes for the label-free voltammetric detection of MS2 bacteriophage.[11] Capture of MS2 bacteriophage by the antibody immobilized into the membrane caused the partial blockage of pSi nanochannels and hindered the diffusion of the electroactive species added in solution towards the gold working electrode attached to the backside of the pSi membrane, observed as a decrease in the intensity current measured by DPV. The oxidation current decreased with increasing bacteriophage concentrations, and the sensitivity of detection was optimized by selecting the adequate nanochannel diameter, as shown in **Figure 2.2**. The device was capable of detecting MS2 bacteriophage spiked in reservoir water samples with very little matrix effect (less than 3%) from interfering species and an impressive LOD of 6 pfu mL^{-1}. This pSi membrane-based immunosensor also showed excellent stability. Another pSi-based electrochemical immunosensor for MS2 bacteriophage detection reported by Brodoceanu et al. using pSi in biosensors based on nanochannel blockage provided the proof of the versatility in pSi structures.[41] Densely packed pSi straight nanochannels with flat bottoms and high aspect ratio enabled a highly sensitive detection of MS2 bacteriophage at concentrations as low as 0.9 pfu/mL. The bottom of the pSi nanochannels with gold discs was selectively modified with

anti-MS2 antibody. The capacitance measured at the antibody-modified working electrodes decreased with increasing phage concentration, as shown in **Figure 2.3**.

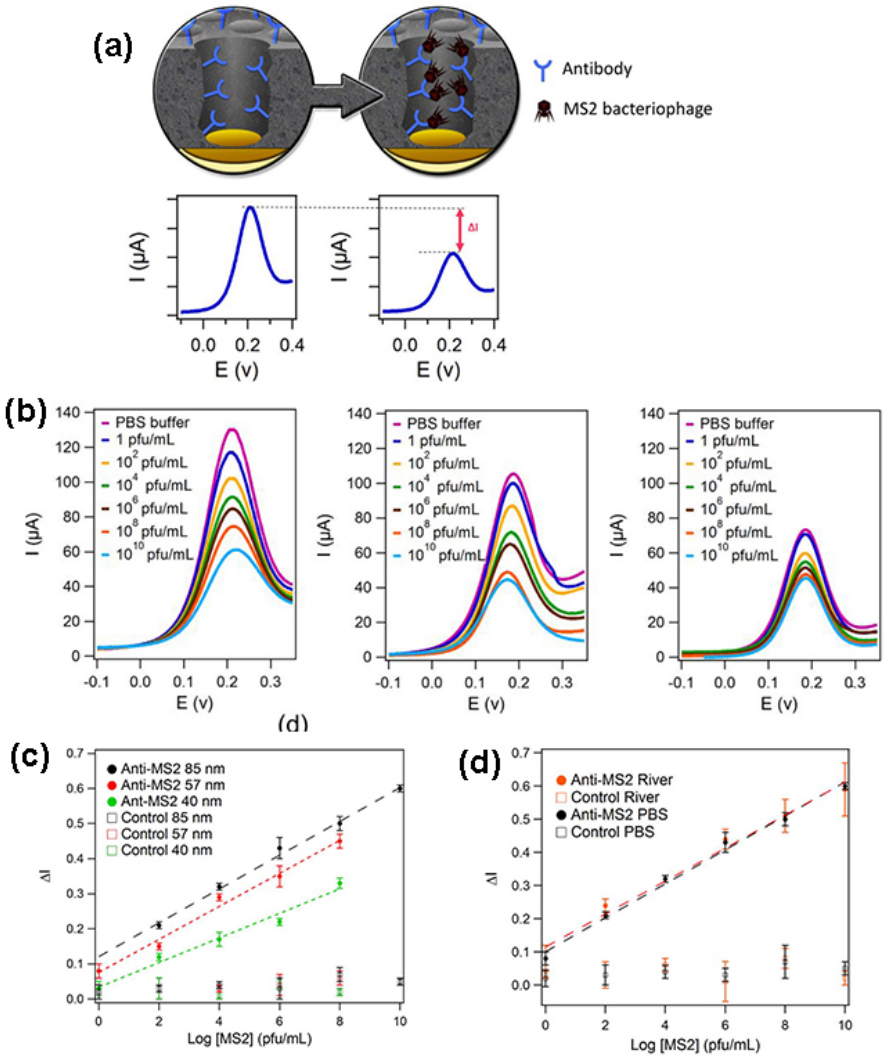

Figure 2.2 (a) Sensing principle of the pSi membrane-modified immunosensors for the label-free detection of MS2 bacteriophage and corresponding DPV trace (left) prior and (right) after bacteriophage interaction; (b) DPV plots for increasing concentration of MS2 in PBS for the anti-MS2 antibody-modified immunosensors with membranes of an average diameter of (left to right) 85, 57 and 40 nm; (c) dose response curves for all immunosensors functionalized with either MS2-specific antibodies or nonspecific antibodies (control) in buffer; (d) dose response curve obtained for the detection of MS2 spiked in river water (orange) and buffer (blue) using the immunosensor modified with a pSi membrane featuring 85 nm nanochannel diameter.[11]

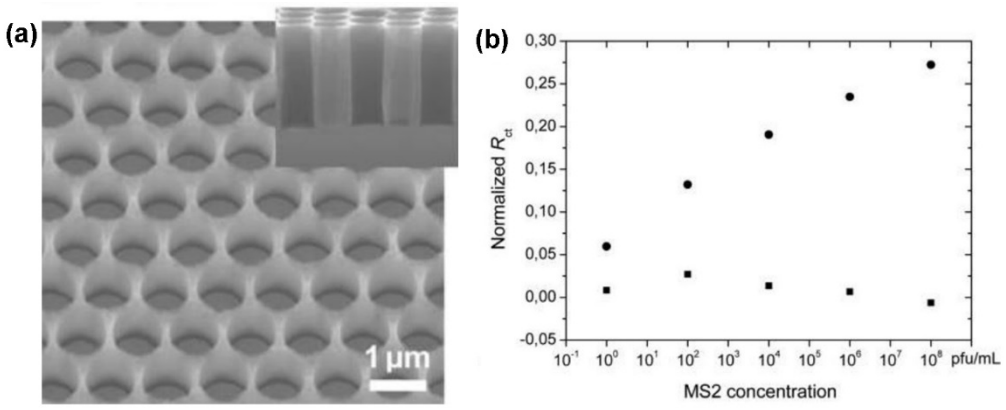

Figure 2.3 (a) Top view SEM image of silicon pore arrays fabricated via MACE. Insert cross-sectional SEM; (b) plots of normalized charge-transfer resistance values as a function of MS2 bacteriophage concentration obtained by using substrates modified with MS2-specific antibodies (●) and BSA (■).[41]

2.4 pSi-based electrochemical DNA sensors

In a typical DNA sensor, a ssDNA probe sequence is usually immobilized within the recognition layer to hybridize the target DNA taking advantage of the DNA base-pairing interaction.[42] Electrochemical detection of DNA hybridization has gained an increasing popularity in biotechnology, diagnostics and clinical analysis since Millan and Mikkelsen introduced the first electrochemical DNA sensor in 1993.[43-44] This type of sensors combine the use of nucleic acids as bioreceptors with electrochemical transducers to provide a specific, accurate and robust detection in biosensing applications.[45]

In the frame of pSi-based electrochemical DNA sensors, Zhang and Alocilja reported a pSi-based voltammetric DNA sensing system for pathogen detection, *Salmonella enteritidis*, with a LOD of 1 ng mL^{-1} (equal to 0.13 nM). They used CV to quantify the current intensity changes caused by the difference in electrostatic repulsion between ssDNA and dsDNA, and a negatively charged redox indicator ($[Fe(CN)_6]^{3-/4-}$).[46] pSi was fabricated from p-type silicon wafers using electrochemical anodization, and silanization was used to facilitate DNA probe immobilization. The authors also performed characterization studies (based on biotinylated

DNA probes binding to streptavidin-horseradish peroxidase (HRP) conjugates, and subsequent colorimetric detection) that prove that pSi-based electrodes feature an electrochemically active surface area 4-fold larger than that of planar Si. It was demonstrated that pSi can provide higher sensitivity for DNA sensing than planar Si. Lugo *et al.* developed another pSi-based voltammetric biosensor capable of detecting DNA hybridization through chemical oxidation of guanine using ruthenium bipyridine ($Ru(bpy)_3^{2+}$) as a redox indicator.[47] PSi was fabricated from p-type silicon by electrochemical anodization, and surface stabilization was performed by thermal oxidation. A DNA probe, complementary to the target DNA, was immobilized onto a pSi surface previously modified with 3-glycidoxypropyltrimethoxysilane. This DNA probe was engineered to minimize the oxidation signal produced upon reaction with $Ru(bpy)_3^{2+}$. Such a sequence contains inosine instead of guanine and is thus less reactive to oxidation. The LOD achieved with this system was an impressive 0.05 nM due to the large internal surface of pSi, as well as to the tunability of pore size only allowing the penetration of molecular compounds of similar size to the analyte.

Vamvakaki *et al.* employed electrochemically etched pSi as a substrate to detect a 21-mer oligonucleotide sequence by monitoring the electrical impedance.[48] The DNA probe was immobilized at the oxidized pSi surface via physical adsorption, then the DNA probe functionalized pSi was exposed to detect a complementary sequence. The hybridization reaction led to a lower interface charge density and thus a reduced capacitance and an increased impedance. pSi fabrication was optimized to achieve pore structures with an average pore size close to that of the target DNA. By monitoring the large and reproducible impedance changes at the interface, hybridization efficiency was demonstrated. Archer and coworkers developed a pSi-based impedimetric DNA sensor from p-type silicon, which afforded label-free and real-time detection of DNA hybridization.[49-50] Macroporous silicon containing pore diameters of 1-2 µm, was oxidized then functionalized with poly-L-lysine before the DNA probe was

immobilized via electrostatic interaction. Hybridization of the complementary DNA to the capture probe was monitored as a reduction in impedance, and a LOD of 100 nM was achieved. Their research concluded that hybridization of the target DNA sequence can be detected because of localized enhancement in charges, a decrease in impedance of pSi substrate and a shift in the phase angle. The impedimetric detection was enabled by the metallic contacts (Al coating or Ag paste) on the backside of the pSi substrate.

2.5 Conclusion

PSi-based electrochemical biosensors have been successfully applied to the detection of a large number of biomolecules, but most of them rely on pSi's semiconductor characteristics, which are greatly affected by its morphological features and the resistivity of the bulk silicon. Non-conductive free-standing pSi membranes have been used in some sensing platforms to increase the surface area of a conductive electrode (e.g. Au, Pt) in order to improve the sensing performance, because pSi's large surface area has high loading capacity of bioreceptors. Instead of using free-standing pSi membranes to modify the electrodes, the possibility to modulate the electrical properties of pSi has also been exploited by introducing electrical contacts at the backside of pSi. In these pSi-related electrochemical biosensors, the stabilization methods of the active surface of freshly etched pSi mainly focus on oxidation. However, the insulating property of the oxide layer limits the use of pSi as electrochemical transducer. An interesting method that can overcome this drawback and render pSi suitable for electrochemical biosensor design is the carbon-stabilization process via thermal decomposition of acetylene, which has not been sufficiently explored in the literature.

2.6 References

1. Lin, V. S.-Y.; Motesharei, K.; Dancil, K.-P. S.; Sailor, M. J.; Ghadiri, M. R., A Porous Silicon-Based Optical Interferometric Biosensor. *Science* **1997,** *278* (5339), 840-843.

2. Sailor, M. J., Preparation of Spatially Modulated Porous Silicon Layers. In *Porous Silicon in Practice*, Wiley-VCH Verlag GmbH & Co. KGaA: 2011; pp 77-117.

3. Sweetman, M. J.; Ronci, M.; Ghaemi, S. R.; Craig, J. E.; Voelcker, N. H., Porous Silicon Films Micropatterned with Bioelements as Supports for Mammalian Cells. *Adv. Func. Mater.* **2012,** *22* (6), 1158-1166.

4. Sweetman, M. J.; McInnes, S. J. P.; Vasani, R. B.; Guinan, T.; Blencowe, A.; Voelcker, N. H., Rapid, Metal-Free Hydrosilanisation Chemistry for Porous Silicon Surface Modification. *Chem. Commun.* **2015,** *51* (53), 10640-10643.

5. Kilian, K. A.; Böcking, T.; Gooding, J. J., The Importance of Surface Chemistry in Mesoporous Materials: Lessons from Porous Silicon Biosensors. *Chem. Commun.* **2009,** (6), 630-640.

6. Langner, A.; Panarello, A.; Rivillon, S.; Vassylyev, O.; Khinast, J. G.; Chabal, Y. J., Controlled Silicon Surface Functionalization by Alkene Hydrosilylation. *J. Am. Chem. Soc.* **2005,** *127* (37), 12798-12799.

7. Cunin, F.; Schmedake, T. A.; Link, J. R.; Li, Y. Y.; Koh, J.; Bhatia, S. N.; Sailor, M. J., Biomolecular Screening with Encoded Porous-Silicon Photonic Crystals. *Nat. Mater.* **2002,** *1* (1), 39.

8. Orosco, M. M.; Pacholski, C.; Sailor, M. J., Real-Time Monitoring of Enzyme Activity in a Mesoporous Silicon Double Layer. *Nat. Nanotechnol.* **2009,** *4* (4), 255-258.

9. Kim, D.; Joo, J.; Pan, Y.; Boarino, A.; Jun, Y. W.; Ahn, K. H.; Arkles, B.; Sailor, M. J., Thermally Induced Silane Dehydrocoupling on Silicon Nanostructures. *Angew. Chem. Int. Ed.* **2016,** *55* (22), 6423-6427.

10. Sweetman, M. J.; Voelcker, N. H., Chemically Patterned Porous Silicon Photonic Crystals Towards Internally Referenced Organic Vapour Sensors. *RSC Adv.* **2012,** *2* (11), 4620-4622.

11. Reta, N.; Michelmore, A.; Saint, C.; Prieto-Simón, B.; Voelcker, N. H., Porous Silicon Membrane-Modified Electrodes for Label-Free Voltammetric Detection of MS2 Bacteriophage. *Biosens. Bioelectron.* **2016,** *80*, 47-53.

12. Bimbo, L. M.; Sarparanta, M.; Santos, H. A.; Airaksinen, A. J.; Mäkilä, E.; Laaksonen, T.; Peltonen, L.; Lehto, V.-P.; Hirvonen, J.; Salonen, J., Biocompatibility of Thermally Hydrocarbonized Porous Silicon Nanoparticles and Their Biodistribution in Rats. *ACS Nano* **2010,** *4* (6), 3023-3032.

13. Salonen, J.; Bjorkqvist, M.; Laine, E.; Niinisto, L., Stabilization of Porous Silicon Surface by Thermal Decomposition of Acetylene. *Appl. Surf. Sci.* **2004,** *225* (1-4), 389-394.

14. Torres-Costa, V.; Salonen, J.; Jalkanen, T.; Lehto, V. P.; Martín-Palma, R.; Martínez-Duart, J., Carbonization of Porous Silicon Optical Gas Sensors for Enhanced Stability and Sensitivity. *Phys. Satatus Solidi A* **2009,** *206* (6), 1306-1308.

15. Tsang, C. K.; Kelly, T. L.; Sailor, M. J.; Li, Y. Y., Highly Stable Porous Silicon–Carbon Composites as Label-Free Optical Biosensors. *ACS Nano* **2012,** *6* (12), 10546-10554.

16. Jane, A.; dronov, R.; Hodges, A.; Voelcker, N. H., Porous Silicon Biosensors on the Advance. *Trends Biotechnol.* **2009,** *27* (4), 230-239.

17. Dhanekar, S.; Jain, S., Porous Silicon Biosensor: Current Status. *Biosens. Bioelectron.* **2013,** *41*, 54-64.

18. Díaz, D. J., Electrochemistry of Porous Materials. *J. Am. Chem. Soc.* **2010,** *132* (12), 4501-4502.

19. Ronkainen, N. J.; Halsall, H. B.; Heineman, W. R., Electrochemical Biosensors. *Chem. Soc. Rev.* **2010,** *39* (5), 1747-1763.

20. Balagurov, L. A.; Yarkin, D. G.; Petrova, E. A., Electronic Transport in Porous Silicon of Low Porosity Made on a P+ Substrate. *Mater. Sci. Eng., B* **2000,** *69-70*, 127-131.

21. Thakur, M.; Isaacson, M.; Sinsabaugh, S. L.; Wong, M. S.; Biswal, S. L., Gold-Coated Porous Silicon Films as Anodes for Lithium Ion Batteries. *J. Power Sources* **2012,** *205*, 426-432.

22. Yu, Y.; Gu, L.; Zhu, C.; Tsukimoto, S.; van Aken, P. A.; Maier, J., Reversible Storage of Lithium in Silver-Coated Three-Dimensional Macroporous Silicon. *Adv. Mater.* **2010,** *22* (20), 2247-2250.

23. Zhang, H.; Zhu, Y.; Qu, L.; Wu, H.; Kong, H.; Yang, Z.; Chen, D.; Mäkilä, E.; Salonen, J.; Santos, H. A.; Hai, M.; Weitz, D. A., Gold Nanorods Conjugated Porous Silicon Nanoparticles Encapsulated in Calcium Alginate Nano Hydrogels Using Microemulsion Templates. *Nano. Lett.* **2018,** *18* (2), 1448-1453.

24. Lin, L.; Ma, Y.; Xie, Q.; Wang, L.; Zhang, Q.; Peng, D.-L., Copper-Nanoparticle-Induced Porous Si/Cu Composite Films as an Anode for Lithium Ion Batteries. *ACS Nano* **2017,** *11* (7), 6893-6903.

25. Yao, Y.; Liu, N.; McDowell, M. T.; Pasta, M.; Cui, Y., Improving the Cycling Stability of Silicon Nanowire Anodes with Conducting Polymer Coatings. *Energy Environ. Sci.* **2012,** *5* (7), 7927-7930.

26. Islam, M. A.; Sinelnikov, R.; Howlader, M. A.; Faramus, A.; Veinot, J. G. C., Mixed Surface Chemistry: An Approach to Highly Luminescent Biocompatible Amphiphilic Silicon Nanocrystals. *Chem. Mater.* **2018,** *30* (24), 8925-8931.

27. Salis, A.; Setzu, S.; Monduzzi, M.; Mula, G., Porous Silicon-Based Electrochemical Biosensors. *Biosensors-Emerging Materials and Applications* **2011**, 333-352.

28. Song, M.-J.; Yun, D.-H.; Min, N.-K.; Hong, S.-I., Electrochemical Biosensor Array for Liver Diagnosis Using Silanization Technique on Nanoporous Silicon Electrode. *J. Biosci. Bioeng.* **2007,** *103* (1), 32-37.

29. Song, M.-J.; Yun, D.-H.; Jin, J.-H.; Min, N.-K.; Hong, S.-I., Comparison of Effective Working Electrode Areas on Planar and Porous Silicon Substrates for Cholesterol Biosensor. *Jpn. J. Appl. Phys.* **2006,** *45* (9R), 7197.

30. Thust, M.; Schöning, M. J.; Frohnhoff, S.; Arens-Fischer, R.; Kordos, P.; Lüth, H., Porous Silicon as a Substrate Material for Potentiometric Biosensors. *Meas. Sci. Technol.* **1996,** *7* (1), 26.

31. Reddy, R. R. K.; Basu, I.; Bhattacharya, E.; Chadha, A., Estimation of Triglycerides by a Porous Silicon Based Potentiometric Biosensor. *Curr. Appl. Phys.* **2003,** *3* (2), 155-161.

32. Reddy, R. R. K.; Chadha, A.; Bhattacharya, E., Porous Silicon Based Potentiometric Triglyceride Biosensor. *Biosens. Bioelectron.* **2001,** *16* (4), 313-317.

33. Setzu, S.; Salis, S.; Demontis, V.; Salis, A.; Monduzzi, M.; Mula, G., Porous Silicon-Based Potentiometric Biosensor for Triglycerides. *Phys. Satatus Solidi A* **2007,** *204* (5), 1434-1438.

34. Basu, I.; Subramanian, R. V.; Mathew, A.; Chadha, A.; Bhattacharya, E., Potentiometric Biosensors Based on Silicon and Porous Silicon.

35. Schöning, M. J.; Ronkel, F.; Crott, M.; Thust, M.; Schultze, J.; Kordos, P.; Lüth, H., Miniaturization of Potentiometric Sensors Using Porous Silicon Microtechnology. *Electrochim. Acta* **1997,** *42* (20-22), 3185-3193.

36. Tembe, S.; Chaudhari, P. S.; Bhoraskar, S.; D'Souza, S.; Karve, M. S., Conductivity-Based Catechol Sensor Using Tyrosinase Immobilized in Porous Silicon. *IEEE Sens. J.* **2008,** *8* (9), 1593-1597.

37. Prabhakar, D.; Kumari, V.; Islam, S., Nanoporous Silicon Based Electrochemical Immunosensor. *Sci. Adv. Materials* **2012,** *4* (1), 121-125.

38. Das, R. D.; Dey, A.; Das, S.; RoyChaudhuri, C., Interdigitated Electrode-Less High-Performance Macroporous Silicon Structure as Impedance Biosensor for Bacteria Detection. *IEEE Sens. J.* **2011,** *11* (5), 1242-1252.

39. Ghosh, H.; RoyChaudhuri, C., Ultrasensitive Food Toxin Biosensor Using Frequency Based Signals of Silicon Oxide Nanoporous Structure. *Appl. Phys. Lett.* **2013,** *102* (24), 243701.

40. Recio-Sanchez, G.; Dominguez-Canizares, G.; Manso, M.; Preda, I.; Torres-Costa, V.; Gutierrez, A.; Soriano, L.; J. Martin-Palma, R., Surface Functionalization of Nanostructured Porous Silicon by Apts: Toward the Fabrication of Electrical Biosensors of Bacterium Escherichia Coli. *Curr. Nanosci.* **2011,** *7* (2), 178-182.

41. Brodoceanu, D.; Elnathan, R.; Prieto-Simón, B.; Delalat, B.; Guinan, T.; Kroner, E.; Voelcker, N. H.; Kraus, T., Dense Arrays of Uniform Submicron Pores in Silicon and Their Applications. *ACS Appl. Mater. Interfaces* **2015,** *7* (2), 1160-1169.

42. drummond, T. G.; Hill, M. G.; Barton, J. K., Electrochemical DNA Sensors. *Nat. Biotechnol.* **2003,** *21*, 1192.

43. Millan, K. M.; Saraullo, A.; Mikkelsen, S. R., Voltammetric DNA Biosensor for Cystic Fibrosis Based on a Modified Carbon Paste Electrode. *Anal. Chem.* **1994,** *66* (18), 2943-2948.

44. Mikkelsen, S. R., Electrochecmical Biosensors for DNA Sequence Detection. *Electroanalysis* **1996,** *8* (1), 15-19.

45. Kerman, K.; Kobayashi, M.; Tamiya, E., Recent Trends in Electrochemical DNA Biosensor Technology. *Meas. Sci. Technol.* **2003,** *15* (2), R1.

46. Zhang, D.; Alocilja, E. C., Characterization of Nanoporous Silicon-Based DNA Biosensor for the Detection of Salmonella Enteritidis. *IEEE Sens. J.* **2008,** *8* (6), 775-780.

47. Lugo, J.; Ocampo, M.; Kirk, A.; Plant, D.; Fauchet, P., Electrochemical Sensing of DNA with Porous Silicon Layers. *J. New. Mat. Electr. Sys.* **2007,** *10* (2), 113.

48. Vamvakaki, V.; Chaniotakis, N. A., DNA Stabilization and Hybridization Detection on Porous Silicon Surface by Eis and Total Reflection Ft-Ir Spectroscopy. *Electroanalysis* **2008,** *20* (17), 1845-1850.

49. Archer, M.; Christophersen, M.; Fauchet, P., Macroporous Silicon Electrical Sensor for DNA Hybridization Detection. *Biomed. Microdevices* **2004,** *6* (3), 203-211.

50. Archer, M.; Christophersen, M.; Fauchet, P. M.; Persaud, D.; Hirschman, K. D. In *Electrical Porous Silicon Microarray for DNA Hybridization Detection*, MRS Proceedings, Cambridge Univ Press: 2003; p A7. 2.

Chapter 3. Porous silicon nanostructures as effective Faradaic electrochemical sensing platforms

3.1 Introduction

PSi has attracted considerable attention as a promising sensing platform for label-free detection of a wide range of chemicals and biomolecules.[1-6] Some of the advantages derived from using these pSi structures are the extensive tailoring of their structural and optical properties, large surface area and well-established surface chemistry.[7-14] An example combining all these advantages is a pSi platform reported by Sailor and co-workers with two porous layers of 6 and 100 nm pores designed to monitor enzyme activity in real time by combining size exclusion and optical reflectivity sensing.[15] Control over pore morphology is a crucial aspect of designing bespoke biosensing systems, where each specific target generally requires appropriate pore size (from micropores, mesopores to macropores), depth (nano- and micro-sized) and porosity.[2, 8, 16-19] The pore morphology of pSi is adjustable by simply varying etching conditions such as current density, etching time or etchant ratio. Moreover, the large surface area of pSi (up to 800 m^2 g^{-1}) provides the ability to immobilize a high density of receptors (e.g. antibodies, DNA) within the porous matrix over a small geometrical area, thereby facilitating the number of receptor-target interactions.[20-24] Along with a fast fabrication process, pSi possesses a versatile surface chemistry that allows the incorporation of the desired chemical functionality into the porous material, mainly but not exclusively by hydrosilylation or silanization reactions.[14, 18, 21, 25-32]

The combination of various architectures and convenient surface chemistry makes pSi conducive to both optical and electrochemical transduction mechanisms, which offer ample possibilities to design pSi-based sensing devices. Indeed, optical transducers based on pSi have been widely explored to develop biosensors since 1997 when Sailor and co-workers reported on the first pSi biosensor that investigated basic biological systems.[33] However, the use of pSi

to develop electrochemical biosensors has been limited even though this type of biosensors is able to offer a promising way to detect target analytes featuring ease of use, rapid and robust detection, low cost, miniaturization potential and hence portability.[34-35] Firstly, the main challenge of using pSi as electrochemical transducer is the unavoidable growth of an insulating SiO_2 layer at the surface, due to the fact that the freshly etched surface of pSi is terminated primarily with hydride species, which are highly reactive and prone to oxidation both in water and air. Secondly, the area and geometry of the electrode surface strongly affect the double-layer capacitance, and thus, in the case of pSi, its large effective surface area can cause significant capacitive effects.[36] As a consequence, the charge transfer is limited to the pore tips.[36] In order to limit the growth of SiO_2 on the pSi and render pSi fit for the purpose of electrochemical sensing, several thin film coatings, such as metal or conductive polymer coatings, have been explored.[37-40] However, strategies that leverage pSi's unique physical and chemical features for electrochemical sensing are elusive to date.

Recently, thermal decomposition of acetylene on pSi to create an ultrathin carbon layer was introduced by Salonen and coworkers.[41] A stable thin carbon layer was formed in situ on the pSi surface without changing the structural features of pSi. The carbon layer enables the incorporation of specific functional groups across the pSi surface, which then can undergo further chemical reactions to incorporate biorecognition elements.[25, 42-44] Furthermore, this carbon stabilization treatment renders pSi suitable for electrochemical transduction. Carbon-based nanomaterials such as carbon nanotubes and fullerenes show remarkable electrical performance and thus present salient benefits in electrochemistry (i.e. increased current signals, improved heterogeneous electron-transfer rates).[45-46] Therefore, the combination of pSi features with a highly conductive ultrathin carbon coating would provide not only a large surface area-to-volume ratio but also an excellent surface for electron transfer, which could result in high sensitivity and fast electrochemical responses. Selectivity can be added to the

carbon-stabilized pSi by crafting functional groups on its surface. Thus, the selectivity is not only driven by the electrochemical transducer (redox selectivity), but also by the recognition element (target specificity) immobilized on it. The combination of structural features of pSi and the excellent electrochemical properties of carbon-based nanomaterials leads to the design of novel electrochemical transducers.

In this chapter, the versatility of THCpSi and TCpSi as electrochemical transducers for Faradaic processes and biosensing applications is demonstrated. The surface morphology and chemical composition of the carbon-stabilized pSi structures were characterized by microscopic and spectroscopic techniques. The electrochemical performance of carbon-stabilized pSi at two different temperatures (THCpSi and TCpSi) was investigated in the presence of redox species differently charged (negative, positive and neutral). Additionally, their performance was benchmarked against flat silicon carbon-stabilized following the same treatment as the pSi substrates, and commercial electrodes such as glassy carbon and carbon-based screen-printed electrodes. Finally, an impedimetric immunosensor, based on the bioconjugation of anti-MS2 bacteriophage antibody onto a THCpSi structure, was developed, showing the feasibility to detect MS2 bacteriophage over a large range of concentrations, from 1 to 10^6 pfu mL^{-1}. The results demonstrate that carbon-stabilized pSi is a promising electrochemical transducer for biosensing applications.

3.2 Experimental section

Reagents: Potassium ferricyanide $K_3[Fe(CN)_6]$, potassium ferrocyanide $K_4[Fe(CN)_6]$, hexamine ruthenium chloride (III) $[Ru(NH_3)_6]Cl_3$, hydroquinone, undecylenic acid, N-hydroxysuccinimide (NHS), N(3-dimethylaminopropyl) N-ethylcarbodiimide hydrochloride (EDC), phosphate buffered saline (PBS) tablets and 2-(N-morpholino)-ethanesulfonic acid (MES) were purchased from Sigma-Aldrich (Australia). Hydrofluoric acid (48%) was purchased from Scharlau (Australia). The acetylene gas cylinder (1 m^3 industrial grade,

dissolved) was purchased from BOC (Australia). Monoclonal antibody (produced in mouse) against MS2 bacteriophage was purchased from Tetracore (USA). All solutions were prepared in ultrapure water (18.2 MΩ cm) from a Milli-Q system.

pSi fabrication: 6 inch, boron doped (p++ type) silicon wafers (100) with 0.00055-0.001 Ω cm and 1.1 – 1.8 Ω cm resistivity were purchased from Siltronix (France). pSi layers prepared with the highest resistivity were only used for IR transmission measurements to characterize surface modification. A whole 6 inch p-type silicon wafer was anodically etched in an electrolyte solution containing 1:1 (v:v) HF and absolute ethanol to produce a first pSi layer, using a MPSB wet etching system (A.M.M.T). Firstly, the sacrificial layer produced with a current density of 60.6 mA cm^{-2} for 30 s was removed with 1 M NaOH.[47] Then the etching cell was rinsed with water, absolute ethanol and dried with N_2 gas. This layer is critical to inhibit the formation of a parasitic layer during further etching of the proper pSi sensing layer. Next, a current density of 53 mA cm^{-2} was applied to obtain a pSi single layer with an average pore diameter of 72 ± 15 nm. The depth of the pSi layer was controlled by the etching time, 50 s and 200 s for 1.2 ± 0.1 µm and 2.9 ± 0.1 µm thickness, respectively. The 2.9 µm-thick pSi layers were used for SEM imaging while the 1.2 µm-thick pSi layers were used for most electrochemical characterization and sensing studies. Additional pSi samples with varying pore size and thickness were fabricated in 1:1 etchant by changing the current density and time to study the effect of the morphological features on their electrochemical performance. The freshly etched pSi was rinsed with ethanol and then immediately used for carbon stabilization.

pSi single layer carbon stabilization by acetylene gas: To improve the stability and conductivity of pSi single layer nanostructures, the freshly etched pSi substrates were thermally hydrocarbonized (THC) and carbonized (TC) by acetylene decomposition as described by Salonen et al [48-49]. *a) Thermal hydrocarbonization of freshly etched pSi (THCpSi).* Briefly, the

freshly etched pSi was placed into a quartz tube under N_2 flow at 2 L min^{-1} for 45 min at room temperature. A 1:1 N_2-acetylene mixture flow was introduced into the tube at room temperature for 15 min after the purging step, then the quartz tube was placed into a preheated tube furnace at 525 °C for another 15 min under the continuous mixture flow. Finally, the tube was allowed to cool down back to room temperature under the N_2 flow. *b) Thermal carbonization of freshly etched pSi (TCpSi).* TC treatment is a two-step carbonization process that starts with THC at 525 °C followed by annealing at 800 °C. After THC process, the tube was left to cool down under N_2 flow. For the second step of TC, without opening the quartz tube, a mixture of 1:1 N_2-acetylene was flown for 10 min at room temperature, followed by annealing at 800 °C for 10 min only under N_2 flow (2 L min^{-1}). Finally, the tube was left to cool down back to room temperature under N_2 flow.

Fourier-transform infrared spectroscopy (FTIR): IR spectra were recorded on a Bruker Hyperion 1000 IR microscope using transmission and reflectance modes. Boron doped (p-type) Si, (100)-orientated with 1.1 – 1.8 Ω cm and 0.00055-0.001 Ω cm resistivity was used for IR transmission and reflectance measurements, respectively. All the spectra were recorded as an average of 64 scans at a resolution of 4 cm^{-1} over the range of 650 to 4000 cm^{-1}. A clean flat silicon substrate was used as background and all the spectra were analyzed using Opus software.

Water contact angle measurements. A custom-built goniometer with a Panasonic CCTV camera (WV-BP550/G) was used to conduct water contact measurements of the pSi structures. After dropping 1 µL ultrapure water with a 10 µL syringe onto the surface, a photograph was immediately taken. ImageJ software (drop Analysis plugin) was employed to determine the contact angle of the water drop in contact with the surface. Contact angle values reported here represent the average of triplicate measurements.

Scanning electron microscopy (SEM): SEM was carried out on a FEI NovaNanoSEM 430, accelerating voltage of 5 kV.

X-ray photoelectron spectroscopy (XPS): XPS analysis was performed using an AXIS Nova spectrometer (Kratos Analytical Inc., Manchester, UK) with a monochromated Al Kα source at a power of 180 W (15 kV × 12 mA) and a hemispherical analyzer operating in the fixed analyzer transmission mode. The total pressure in the main vacuum chamber during analysis was typically between 10^{-9} and 10^{-8} mbar. Survey spectra were acquired at a pass energy of 160 eV. To obtain more detailed information about chemical structure, oxidation states etc., high resolution spectra were recorded. Each specimen was analyzed at an emission angle of 0° as measured from the surface normal. Since the actual emission angle is ill-defined in the case of rough surfaces (ranging from 0º to 90º) the sampling depth may range from 0 nm to approx. 10 nm. Data processing was performed using CasaXPS processing software version 2.3.15 (Casa Software Ltd., Teignmouth, UK). All elements present were identified from survey spectra. The atomic concentrations of the detected elements were calculated using integral peak intensities and the sensitivity factors supplied by the manufacturer. Binding energies were referenced to the C 1s peak at 285 eV (aliphatic hydrocarbon).

Electrochemical measurements. All the electrochemical measurements were performed on an electrochemical analyzer (CH Instruments, model 600D series) using a three-electrode electrochemical cell. Data acquisition and analysis were accomplished using CH Instruments software (CH Instruments, Inc., Austin, TX). SPEs employed in this study were supplied by DropSens (150BT) and consisted in a three-electrode system with a 4 mm diameter working carbon-based electrode, a platinum counter electrode and a silver pseudo-reference electrode. GCEs were from CH Instruments (CHI 104), 3 mm diameter. The flat silicon and pSi electrode area was delimited by an O-ring (internal diameter, 7.5 mm) used in an in-house built three-

electrode Teflon cell. GCE, flat silicon and pSi electrodes were employed together with an external Pt electrode (counter electrode) and a Ag/AgCl electrode (reference electrode). All the potentials are provided versus Ag/AgCl. Cyclic voltammetric measurements were performed by scanning the potential in a potential range that depends on the redox species used, at a scan rate of 0.1 V s^{-1}. EIS measurements were performed under open circuit potential conditions, scanning frequencies from 100 kHz to 0.1 Hz in logarithmic scale, with an ac amplitude of 5 mV.

MS2 bacteriophage immunosensor preparation and electrochemical detection protocol: Firstly, COOH groups were introduced on the THCpSi surface (72 ± 15 nm average pore diameter, 1.2 ± 0.1 µm thickness) by thermal hydrosilylation with undecylenic acid. The substrates were immersed in pure undecylenic acid at 150 °C for 10 h under inert atmosphere (N_2). After cooling down to room temperature, the samples were rinsed with absolute dichloromethane and then ethanol. Secondly, the COOH groups were activated by incubating the functionalized substrates in 10 mg mL^{-1} EDC and 15 mg mL^{-1} NHS in 0.1 M MES buffer, pH 5.5, at room temperature for 30 min, to produce succinimidyl ester groups. Thirdly, immediately after carbodiimide activation, 25 µg mL^{-1} monoclonal anti-MS2 bacteriophage antibody in 10 mM PBS was added and incubated overnight at 4 °C. The same concentration of a non-specific antibody was used to prepare the sensors used as control. The remaining ester groups were deactivated with 0.1 M ethanolamine in 10 mM PBS buffer for 45 min. Various MS2 bacteriophage solutions from 1 to 10^6 pfu mL^{-1} prepared in 10 mM PBS buffer were incubated on the biosensor surface for 30 min. After each incubation, the biosensor was thoroughly rinsed with PBS. Prior and after MS2 bacteriophage incubation EIS measurements were performed in a 2 mM $[Fe(CN)_6]^{3-/4-}$ solution prepared in 10 mM PBS, pH 7.4. EIS measurements were performed using three immunosensors.

3.3 Results and discussion

3.3.1 Fabrication and carbon stabilization of pSi single layers

As described in the introduction, pore size, morphology and depth of pSi can be easily controlled and adjusted by tuning the anodization conditions. SEM was used to determine the pore size and depth (**Figure 3.1)** of the pSi structures fabricated by electrochemical anodization of crystalline silicon (100) in the presence of HF. To stabilize the pSi surface and increase the electrical conductivity of the semiconductor, freshly etched pSi samples were subjected to thermal treatment at 525 °C (THC) and at 800 °C (TC). **Figure 3.1** presents the SEM images of pSi, THCpSi and TCpSi surfaces. Under the etching conditions employed, the average pore diameter of pSi single layer was 72 ± 15 nm, whilst the layer thickness was 3.8 µm. As shown from the top and cross-sectional SEM images of carbon-stabilized pSi, both THCpSi and TCpSi retain the features of pSi. Compared to pSi, neither THCpSi nor TCpSi alter the nanostructured morphology and dimensions (pore opening, diameter and depth). However, differences in their respective water contact angles provide evidence of the changing surface chemistry. THCpSi substrates presented a contact angle of 125 ± 4° whilst TCpSi showed a significantly lower contact angle of 29 ± 4°, which are in agreement with a hydrophobic behavior of the surface caused by the CH_x present at the THCpSi, and a hydrophilic behavior for TCpSi as a result of its thin oxide layer.[50]

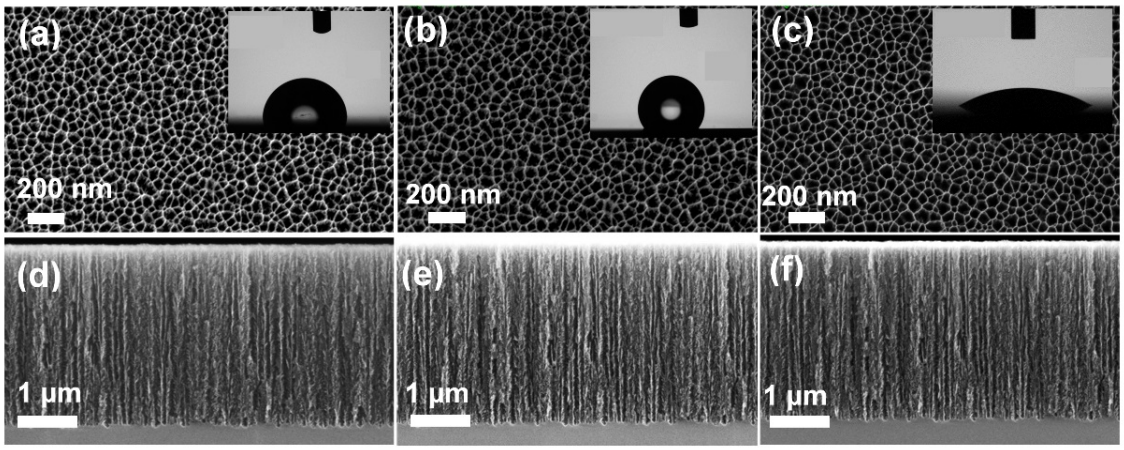

Figure 3.1 Top SEM images and water contact angle photographs (insets), and corresponding cross-sectional SEM images of (a,d) freshly etched pSi, (b,e) THCpSi and (c,f) TCpSi. pSi single layers were electrochemically etched by applying a current density of 53 mA cm^{-2} for 200 s in 1:1 HF/EtOH. Water contact angle standard error is ± 4° from 3 replicated measurements.

Fourier transform infrared (FTIR) spectra recorded for freshly etched pSi, THCpSi and TCpSi structures, revealed changes of the chemical composition of these substrates (**Figure 3.2**). As expected, freshly etched pSi displays bands characteristic of Si-H and Si-H_2 stretching vibrations at 2087 and 2114 cm^{-1} with an additional band associated with the Si-H deformation mode at 905 cm^{-1} (**Figure 3.2a**).[51] The characteristic bands of freshly etched pSi are not shown in the FTIR spectra of both THCpSi and TCpSi (**Figure 3.2b-c**) indicating chemical coverage of these Si-H_x moieties after the carbon stabilization process at 525 and 800 °C, respectively. After both thermal treatments, new vibration bands associated to stretching vibrations of saturated C-H appeared at 873, 1436, 2920 and 3047 cm^{-1}, unsaturated carbon double bond stretching at 1600 cm^{-1}, and CH_3 symmetric deformation mode of Si-CH_3 at 1250-1260 cm^{-1}.[52] Furthermore, peaks in the FTIR spectra of both THCpSi and TCpSi found between 1000 and 1150 cm^{-1} are assigned to the oxidation caused by the carbonization process at high temperature in the presence of oxygen traces left after the purging process.

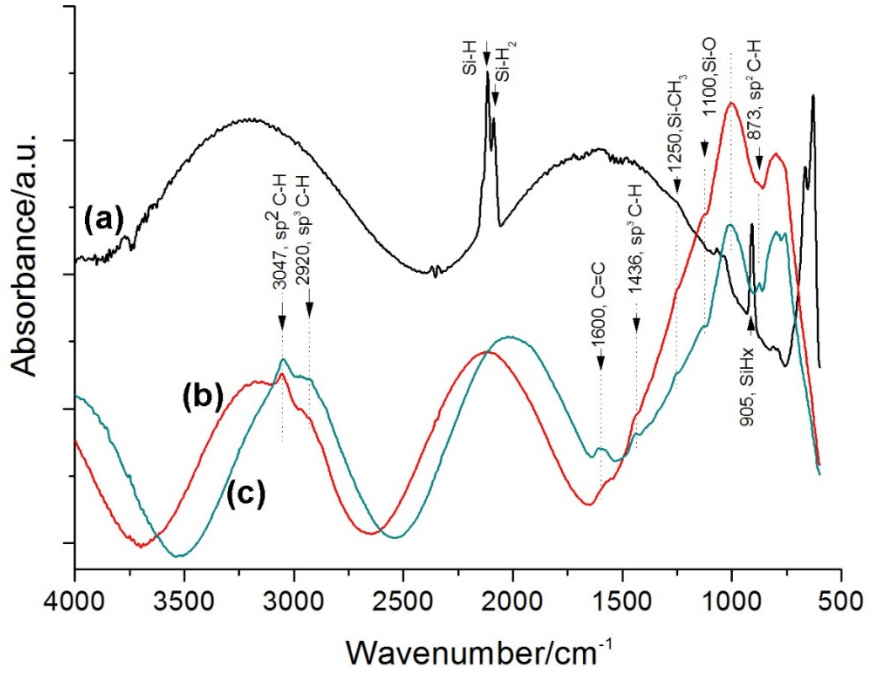

Figure 3.2 Transmittance FTIR spectra of (a) freshly etched pSi, (b) THCpSi and (c) TCpSi. pSi single layers were electrochemically etched in 1:1 HF/EtOH with a current density of 100 mA cm^{-2} for 300 s using p-type silicon wafers with a resistivity of 1.1 -1.8 Ω cm.

X-ray photoelectron spectroscopy (XPS) was performed to further characterize the surface chemistry of the THCpSi and TCpSi surfaces. The XPS C 1s spectra in **Figure 3.3** and elemental analysis shown in **Table 3.1** verify the formation of a carbon layer during the carbon stabilization treatments, agreeing with the previously discussed FTIR results. The carbon content of THC-flat silicon (26%) and TC-flat silicon (22%) is significantly higher than that of flat silicon (13%). Similarly, the high carbon content characteristic for the carbon stabilization treatments is also observed in both THCpSi (42%) and TCpSi (50%) surfaces, where minor contribution from the C-Si species at *ca.* 283.6 eV and major contribution from hydrocarbons at *ca.* 285 eV are evident. These higher carbon percentages for THCpSi and TCpSi compared to their corresponding flat counterparts, THC- and TC-flat Si, respectively, agree with the increased surface area provided by the porous structures. From **Table 3.1**, THCpSi and TCpSi demonstrate a high carbon-to-silicon ratio (C/Si) of 1.02 and 1.62, respectively. These values are significantly higher than those of the respective THC- (0.44) and TC-flat silicon (0.47)

surfaces. Furthermore, the C/Si ratio of TCpSi is significantly higher than that of THCpSi, indicating TCpSi carbon coverage is higher than that of THCpSi. The large surface area of THCpSi and TCpSi coupled with the presence of a carbon layer is of particular relevance from an electrochemical point of view. Hence, further investigation of the potential to use these nanostructured films as electrochemical transducers for biosensing applications is discussed.

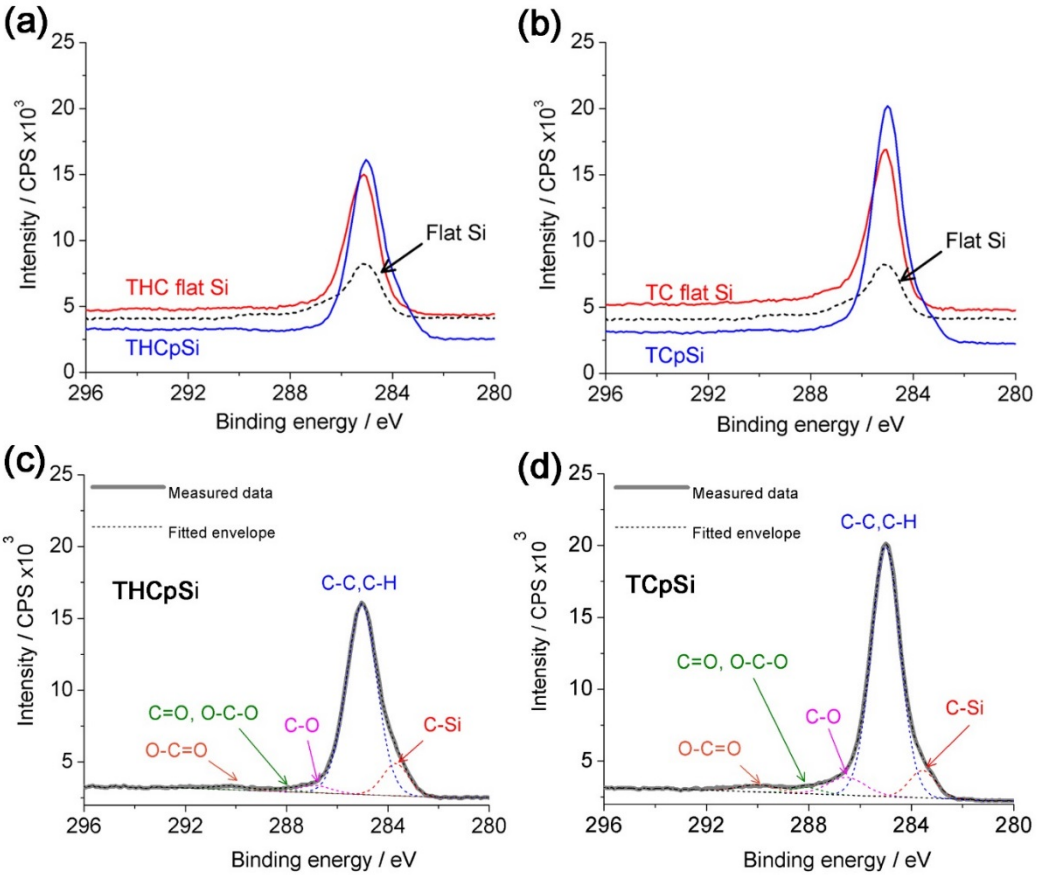

Figure 3.3 XPS high resolution C 1s spectra of (a) flat Si, THC-flat silicon and THCpSi, and (b) flat Si, TC-flat silicon and TCpSi. XPS high resolution C 1s spectra curve-fits of (c) THCpSi and (d) TCpSi were calculated using five components of C-Si, sp^2 (C-C, C-H), C-O, C=O and O-C-O, O-C=O groups.

Table 3.1 Average elemental composition obtained from XPS survey spectra of various silicon and pSi structures before and after undergoing two cyclic voltammograms in a 2 mM $[Fe(CN)_6]^{3-/4-}$ solution in 10 mM PBS, pH 7.4.

Elemental composition		Flat Si	THC-flat Si	THCpSi	THCpSi after CV	TC-flat Si	TCpSi	TCpSi after CV
Element (at%)	C	13.05	25.61	41.99	41.40	22.38	49.72	49.08
	O	30.31	15.27	14.50	23.20	30.35	18.22	23.89
	Si	55.73	58.45	41.17	34.53	47.23	30.76	26.38
	F	0.32	0.60	2.06	0.79	0.05	1.30	0.39
	N	0.61	0.07	0.27	0.08	0.00	0.00	0.27
Si species (at%)	Si(0)	42.12	51.94	26.59	15.24	27.41	12.27	8.30
	Si-C	0.01	0.84	5.08	3.45	0.32	4.01	2.57
	SiOx	13.61	6.51	14.58	19.29	19.82	18.49	18.08
Ratio	C/Si	0.23	0.44	1.02	1.20	0.47	1.62	1.86
	SiOx/Si(0)	0.32	0.13	0.55	1.27	0.72	1.51	2.18

3.3.2. THCpSi and TCpSi electrochemical characterization via CV

CV is a useful characterization technique for the investigation of electrochemical events. The evolution of oxidation and reduction reactions are monitored by changes in current intensity, as well as by the shift of redox potentials, when the potential applied between the working and reference electrodes is cycled. The carbon-stabilized surfaces (THC or TC) were electrochemically characterized in the presence of model redox electroactive pairs via CV as this technique can provide insights into their performance as electrochemical transducers and their intrinsic surface properties. Firstly, to evaluate the differences in the electrochemical behavior of flat Si, THCpSi and TCpSi, CV characterization in the presence of a common anionic inner-sphere redox pair was investigated. Using a 2 mM ferrocyanide and 2 mM

ferricyanide solution ($[Fe(CN)_6]^{3-/4-}$) in 10 mM PBS at pH 7.4 (**Figure 3.4**), the electrochemical performance of THCpSi and TCpSi was evaluated through their potential to measure Faradaic currents. Carbon-stabilized (THC and TC) flat boron doped silicon semiconductor (**Figure 3.4**, black lines) showed poor performance as electrochemical transducer to evaluate redox events (-0.2 to 0.6 V vs Ag/AgCl), as shown by the low oxidation and reduction peak currents and large peak-to-peak potential difference ($\Delta Ep = |E_{oxi} - E_{red}|$). THCpSi and TCpSi (**Figure 3.4**, red lines) showed fast and reversible electrochemical response to $[Fe(CN)_6]^{3-/4-}$: ΔEp were 58 and 66 mV, respectively, representing near ideal reversible electron-transfer reactions (**Table 3.2**). These ΔEp values, very close to the expected theoretical value of 59 mV at 25 °C for one-electron transfer reactions, indicate that both THCpSi and TCpSi transducers possess the required surface structure and electronic properties to enable rapid electron transfer of the $[Fe(CN)_6]^{3-/4-}$ redox system.[53] These data demonstrate the improvement in the performance of carbon-stabilized pSi as electrochemical transducer by simply varying the crystal structure (nanocrystal) of the material (Si) in combination with its surface stabilization by introducing a thin carbon layer, which is responsible for the significant increase in the charge carrier mobility.

Table 3.2 Summary of peak currents $i_{p(oxi)}$ and $i_{p(red)}$, peak current ratio $i_{p(red)}/i_{p(oxi)}$, peak-to-peak potential difference **ΔEp**, and half-wave potential ($E_{1/2}$), extracted from the cyclic voltammograms obtained using GCE, SPE, THCpSi and TCpSi, measured in 2 mM $[Fe(CN)_6]^{3-/4-}$, $[Ru(NH_3)_6]^{2+/3+}$ and HQ/Q solutions in 10 mM PBS, pH 7.4.

Electrode	GCE					SPE					THCpSi					TCpSi				
	$i_{p(oxi)}$ /µA	$i_{p(red)}$ /µA	$i_{p(red)}/i_{p(oxi)}$	ΔEp /mV	$E_{1/2}$ /mV	$i_{p(oxi)}$ /µA	$i_{p(red)}$ /µA	$i_{p(red)}/i_{p(oxi)}$	ΔEp /mV	$E_{1/2}$ /mV	$i_{p(oxi)}$ /µA	$i_{p(red)}$ /µA	$i_{p(red)}/i_{p(oxi)}$	ΔEp /mV	$E_{1/2}$ /mV	$i_{p(oxi)}$ /µA	$i_{p(red)}$ /µA	$i_{p(red)}/i_{p(oxi)}$	ΔEp /mV	$E_{1/2}$ /mV
$[Fe(CN)_6]^{3-/4-}$	53	-45	0.853	86	185	62	-65	1.049	213	117	344	-249	0.724	58	208	431	-342	0.794	66	210
$[Ru(NH_3)_6]^{2+/3+}$	21	-20	0.938	70	-175	23	-45	1.952	96	-220	107	-139	1.300	66	-163	134	-171	1.276	81	-165
HQ/Q	62	-54	0.872	282	70	102	-92	0.897	494	150	381	-305	0.801	304	218	477	-477	1	335	120

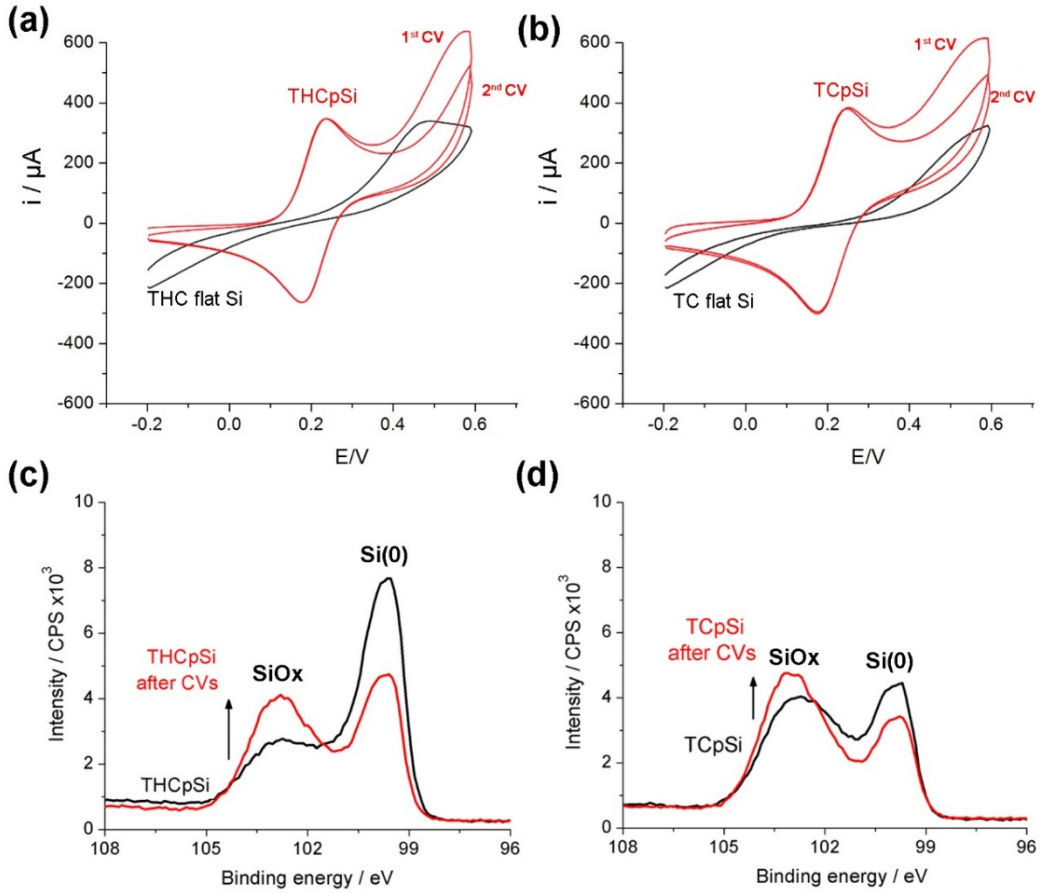

Figure 3.4 Cyclic voltammograms using (a) THC-flat silicon and THCpSi (black and red lines, respectively) and (b) TC-flat silicon and TCpSi (black and red lines, respectively), as working electrodes. XPS high resolution silicon 2p spectra of (c) THCpSi and (d) TCpSi before (black lines) and after (red lines) two cyclic voltammograms. Electrochemical measurements were performed in a 2 mM $[Fe(CN)_6]^{3-/4-}$ solution in 10 mM PBS.

Cyclic voltammograms for THCpSi (**Figure 3.4a**) and TCpSi (**Figure 3.4b**) show an initial decrease in current at potentials higher than +0.4 V which stabilizes after three consecutive cycles. This effect may be attributed to the self-oxidation of a small percentage of unmodified pSi. XPS characterization of the surfaces illustrates a decrease in elemental silicon species and an increase in silicon oxide species after two consecutive cyclic voltammograms (**Figure 3.4c-d**): a 2.3- and 1.4-fold increase in the silicon oxide-to-elemental silicon ratio (SiOx/Si(0)) of THCpSi and TCpSi, respectively (**Table 3.1**). The smaller change in SiOx/Si(0) for TCpSi

after having undergone two consecutive cyclic voltammograms compared to that of THCpSi points toward higher chemical stability of the former which may be explained by its higher initial SiOx/Si(0) of 1.51 compared to that of THCpSi (0.55), thus experiencing less pSi self-oxidation when an oxidizing potential is applied. The superior electrochemical performance of TCpSi, underpinned by anodic currents that are larger than those measured with THCpSi, is consistent with both its higher chemical stability and carbon coverage as observed earlier from XPS analysis (**Table 3.1**). Hence, the advantageous nature of this carbon layer for electrochemical sensing purposes was exploited.

3.3.3 Electrochemical properties of THCpSi and TCpSi-based electrodes vs conventional carbon-based electrodes

Figure 3.5 summarizes the cyclic voltammograms obtained for the redox pair $[Fe(CN)_6]^{3-/4-}$ (2 mM in 10 mM PBS, pH 7.4) using various carbon-based transducers, including glassy carbon electrode (GCE) and carbon screen-printed electrode (SPE), THCpSi and TCpSi. The voltammograms of pSi platforms without carbon stabilization, and thus without carbon coating, are not presented here as those materials are highly reactive in air and aqueous media and as a result quickly oxidize and degrade.

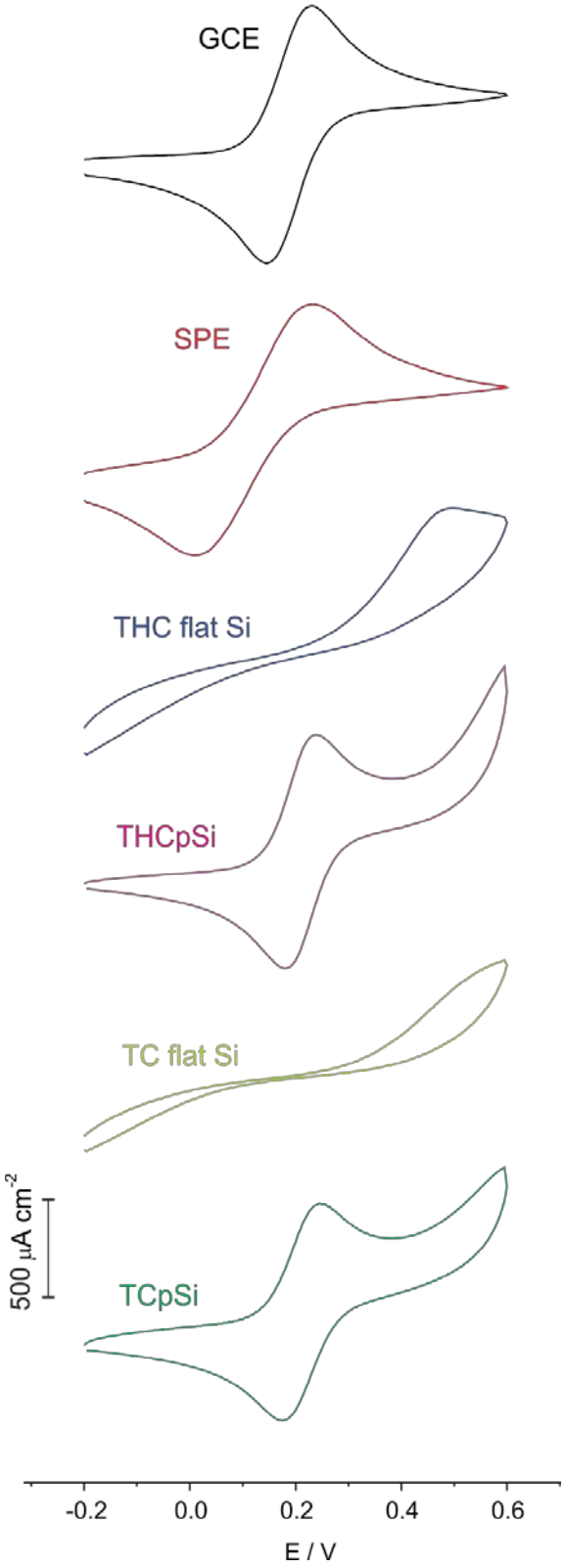

Figure 3.5 Normalized current density from cyclic voltammograms using various working electrodes: GCE, SPE, THC flat Si, THCpSi, TC flat silicon and TCpSi. Measurements performed in a 2 mM $[Fe(CN)_6]^{3/4-}$ solution in 10 mM PBS, pH 7.4. Note that the current density was calculated using the geometric diameter of the GCE (3.0 mm), SPE (4.0 mm) and

the O-ring (7.5 mm) which delimits the silicon (flat or porous) area exposed for electrochemical analysis.
The well-defined redox peaks shown for $[Fe(CN)_6]^{3/4-}$ by both THCpSi and TCpSi electrodes (**Figure 3.5** and **Figure 3.6** black lines) clearly indicate the fast electron transfer kinetics of this quasi-reversible redox system at both electrode surfaces. This is further supported by the ΔEp values shown by both THCpSi (58 mV) and TCpSi (66 mV) electrodes, which are lower than those shown by GCE (86 mV) and SPE (213 mV) under the same conditions (**Table 3.2)**. The voltammetric analysis of THCpSi and TCpSi platforms suggests that they are suitable to elucidate oxidation and reduction processes in a similar manner to commercial GCE without altering the nature of the redox process (i.e. electron transfer mechanism and kinetics). However, in contrast to GCE or SPE, the electrode surface area of THCpSi and TCpSi can be easily tuned by changing the etching conditions. This is important since the current measured in voltammetry is directly proportional to the surface area (**Figure 3.7**). Therefore, one of the main advantages of carbon-stabilized pSi over conventional carbon electrodes is that the sensitivity of the sensing platform can be improved by increasing the pSi thickness and adjusting the pore dimensions to the desired application. However, it is worth noting that such electrode surface area increase can result in a significant rise of the capacitance which could be a benefit (e.g. in the case of supercapacitors) or pose a limitation depending on the application. Capacitive effects are further discussed further below.

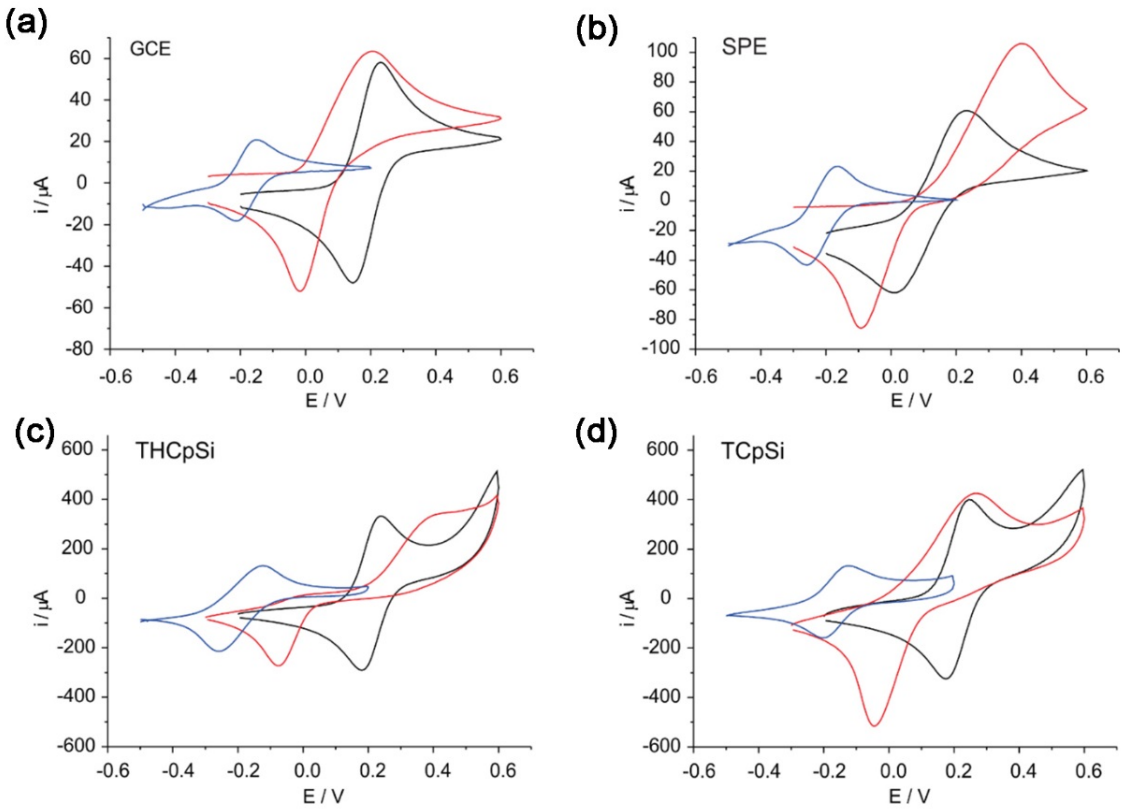

Figure 3.6 Cyclic voltammograms using various working electrodes, (a) GCE, (b) SPE, (c) THCpSi and (d) TCpSi. Measurements performed in 2 mM $[Fe(CN)_6]^{3-/4-}$ (black line), $[Ru(NH_3)_6]^{2+/3+}$ (blue line) and HQ/Q (red line) solutions in 10 mM PBS, pH 7.4.

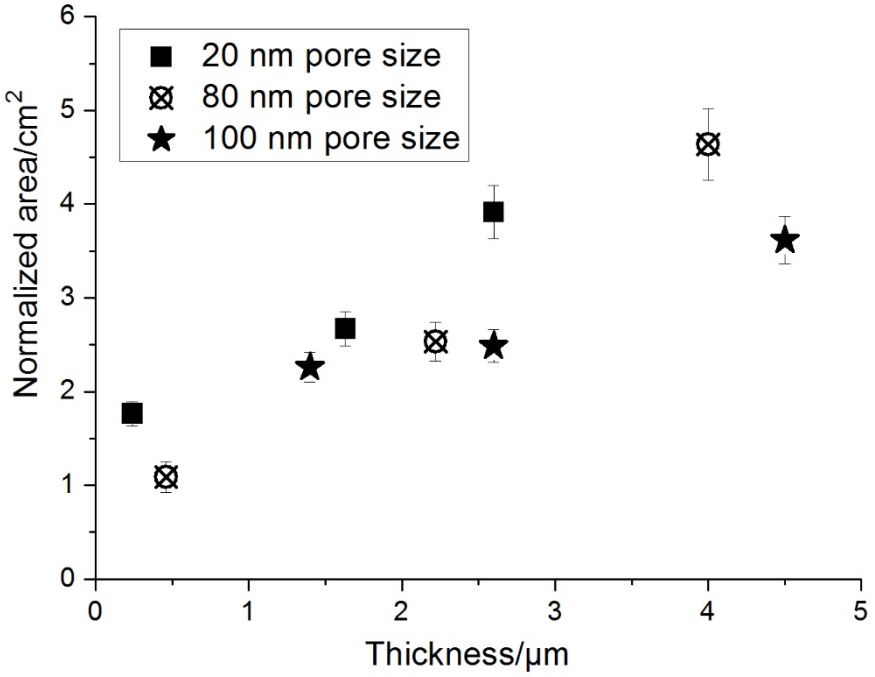

Figure 3.7 Plot of normalized area, calculated via CC, vs pSi thickness of various THCpSi electrodes. Each plot corresponds to THCpSi structures of a specific average pore diameter

(20, 80 and 100 nm). Measurements were performed in a 2 mM $[Fe(CN)_6]^{3-/4-}$ solution in 10 mM PBS, pH 7.4.

3.3.4 Electrochemical behavior of carbon-stabilized pSi nanostructures exposed to three model redox species

Apart from $[Fe(CN)_6]^{3-/4-}$, $[Ru(NH_3)_6]^{2+/3+}$ and hydroquinone/quinone (HQ/Q) were selected as alternative redox species with different electrode kinetics, to study the electrochemical performance of THCpSi and TCpSi. Each one of these redox systems behaves differently depending on the electronic properties, and surface structure and chemistry of the working electrode. As previously described, $[Fe(CN)_6]^{3-/4-}$ is an anionic inner-sphere redox probe. $[Ru(NH_3)_6]^{2+/3+}$ is a cationic outer-sphere redox active complex and finally HQ/Q is a neutral aromatic organic compound which is proton sensitive. PBS solutions of these three redox pairs at 2 mM concentration were electrochemically analyzed using THCpSi and TCpSi as working electrode (**Figure 3.6**) in an attempt to recognize possible structural defects and physicochemical properties that can impact the electron transfer of each redox pair at the electrode surface. The magnitude of the oxidation and reduction current intensity values, ΔEp and half-wave potential ($E_{1/2}$) extracted from **Figure 3.6** are summarized in **Table 3.2**.

In the case of $[Fe(CN)_6]^{3-/4-}$, both THCpSi and TCpSi transducers possess the required surface structure and electronic properties to enable rapid electron transfer. The ΔEp values for $[Fe(CN)_6]^{3-/4-}$ using THCpSi (58 mV) and TCpSi (66 mV) electrodes agree with the ideal behavior of a quasi-reversible redox system.

$[Ru(NH_3)_6]^{2+/3+}$ is known to be relatively insensitive to the surface microstructure and chemistry of carbon electrodes. But the electronic properties at the electrode interface, namely the density of the electronic states near the formal potential, play a key role in affecting the reaction rate for $[Ru(NH_3)_6]^{2+/3+}$.[54] The low ΔEp for THCpSi (66 mV) and TCpSi (81 mV) along with their low formal potential values (i.e. $E_{1/2}$), -163 mV and -165 mV, respectively,

demonstrate that the density of the electronic states on both THCpSi and TCpSi electrodes is sufficient to support the rapid electron transfer of $[Ru(NH_3)_6]^{2+/3+}$.

The electron transfer reactions involving HQ/Q generally undergo a reversible two-electron redox reaction. HQ/Q is proton sensitive, its redox potential strongly depending on pH.[55] Reactions involving protons might slow down the electrochemical kinetics and ultimately increase the charge-transfer resistance.[56] At the conditions used in this study (i.e. PBS at pH 7.4), the ΔEp for HQ/Q using THCpSi (304 mV) and TCpSi (335 mV) electrodes were similar to that of a GCE (282 mV), and even lower than that of a commercial SCE (494 mV), demonstrating the suitability of both THCpSi and TCpSi as Faradaic platforms to support HQ/Q redox processes.

To summarize, the data shown in **Table 3.2** demonstrate the potential of carbon-stabilized pSi electrodes as an alternative to conventional carbon-based electrodes, as in all cases the ΔEp values for THCpSi and TCpSi are lower than those of SPEs, which indicates improved electron transfer at these electrodes. Carbon-stabilized pSi electrodes show low surface interactions with the three redox probes under oxidation/reduction conditions. Nevertheless, TCpSi electrodes provide larger ΔEp than GCE for $[Ru(NH_3)_6]^{2+/3+}$ and HQ/Q which may be a result of the chemical composition of the surface. As shown by XPS elemental analysis (**Table 3.1**), TCpSi displays higher carbon coverage (C/Si) and higher content of unreactive silicon oxide species (SiOx/Si(0)) than THCpSi. The higher carbon coverage of TCpSi translates to larger current intensities and superior electron transfer efficiency compared to that of THCpSi as observed for the three model redox species investigated. The higher content of unreactive silicon oxide species of TCpSi contributes to its improved chemical stability during redox processes and hence, consistently enhanced electrochemical performance compared to THCpSi as pSi self-oxidation when an oxidizing potential is applied is minimized.

3.3.5 Estimation of the electrode effective area by chronocoulometry (CC)

As one of the classical electrochemical techniques used in electrochemical chemistry, CC measures the charge (coulombs) as a function of time.[57] In other words, by applying a fast-rising potential pulse to the working electrode, the electrical charge passing through this electrode is recorded over time.[58] This technique is particularly useful for the nanostructured transducers considered in this work, where the real electroactive surface area is significantly larger than the geometric surface area.[59-61] The large surface area of pSi can provide high sensitivity, however, the electrode effective area is key in Faradaic electrochemistry.[59, 62] To establish the electroactive surface area of the nanostructured pSi electrodes, chronocoulometric measurements were carried out to firstly calculate the diffusion coefficients for the redox probe $[Fe(CN)_6]^{3-/4-}$ and then estimate the active electrode area.

For the chronocoulometric analysis, a GCE was taken as a reference, considering its real surface area (0.074 cm^2) almost equivalent to its geometric surface area (0.071 cm^2). Chronocoulometric data are analyzed by using the Cottrell equation (**Equation 3.1**):[61]

$$i_p = \frac{nFACD^{1/2}}{\pi^{1/2}t^{1/2}} \qquad (3.1)$$

wherein i_p is the peak current (A), n represents the number of electrons, A represents the surface area (cm^2), D is the diffusion coefficient of the reduced species ($cm^2\ s^{-1}$), F is Faraday's constant (96485.3 C mol^{-1}), C is the concentration of the electroactive species (mol cm^{-3}) and t is time (s).

The slope of the Anson plot (Q vs $t^{1/2}$), calculated from the chronocoulometric data (i_p vs t) of a GCE, was used in the integrated Cottrell equation (**Equation 3.2**), to obtain the diffusion coefficient for the redox species $[Fe(CN)_6]^{3-/4-}$.

$$Q = \frac{2nFACD^{1/2}t^{1/2}}{\pi^{1/2}} \qquad (3.2)$$

The diffusion coefficient for $[Fe(CN)_6]^{4-}$, prepared in 10 mM PBS at pH 7.4, was calculated to be 1.5 x 10^{-5} cm^2 s^{-1}. This value is in agreement with published data obtained in similar electrolyte conditions.[26] The effective area can be calculated from the chronocoulometric data obtained for each electrode using **Equation 3.1** inputting the previously calculated diffusion coefficient **(Table 3.2**). As expected from the peak current intensity values of the cyclic voltammograms for $[Fe(CN)_6]^{3-/4-}$ shown in **Figure 3.6**, THCpSi and TCpSi present larger normalized effective surface areas than GCE and SPE (**Table 3.3**). Furthermore, the effective area values calculated for TCpSi are higher than those obtained for THCpSi. The effective area for both TCpSi and THCpSi could be further increased by modifying the thickness and pore diameter of the pSi structures (see example for THCpSi in **Figure 3.7**). These parameters can be easily altered by varying the electrochemical etching rate, time, current density and electrolyte composition. At the same time, this allows for size exclusion effects to be introduced. The versatility of these carbon-stabilized pSi materials with increased electron mobility makes them highly adaptable electrochemical transducers for multiple sensing applications.

Table 3.3 Effective, geometric and normalized surface area of various working electrodes.

Electrodes	GCE	SPE	THCpSi	TCpSi
*Effective surface area / cm^2	0.074	0.117	0.588	0.770
Geometric surface area / cm^2	0.071	0.126	0.442	0.442
**Normalized surface area	1.04	0.93	1.33	1.74

* Effective surface area calculated using the Cottrell equation.
**Normalized surface area = effective surface area/geometric surface area.

3.3.6 Electrochemical characterization of THCpSi and TCpSi via EIS

The electrochemical phenomena involving electron transfer processes through the interface between carbon-stabilized pSi (THCpSi and TCpSi) and $[Fe(CN)_6]^{3-/4-}$ were further explored by means of EIS, a highly sensitive technique that affords important information on the interfacial properties of an electrode. Impedance measurements were performed at the open circuit potential for a range of frequencies (100 kHz - 0.1 Hz) and 5 mV amplitude. The impedance spectra were fitted to a Randles circuit (inset in **Figure 3.8b**), which is an equivalent electrical circuit composed of solution resistance (R_s), charge-transfer resistance (R_{ct}), Warburg impedance (W) and double-layer capacitance (C_{dl}). The obtained results are summarized in **Table 3**. As expected, R_{ct} values were significantly larger for THC-flat silicon (7400 ± 260 Ω) and TC-flat silicon (23500 ± 1300 Ω) than for THCpSi (70 ± 24 Ω) and TCpSi (40 ± 16 Ω), due to the high resistance the former electrodes show to electron transfer, likely caused by a low carbon coverage compared to their equivalent porous nanostructures. It is worth noting that both THCpSi and TCpSi electrodes display smaller R_{ct} values than those of commercial GCE (105 ± 35 Ω) and SPE (747 ± 70 Ω), further indicating the potential of these carbon-stabilized pSi platforms to be used as nanostructured electrochemical transducers. The C_{dl} features the capacitive behavior of the double layer associated with the charge separation at the electrode surface-solution interface, and plays a key role on the signal-to-noise ratio achieved by a sensor and thus affects its sensitivity. In principle, the C_{dl} rises as the electrode surface

area increases. Therefore, it is expected that porous electrodes like THCpSi and TCpSi show large C_{dl} values negatively impacting on the electrochemical readout. However, C_{dl} values for THCpSi (1.3 ± 0.2 µF) and TCpSi (1.7 ± 0.1 µF) were reasonably close to those of GCE (0.8 ± 0.1 µF) and SPE (0.9 ± 0.1 µF). Hence, as indicated by the low R_{ct} and C_{dl} values for carbon-stabilized pSi, no negative impact on the signal-to-noise ratio is expected even though the effective surface area is increased. This result speaks to the feasibility of using these carbon-stabilized pSi nanostructures as promising electrochemical transducers.

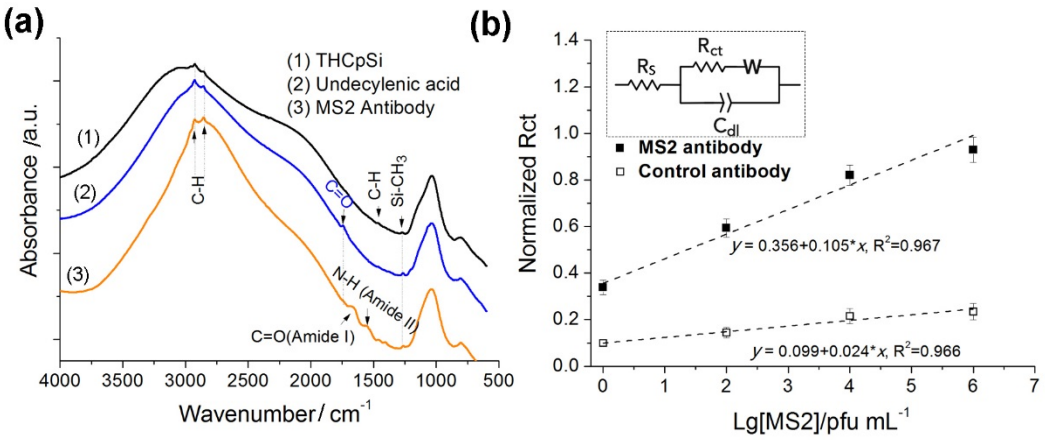

Figure 3.8 (a) Reflectance mode FTIR spectra of 1) unmodified THCpSi, 2) THCpSi after thermal hydrosilylation with undecylenic acid, and 3) antibody-modified THCpSi; (b) dose response curves for MS2 bacteriophage using THCpSi immunosensors prepared with anti-MS2 antibody (black squares) and non-specific antibody (white square) (data are shown as mean ± RSD, n= 3). Impedimetric measurements were performed in a 2 mM $[Fe(CN)_6]^{3-/4-}$ solution in 10 mM PBS, pH 7.4. Inset in (b) Randles circuit used for EIS data fitting.

Table 3.4 Summary of the solution resistance (R_s), charge-transfer resistance (R_{ct}) and double-layer capacitance (C_{dl}), extracted from EIS spectra of various electrodes, measured in a 2 mM $[Fe(CN)_6]^{3-/4-}$ solution in 10 mM PBS, pH 7.4.

Electrodes	**R_s / Ω**	**R_{ct} / Ω**	**C_{dl} / µF**
GCE	100 ± 15	105 ± 35	0.8 ± 0.1
SPE	398 ± 86	747 ± 70	0.9 ± 0.1
THC-flat Si	41 ± 21	7400 ± 260	2.8 ± 0.3
TC-flat Si	34 ± 19	23500 ± 1300	2.9 ± 0.4
THCpSi	4.6 ± 0.9	70 ± 24	1.3 ± 0.2
TCpSi	6.5 ± 1.4	40 ± 16	1.7 ± 0.1

3.3.7 THCpSi-based electrochemical biosensing platform for MS2 bacteriophage detection

Apart from featuring intact porous nanostructure, adjustable surface hydrophilicity, significantly increased stability and improved electrochemisty, THCpSi and TCpSi offer the possibility to be functionalized with a wide range of chemical groups. Hydrogen-terminated THCpSi can undergo hydrosilylation reactions similarly to freshly etched pSi.[48, 63] In contrast to the hydrogen-terminated hydrophobic THCpSi, HF-rinsed TCpSi is hydrophilic and features stable OH terminations, which are suitable for silanization reactions to introduce various chemical functionalities on the surface.[48, 64] Here, an immunosensor for MS2 bacteriophage detection was developed using THCpSi as electrochemical sensing platform. MS2 bacteriophage is used as a model of enteric viruses, and thus as surrogate of microbiological contamination in water.[65] THCpSi, with an average pore diameter of 72 ± 15 nm and a thickness of 1.2 ± 0.1 µm, was selected due to its low C_{dl} and the ease of grafting COOH groups on its surface via hydrosilylation with undecylenic acid, to allow covalent binding of a monoclonal anti-MS2 bacteriophage antibody upon carbodiimide activation. **Figure 3.8a** presents the FTIR spectra in reflectance mode of the THCpSi surface at each step of modification: 1) unmodified THCpSi, 2) THCpSi thermally hydrosilylated with undecylenic acid, and 3) antibody-modified

THCpSi. Apart from the feature bands of THCpSi discussed previously (**Figure 3.2)**, the C=O stretching vibrational mode at 1714 cm^{-1} suggests successful grafting of undecylenic acid to the THCpSi surface. Prior to the immobilization of the antibody, the COOH-terminated THCpSi surface was activated by EDC/NHS reaction to generate succinimidyl ester groups, which are known to react with available primary amino groups on proteins. This reaction led to two new peaks, corresponding to peptide C=O stretching (amide I) at 1650 cm^{-1} and peptide N-H stretching (amide II) at 1550 cm^{-1}, indicating the successful immobilization of the anti-MS2 antibodies onto THCpSi via carbodiimide coupling.

Additionally, antibody immobilization on THCpSi surface was electrochemically characterized by CV and EIS, in the presence of 2 mM $[Fe(CN)_6]^{3-/4-}$ in 10 mM PBS at pH 7.4 (**Figure 3.9**). The cyclic voltammograms of antibody-modified THCpSi feature a larger peak separation (275 ± 7% increase) and lower peak current (43 ± 4% decrease) than those of bare THCpSi, consistent with the immobilization of the antibody on the THCpSi surface. The EIS of antibody-modified THCpSi shows an increase in R_{ct} value (1130 ± 50 Ω) compared to the R_{ct} value (70 ± 24 Ω) of bare THCpSi electrodes also supporting antibody binding to the electrode surface. Importantly, impedance measurements proved to be stable and reproducible at the open circuit potential (*ca.* 0.22 V) which might be relevant to limit the possible disturbance to the modified THCpSi platform at the potentials used by voltammetric techniques. As shown in **Figure 3.9b**, R_{ct} values of both THCpSi and antibody-modified THCpSi electrodes were measured every 4 h over a 16 h period, showing relative standard deviations of 5.1 % and 4.5%, respectively.

The developed immunosensor was able to successfully detect MS2 bacteriophage over a wide range of concentrations, from 1 to 10^6 pfu mL^{-1} via EIS measurements as shown in **Figure 3.8b**. Among the various parameters derived from fitting the Nyquist plots of the impedance

spectra with a Randles circuit (inset in **Figure 3.8b**), R_{ct} is strongly affected by changes on the electrode surface, showing a significant increase as the concentration of the MS2 incubated increases. Therefore, R_{ct} values were used as the measured signal in response to the presence of MS2 bacteriophage. R_{ct} values were normalized as follows: $(R_{ct}^{f} - R_{ct}^{0})/R_{ct}^{0}$, where R_{ct}^{0} and R_{ct}^{f} are R_{ct} values prior and after bacteriophage incubation. Normalized R_{ct} values were plotted as a function of the logarithmic concentration of MS2 bacteriophage (**Figure 3.8b**), increasing linearly with the concentration of MS2 bacteriophage ($y= 0.356 + 0.105x$, $R^2= 0.967$). Normalized R_{ct} values obtained with the control sensor, prepared with a non-specific antibody, were negligible compared to those measured with the MS2 immunosensor, proving that changes in R_{ct} were caused by the specific binding between the anti-MS2 antibodies immobilized on the porous structure and the MS2 bacteriophage. The LOD is defined as the concentration corresponding to a signal equal to the average value of normalized R_{ct} plus three times of standard deviation (SD) in blank buffer.[36] A LOD of 4.9 pfu mL^{-1} was calculated using the equation $y_b + 3*SD$, where y_b is the value for the blank (normalized R_{ct} in PBS buffer) and SD is the associated standard deviation (n = 3). The LOD is comparable to previous results reported by our research group using pSi membrane- and silicon micropore array-based electrochemical immunosensors (6 pfu mL^{-1} and 0.9 pfu mL^{-1}, respectively), but increasing the robustness and stability of the former and greatly simplifying and reducing the fabrication cost of the latter.[24] Results can be further improved by harnessing the oriented immobilization of the antibodies used as bioreceptors as shown by our previous work on electrochemical sensing of MS2 (LOD < 2.2 pfu mL^{-1} using various functionalization strategies).[66-67] Successful impedimetric detection of MS2 bacteriophage highlights the potential of pSi-based electrochemical sensor platforms as dual capture and sensing devices. In addition, size exclusion effects can be introduced using adequately tuned pore dimensions to further increase selectivity.

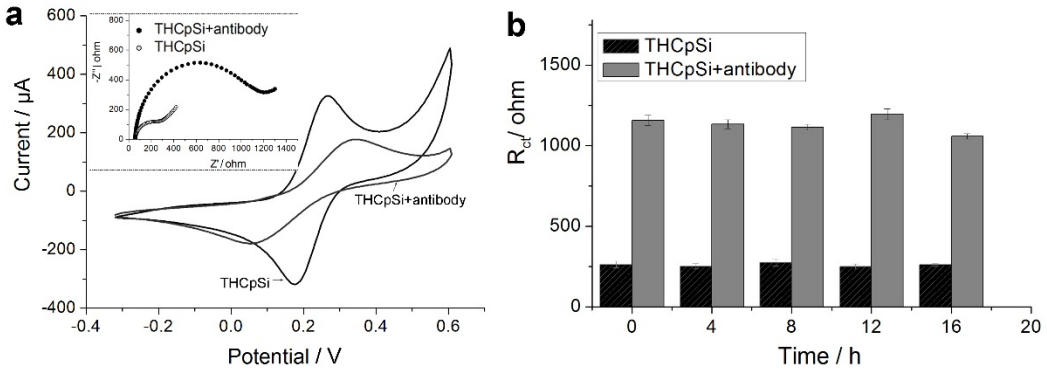

Figure 3.9 (a) Cyclic voltammograms and EIS spectra (inset), and (b) R_{ct} measurements over time (every 4 h), obtained using unmodified and antibody-modified THCpSi in the presence of 2 mM $[Fe(CN)6]^{3-/4-}$ solution in 10 mM PBS, pH 7.4.

3.4 Conclusion

The promising electrochemical properties of THCpSi and TCpSi stabilized via thermal decomposition of acetylene at two temperatures (525 and 800 °C, respectively) have been successfully demonstrated. The electrochemical performance of THCpSi and TCpSi was systematically studied by CV, CC and EIS, in the presence of three redox species, $[Fe(CN)_6]^{3-/4-}$, $[Ru(NH_3)_6]^{2+/3+}$ and HQ/Q. Results enable correlations between the chemical composition of the carbon layer formed onto the pSi nanostructures and the electrochemical behavior. Compared to THCpSi, TCpSi not only presents a more effective charge transfer process due to its higher content percentage of Si-C species, but also shows better chemical stability to prevent self-oxidation thanks to its increased content percentage of Si-O species. The fast electron transfer kinetics and effective surface area of carbon-stabilized pSi are comparable to those shown by carbon-based commercial electrodes like SPEs and GCEs without yielding significant double-layer capacitance effect. Apart from providing excellent electrochemical performance and stability, the novel electrochemical platform retains the unique physical and chemical features of pSi nanostructures such as large surface area, convenient surface chemistry and adjustable pore morphology. Proof of principle of applying these nanostructures

as electrochemical platforms was demonstrated by developing a THCpSi-based immunosensor for impedimetric detection of MS2 bacteriophage. Changes in R_{ct} of the developed immunosensor enabled MS2 bacteriophage detection with a LOD of 4.9 pfu mL^{-1}, highlighting the future potential of carbon-stabilized pSi nanostructures as efficient biosensing systems.

3.5 References

1. Arshavsky-Graham, S.; Massad-Ivanir, N.; Segal, E.; Weiss, S., Porous Silicon-Based Photonic Biosensors: Current Status and Emerging Applications. *Anal. Chem.* **2019,** *91* (1), 441-467.

2. Mariani, S.; Robbiano, V.; Strambini, L. M.; Debrassi, A.; Egri, G.; Dähne, L.; Barillaro, G., Layer-by-Layer Biofunctionalization of Nanostructured Porous Silicon for High-Sensitivity and High-Selectivity Label-Free Affinity Biosensing. *Nat. Commun.* **2018,** *9* (1), 5256.

3. Krismastuti, F. S.; Pace, S.; Voelcker, N. H., Porous Silicon Resonant Microcavity Biosensor for Matrix Metalloproteinase Detection. *Adv. Func. Mater.* **2014,** *24* (23), 3639-3650.

4. Harraz, F. A., Porous Silicon Chemical Sensors and Biosensors: A Review. *Sens. Actuators B Chem.* **2014,** *202*, 897-912.

5. Jane, A.; dronov, R.; Hodges, A.; Voelcker, N. H., Porous Silicon Biosensors on the Advance. *Trends Biotechnol.* **2009,** *27* (4), 230-239.

6. Dhanekar, S.; Jain, S., Porous Silicon Biosensor: Current Status. *Biosens. Bioelectron.* **2013,** *41*, 54-64.

7. Tong, W. Y.; Sweetman, M. J.; Marzouk, E. R.; Fraser, C.; Kuchel, T.; Voelcker, N. H., Towards a Subcutaneous Optical Biosensor Based on Thermally Hydrocarbonised Porous Silicon. *Biomaterials* **2016,** *74*, 217-230.

8. Dancil, K.-P. S.; Greiner, D. P.; Sailor, M. J., A Porous Silicon Optical Biosensor: Detection of Reversible Binding of Igg to a Protein a-Modified Surface. *J. Am. Chem. Soc.* **1999,** *121* (34), 7925-7930.

9. Orosco, M. M.; Pacholski, C.; Miskelly, G. M.; Sailor, M. J., Protein-Coated Porous-Silicon Photonic Crystals for Amplified Optical Detection of Protease Activity. *Adv. Mater.* **2006,** *18* (11), 1393-1396.

10. Zuidema, J. M.; Kumeria, T.; Kim, D.; Kang, J.; Wang, J.; Hollett, G.; Zhang, X.; Roberts, D. S.; Chan, N.; Dowling, C., Oriented Nanofibrous Polymer Scaffolds Containing Protein-Loaded Porous Silicon Generated by Spray Nebulization. *Adv. Mater.* **2018,** *30* (12), 1706785.

11. Li, W.; Liu, Z.; Fontana, F.; Ding, Y.; Liu, D.; Hirvonen, J. T.; Santos, H. A., Tailoring Porous Silicon for Biomedical Applications: From drug Delivery to Cancer Immunotherapy. *Adv. Mater.* **2018**, 1703740.

12. Kang, J.; Kim, D.; Wang, J.; Han, Y.; Zuidema, J. M.; Hariri, A.; Park, J. H.; Jokerst, J. V.; Sailor, M. J., Enhanced Performance of a Molecular Photoacoustic Imaging Agent by Encapsulation in Mesoporous Silicon Nanoparticles. *Adv. Mater.* **2018**, 1800512.

13. Islam, M. A.; Sinelnikov, R.; Howlader, M. A.; Faramus, A.; Veinot, J. G. C., Mixed Surface Chemistry: An Approach to Highly Luminescent Biocompatible Amphiphilic Silicon Nanocrystals. *Chem. Mater.* **2018,** *30* (24), 8925-8931.

14. Escorihuela, J.; Zuilhof, H., Rapid Surface Functionalization of Hydrogen-Terminated Silicon by Alkyl Silanols. *J. Am. Chem. Soc.* **2017,** *139* (16), 5870-5876.

15. Orosco, M. M.; Pacholski, C.; Sailor, M. J., Real-Time Monitoring of Enzyme Activity in a Mesoporous Silicon Double Layer. *Nat. Nanotechnol.* **2009,** *4* (4), 255-258.

16. Khung, Y. L.; Graney, S. D.; Voelcker, N. H., Micropatterning of Porous Silicon Films by Direct Laser Writing. *Biotechnol. Prog.* **2006,** *22* (5), 1388-1393.

17. Tsang, C. K.; Kelly, T. L.; Sailor, M. J.; Li, Y. Y., Highly Stable Porous Silicon–Carbon Composites as Label-Free Optical Biosensors. *ACS Nano* **2012,** *6* (12), 10546-10554.

18. Vilensky, R.; Bercovici, M.; Segal, E., Oxidized Porous Silicon Nanostructures Enabling Electrokinetic Transport for Enhanced DNA Detection. *Adv. Func. Mater.* **2015,** *25* (43), 6725-6732.

19. Chen, M. Y.; Klunk, M. D.; Diep, V. M.; Sailor, M. J., Electric-Field-Assisted Protein Transport, Capture, and Interferometric Sensing in Carbonized Porous Silicon Films. *Adv. Mater.* **2011,** *23* (39), 4537-4542.

20. Kim, B.; Pang, H.-B.; Kang, J.; Park, J.-H.; Ruoslahti, E.; Sailor, M. J., Immunogene Therapy with Fusogenic Nanoparticles Modulates Macrophage Response to Staphylococcus Aureus. *Nat. Commun.* **2018,** *9* (1), 1969.

21. Rémond, E.; Martin, C.; Martinez, J.; Cavelier, F., Silicon-Containing Amino Acids: Synthetic Aspects, Conformational Studies, and Applications to Bioactive Peptides. *Chem. Rev.* **2016,** *116* (19), 11654-11684.

22. Mann, A. P.; Scodeller, P.; Hussain, S.; Joo, J.; Kwon, E.; Braun, G. B.; Mölder, T.; She, Z.-G.; Kotamraju, V. R.; Ranscht, B.; Krajewski, S.; Teesalu, T.; Bhatia, S.; Sailor, M. J.; Ruoslahti, E., A Peptide for Targeted, Systemic Delivery of Imaging and Therapeutic Compounds into Acute Brain Injuries. *Nat. Commun.* **2016,** *7*, 11980.

23. Tzur-Balter, A.; Shatsberg, Z.; Beckerman, M.; Segal, E.; Artzi, N., Mechanism of Erosion of Nanostructured Porous Silicon drug Carriers in Neoplastic Tissues. *Nat. Commun.* **2015,** *6*, 6208.

24. Reta, N.; Michelmore, A.; Saint, C.; Prieto-Simón, B.; Voelcker, N. H., Porous Silicon Membrane-Modified Electrodes for Label-Free Voltammetric Detection of Ms2 Bacteriophage. *Biosens. Bioelectron.* **2016,** *80*, 47-53.

25. Sweetman, M. J.; Ronci, M.; Ghaemi, S. R.; Craig, J. E.; Voelcker, N. H., Porous Silicon Films Micropatterned with Bioelements as Supports for Mammalian Cells. *Adv. Func. Mater.* **2012,** *22* (6), 1158-1166.

26. Sweetman, M. J.; Shearer, C. J.; Shapter, J. G.; Voelcker, N. H., Dual Silane Surface Functionalization for the Selective Attachment of Human Neuronal Cells to Porous Silicon. *Langmuir* **2011,** *27* (15), 9497-9503.

27. Ciampi, S.; Harper, J. B.; Gooding, J. J., Wet Chemical Routes to the Assembly of Organic Monolayers on Silicon Surfaces Via the Formation of Si–C Bonds: Surface Preparation, Passivation and Functionalization. *Chem. Soc. Rev.* **2010,** *39* (6), 2158-2183.

28. Kim, D.; Zuidema, J. M.; Kang, J.; Pan, Y.; Wu, L.; Warther, D.; Arkles, B.; Sailor, M. J., Facile Surface Modification of Hydroxylated Silicon Nanostructures Using Heterocyclic Silanes. *J. Am. Chem. Soc.* **2016,** *138* (46), 15106-15109.

29. Kim, D.; Joo, J.; Pan, Y.; Boarino, A.; Jun, Y. W.; Ahn, K. H.; Arkles, B.; Sailor, M. J., Thermally Induced Silane Dehydrocoupling on Silicon Nanostructures. *Angew. Chem. Int. Ed.* **2016,** *55* (22), 6423-6427.

30. Pujari, S. P.; Scheres, L.; Marcelis, A. T.; Zuilhof, H., Covalent Surface Modification of Oxide Surfaces. *Angew. Chem. Int. Ed.* **2014,** *53* (25), 6322-6356.

31. Zhukhovitskiy, A. V.; Mavros, M. G.; Queeney, K. T.; Wu, T.; Voorhis, T. V.; Johnson, J. A., Reactions of Persistent Carbenes with Hydrogen-Terminated Silicon Surfaces. *J. Am. Chem. Soc.* **2016,** *138* (27), 8639-8652.

32. Sweetman, M. J.; McInnes, S. J. P.; Vasani, R. B.; Guinan, T.; Blencowe, A.; Voelcker, N. H., Rapid, Metal-Free Hydrosilanisation Chemistry for Porous Silicon Surface Modification. *Chem. Commun.* **2015,** *51* (53), 10640-10643.

33. Lin, V. S.-Y.; Motesharei, K.; Dancil, K.-P. S.; Sailor, M. J.; Ghadiri, M. R., A Porous Silicon-Based Optical Interferometric Biosensor. *Science* **1997,** *278* (5339), 840-843.

34. Lugo, J.; Ocampo, M.; Kirk, A.; Plant, D.; Fauchet, P., Electrochemical Sensing of DNA with Porous Silicon Layers. *J. New. Mat. Electr. Sys.* **2007,** *10* (2), 113.

35. Melikjanyan, G.; Martirosyan, K. S., Possibility of Application of Porous Silicon as Glucose Biosensor. *Armenian Journal of Physics* **2011,** *4* (4), 225-227.

36. Díaz, D. J., Electrochemistry of Porous Materials. ACS Publications: 2010.

37. Yu, Y.; Gu, L.; Zhu, C.; Tsukimoto, S.; van Aken, P. A.; Maier, J., Reversible Storage of Lithium in Silver-Coated Three-Dimensional Macroporous Silicon. *Adv. Mater.* **2010,** *22* (20), 2247-2250.

38. Thakur, M.; Isaacson, M.; Sinsabaugh, S. L.; Wong, M. S.; Biswal, S. L., Gold-Coated Porous Silicon Films as Anodes for Lithium Ion Batteries. *J. Power Sources* **2012,** *205*, 426-432.

39. Wu, H.; Yu, G.; Pan, L.; Liu, N.; McDowell, M. T.; Bao, Z.; Cui, Y., Stable Li-Ion Battery Anodes by in-Situ Polymerization of Conducting Hydrogel to Conformally Coat Silicon Nanoparticles. *Nat. Commun.* **2013,** *4*, 1943.

40. Du, F. H.; Li, B.; Fu, W.; Xiong, Y. J.; Wang, K. X.; Chen, J. S., Surface Binding of Polypyrrole on Porous Silicon Hollow Nanospheres for Li-Ion Battery Anodes with High Structure Stability. *Adv. Mater.* **2014,** *26* (35), 6145-6150.

41. Salonen, J.; Lehto, V. P.; Björkqvist, M.; Laine, E.; Niinistö, L., Studies of Thermally-Carbonized Porous Silicon Surfaces. *Phys. Satatus Solidi A* **2000,** *182* (1), 123-126.

42. Schwartz, M. P.; Cunin, F.; Cheung, R. W.; Sailor, M. J., Chemical Modification of Silicon Surfaces for Biological Applications. *Phys. Satatus Solidi A* **2005,** *202* (8), 1380-1384.

43. Salonen, J.; Mäkilä, E., Thermally Carbonized Porous Silicon and Its Recent Applications. *Adv. Mater.* **2018,** *30* (24), 1703819.

44. Salonen, J.; Björkqvist, M.; Laine, E.; Niinistö, L., Stabilization of Porous Silicon Surface by Thermal Decomposition of Acetylene. *Appl. Surf. Sci.* **2004,** *225* (1), 389-394.

45. Pumera, M., The Electrochemistry of Carbon Nanotubes: Fundamentals and Applications. *Trends Biotechnol.* **2009,** *15* (20), 4970-4978.

46. Nugent, J.; Santhanam, K.; Rubio, A.; Ajayan, P., Fast Electron Transfer Kinetics on Multiwalled Carbon Nanotube Microbundle Electrodes. *Nano. Lett.* **2001,** *1* (2), 87-91.

47. Sciacca, B.; Secret, E.; Pace, S.; Gonzalez, P.; Geobaldo, F.; Quignard, F.; Cunin, F., Chitosan-Functionalized Porous Silicon Optical Transducer for the Detection of Carboxylic Acid-Containing drugs in Water. *J. Mater. Chem.* **2011,** *21* (7), 2294-2302.

48. Makila, E.; Bimbo, L. M.; Kaasalainen, M.; Herranz, B.; Airaksinen, A. J.; Heinonen, M.; Kukk, E.; Hirvonen, J.; Santos, H. A.; Salonen, J., Amine Modification of Thermally Carbonized Porous Silicon with Silane Coupling Chemistry. *Langmuir* **2012,** *28* (39), 14045-14054.

49. Salonen, J.; Bjorkqvist, M.; Laine, E.; Niinisto, L., Stabilization of Porous Silicon Surface by Thermal Decomposition of Acetylene. *Appl. Surf. Sci.* **2004,** *225* (1-4), 389-394.

50. Salonen, J.; Mäkilä, E., Thermally Carbonized Porous Silicon and Its Recent Applications. *Adv. Mater.* **2018**, 1703819.

51. Sciacca, B.; Alvarez, S. D.; Geobaldo, F.; Sailor, M. J., Bioconjugate Functionalization of Thermally Carbonized Porous Silicon Using a Radical Coupling Reaction. *Dalton Trans.* **2010,** *39* (45), 10847-10853.

52. Buriak, J. M.; Stewart, M. P.; Geders, T. W.; Allen, M. J.; Choi, H. C.; Smith, J.; Raftery, D.; Canham, L. T., Lewis Acid Mediated Hydrosilylation on Porous Silicon Surfaces. *J. Am. Chem. Soc.* **1999,** *121* (49), 11491-11502.

53. Bard, A.; Faulkner, L., Lr, Electrochemical Methods. *Jonhs Wiley & Sons, Inc. New York* **1980**.

54. Tang, L.; Wang, Y.; Li, Y.; Feng, H.; Lu, J.; Li, J., Preparation, Structure, and Electrochemical Properties of Reduced Graphene Sheet Films. *Adv. Func. Mater.* **2009,** *19* (17), 2782-2789.

55. Guin, P. S.; Das, S.; Mandal, P., Electrochemical Reduction of Quinones in Different Media: A Review. *Int. J. Electrochem.* **2011,** *2011*.

56. Wedege, K.; dražević, E.; Konya, D.; Bentien, A., Organic Redox Species in Aqueous Flow Batteries: Redox Potentials, Chemical Stability and Solubility. *Sci. Rep.* **2016,** *6*, 39101.

57. Anson, F. C., Innovations in the Study of Adsorbed Reactants by Chronocoulometry. *Anal. Chem.* **1966,** *38* (1), 54-57.

58. Anson, F. C.; Osteryoung, R. A., Chronocoulometry: A Convenient, Rapid and Reliable Technique for Detection and Determination of Adsorbed Reactants. *J. Chem. Educ.* **1983,** *60* (4), 293.

59. Łukaszewski, M.; Soszko, M.; Czerwiński, A., Electrochemical Methods of Real Surface Area Determination of Noble Metal Electrodes–an Overview. *Int. J. Electrochem. Sci* **2016,** *11*, 4442-4469.

60. Zhong, G.; Liu, A.; Xu, X.; Sun, Z.; Chen, J.; Wang, K.; Liu, Q.; Lin, X.; Lin, J., Detection of Femtomolar Level Osteosarcoma-Related Gene Via a Chronocoulometric DNA Biosensor Based on Nanostructure Gold Electrode. *Int. J. Nanomedicine* **2012,** *7*, 527.

61. Fragkou, V.; Ge, Y.; Steiner, G.; Freeman, D.; Bartetzko, N.; Turner, A. P., Determination of the Real Surface Area of a Screen-Printed Electrode by Chronocoulometry. *Int. J. Electrochem. Sci.* **2012,** *7*, 6214-6220.

62. Sunday, C. E.; Bilibana, M.; Qakala, S.; Tovide, O.; Molapo, K. M.; Fomo, G.; Ikpo, C. O.; Waryo, T.; Mbambisa, G.; Mpushe, B., Modulation of the Matrix Effect of Nafion on Tris (Bipyridine) Ruthenium (Ii) Electrochemical Probes by Functionalisation with 4-Nitrophenylazo Graphene-Gold Nanocomposite. *Electrochimica Acta* **2014,** *128*, 128-137.

63. Salonen, J.; Mäkilä, E., Thermally Carbonized Porous Silicon and Its Recent Applications. *Adv. Mater.* **2018**.

64. Dhar, S.; Seitz, O.; Halls, M. D.; Choi, S.; Chabal, Y. J.; Feldman, L. C., Chemical Properties of Oxidized Silicon Carbide Surfaces Upon Etching in Hydrofluoric Acid. *J. Am. Chem. Soc.* **2009,** *131* (46), 16808-16813.

65. Monis, P.; Blackbeard, J., *Pathogen Risk Indicators for Wastewater and Biosolids*. Water Environment Research Foundation: **2010**.

66. Prieto-Simón, B.; Saint, C.; Voelcker, N. H., Electrochemical Biosensors Featuring Oriented Antibody Immobilization Via Electrografted and Self-Assembled Hydrazide Chemistry. *Anal. Chem.* **2014,** *86* (3), 1422-1429.

67. Brehant, A.; Glucina, K.; Le Moigne, I.; Laine, J.-M., Risk Management Approach for Monitoring Uf Membrane Integrity and Experimental Validation Using Ms2-Phages. *Desalination and Water Treatment* **2009,** *9* (1-3), 195-200.

Chapter 4. Rapid and label-free detection of *Escherichia coli* 16S rRNA using a carbon-stabilized porous silicon-based voltammetric biosensor

4.1 Introduction

Infectious diseases have remained one of the top ten global leading causes of death in the last two decades according to the WHO statistics in 2016.[1] Standard methods to diagnose bacterial infections, such as polymerase chain reaction (PCR), are laborious, complex and time-consuming.[2-3] The development of a rapid, accurate, low cost and PCR-free method to identify bacteria in complex biological samples is in high demand. The use of genetic markers of bacterial species to directly target pathogens makes a rapid identification without culture-involved process possible.[4-5] As one of the most attractive genetic markers for bacterial identification, the 16S rRNA gene sequences have demonstrated their capabilities of highly accurate detection of many clinically relevant bacterial pathogens including slow-growing, unusual and fastidious bacteria in addition to bacteria that are poorly differentiated by traditional methods.[6-7] First, the 16S rRNA sequences are not only species-specific but also are highly expressed in all bacteria.[8] Second, as a growth marker for bacterial identification, the functional stability of 16S rRNA has remained constant over a long period allowing reliable and precise assessments.

Biosensors are promising tools for sensitive and label-free detection of 16S rRNA due to the demonstrated advantages such as high sensitivity, selectivity and robustness at low cost.[9-12] Particularly, electrochemical biosensors, as an integrated low-cost sensing system, not only possess the high sensitivity and specificity provided by the transducer and bioreceptor, but also the possibility to miniaturize the electrodes.[13-14] Attention has been primarily paid to the exploitation of new nanostructured materials as electrochemical transducers, such as metal nanowires [15-16], carbon nanotubes[17-19], graphene[20-24], metal nanoparticles[15, 25], and porous

materials[26-27]. Among these candidate materials, THCpSi is a very promising one, due to the pSi features, such as extensive tailoring of its structural properties (pore diameter and depth, porosity), high surface area, easy and cheap fabrication and biocompatibility.[28-31] More importantly, thanks to the thin carbon coating, THCpSi not only possesses the capability to passivate the surface against degradation, but has also demonstrated excellent performance as highly sensitive electrochemical transducer.[32-35] Particularly interesting is the versatile surface chemistry of THCpSi to allow further immobilization of specific recognition biomolecules such as DNA probes. There are thus several reasons that make THCpSi ideal for electrochemical biosensing. First, the large surface area of THCpSi facilitates the immobilization of a large number of DNA bioreceptors.[36] Second, the high stability renders THCpSi very suitable for long-term applications.[37-38] Third, the nanochannel structural feature of THCpSi is conducive to the direct and label-free sensing strategy based on nanochannel blockage to monitor analyte binding to the capture probe immobilized in the nanochannels.

Herein, a voltammetric biosensor using externally insulated THCpSi as transducer was developed for the direct and label-free detection of *Escherichia coli* (*E. coli*) 16S rRNA. A biosensor based on a nanochannel blockage sensing mechanism is suitable for the detection of 16S rRNA with a LOD of 0.183 pM in buffer was demonstrated. The specific hybridization of 16S rRNA to the ssDNA probes immobilized at the inner surface of the porous electrodes causes the partial blockage of THCpSi nanochannels and impedes the diffusion of the electroactive species $[Fe(CN)_6]^{3-/4-}$ added in solution towards the transducer surface. As a result, the decrease in output current signal was easily monitored via differential pulse DPV. In addition, the use of an insulating layer to minimize non-specific binding at the outer surface and enhance the confinement of hybridization into the nanochannels of the label-free voltammetric sensor was tested.[39-41]

4.2 Experimental section

Materials: p-type silicon wafers with 0.00055-0.001 Ω cm resistivity (100)-oriented were purchased from Siltronix (France). Hydrofluoric acid (HF) (48%, AR grade) was purchased from Scharlau (Australia). Potassium ferrocyanide ($K_4[Fe(CN)_6]$), potassium ferricyanide ($K_3[Fe(CN)_6]$), undecylenic acid, N-hydroxysuccinimide (NHS), N(3-dimethylaminopropyl) N-ethylcarbodiimide hydrochloride (EDC), phosphate buffered saline (PBS) tablets, 2-(N-morpholino)-ethanesulfonic acid (MES), tris(hydroxymethyl)aminomethane and ethanolamine were purchased from Sigma-Aldrich (Australia). Solutions were prepared in ultrapure water (18.2 MΩ cm) from a Milli-Q system, except those for *E. coli* 16S rRNA detection, that were prepared in RNase-free water bought from Sigma-Aldrich. The acetylene gas cylinder (1 m^3 industrial grade, dissolved) was purchased from BOC (Australia). All the DNA strands were purchased from Integrated DNA Technologies Pte Ltd (Singapore). The sequence of ssDNA probe is 5'-/5AmMC6/GTC CAC GCC GTA AAC GAT GTC GAC TTG G-3'. The non-specific ssDNA probe is 5'-/5AmMC6/CAC AAA TTC GGT TCT ACA GGG TA-3'. The sequence of the target ssDNA is 5'-CCA AGT CGA CAT CGT TTA CGG CGT GGA C-3'. The 2-mismatch ssDNA sequence is 5'-CCA ACT CGA GAT CGT TTA CGG CGT GGA C-3'. The 1-mismatch ssDNA sequence is 5'-CCA AGT CGA GAT CGT TTA CGG CGT GGA C-3'. The sequence of *E. coli* 16SrRNA is 5'-CCA AGU CGA CAU CGU UUA CGG CGU GGA C-3'.

Apparatus: pSi samples were fabricated with a MPSB wet etching system (A.M.M.T). Scanning electron microscopy (SEM) images were obtained with a FEI NovaNano SEM 430 at an accelerating voltage of 10 kV. Attenuated total reflectance Fourier transform infrared (ATR-FTIR) spectroscopy was performed with a Thermo Scientific Nicolet 6700 FTIR spectrometer. Si_3N_4 coating was deposited with an Oxford plasma lab 100 plasma enhanced chemical vapor deposition (PECVD) system. Electrochemical measurements were carried out

on an electrochemical analyzer (CH Instruments, model 600D series, USA) using a three-electrode configuration in a Teflon cell containing the silicon chip on an aluminum film as the working electrode, Ag/AgCl reference electrode and a platinum wire as counter electrode.

Fabrication of pSi single layer: A whole 6 inch p-type silicon wafer was anodically etched in an electrolyte solution containing 1:1 (v:v) HF and absolute ethanol to produce a first pSi layer. Firstly, the sacrificial layer produced with a current density of 60.6 mA cm^{-2} for 30 s was removed with 1 M sodium hydroxide.[42] Then the etching cell was rinsed with water, absolute ethanol and dried with N_2 gas. Next, various current densities were applied to fabricate the porous layers with different pore size. Current densities of 12.1, 18.9 and 53 mA cm^{-2} were applied to the etching cell to form 12 ± 5, 27 ± 9 and 72 ± 15 nm pore size, respectively. The thickness of the single layers was controlled by the etching time. The freshly etched pSi was finally rinsed with ethanol and kept in a desiccator.

Thermal hydrocarbonization of pSi (THCpSi) single layer: The freshly etched pSi substrates were cut into 1.5 cm × 1.5 cm pieces and stabilized using the thermal hydrocarbonization (THC) treatment with acetylene decomposition described by Salonen et al.[43-44]

Si_3N_4 deposition: Si_3N_4 coating was deposited onto the top surface of THCpSi layer via PECVD at 250 °C with a deposition rate of 22 nm per min.

Carboxylic functionalization of Si_3N_4 externally insulated THCpSi structures: In order to functionalize the inner surface of THCpSi with COOH groups, the sample was immersed into a glass vial to undergo hydrosilylation with pure undecylenic acid at 150 °C for 10 h under inert atmosphere (N_2). After cooling down to room temperature, the sample was rinsed with absolute ethanol.

DNA probe immobilization: The -COOH groups at the inner surface of THCpSi were activated by incubating a mixture of 10 mg/mL EDC and 15 mg/mL NHS in 0.1 M MES buffer, pH 5.5, at room temperature for 30 min to produce succinimidyl ester groups. Subsequently, the samples were incubated with 100 µL of 10 µM NH_2-terminated ssDNA probe or NH_2-terminated non-specific ssDNA probe in MES buffer at room temperature for 1 h, and then rinsed thoroughly with PBS. The leftover active ester groups that did not covalently bind to the NH_2-modified ssDNA probes, were blocked by incubating with 200 µL of 0.5 mg/mL ethanolamine in 0.01 M PBS, pH 7.4 for 25 min. The sample was rinsed with 10 mM PBS buffer three times, and stabilized in 10 mM Tris buffer with 75 mM sodium chloride, pH 7.5, for 15 min. DPV measurements were conducted every 15 min to make sure the signal was stable.

DNA detection: ssDNA target solutions prepared in 10 mM Tris buffer with 75 mM NaCl were incubated on the sensor surface for 15 min over a range of concentrations from 0.1 to 1000 pM at room temperature. After each incubation step, the surface were thoroughly washed with PBS, then differential pulse voltammograms were measured in 2 mM $[Fe(CN)_6]^{3-/4-}$ in 10 mM PBS by scanning the potential from -0.2 to 0.6 V vs Ag/AgCl. In order to verify the current changes were only caused from the specific hybridization between ssDNA probe and the target ssDNA, control sensors with immobilized ssDNA of random sequence were treated under identical conditions. Triplicate measurements were performed with each sensor.

E. coli 16S rRNA detection: 16S rRNA target solutions prepared in 10 mM Tris buffer-75 mM NaCl with nuclease-free water were also incubated on the sensor and control surfaces for 15 min over a range of concentrations from 0.1 to 1000 pM. Measurements were performed as detailed above.

4.3 Results and discussion

4.3.1 Preparation of THCpSi transducers

The initial pSi single layers were fabricated via established electrochemical anodization. The nanochannel diameter of anodically etched pSi films can be easily tuned by applying different current density, while the thickness of the porous layers can be well controlled via etching time. After fabrication, these freshly etched pSi single layers were immediately carbon-stabilized at 525 °C via thermal decomposition of acetylene gas, following the protocol described by Salonen.[43-44] By applying various current densities, 12.1, 18.9 and 53 mA cm^{-2}, in 1:1 (volume) HF/EtOH etchant, THCpSi single layers with 12 ± 5, 27 ± 9 and 72 ± 15 nm nanochannel diameter, were obtained, respectively, as shown in **Figure 4.1**. The thickness of these THCpSi single layers can also be easily controlled. For instance, as shown in **Figure 4.2** for a THCpSi layer with 27 ± 9 nm nanochannel diameter, by applying different etching times, 40, 80 and 160 s, various thicknesses, 0.7, 1.6 and 3.4 µm, respectively, were achieved.

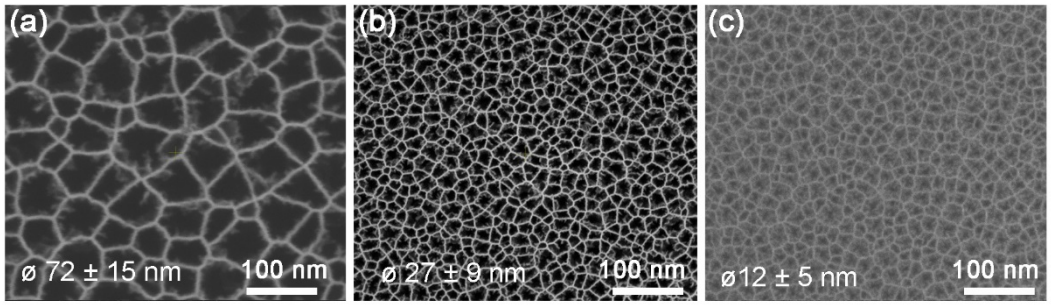

Figure 4.1 Top view SEM images of THCpSi with different nanochannel diameter: (a) 72 ± 15 nm, (b) 27 ± 9 nm and (c) 12 ± 5 nm.

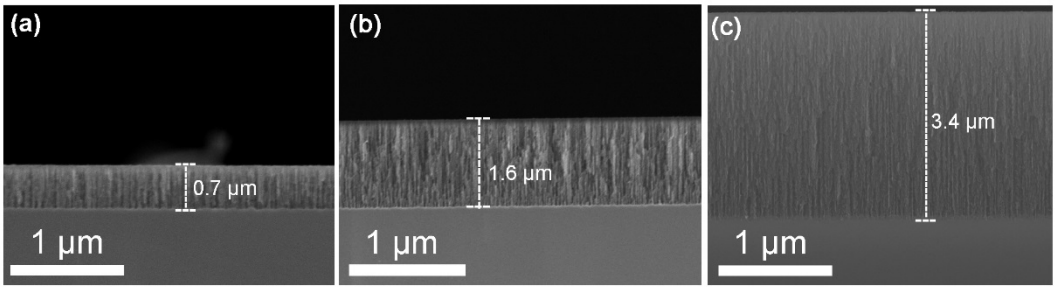

Figure 4.2 Cross sectional SEM images of THCpSi with a nanochannel diameter of 27 ± 9 nm and different depth (a) 0.7 µm, (b) 1.6 µm and (c) 3.4 µm.

4.3.2 External insulating Si_3N_4 coating

In order to minimize non-specific absorption on the external surface of the porous structure and maximize the blockage efficiency during the sensing process, a thin insulating layer of Si_3N_4 was deposited on THCpSi surface via PECVD. With a deposition rate of 22 nm per min, Si_3N_4 coatings of different thicknesses were deposited by controlling the deposition time. **Figure 4.3** shows the SEM images of the Si_3N_4-insulated THCpSi with controlled deposition thickness of ~7 nm (**Figure 4.3a**) and ~22 nm (**Figure 4.3b**). While the THCpSi substrate with 7 nm-Si_3N_4 coating had not significantly changed its morphology, featuring open pores, most of the pores of the THCpSi substrate with 22 nm-Si_3N_4 coating were blocked.

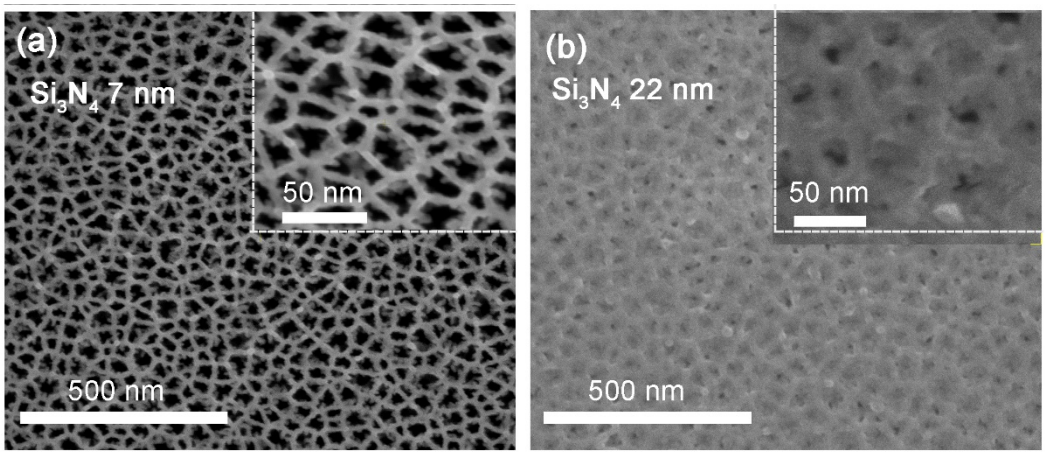

Figure 4.3 Top view SEM images of THCpSi single layers with a nanochannel diameter of 27 ± 9 nm after Si_3N_4 coating of different thickness: (a) 7 nm, and (b) 22 nm.

4.3.3 Immobilization of ssDNA probes

The ease of grafting COOH groups on Si_3N_4-insulated THCpSi surface via hydrosilylation with undecylenic acid allows further covalent binding of NH_2-terminated ssDNA probes upon carbodiimide activation. **Figure 4.4** presents the ATR- FTIR spectra at each step of surface modification. Apart from the feature bands of THCpSi described by Salonen et al.[43-44], the C=O stretching vibrational mode at 1714 cm^{-1} suggests successful grafting of undecylenic acid to the THCpSi surface (**Figure 4.4a**). Prior to the immobilization of the NH_2-ssDNA probes, the COOH-terminated THCpSi surface was activated by EDC/NHS reaction to generate succinimidyl ester groups (shown as triplet peaks in the range of C=O at 1736, 1787 and 1819 cm^{-1}), which are known to react with available primary amino groups (**Figure 4.4b**). The attachment of ssDNA probes led to a new peak, corresponding to peptide C=O stretching (amide I) at 1650 cm^{-1}, indicating the successful immobilization of the ssDNA probes onto THCpSi via carbodiimide coupling (**Figure 4.4c**). Finally, the unreacted ester groups were blocked with ethanolamine, as shown by the disappearance of triplet peaks in the spectrum (**Figure 4.4d**).

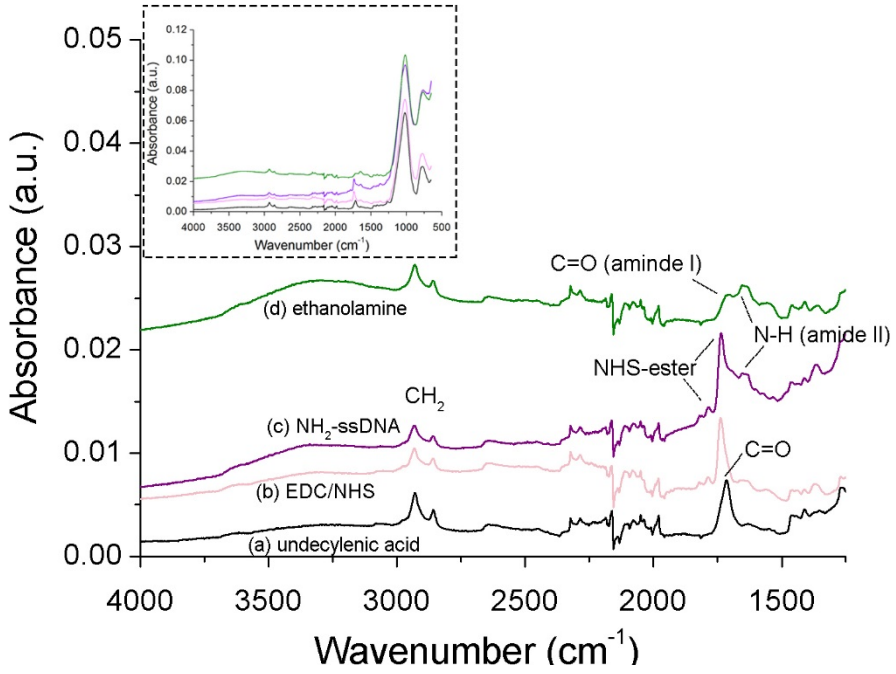

Figure 4.4 ATR-FTIR spectra of the Si_3N_4-insulated THCpSi single layer (a) after thermal hydrosilylation, (b) EDC/NHS activation, (c) ssDNA probe immobilization and (d) blocking with ethanolamine.

Additionally, the immobilization of ssDNA probes on the inner surface of Si_3N_4 externally insulated THCpSi transducer was electrochemically characterized via CV and EIS, in the presence of 2 mM $[Fe(CN)_6]^{3-/4-}$ solution in 10 mM PBS, pH 7.4 (**Figure 4.5**). The Si_3N_4 externally insulated THCpSi transducer with COOH functionalization prior to immobilization of ssDNA presents a difference between the anodic and cathodic peak potentials, known as peak-to-peak separation (ΔEp), of 365 mV. After immobilization of ssDNA probes, the ΔEp (438 mV) shows a 28% increase (**Figure 4.5a**). Also a 34% decrease in the oxidation and reduction currents was observed compared to the values measured before immobilization of the ssDNA probes (**Figure 4.5a**). The observed increase in ΔEp and decrease in peak currents after immobilization of ssDNA probes were partially attributed to the electrostatic repulsion between the negative charges of both the redox species $[Fe(CN)_6]^{3-/4-}$ added in solution and the ssDNA probes immobilized on the surface, as well as the steric blockage of the electron transfer

on the electrode surface caused by the presence of ssDNA probes. Characterization via the highly sensitive EIS reveals the change in charge-transfer resistance (R_{ct}) happened at the inner surface of the transducer upon ssDNA immobilization (**Figure 4.5b**). The R_{ct} value can be obtained by fitting the impedance spectra to the Randles circuit (inset in **Figure 4.5b**), which is an equivalent electrical circuit composed of solution resistance (R_s), charge-transfer resistance (R_{ct}), Warburg impedance (W) and double-layer capacitance (C_{dl}).[45] The R_{ct} increased from 987 Ω to 1453 Ω after ssDNA probe immobilization. This 47% increase in the R_{ct} is consistent with the successful immobilization of ssDNA probes producing a negatively charged surface.[46]

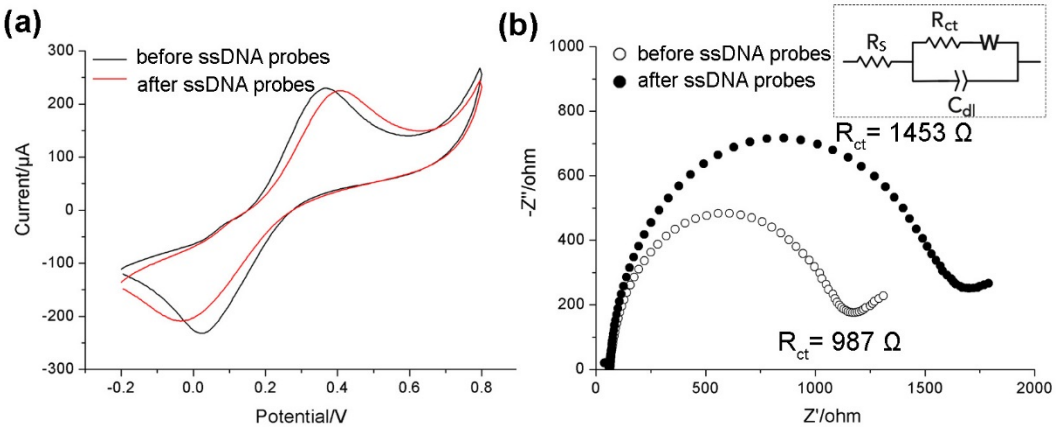

Figure 4.5 (a) Cyclic voltammograms and (b) impedance spectra obtained before and after NH_2-modified ssDNA probe immobilization on Si_3N_4-insulated THCpSi single layer functionalized with carboxylic groups. Inset in (b) Randles circuit used for EIS data fitting.

4.3.4 Sensing mechanism

The sensing mechanism based on nanochannel blockage for label-free detection of 16S rRNA is shown in **Figure 4.6**. Specific hybridization of the target 16S rRNA to the ssDNA probe immobilized at the inner surface of the nanochannels, causes partial blockage of the

nanochannels. This partial nanochannel blockage hinders the diffusion of redox species such as $[Fe(CN)_6]^{3-/4-}$ towards the transducer surface, resulting in a decrease in the intensity of peak current monitored by DPV.

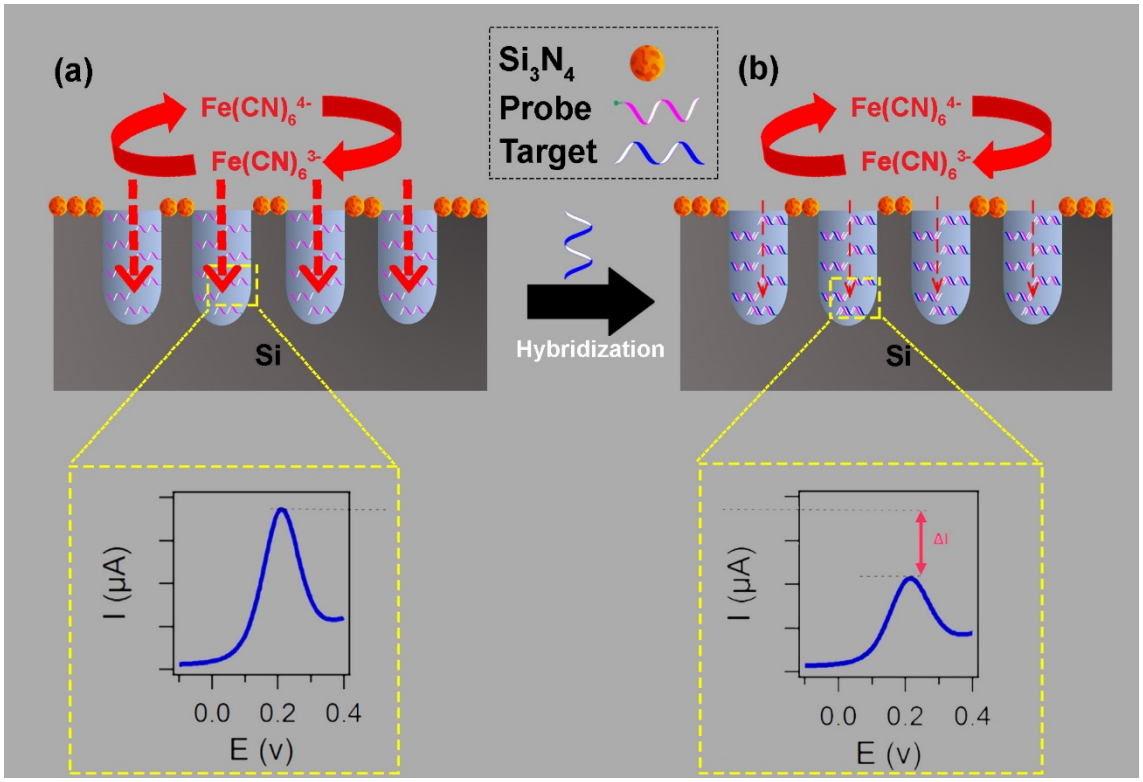

Figure 4.6 Sensing mechanism of the designed voltammetric sensor for label-free detection of 16 S rRNA.

In order to analyze the sensitivity of the designed voltammetric sensors, peak current intensity values measured upon incubation in each specific concentration of target analyte were firstly normalized using the following equation [28]:

$$\Delta i = (i° - i)/i° \qquad (4.1)$$

Where Δi is the normalized peak current after hybridization, $i°$ is the initial peak current intensity value measured in blank buffer solution, and i is the peak current value measured after hybridization for each target concentration. Then, the normalized Δi is plotted as a function of Log [target analyte], and the slope of the linear fitted curve determines the sensitivity of the

sensor. The LOD is defined as the concentration corresponding to a signal equal to the average value of Δi plus three times of standard deviation (SD) in blank buffer.[28] A LOD was calculated using the equation y_b + 3*SD, where y_b is the value for the blank (normalized Δi in buffer) and SD is the associated standard deviation (n = 3).

4.3.5 Optimization of sensors performance using complementary ssDNA as target

Prior to the detection of *E. coli* 16S rRNA, the performance of the designed voltammetric sensors was systematically optimized using as target analyte a ssDNA sequence complementary to the immobilized ssDNA probe, with higher stability than RNA.

4.3.5.1 External insulating Si_3N_4 coating

The effect of depositing a Si_3N_4 insulating layer on the external sensor surface was initially explored by comparing the sensing performance of structures with and without the insulating coating. More specifically, the sensitivity of the designed DNA sensors with and without Si_3N_4 insulating layer was compared (**Figure 4.7a**). These DNA sensors were developed using a THCpSi transducer with an average nanochannel diameter of 27 ± 9 nm and 1.6 µm depth. Sensor modification was performed with a 10 µM NH_2-ssDNA solution incubated during 1 h on a carbodiimide activated THCpSi surface previously hydrosilylated with undecylenic acid. Among these sensors, the DNA sensors externally insulated with a ~ 7 nm Si_3N_4 layer provided the highest sensitivity (plot 1, Δi = 0.298 + 0.133*Log [target ssDNA], R^2 = 0.996). Plot 2 (Δi = 0.174 + 0.049*Log [target ssDNA], R^2 = 0.890) represents the dose response curve of the DNA sensors prepared without external insulating layer. The sensitivity of the DNA sensors with an insulating layer is 171% higher than that of the DNA sensors without insulating layer. This indicates that having an external insulating layer on top of the THCpSi transducers maximizes the nanochannel blockage efficiency, due to the nanochannel confinement of the hybridization events, and thus the sensitivity. The external Si_3N_4 coating specifically deposited

at the top entrance of the nanochannels prevents hybridization events to take place at the external surface, minimizing the effect those events outside the nanochannels could have on the efficiency of the nanochannel blockage. Moreover, the external Si_3N_4 coating with high hydrophilicity can avoid interfacial reactions leading to non-specific binding, due to the fact that hydrophobic interactions usually dominate the adsorption process.[39-41]

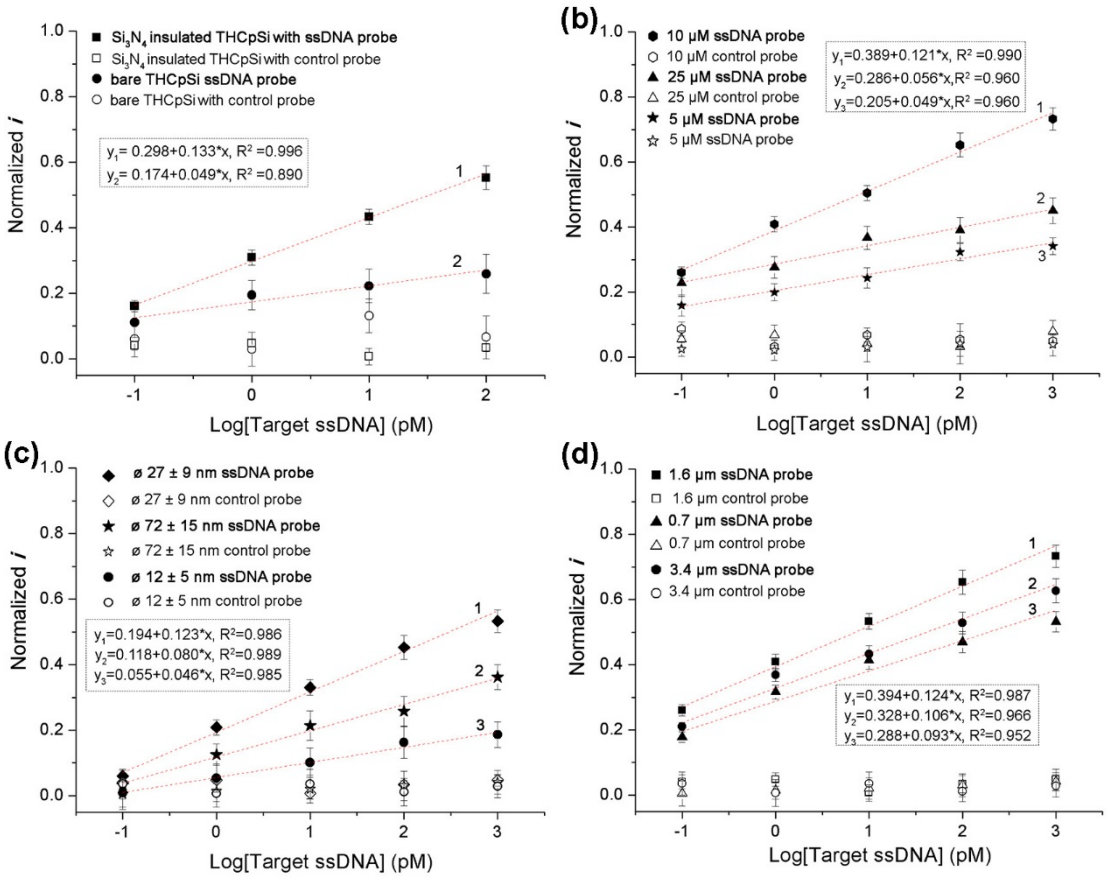

Figure 4.7 Calibration curves of DNA sensors developed from various THCpSi platforms. Effect on the DNA sensor response of (a) Si_3N_4 insulating layer, (b) ssDNA probe concentration used for the immobilization step, (c) THCpSi pore size and (d) THCpSi thickness.

4.3.5.2 Optimization of the concentration of ssDNA probe used to modify the THCpSi surface

The number of available ssDNA probes immobilized on the inner surface of the nanochannels determines the efficiency of the hybridization process, which is related to the sensor sensitivity and LOD. To optimize the concentration of the ssDNA probe solution used to modify the inner surface of the THCpSi structure, THCpSi with an average nanochannel diameter of 27 ± 9 nm, 1.6 μm depth and a ~7 nm Si_3N_4 coating, was used. The surface coverage achieved upon ssDNA probe immobilization was controlled by incubating ssDNA solutions of various concentrations, 5, 10 and 25 μM, for 1 h on the transducer surface. The effect of the concentration of the ssDNA probe solution used to modify the sensor surface on the performance of the designed DNA sensor is shown by the normalized dose response curves in **Figure 4.7b**. The normalized current exhibits a linear relationship with the target ssDNA concentration from 0.1 to 1000 pM. The control sensors prepared by immobilizing ssDNA probes of random sequence (hollow symbols) on the THCpSi surface present nearly no electrochemical response compared to the specific DNA sensors (solid symbols). As shown by the slope of the dose response curves in **Figure 4.7b**, the sensor prepared by incubating a 10 μM ssDNA probe solution presents the highest sensitivity (Δi = 0.389 + 0.121*Log [target ssDNA], R^2 = 0.990), being 147% and 116% higher than that of the sensors prepared with ssDNA probe solutions of 5 and 25 μM in concentration, respectively. As it has been proved by the CV and EIS results shown in **Figure 4.5**, the immobilization of ssDNA probes causes certain degree of electrostatic repulsion, increasing the R_{ct}, so a compromise has to be found between having enough ssDNA probes available for hybridization, but not too many to hinder the access of the target ssDNA in solution towards the immobilized probes for hybridization.

4.3.5.3 Optimization of the nanochannel diameter

The ease of control of the nanochannel diameter in pSi structures has led to great advances in the detection of numerous biological species of various sizes.[34] The nanochannel diameter of the THCpSi transducer has to be large enough to allow the analyte to access the structure, but small enough to maximize the nanochannel blockage efficiency. The estimated size of a 28-base oligonucleotide is roughly 9 nm.[47] In order to select the most suitable nanochannel diameter for such target, various DNA sensors were prepared with THCpSi single layers with similar thickness, 1.6 μm, but different nanochannel diameters: 12 ± 5, 27 ± 9 and 72 ± 15 nm. A Si_3N_4 insulating layer with a thickness of 7 nm was deposited on the external surface of these THCpSi transducers. The effect of nanochannel diameter on the performance of these DNA sensors is shown in **Figure 4.7c**. Among these sensors, the DNA sensors prepared with structures of 27 ± 9 nm in nanochannel diameter show the highest sensitivity as shown by the slope value of their dose response curve (plot 1, Δi = 0.194 + 0.123*Log [target ssDNA], R^2 = 0.986). Plot 2 (Δi = 0.118 + 0.080*Log [target ssDNA], R^2 = 0.989) represents the DNA sensors having nanochannel diameter 72 ± 15 nm, while plot 3 (Δi = 0.055 + 0.046*Log [target ssDNA], R^2 = 0.985) represents the DNA sensors having nanochannel diameter 12 ± 5 nm. The sensitivity obtained by sensors prepared with structures of 27 ± 9 nm in nanochannel diameter is 167% and 54% higher than that of sensors featuring nanochannels of 12 ± 5 nm and 72 ± 15 nm in diameter, respectively. In terms of the detection of a 28-base oligonucleotide, THCpSi structures with a nanochannel diameter of 27 ± 9 nm are suitable to design highly sensitive sensors, achieving the maximum nanochannel blockage efficiency. This observation can be explained by considering the three-dimensional channel structure of THCpSi transducers. In the case of nanochannels with an average diameter of 27 nm, the immobilization of ssDNA probes partially blocked the nanochannels, although there was still enough space left inside the channels for target hybridization. The hybridization events that happened inside nanochannels

of such diameter caused the maximum nanochannel blockage, greatly hindering the diffusion of $[Fe(CN)_6]^{3-/4-}$. In the case of structures featuring nanochannels with an average diameter of 12 nm, the immobilization of ssDNA probes almost totally blocked the nanochannels as the size of the ssDNA probe (~9 nm) was similar to the diameter of the nanochannels. Therefore, the target analyte can hardly enter into the nanochannels for further hybridization to the ssDNA probes immobilized inside the nanochannels. On the contrary, the use of structures with a large nanochannel diameter such as 72 nm, does not provide proper nanochannel blockage: the target analyte can easily enter into such nanochannels and hybridize to the immobilized probes, but there is still big enough space left for the redox species $[Fe(CN)_6]^{3-/4-}$ to freely diffuse to the transducer surface. The hybridization happened in such large nanochannels can cause partial channel blockage but with a very low efficiency.

4.3.5.4 Optimization of the transducer thickness

In this section, the transducer thickness was adjusted to study its effect on the sensitivity and LOD of these DNA sensors (**Figure 4.7d**). DNA sensors were prepared with THCpSi transducers having the same nanochannel diameter of 27 ± 9 nm, but various thicknesses, 0.7, 1.6 and 3.4 µm. A Si_3N_4 insulating layer with a thickness of 7 nm was deposited on the external surface of all these sensors. Among these sensors, the DNA sensors prepared with a transducer thickness of 1.6 µm provided the highest sensitivity, as shown by their slope value (plot 1, Δi = 0.394 + 0.124*Log [target ssDNA], R^2 = 0.987). The sensitivity of the designed DNA sensors with a transducer thickness of 1.6 µm is 17% and 33% higher than that of sensors prepared with transducers of 0.7 µm (plot 2) and 3.4 µm (plot 3) thickness, respectively. The calculated LODs were 0.459, 0.002 and 0.048 pM for sensors with transducer thicknesses of 0.7, 1.6 and 3.4 µm, respectively. For structures with a fixed nanochannel diameter, the one with the thickest layer presents the largest surface area available for bioreceptor immobilization, which is expected to provide the best sensing performance. On the one hand, thin THCpSi transducers

such as those with 0.7 μm thickness, have limited surface area available for bioreceptor immobilization and further hybridization. This translates into low signal responses. On the other hand, thick THCpSi transducers such as those with 3.4 μm thickness, have a large surface area and a large number of bioreceptors available for hybridization. However, at a certain thickness, the free diffusion of both the oligonucleotides (target and probe) and the redox species $[Fe(CN)_6]^{3-/4-}$ begins to be hindered along the long intricate pore structures. As a result, the most suitable thickness of the transducer is 1.6 μm as the DNA sensors developed with such structure showed the highest sensitivity and the lowest LOD (0.002 pM).

4.3.5.5 Selectivity of DNA sensors

Having successfully optimized the structure of the THCpSi transducer (i.e. nanochannel diameter and thickness) and its modification (i.e. concentration of ssDNA probe used for sensor modification and inclusion of an external insulating layer) to provide the most sensitive DNA sensor, selectivity was then explored by exposing such DNA sensors to solutions containing 1-base mismatch ssDNA sequence, and 2-base mismatch ssDNA sequence, instead of the target complementary ssDNA. All the sequences of probes and targets, including these mismatched sequences, are listed in **Table 4.1**. The DNA sensors were prepared with Si_3N_4-insulated THCpSi transducers with a nanochannel diameter of 27 ± 9 nm, and a thickness of 1.6 μm. The DNA sensors' response to increasing concentrations of target ssDNA is shown in **Figure 4.8**. The dose response curve obtained by the DNA sensors upon incubation in solutions of the complementary ssDNA provides a significantly higher sensitivity (**Figure 4.8a**) than the response of the same DNA sensors upon incubation in solutions of a 2-base mismatch ssDNA sequence (**Figure 4.8b**), and 1-base mismatch ssDNA sequence (**Figure 4.8c**). The response is also compared to the one obtained by the negative control prepared by immobilization of a random sequence of ssDNA probe, incubated in solutions of the target analyte (**Figure 4.8d**).

The latter, used as negative control, show no response to the target ssDNA sequence. The sensitivity of the DNA sensors towards the fully complementary target analyte is 164 % and 210 % higher than that obtained when the sensors are exposed to ssDNA sequences with 1-base mismatch, and 2-base mismatch, respectively. However, compared to the negative control incubating the target analyte on a sensor modified with a ssDNA probe of random sequence (**Figure 4.8d**), the response of the DNA sensor towards ssDNA sequences with 1 or 2 mismatches is still significant. Further work should be conducted to optimize the sensing conditions (e.g. incubation time, incubation temperature) to minimize this undesired response.

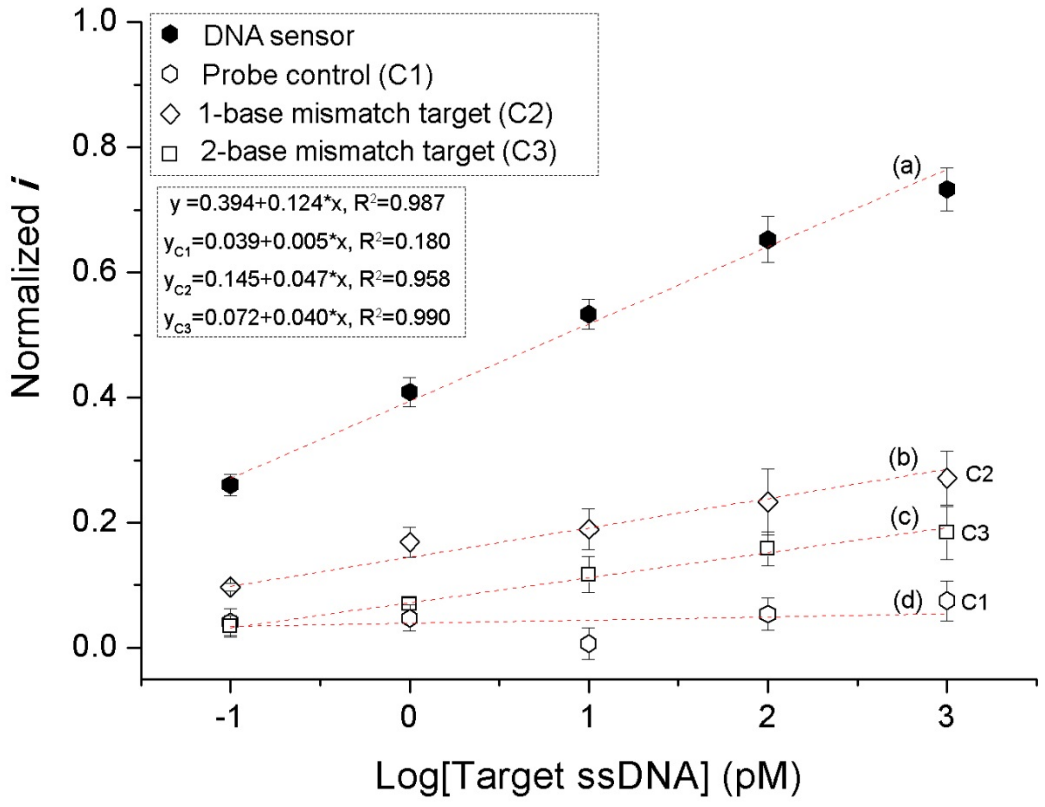

Figure 4.8. Selectivity test of DNA sensors prepared from Si_3N_4-insulated THCpSi with a nanochannel diameter of 27 ± 9 nm, and a thickness of 1.6 µm. The sensors were tested in front of: (a) complementary ssDNA, (b) 1-mismatch ssDNA sequence, and (c) 2-mismatch ssDNA sequence. (d) Control DNA sensor prepared with a ssDNA probe of random sequence tested in front of the target ssDNA.

Table 4.1 The sequence of ssDNA and 16S rRNA used in this study.

ssDNA probes	Targets
NH_2-modified ssDNA probe 5'-/5AmMC6/GTC CAC GCC GTA AAC GAT GTC GAC TTG G-3'	Complementary ssDNA target 5'-CCA AGT CGA CAT CGT TTA CGG CGT GGA C-3'
Negative control probe 5'-/5AmMC6/CAC AAA TTC GGT TCT ACA GGG TA-3'	1-base mismatch ssDNA target 5'-CCA AGT CGA GAT CGT TTA CGG CGT GGA C-3'
	2-base mismatch ssDNA target 5'-CCA ACT CGA GAT CGT TTA CGG CGT GGA C-3'
	16S rRNA target 5'-CCA AGU CGA CAU CGU UUA CGG CGU GGA C-3'

4.3.6 *E. coli* 16S rRNA detection

After successful optimization of the THCpSi transducer structure to provide a DNA sensor with high sensitivity and selectivity towards a target ssDNA sequence, detection of *E. coli* 16S rRNA in buffer was attempted. Sensors prepared with the optimized nanochannel diameter of 27 ± 9 nm, thickness of 1.6 µm, 10 µM ssDNA probe concentration for immobilization, and Si_3N_4 insulating layer, were tested as 16S rRNA sensors. The DPV traces obtained for the sensors and control in a range of 16S rRNA concentrations from 0.1 to 1000 pM are shown as inset in **Figure 4.9**. In the case of the sensors, the peak current significantly decreases with the 16S rRNA concentration increase. The control sensors prepared with ssDNA probes of random sequence present similar peak current intensity even with increasing 16S rRNA concentrations. The normalized peak current Δi plotted as a function of Log [16S rRNA] is shown in **Figure**

4.9. The Δi of the sensors exhibit a linear relationship with the 16S rRNA concentrations, while the control sensors prepared with probes of random sequence show no significant response. However, the sensitivity of such 16S rRNA sensors (Δi = 0.162 + 0.084*Log [target ssDNA], R^2 = 0.995) is 48% lower than that of the DNA sensors (Δi = 0.394 + 0.124*Log [target ssDNA], R^2 = 0.890). This could be attributed to the inherent instability of RNA compared to DNA. There is the possibility that the 16S rRNA sequence degraded to a certain extent during the incubation process (even though being a short period of 15 min). While further studies should be performed to find out the reason of this decreased sensitivity, the calculated LOD for the detection of 16S rRNA in buffer based on these results was 0.183 pM. Nevertheless, the analytical performance of the designed sensors for *E. coli* 16S rRNA detection is still comparable to those reported recently using electrochemical sensing methods. Purwidyantri et. al reported a LOD of 10 pM for the detection of *Staphylococcus aureus* 16S rRNA upon 1 h incubation using a gold nanohole array-modified ITO as electrochemical transducer.[2] Even though Esfandiari and coworkers reported a low LOD of 0.01 pM for the detection of *E. coli* 16S rRNA by measuring the ionic current change caused by the hybridization between peptide nucleic acid (PNA)-modified polystyrene beads and the target, a very long detection time (overnight) was required.[48] The main advantage of the designed system discussed here compared to those reported elsewhere is the fast analysis time (15 min at room temperature), which could be further reduced by adjusting the incubation temperature or incorporating additional shaking. Furthermore, the fabrication process of the THCpSi transducers at large scale (e.g. 6 inch wafer) is fast, cost-effective and straightforward, without the need of expensive micro-fabrication processes.

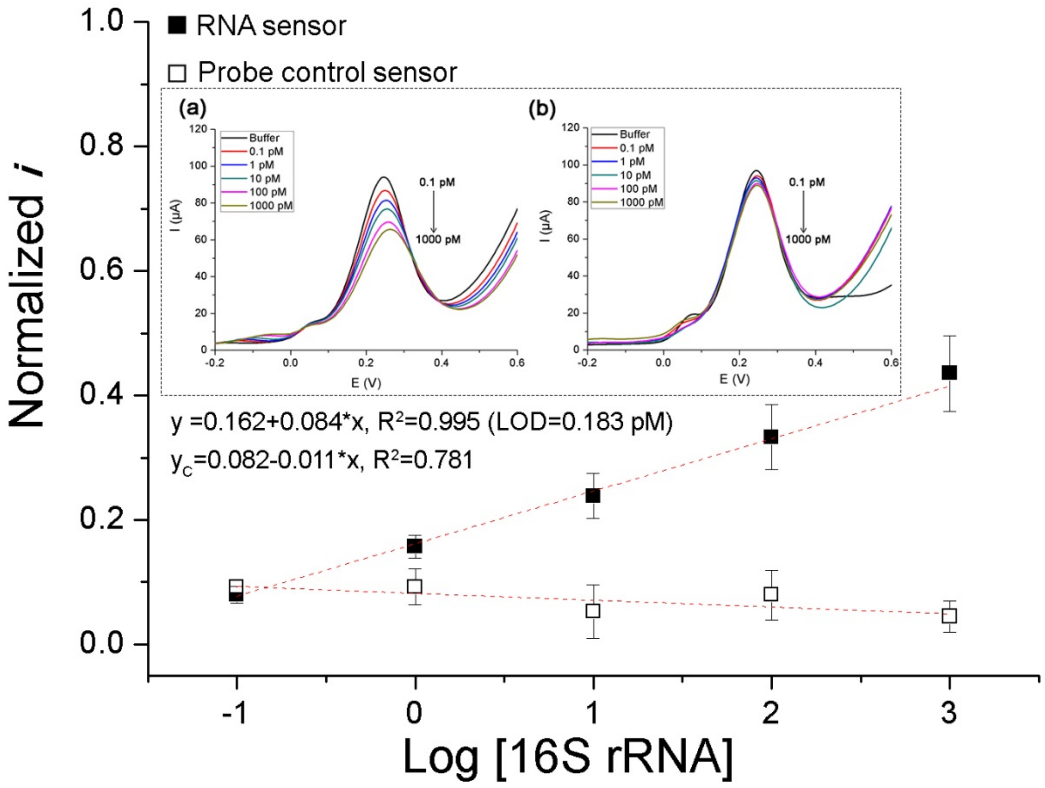

Figure 4.9 Calibration curves obtained for the detection of *E. coli* 16S rRNA. Inset: corresponding DPV voltammograms of sensors modified with (a) specific ssDNA probe, and (b) ssDNA probe of random sequence.

4.4 Conclusion

In summary, a simple, cost-effective, label-free and portable voltammetric DNA sensor has been developed using carbon-stabilized pSi as transducer. The designed sensors are able to detect the specific bacteria biomarker 16S rRNA with high sensitivity and a LOD down to 0.183 pM in buffer, only requiring 15 min incubation. A simple, direct and label-free sensing mechanism based on nanochannel blockage is used. The sensing conditions of using such porous transducers were firstly optimized by detecting a ssDNA sequence complementary to the immobilized ssDNA probe, and of equivalent sequence to the target 16S rRNA. The calculated LOD for the sensitive detection of complementary ssDNA in buffer is 0.002 pM. The selectivity of the sensor was tested in the presence of sequences with 1 or 2 mismatches. Although showing low sensitivity for those sequences, further optimization of the working

conditions is envisaged to completely suppress the undesired response towards those non-complementary sequences. The study on this simple label-free sensing strategy using such promising carbon-stabilized pSi as transducer will facilitate the design of more practically useful biosensors.

4.5 References

1. Tacconelli, E.; Carrara, E.; Savoldi, A.; Harbarth, S.; Mendelson, M.; Monnet, D. L.; Pulcini, C.; Kahlmeter, G.; Kluytmans, J.; Carmeli, Y., Discovery, Research, and Development of New Antibiotics: The Who Priority List of Antibiotic-Resistant Bacteria and Tuberculosis. *Lab. Res. Methods Biol. Med.* **2018,** *18* (3), 318-327.

2. Purwidyantri, A.; Chen, C.-H.; Hwang, B.-J.; Luo, J.-D.; Chiou, C.-C.; Tian, Y.-C.; Lin, C.-Y.; Cheng, C.-H.; Lai, C.-S., Spin-Coated Au-Nanohole Arrays Engineered by Nanosphere Lithography for a Staphylococcus Aureus 16s Rrna Electrochemical Sensor. *Biosens. Bioelectron.* **2016,** *77*, 1086-1094.

3. Zimdars, A.; Gebala, M.; Hartwich, G.; Neugebauer, S.; Schuhmann, W., Electrochemical Detection of Synthetic DNA and Native 16s Rrna Fragments on a Microarray Using a Biotinylated Intercalator as Coupling Site for an Enzyme Label. *Talanta* **2015,** *143*, 19-26.

4. Lehmann, L. E.; Hunfeld, K.-P.; Emrich, T.; Haberhausen, G.; Wissing, H.; Hoeft, A.; Stüber, F., A Multiplex Real-Time Pcr Assay for Rapid Detection and Differentiation of 25 Bacterial and Fungal Pathogens from Whole Blood Samples. *Med. Microbiol. Immunol.* **2008,** *197* (3), 313-324.

5. Yarza, P.; Yilmaz, P.; Pruesse, E.; Glöckner, F. O.; Ludwig, W.; Schleifer, K.-H.; Whitman, W. B.; Euzéby, J.; Amann, R.; Rosselló-Móra, R., Uniting the Classification of Cultured and Uncultured Bacteria and Archaea Using 16s Rrna Gene Sequences. *Nat. Rev. Microbiol.* **2014,** *12* (9), 635.

6. Srinivasan, R.; Karaoz, U.; Volegova, M.; MacKichan, J.; Kato-Maeda, M.; Miller, S.; Nadarajan, R.; Brodie, E. L.; Lynch, S. V., Use of 16s Rrna Gene for Identification of a Broad Range of Clinically Relevant Bacterial Pathogens. *PloS One* **2015,** *10* (2), e0117617.

7. Langille, M. G.; Zaneveld, J.; Caporaso, J. G.; McDonald, D.; Knights, D.; Reyes, J. A.; Clemente, J. C.; Burkepile, D. E.; Thurber, R. L. V.; Knight, R., Predictive Functional

Profiling of Microbial Communities Using 16s Rrna Marker Gene Sequences. *Nat. Biotechnol.* **2013,** *31* (9), 814.

8. Janda, J. M.; Abbott, S. L., 16s Rrna Gene Sequencing for Bacterial Identification in the Diagnostic Laboratory: Pluses, Perils, and Pitfalls. *J. Clin. Microbiol.* **2007,** *45* (9), 2761-2764.

9. Kilian, K. A.; Böcking, T.; Gaus, K.; Gooding, J. J., Introducing Distinctly Different Chemical Functionalities onto the Internal and External Surfaces of Mesoporous Materials. *Angew. Chem. Int. Ed.* **2008,** *47* (14), 2697-2699.

10. Gerasimova, Y. V.; Kolpashchikov, D. M., Detection of Bacterial 16s Rrna Using a Molecular Beacon-Based X Sensor. *Biosens. Bioelectron.* **2013,** *41*, 386-390.

11. Joung, H.-A.; Lee, N.-R.; Lee, S. K.; Ahn, J.; Shin, Y. B.; Choi, H.-S.; Lee, C.-S.; Kim, S.; Kim, M.-G., High Sensitivity Detection of 16s Rrna Using Peptide Nucleic Acid Probes and a Surface Plasmon Resonance Biosensor. *Anal. Chim. Acta* **2008,** *630* (2), 168-173.

12. Koo, B.; Yorita, A. M.; Schmidt, J. J.; Monbouquette, H. G., Amplification-Free, Sequence-Specific 16s Rrna Detection at 1 Am. *Lab Chip* **2018,** *18* (15), 2291-2299.

13. Kirsch, J.; Siltanen, C.; Zhou, Q.; Revzin, A.; Simonian, A., Biosensor Technology: Recent Advances in Threat Agent Detection and Medicine. *Chem. Soc. Rev.* **2013,** *42* (22), 8733-8768.

14. Ronkainen, N. J.; Halsall, H. B.; Heineman, W. R., Electrochemical Biosensors. *Chem. Soc. Rev.* **2010,** *39* (5), 1747-1763.

15. Guo, S.; Wen, D.; Dong, S.; Wang, E., Gold Nanowire Assembling Architecture for H 2 O 2 Electrochemical Sensor. *Talanta* **2009,** *77* (4), 1510-1517.

16. Xia, C.; Ning, W., A Novel Non-Enzymatic Electrochemical Glucose Sensor Modified with Feooh Nanowire. *Electrochem. Commun.* **2010,** *12* (11), 1581-1584.

17. Ramnani, P.; Saucedo, N. M.; Mulchandani, A., Carbon Nanomaterial-Based Electrochemical Biosensors for Label-Free Sensing of Environmental Pollutants. *Chemosphere* **2016,** *143*, 85-98.

18. Zhao, Q.; Gan, Z.; Zhuang, Q., Electrochemical Sensors Based on Carbon Nanotubes. *Electroanalysis* **2002,** *14* (23), 1609-1613.

19. Zhang, M.; Smith, A.; Gorski, W., Carbon Nanotube− Chitosan System for Electrochemical Sensing Based on Dehydrogenase Enzymes. *Anal. Chem.* **2004,** *76* (17), 5045-5050.

20. Pumera, M.; Ambrosi, A.; Bonanni, A.; Chng, E. L. K.; Poh, H. L., Graphene for Electrochemical Sensing and Biosensing. *Trends Anal. Chem.* **2010,** *29* (9), 954-965.

21. Guo, S.; Wen, D.; Zhai, Y.; Dong, S.; Wang, E., Platinum Nanoparticle Ensemble-on-Graphene Hybrid Nanosheet: One-Pot, Rapid Synthesis, and Used as New Electrode Material for Electrochemical Sensing. *ACS Nano* **2010,** *4* (7), 3959-3968.

22. Zhang, Y.; Sun, X.; Zhu, L.; Shen, H.; Jia, N., Electrochemical Sensing Based on Graphene Oxide/Prussian Blue Hybrid Film Modified Electrode. *Electrochim. Acta* **2011,** *56* (3), 1239-1245.

23. Zeng, Q.; Cheng, J.; Tang, L.; Liu, X.; Liu, Y.; Li, J.; Jiang, J., Self-Assembled Graphene–Enzyme Hierarchical Nanostructures for Electrochemical Biosensing. *Adv. Func. Mater.* **2010,** *20* (19), 3366-3372.

24. Pumera, M.; Ambrosi, A.; Bonanni, A.; Chng, E. L. K.; Poh, H. L., Graphene for Electrochemical Sensing and Biosensing. *Trends Anal. Chem.* **2010,** *29* (9), 954-965.

25. Hrapovic, S.; Liu, Y.; Male, K. B.; Luong, J. H., Electrochemical Biosensing Platforms Using Platinum Nanoparticles and Carbon Nanotubes. *Anal. Chem.* **2004,** *76* (4), 1083-1088.

26. Rai, V.; Deng, J.; Toh, C.-S., Electrochemical Nanoporous Alumina Membrane-Based Label-Free DNA Biosensor for the Detection of Legionella Sp. *Talanta* **2012,** *98*, 112-117.

27. Ye, W.; Xu, Y.; Zheng, L.; Zhang, Y.; Yang, M.; Sun, P., A Nanoporous Alumina Membrane Based Electrochemical Biosensor for Histamine Determination with Biofunctionalized Magnetic Nanoparticles Concentration and Signal Amplification. *Sensors* **2016,** *16* (10), 1767.

28. Reta, N.; Michelmore, A.; Saint, C.; Prieto-Simón, B.; Voelcker, N. H., Porous Silicon Membrane-Modified Electrodes for Label-Free Voltammetric Detection of Ms2 Bacteriophage. *Biosens. Bioelectron.* **2016,** *80*, 47-53.

29. Jane, A.; dronov, R.; Hodges, A.; Voelcker, N. H., Porous Silicon Biosensors on the Advance. *Trends Biotechnol* **2009,** *27* (4), 230-239.

30. Anglin, E. J.; Cheng, L. Y.; Freeman, W. R.; Sailor, M. J., Porous Silicon in drug Delivery Devices and Materials. *Adv. Drug Deliv. Rev.* **2008,** *60* (11), 1266-1277.

31. Wang, J., Electrochemical Biosensors: Towards Point-of-Care Cancer Diagnostics. *Biosens. Bioelectron.* **2006,** *21* (10), 1887-1892.

32. Buriak, J. M., Silicon-Carbon Bonds on Porous Silicon Surfaces. *Adv. Mater.* **1999,** *11* (3), 265-267.

33. Schwartz, M. P.; Cunin, F.; Cheung, R. W.; Sailor, M. J., Chemical Modification of Silicon Surfaces for Biological Applications. *Phys. Satatus Solidi A* **2005,** *202* (8), 1380-1384.

34. Sweetman, M. J.; Ronci, M.; Ghaemi, S. R.; Craig, J. E.; Voelcker, N. H., Porous Silicon Films Micropatterned with Bioelements as Supports for Mammalian Cells. *Adv. Func. Mater.* **2012,** *22* (6), 1158-1166.

35. Salonen, J.; Björkqvist, M.; Laine, E.; Niinistö, L., Stabilization of Porous Silicon Surface by Thermal Decomposition of Acetylene. *Appl. Surf. Sci.* **2004,** *225* (1), 389-394.

36. de la Escosura-Muñiz, A.; Merkoçi, A., Nanochannels Preparation and Application in Biosensing. **2012**.

37. Torres-Costa, V.; Salonen, J.; Jalkanen, T. M.; Lehto, V. P.; Martin-Palma, R. J.; Martinez-Duart, J. M., Carbonization of Porous Silicon Optical Gas Sensors for Enhanced Stability and Sensitivity. *Phys. Status Solidi A* **2009,** *206* (6), 1306-1308.

38. Bjorkqvist, M.; Paski, J.; Salonen, J.; Lehto, V. P., Studies on Hysteresis Reduction in Thermally Carbonized Porous Silicon Humidity Sensor. *IEEE Sens. J.* **2006,** *6* (3), 542-547.

39. RoyChaudhuri, C., A Review on Porous Silicon Based Electrochemical Biosensors: Beyond Surface Area Enhancement Factor. *Sens. Actuators B Chem.* **2015,** *210*, 310-323.

40. Kaneki, N.; Xu, Y.; Kumari, A.; Halsall, H. B.; Heineman, W. R.; Kissinger, P. T., Electrochemical Enzyme Immunoassay Using Sequential Saturation Technique in a 20-Ml Capillary: Digoxin as a Model Analyte. *Anal. Chim. Acta* **1994,** *287* (3), 253-258.

41. Jenkins, S. H.; Heineman, W. R.; Halsall, H. B., Extending the Detection Limit of Solid-Phase Electrochemical Enzyme Immunoassay to the Attomole Level. *Anal. Biochem.* **1988,** *168* (2), 292-299.

42. Sciacca, B.; Secret, E.; Pace, S.; Gonzalez, P.; Geobaldo, F.; Quignard, F.; Cunin, F., Chitosan-Functionalized Porous Silicon Optical Transducer for the Detection of Carboxylic Acid-Containing drugs in Water. *J. Mater. Chem.* **2011,** *21* (7), 2294-2302.

43. Makila, E.; Bimbo, L. M.; Kaasalainen, M.; Herranz, B.; Airaksinen, A. J.; Heinonen, M.; Kukk, E.; Hirvonen, J.; Santos, H. A.; Salonen, J., Amine Modification of Thermally Carbonized Porous Silicon with Silane Coupling Chemistry. *Langmuir* **2012,** *28* (39), 14045-14054.

44. Salonen, J.; Bjorkqvist, M.; Laine, E.; Niinisto, L., Stabilization of Porous Silicon Surface by Thermal Decomposition of Acetylene. *Appl. Surf. Sci.* **2004,** *225* (1-4), 389-394.

45. Rodriguez, M. C.; Kawde, A.-N.; Wang, J., Aptamer Biosensor for Label-Free Impedance Spectroscopy Detection of Proteins Based on Recognition-Induced Switching of the Surface Charge. *Chem. Commun.* **2005,** (34), 4267-4269.

46. Bogomolova, A.; Komarova, E.; Reber, K.; Gerasimov, T.; Yavuz, O.; Bhatt, S.; Aldissi, M., Challenges of Electrochemical Impedance Spectroscopy in Protein Biosensing. *Anal. Chem.* **2009,** *81* (10), 3944-3949.

47. Gregory, T. R.; Nicol, J. A.; Tamm, H.; Kullman, B.; Kullman, K.; Leitch, I. J.; Murray, B. G.; Kapraun, D. F.; Greilhuber, J.; Bennett, M. D., Eukaryotic Genome Size Databases. *Nucleic Acids Research* **2006,** *35* (suppl_1), D332-D338.

48. Esfandiari, L.; Wang, S.; Wang, S.; Banda, A.; Lorenzini, M.; Kocharyan, G.; Monbouquette, H. G.; Schmidt, J. J., Pcr-Independent Detection of Bacterial Species-Specific 16s Rrna at 10 Fm by a Pore-Blockage Sensor. *Biosensors* **2016,** *6* (3), 37.

Chapter 5. Designing versatile biosensing platforms using layered carbon-stabilized porous silicon nanostructures

5.1 Introduction

PSi has demonstrated its advantages and versatility in various biomedical applications, such as biosensing and drug delivery.[1-13]. The ease of controlling pore morphology has implications in its sensing capabilities and has driven advances in the detection of a large range of chemical and biological species.[2, 13-17] Other features of pSi, such as the large available internal surface area and excellent biocompatibility, have also been harnessed to develop highly performing biosensing platforms.[18-22] Of particular interest for biosensing purposes is the versatile surface chemistry of pSi, allowing a broad range of functionalization routes (e.g. hydrosilylation,[23-30] silanization[31-33]) to introduce functional groups further used to covalently immobilize diverse biomolecules as bioreceptors (e.g. antibodies,[33-34] oligonucleotides,[17] enzymes[35-36]).

The hydride terminated surface of freshly etched pSi is highly reactive and prone to oxidation and further degradation when exposed to water and air.[37-38] This limitation hinders pSi to be used for long-term biosensing applications as most biosensing processes are conducted in aqueous solution. To address this shortcoming, various techniques to stabilize the freshly etched pSi surface have been extensively explored. Thermal and ozone oxidation have been reported to generate Si-OH groups, providing excellent hydrophilicity and improved stability.[27, 39] However, the slow hydrolysis of the oxidized pSi matrix in water can negatively contribute to the biosensor read-out.[40] Alternatively, hydrosilylation reactions are also used to produce stable and robust surfaces via formation of Si-C bonds upon coupling alkene or alkyne species onto the freshly etched pSi surface.[28, 40-41] Although hydrosilylation often provides stable surfaces, simultaneously allowing the incorporation of functional groups, its main drawback is that the reaction requires an air- and water-free environment to prevent oxidative side reactions.[42] In 2004, Salonen and co-workers reported a novel approach to stabilize pSi by

introducing a thin carbon coating via thermal decomposition of acetylene.[43] One of the key advantages of this carbon-stabilization process is that the thin carbon layer on the pSi surface is formed in situ, leaving the pore structure intact after stabilization. Moreover, carbon-stabilized pSi not only preserves the flexibility of pSi to design high quality optical sensing platforms, but also presents effectively stabilized optical performance even in strongly oxidizing environments.[44-45] Additionally, the carbon layer protects pSi from surface degradation and enables incorporation of specific recognition biomolecules on the surface.[46-48]

Thanks to these stabilization methods, the advantages of pSi-based optical interferometric sensing have been well demonstrated using different pSi nanostructures, including single layer,[49-50] double layer[15-16] and multilayer structures,[51-52] since Sailor et al. first reported in 1997 the use of oxidized pSi as optical transducer to investigate basic biological systems.[38] To the best of our knowledge, only a few reports describe the use of pSi as electrochemical transducer in the development of sensors compared to its optical counterparts.[53] The key reasons for the lack of published research in this area are the spontaneous growth of the insulating oxide layer on pSi[54] and the fact that the charge transfer is limited to the pore tips where the high radius of curvature is responsible of generating a region of enhanced electric field.[55] To indirectly overcome the limitations in using pSi for electrochemical sensing purposes, our research group recently explored the use of pSi membranes which were hydrosilylated, not only to introduce functional groups but also to provide stability, for developing label-free immunosensors based on voltammetric detection.[56] The non-conductive pSi membrane firmly attached to a gold working electrode enabled high-sensitivity detection via electrochemical measurement of the nanochannel blockage caused upon analyte binding. The device was capable of detecting MS2 bacteriophage spiked in reservoir water samples with an impressive LOD of 17 pfu mL^{-1} and negligible matrix effects. Other researchers have reported various pSi modifications to preserve the semiconductor properties of silicon or to

introduce conductive coatings (e.g. metal[57-60] or conductive polymeric layers[23, 61]) with the aim of developing pSi-based electrochemical biosensors.

The advantages of using pSi multilayer structures as optical transducers are well demonstrated. As reported by Sailor and coworkers, interferometric biosensors based on pSi double layers have been used not only to separate biomolecules based on size exclusion, but also to effectively measure biomolecule penetration into specific layers by monitoring shifts of the fast Fourier transform (FFT) peaks.[15-16] Control of surface functionalization for each porous layer separately is of particular interest because it allows size-exclusion separation and detection of biomolecules, as well as discrimination on the basis of molecular affinity via the specific capture probes grafted on selected layers.

In this chapter, a pSi double layer nanostructure was fabricated, each layer featuring a specific pore size distribution, as well as different surface chemistry achieved by in situ carbon stabilization under different conditions. Most importantly, the fast electron-transfer kinetics of the carbon-stabilized pSi double layer nanostructures when used as electrochemical transducer, and their versatile surface chemistry by undergoing layer-selective silanization and hydrosilylation reactions were demonstrated. These carbon-stabilized pSi nanostructures show great potential as an advanced biointerface and electrochemical transducer for biosensing applications. An electrochemical DNA sensor fabricated using the TCpSi-THCpSi double layer structure provided an excellent LOD of 0.4 pM to detect a 28 base ssDNA sequence.

5.2 Experimental section

Materials: p-type silicon wafers with 0.00055-0.001 Ω cm resistivity, (100)-oriented were purchased from Siltronix (France). Hydrofluoric acid (HF) (48%, AR grade) was purchased from Scharlau (Australia). Potassium ferrocyanide ($K_4[Fe(CN)_6]$), potassium ferricyanide ($K_3[Fe(CN)_6]$), undecylenic acid, N-hydroxysuccinimide (NHS), N(3-dimethylaminopropyl) N-ethylcarbodiimide hydrochloride (EDC), phosphate buffered saline (PBS) tablets, 2-(N-morpholino)-ethanesulfonic acid (MES), (3-aminopropyl) triethoxysilane (APTES), (3-glycidylxypropyl) trimethoxysilane, sodium chloride, tris(hydroxymethyl)aminomethane, hydrochloric acid (37%) and fluorescein isothiocyanate (FITC) were purchased from Sigma-Aldrich (Australia). Cyanine5 amine ($Cy5\text{-}NH_2$) was purchased from Luminoprobe (USA). The acetylene gas cylinder (1 m^3 industrial grade, dissolved) was purchased from BOC (Australia). All the DNA strands were purchased from Integrated DNA Technologies Pte Ltd (Singapore). The sequence of the amino-modified ssDNA capture probe was 5'-/5AmMC6/GTC CAC GCC GTA AAC GAT GTC GAC TTG G-3'. The amino-modified non-specific ssDNA capture probe was 5'-/5AmMC6/CAC AAA TTC GGT TCT ACA GGG TA-3'. The sequence of the target ssDNA was 5'-CCA AGT CGA CAT CGT TTA CGG CGT GGA C-3'.

Apparatus: SEM images were obtained with a FEI NovaNano SEM 430 at an accelerating voltage of 10 kV. Attenuated total reflectance Fourier transform infrared (ATR-FTIR) spectroscopy was performed with a Thermo Scientific Nicolet 6700 FTIR spectrometer. Raman spectra were acquired using a Renishaw inVia Raman microscope with a 100 mW 532 nm laser excitation source. A 10% excitation power density was applied to avoid damage of the surface. Fluorescence microscopy images were collected with a laser scanning confocal microscope (Nikon Instrument TIRF with Ti-U system).

Fabrication of pSi single layer: A whole 6 inch p-type silicon wafer was anodically etched in an electrolyte solution containing 1:1 (v:v) HF/ethanol to produce a first pSi layer, using a MPSB wet etching system (A.M.M.T GmbH, Germany), which can load a 6 inch silicon wafer with an exposed etching area of 132 cm^2 (details can be found from the website: https://www.ammt.com/products/porous-silicon-etching/mpsb/). Firstly, the sacrificial layer produced with a current density of 60.6 mA cm^{-2} for 30 s was removed with 1 M NaOH.[62] Then the etching cell was rinsed with water, absolute ethanol and dried with N_2 gas. Next, various current densities were applied to fabricate porous layers with different pore size. A current density of 18.9 mA cm^{-2} was applied to the etching cell to form pores of 27 ± 9 nm diameter. The freshly etched pSi was finally rinsed with ethanol and kept in a desiccator.

Thermal carbonization of pSi single layer (TCpSi). The freshly etched pSi substrates were cut into 1.5 cm × 1.5 cm pieces and stabilized using the thermal carbonization (TC) treatment with acetylene decomposition described by Salonen et al.[43, 46] TC is a two-step carbonization process that starts with the thermal hydrocarbonization (THC) treatment at 525 °C followed by annealing at 800 °C. For the THC step, the freshly etched pSi was placed into a quartz tube under N_2 flow at 2 L min^{-1} for 45 min at room temperature. A 1:1 N_2/acetylene mixture flow was introduced into the tube at room temperature for 15 min after the purging step, then the quartz tube was placed into a preheated tube furnace at 525 °C for another 15 min under continuous mixture flow. After THC process, the tube was left to cool down under N_2 flow. For the second step of TC, without opening the quartz tube, a mixture of 1:1 N_2-acetylene was flown for 10 min at room temperature, followed by annealing at 800 °C for 10 min only under N_2 flow (2 L min^{-1}). Finally, the tube was left to cool down back to room temperature under N_2 flow.

Fabrication of pSi double layer: A second etching step was applied on the carbon-stabilized TCpSi single layer using a small cell with a 1.5-cm internal diameter O-ring (the etching cell design can be found in the book Porous Silicon in Practice[14]). Each TCpSi substrate was anodically etched in 3:1 (v:v) HF/ethanol by applying a specific current density to form a bottom layer with small pores.

Thermal hydrocarbonization of the freshly etched pSi bottom layer (THCpSi): The freshly etched pSi bottom layer within the double layer structure was thermally hydrocarbonized following the THC process previously described in the section *Thermal carbonization of pSi single layer*.

Layering surface functionalities on TCpSi-THCpSi double layer: Differential functionalization of the TC top layer and THC bottom layer of the prepared TCpSi-THCpSi nanostructures was performed. Firstly, in order to functionalize the THCpSi bottom layer with COOH groups, the double layer sample was immersed into a glass vial to undergo hydrosilylation with pure undecylenic acid at 150 °C for 10 h under inert atmosphere (N_2). After cooling down to room temperature, the sample was rinsed with absolute ethanol. The TCpSi top layer is natively covered with a thin oxide layer, preventing from potential grafting of -COOH groups during the hydrosilylation process. Prior to further reaction, the COOH-modified sample was immersed into 1:1 (v:v) HF/ethanol solution for 15 min at room temperature, then vacuum filtered from the solution and finally dried at 65 °C for 3 h.[46] The COOH-terminated THCpSi bottom layer resisted HF attack and was stable until further modification. However, exposure to HF enables hydroxylation of the TCpSi surface. The OH-terminated TCpSi top layer was subsequently functionalized by silanization upon immersion in 10 mL 0.5% APTES in anhydrous toluene for 30 min at room temperature. The silane solution was then removed and replaced by anhydrous toluene. Then, the sample was sonicated for 3 min in successive

washing steps with fresh toluene, 1:1 (v:v) toluene/methanol, methanol, and ethanol, to remove any traces of loosely bound APTES. The sample was dried at 80°C overnight. To characterize the layered functionalities, the next steps focused on binding two different fluorophores to the COOH-terminated THCpSi bottom layer and NH_2-terminated TCpSi top layer. The -COOH groups at the THCpSi bottom layer were activated by incubating the functionalized substrates in 10 mg mL^{-1} EDC and 15 mg mL^{-1} NHS in 0.1 M MES buffer, pH 5.5, at room temperature for 30 min to produce succinimidyl ester groups. Subsequently, a 10 µg mL^{-1} Cy5-NH_2 solution in 10 mM PBS was incubated on the activated surface for 30 min. The Cy5-modified sample was finally rinsed with PBS and absolute ethanol. To modify the NH_2-terminated TCpSi top layer, a 10 µg mL^{-1} FITC solution in 10 mM PBS was incubated onto the surface for 30 min. The FITC-modified sample was rinsed with PBS and then absolute ethanol. Control samples exclusively modified either with FITC or Cy5, were simultaneously prepared.

Optical characterization of pSi double layer: Interferometric reflectance spectra were collected using a tungsten lamp (Ocean Optics) and a CCD spectrometer (Ocean Optics S-2000). White light was fed through one end of a bifurcated fiber optic cable and focused through a lens onto the pSi surface with a spot size of approximately 1 mm in diameter. Light reflected from the pSi layer was collected through the same optical lens and transferred to the CCD spectrometer via the second arm of the bifurcated optic cable. Fast Fourier transform using algorithm from the WaveMetrics Inc. Igor program library was applied to the resulting spectra.

Electrochemical characterization: Electrochemical measurements were carried out on an electrochemical analyzer (CH Instruments, model 600D series, USA) using a three-electrode configuration in a Teflon cell containing the pSi nanostructure on an Al film as the working electrode, a Ag/AgCl reference electrode and a platinum wire as counter electrode.

DNA detection using a TCpSi-THCpSi double layer-based sensor: In order to fine-tune the pore size to enable DNA hybridization, the pSi top layer was electrochemically etched in a 1:1 (v:v) HF/ethanol solution, by applying a current density of 18.9 mA cm^{-2} for 80 s using a MPSB wet etching system. Then the pSi bottom layer was etched in a 3:1 (v:v) HF/ethanol solution, using a small cell and applying a current density of 21.4 mA cm^{-2} for 60, 150 and 300 s, to obtain samples with different bottom layer thickness. Firstly, in order to form hydroxyl groups on the TCpSi layer, the TCpSi-THCpSi double layer was treated in 1:1 (v:v) HF/ethanol solution for 15 min and dried at 65°C for 3 h. Secondly, the OH-terminated TCpSi top layer was subsequently functionalized by silanization using 10 mL 10% (3-glycidylxypropyl)trimethoxysilane dissolved in anhydrous toluene for 30 min at room temperature. After silanization, the samples were thoroughly rinsed with 1:1 (v:v) anhydrous toluene/methanol, methanol, and ethanol. Thirdly, 100 µL of either 10 µM of NH_2-ssDNA capture probe or non-specific ssDNA capture probe, both prepared in 10 mM PBS buffer, were incubated on the double layer nanostructures for 2 h at room temperature. Samples were subsequently rinsed thoroughly with PBS. Fourthly, ssDNA target solutions prepared at various concentrations (from 1 to 1000 pM) in 10 mM tris buffer with 75 mM NaCl, pH 7.5, were incubated on the sensor surface for 15 min. After each incubation step, the sensors were thoroughly washed with PBS and transferred to a 2 mM $[Fe(CN)_6]^{3-/4-}$ solution in 10 mM PBS, where DPV measurements were acquired by scanning the potential from -0.3 to 0.6 V vs Ag/AgCl. In order to verify the current changes were only caused from the specific hybridization between the immobilized ssDNA capture probe on the carbon-stabilized pSi surface and the incubated target ssDNA, control sensors were prepared under identical conditions but using random sequences for the ssDNA capture probe. Triplicate measurements were performed with each sensor.

5.3 Result and discussion

5.3.1 TCpSi-THCpSi double layer fabrication

The fabrication process of the TCpSi-THCpSi double layer is divided into four steps: first, pSi top layer fabrication via electrochemical anodization; second, pSi carbonization at high temperature (800 °C) to generate a TCpSi top layer; third, pSi bottom layer fabrication via second anodization, and four, pSi carbonization at low temperature (525°C) to generate a THCpSi bottom layer (**Schematic 5.1**). Stepwise carbon-stabilization of pSi via thermal decomposition of acetylene led to a thermally carbonized pSi (TCpSi) top layer and a thermally hydrocarbonized pSi (THCpSi) bottom layer, each one featuring distinct tunable hydrophilicity and surface chemistry.[48, 63-65] The differences in hydrophilicity were shown by the water contact angles of THCpSi and TCpSi single layers **(Figure 5.1**). In contrast to the hydrophobic THCpSi surface (water contact angle 122°), the surface of TCpSi is hydrophilic, featuring a thin oxide layer (water contact angle 31°).

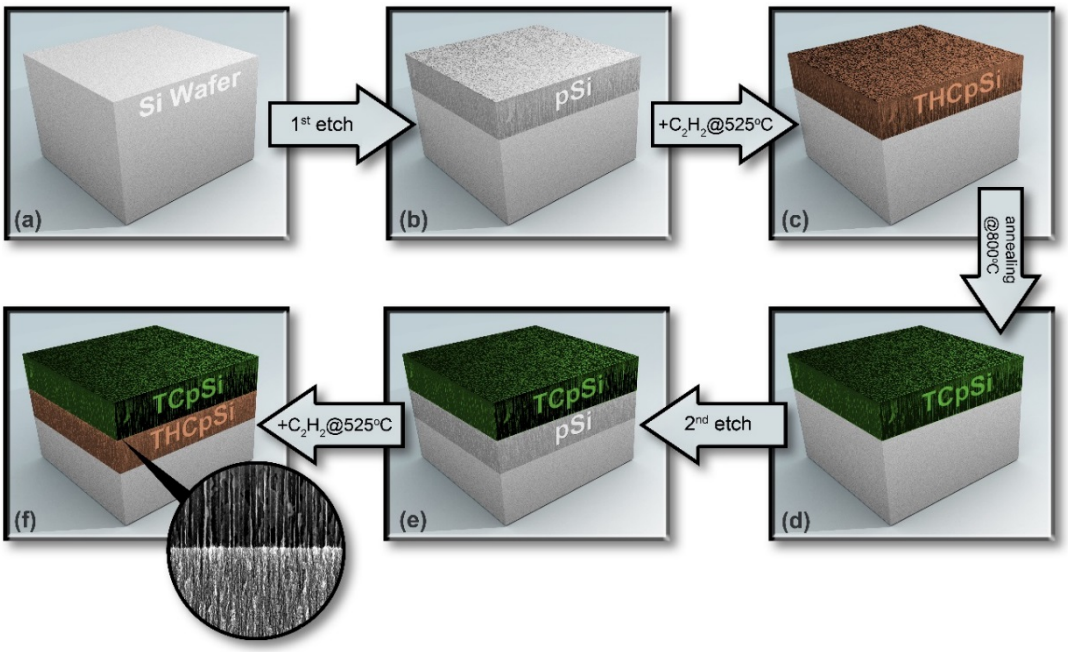

Schematic 5.1 Fabrication process of the TCpSi-THCpSi double-layer nanostructure.

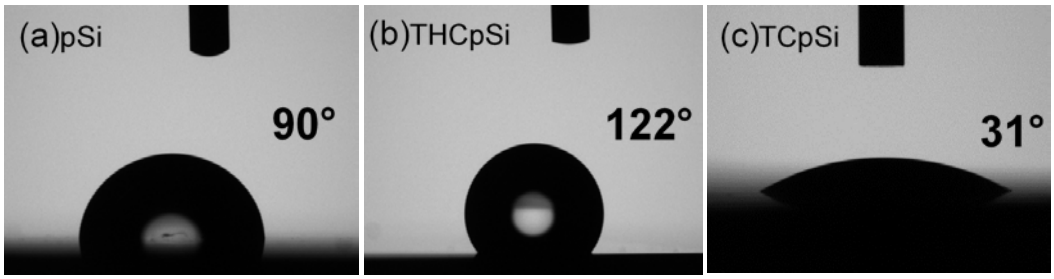

Figure 5.1 Water contact angle of (a) freshly etched pSi, (b) THCpSi, and (c) TCpSi. Water contact angle standard error is ± 6° from 3 replicate measurements.

5.3.2 Morphology and optical characterization of TCpSi-THCpSi double layer

SEM was used to reveal the morphological features of the TCpSi-THCpSi double layer (**Figure 5.2)**. The SEM images display a double layer nanostructure, in which the TCpSi layer with large pores is on top of the THCpSi layer with small pores. The effect of the carbon-stabilization process on the morphology of both THCpSi and TCpSi single layers was investigated prior to the second etching. SEM images show that both THCpSi and TCpSi single layers retain the original pSi features (i.e. pore size and shape, porosity) (**Figure 5.3**). This shows that THC and TC treatments with acetylene gas are an ideal approach to in situ stabilize and modify pSi nanostructures without detrimental effect on their morphology.

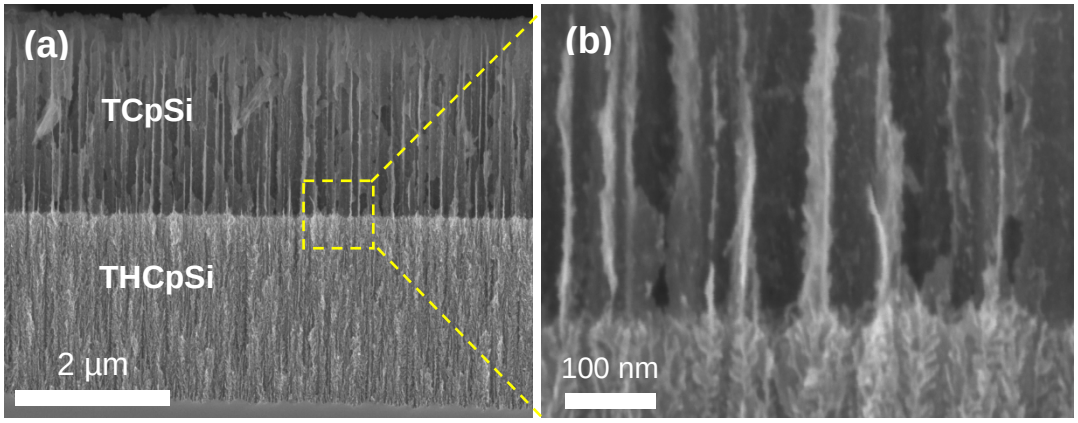

Figure 5.2 Cross-sectional SEM images of TCpSi-THCpSi double layer at (a) low magnification and (b) high magnification.

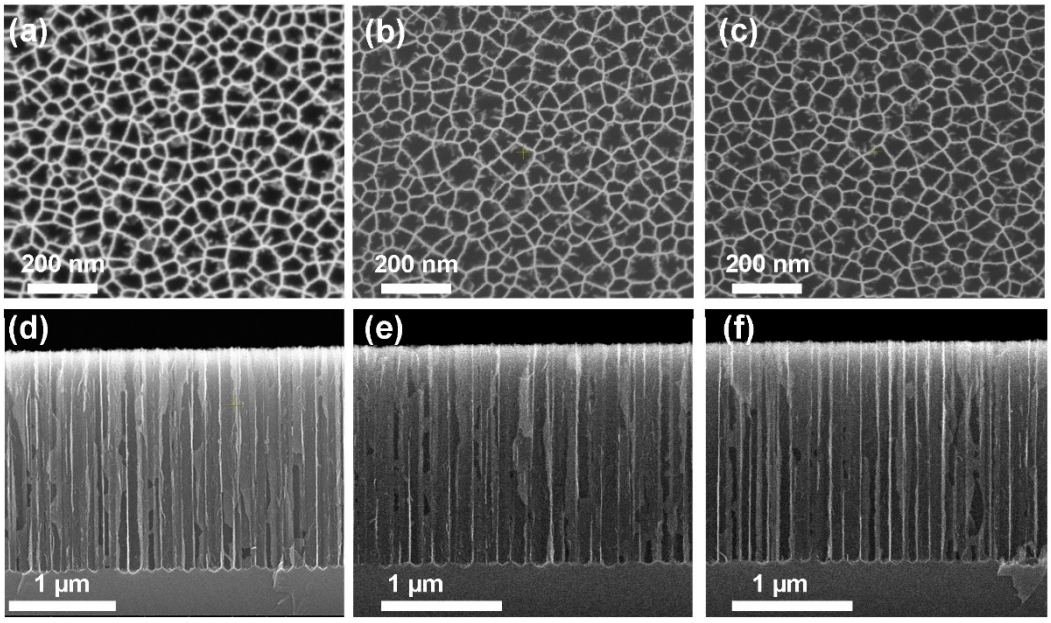

Figure 5.3 SEM images of pSi single layer structures fabricated using a wet bench with a current density of 65 mA cm^{-2} in 1:1 (v:v) HF/ethanol solution during 90 s: Top view of (a) pSi, (b) THCpSi and (c) TCpSi structures; and corresponding cross-sectional view of (d) pSi, (e) THCpSi and (f) TCpSi structures.

The effect of carbon-stabilization process on the morphological features of pSi is further proved by the reflectance spectra of pSi single layer, TCpSi single layer, and TCpSi-THCpSi double layer (**Figure 5.4**). TCpSi single layer almost retains the same Fabry-Pérot fringe pattern as pSi, although with a lower intensity, while the TCpSi-THCpSi double layer shows an interference pattern that combines Fabry-Pérot interferences from both the top and bottom interfaces of each porous layer. The fringe maxima still follows the Fabry-Pérot relationship[16]:

$$m\lambda = 2nL \qquad (5.1)$$

where m is an integer, λ is the wavelength of incident light, n is the average refractive index of the porous matrix (including the contents of the pores), and L is the physical thickness of the pSi layer. The light reflected from the double layer structure comprises three superimposed interference patterns. The analysis of the reflectance spectra can be simplified by transforming

reflectance oscillations into three peaks via FFT. The value of *2nL* of each porous layer can be directly interpreted as the position of the FFT peaks (**Figure 5.5**). The double layer film in air produces peak 1 at 6580 nm, peak 2 at 17072 nm, and peak 3 at 23652 nm, corresponding to the values of *2nL* for top layer 1, bottom layer 2 and double layer 3, respectively. The effective optical thickness (EOT), equivalent to *2nL*, can be used to measure changes in refractive index, thus providing a simple and effective approach to monitor changes in complicated optical structures.[15]

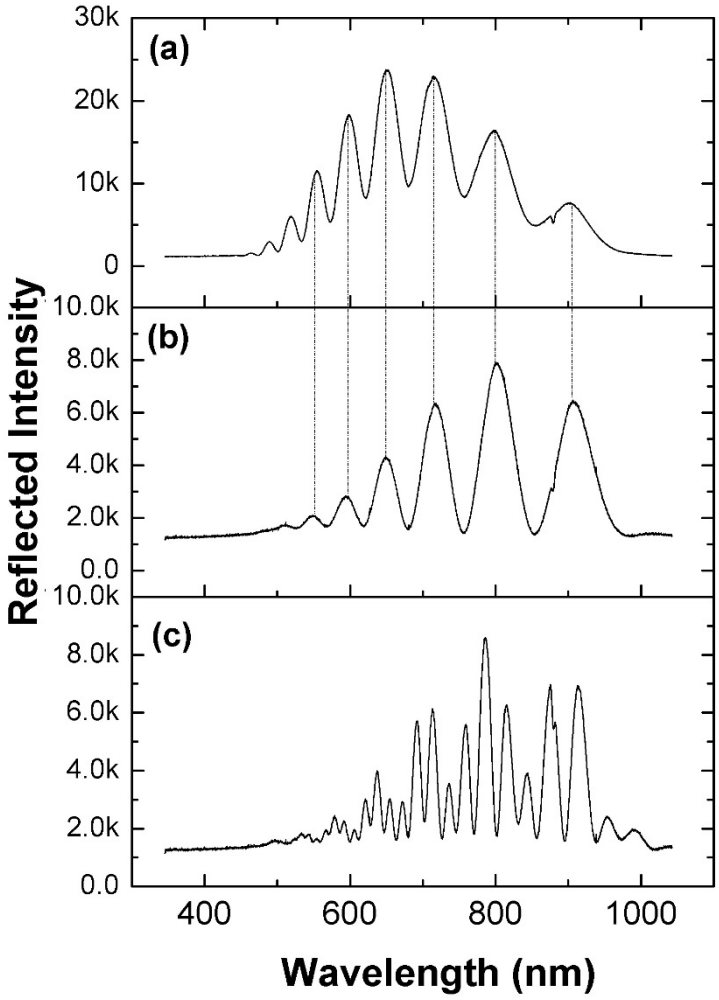

Figure 5.4 Reflectance spectra of (a) pSi single layer, (b) TCpSi single layer, and (c) TCpSi-THCpSi double layer. The top pSi layer was fabricated using the small etching cell with a current density of 50 mA cm^{-2} in 1:1 (v:v) HF/ethanol solution for 300 s, then the TCpSi top layer was subjected to the second etch using the small etching cell with a current density of 67 mA cm^{-2} in 3:1 (v:v) HF/ethanol solution for 120 s. The thicknesses of the TCpSi top layer and THCpSi bottom layer are 7.3 and 2.8 μm, respectively.

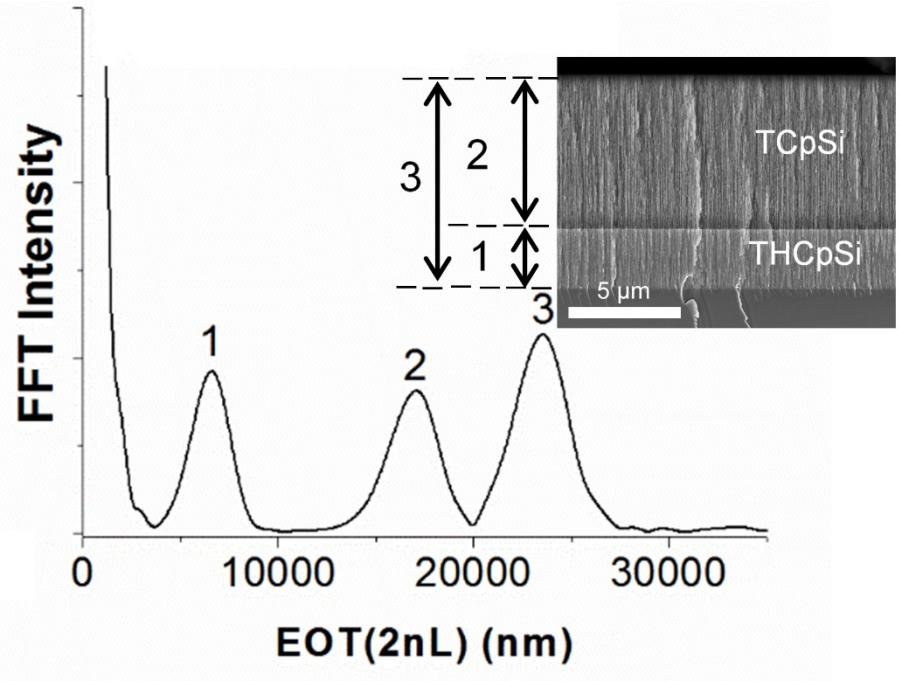

Figure 5.5 Corresponding Fourier transform of the reflectance spectrum shown in **Figure 5.4**.

5.3.3 ATR-FTIR characterization of TCpSi-THCpSi double layer

Surface chemistry was firstly characterized by attenuated total reflectance Fourier transform infrared (ATR-FTIR) spectroscopy. Freshly etched pSi displays bands characteristic of Si-H and Si-H_2 stretching vibrations at 2087 and 2114 cm^{-1}, respectively, and a band associated to Si-H deformation mode at 905 cm^{-1} (**Figure 5.6a**). Compared to freshly etched pSi, TCpSi (**Figure 5.7**) does not show the featured bands of Si-H, but displays new bands associated to carbon layers: the stretching vibrations of saturated C-H at 2920 and 3047 cm^{-1}, the unsaturated carbon double bond stretching at 1600 cm^{-1}, and the CH_3 symmetric deformation mode of Si-CH_3 at 1250-1260 cm^{-1}. **Figure 5.6b** displays the ATR-FTIR spectrum of TCpSi-pSi double layer, which was derived from an initial TCpSi single layer subjected to a second electrochemical anodization process that produced a freshly etched pSi bottom layer. After a

second electrochemical etching step in 3:1 HF/ethanol, a new peak associated to Si-H_x at around 2100 cm^{-1} was present in the TCpSi-pSi double layer. All the featured peaks of TCpSi (e.g. C-H, C=C) are still present in the TCpSi-pSi double layer suggesting that carbon stabilization resists HF. In the case of the TCpSi-THCpSi double layer, the peak associated to Si-H disappeared, while the featured peaks associated to carbon layers such as C-H, carbon double bond and CH_3, are displayed (**Figure 5.6c**).

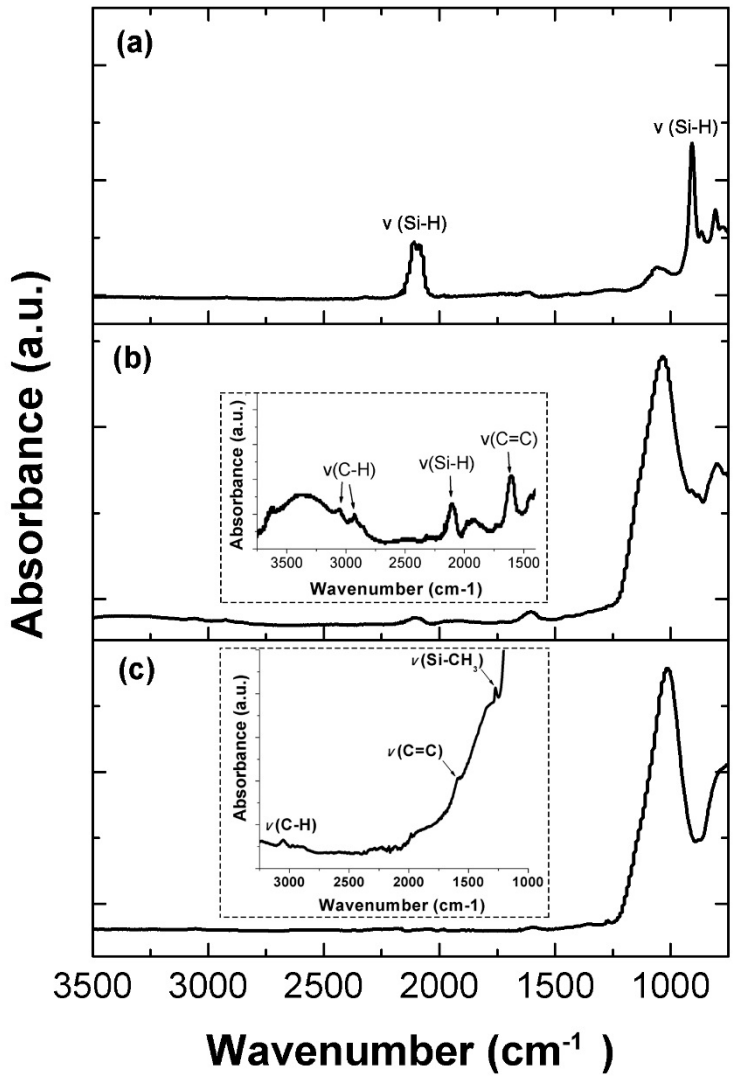

Figure 5.6 ATR-FTIR spectra of (a) freshly etched pSi single layer, (b) TCpSi top layer and freshly etched pSi bottom layer, and (c) TCpSi-THCpSi double layer.

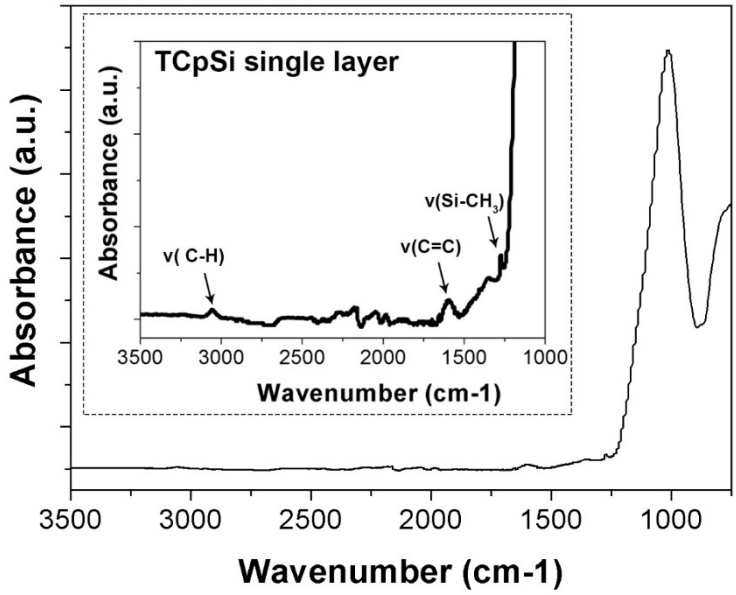

Figure 5.7 ATR-FTIR spectra of TCpSi single layer.

5.3.4 Raman characterization of TCpSi-THCpSi double layer

Raman spectroscopy was used to characterize the carbon layers introduced on the pSi surface (**Figure 5.8)**. Both TCpSi single layer (**Figure 5.8b**) and TCpSi-THCpSi double layer (**Figure 5.8c**) present the silicon lattice mode at 515 cm^{-1} demonstrating that the crystallinity of silicon was preserved after carbon-stabilization.[66] Unlike freshly etched pSi (**Figure 5.8a**), TCpSi single layer presents two peaks at 1350 (D band) and 1580 cm^{-1} (G band), which represent Raman signatures of carbon materials.[67] The D band is due to the breathing mode of sp^2 atoms in rings, and requires a defect for its activation, so it is strongly linked to defects in the structure. The first-order D band is not usually present in pristine graphene due to its crystal symmetries. Hence, the presence of the D band in Raman spectra for both TCpSi single layer and TCpSi-THCpSi double layer suggests the presence of a disordered carbon layer with defects.[68] On the other hand, the G band, a primary in-plane vibrational mode of sp^2 atoms in hydrocarbon chains and rings, is indicative of high crystallinity of the carbon layer.[69] The peak intensity ratio of D and G bands (I_D/I_G) can be used to evaluate the disorder level of the thin carbon coating on the

pSi surface. When calculating I_D/I_G using intensity values obtained by a Lorentzian fitting of the Raman spectra after baseline subtraction (**Figure 5.8**), the lower I_D/I_G value for the TCpSi-THCpSi double layer (0.83) than that for the TCpSi single layer (0.95) suggests the presence of less defects within the carbon coating of the double layer nanostructure.

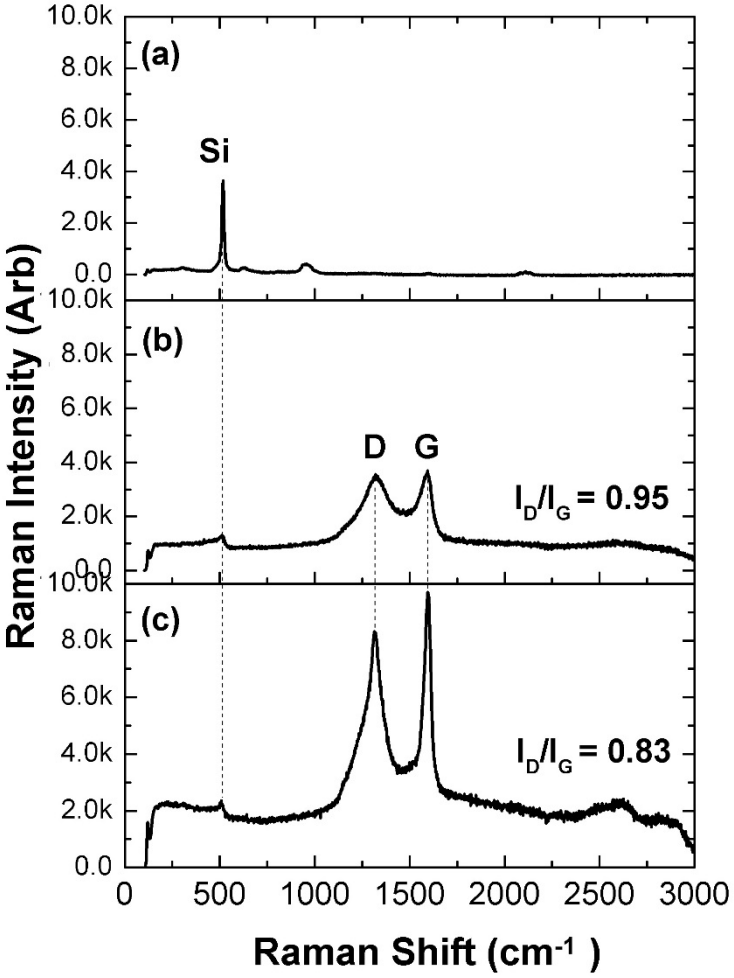

Figure 5.8 Raman spectra of (a) freshly etched pSi single layer, (b) TCpSi single layer and (c) TCpSi-THCpSi double layer.

The carbon coating was shown to provide resistance to HF, enabling the fabrication of multilayered nanostructures. Both THCpSi and TCpSi single layers were subjected to a second electrochemical etching step in 3:1 HF/ethanol etchant, providing THCpSi-pSi and TCpSi-pSi double layers with freshly etched pSi bottom layer. Their Raman spectra **(Figure 5.9a-b)** and

those of both THCpSi and TCpSi single layers (**Figure 5.9d-e**) were collected. The intensities of the D and G bands increase for both THCpSi-pSi and TCpSi-pSi after the second etching step. This change could be caused by the removal of any SiO_2 formed on the TCpSi surface, as well as the disordered carbon layer attached to this oxide layer.[45]

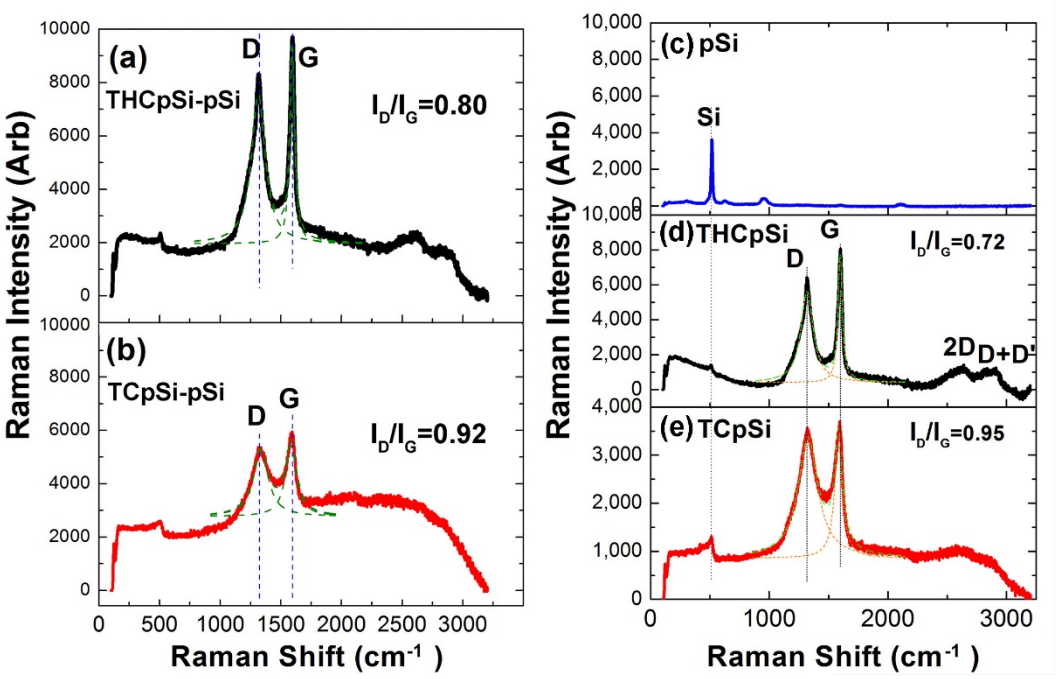

Figure 5.9 Raman spectra of (a) THCpSi-pSi and (b) TCpSi-pSi double layers, and (c) freshly etched pSi, (d) THCpSi and (e) TCpSi single layers. The peaks at ~1350 and ~1580 cm^{-1} are attributed to the D and G bands of carbon. The intensity ratio of the D and G bands (I_D/I_G) was calculated by a Lorentzian fitting of the data.

5.3.5 Layering surface functionalities on TCpSi-THCpSi double layer nanostructures

The versatile surface chemistry of carbon-stabilized pSi was exploited to tailor different bio-interfaces by layering first site-specific functional groups. Selective silanization and hydrosilylation of the TCpSi and THCpSi surfaces, respectively, within the double layer nanostructure, were confirmed by confocal microscopy imaging (**Figure 5.10**). A thick TCpSi-THCpSi double layer with the structure depicted in **Figure 5.10a** was prepared, where each layer was further modified by covalent immobilization of a fluorescent dye. The TCpSi top layer and THCpSi bottom layer were approximately 2.4 and 5.3 µm thick, respectively, as shown by the SEM image in **Figure 5.11**.

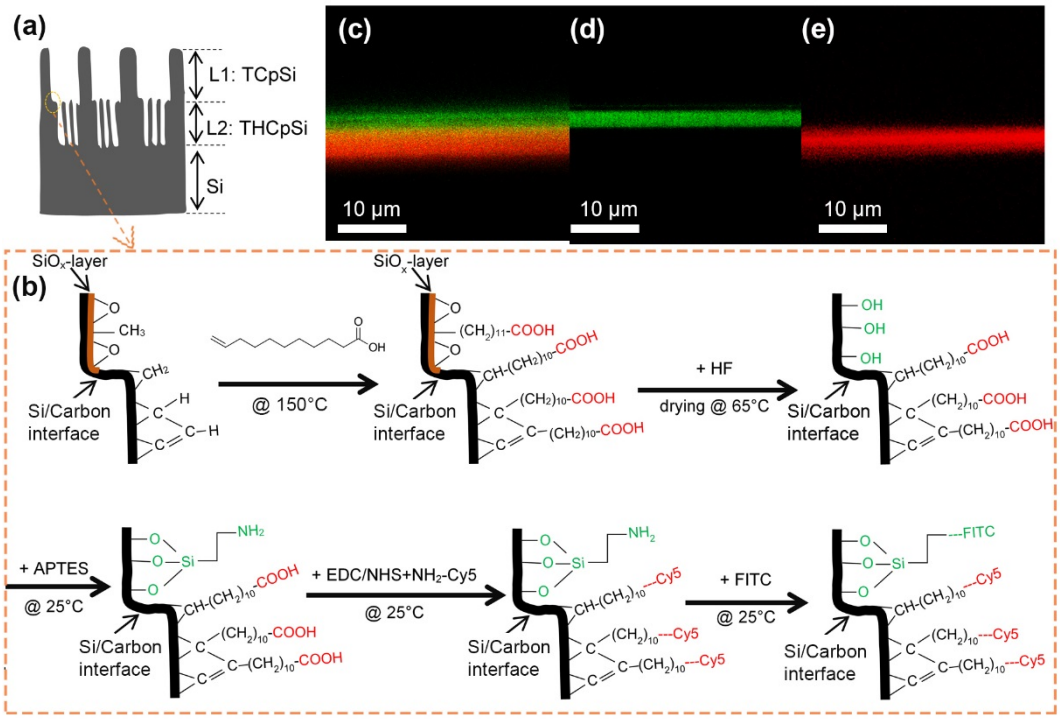

Figure 5.10 Laser scanning confocal microscopy characterization of the layered functionalities, within the TCpSi-THCpSi double-layer nanostructures, to enable selective fluorescence labeling. (a) Schematic of the TCpSi-THCpSi double layer: TCpSi top layer (L1), and THCpSi bottom layer (L2); (b) Fluorescence labeling process of the TCpSi-THCpSi double layer; (c) Confocal microscopy image of FITC labeled L1 (green) and Cy5 labeled L2 (red); (d) Confocal microscopy image of control sample with only FITC labeled L1; (e) Confocal microscopy image of control sample with only Cy5 labeled L2.

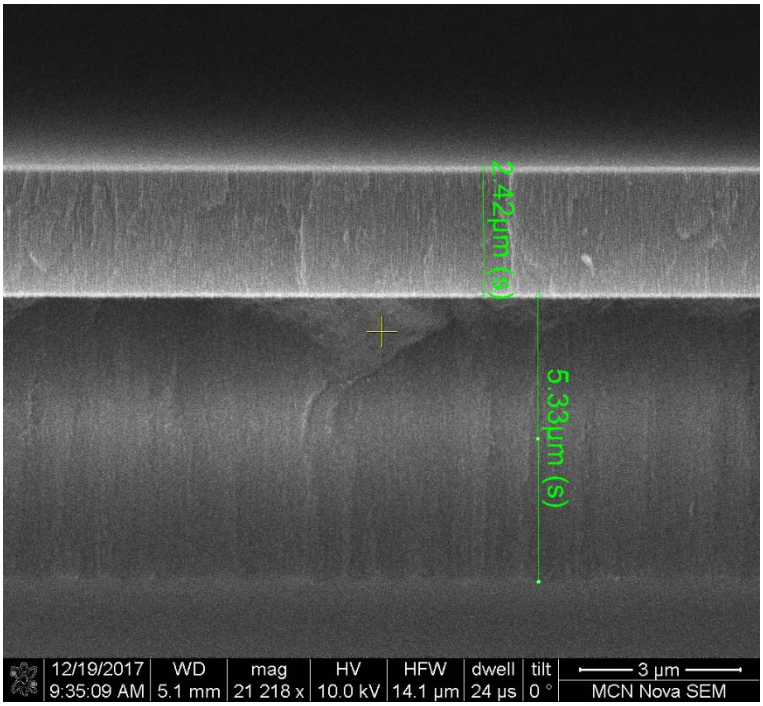

Figure 5.11 Cross-sectional SEM image of the pSi double layer sample used for confocal microscopy characterization after selective dye labeling. The thicknesses of the top and bottom porous layers are approximately 2.4 and 5.3 µm, respectively. The pSi top layer was electrochemically etched in a 1:1 (v:v) HF/ethanol solution, by applying a current density of 12.1 mA cm^{-2} for 360 s in a MPSB wet etching system, while the pSi bottom layer was etched using a small cell in 3:1 (v:v) HF/ethanol with a current density of 83.3 mA cm^{-2} applied for180 s.

The site-specific dye labeling process of the TCpSi-THCpSi double layer is described in **Figure 5.10b**. First, the hydrogen-terminated THCpSi bottom layer was functionalized with COOH groups via hydrosilylation with undecylenic acid.[56] Second, prior to proceed with silanization of the TCpSi top layer, the TCpSi-THCpSi double layer is treated with HF and dried at 65°C. While the COOH-terminated THCpSi bottom layer has the ability to resist HF, HF etching of the TCpSi top layer introduces stable OH groups.[46] The TCpSi surface was natively covered with a thin oxide layer, and thus hydroxylation occurs on SiC upon exposure to HF due to the inability to totally remove the surface oxides, especially the silicon oxide layer that was back-bonded to the carbon atoms.[45] Third, the hydroxylated TCpSi top layer was functionalized with APTES. Next, the COOH-terminated THCpSi bottom layer is modified

with NH_2-terminated Cy5 via carbodiimide coupling. Finally, the NH_2-terminated TCpSi top layer is modified with FITC.

5.3.6 Electrochemical performance of TCpSi-THCpSi double layer

The electrochemical properties of the TCpSi-THCpSi double layer nanostructure were investigated via CV in the presence of $[Fe(CN)_6]^{3-/4-}$ (**Figure 5.12)**. The $[Fe(CN)_6]^{3-/4-}$ redox system, extensively used in the electrochemical characterization of sp^2 carbon materials (e.g. graphite and glassy carbon), was chosen because it behaves as a quasi-reversible redox system on carbon electrodes.[70] The TCpSi-THCpSi double layer structure shows good performance as electrochemical transducer to evaluate redox events in the range from -0.2 to 0.6 V vs Ag/AgCl, as shown by the high oxidation and reduction peak currents and small peak-to-peak potential difference ($\Delta Ep = |E_{ox} - E_{red}|$) obtained in a 2 mM $[Fe(CN)_6]^{3-/4-}$ solution (**Figure 5.12a**). The ΔEp value of 108 mV is close to the expected theoretical value of 59 mV at 25 °C for a reversible one-electron transfer reaction, representing a quasi-reversible electron-transfer system.[71-72] This is further supported by the ratio of peak current ($|Ip(Ox)|/|Ip(Re)|=1.03$, **Table 5.1**), indicating that the stabilized TCpSi-THCpSi double layer nanostructure possesses the required surface and electronic properties to allow rapid electron transfer. The stability was also studied by recording the Ip(Ox) and Ip(Re) values over time, showing a stable response with a relative standard deviation of 5.0% (**Figure 5.12b**). Moreover, Ip(Ox) and Ip(Re) increase linearly with the square root of scan rate $\nu^{1/2}$ (**Figure 5.12c-d**), showing that the reaction is controlled by the semi-infinite linear diffusion.[73]

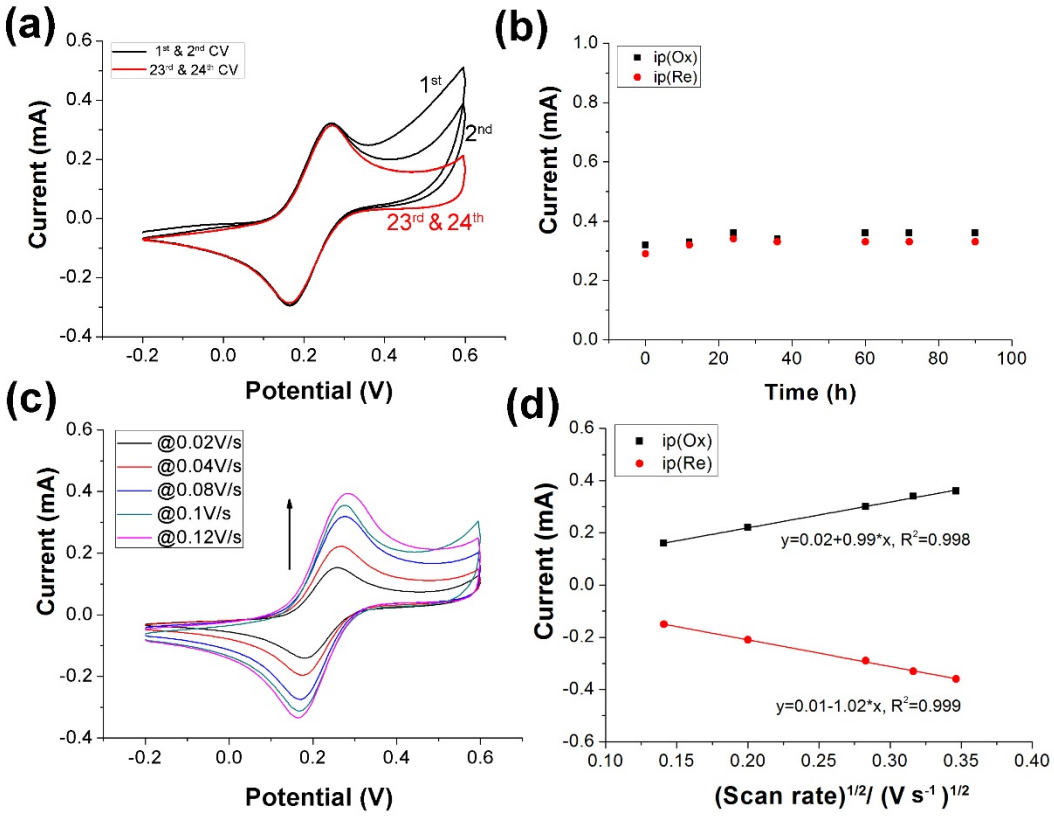

Figure 5.12 Electrochemical characterization of the TCpSi-THCpSi double layer nanostructure in a 2 mM $[Fe(CN)_6]^{3-/4-}$ solution. (a) Cyclic voltammograms (1st, 2nd, 23rd and 24th) obtained by sweeping the potential from -0.2 to 0.6 V vs Ag/AgCl at a scan rate of 0.1 V s^{-1}; (b) Oxidation (ip(Ox)) and reduction (ip(Re)) current intensity values vs time from cyclic voltammograms obtained under the same conditions as (a); (c) Cyclic voltammograms obtained by sweeping the potential from -0.2 to 0.6 V vs Ag/AgCl at scan rates ranging from 0.02 to 0.12 V s^{-1}; (d) Plot of ip(Ox) and ip(Re) extracted from the cyclic voltammograms in (c) vs $v^{1/2}$.

Table 5.1 Summary of peak current (Ip(Ox) and Ip(Re)) extracted from the cyclic voltammograms obtained using TCpSi-THCpSi double layer structures in a 2 mM $[Fe(CN)_6]^{3-/4-}$ solution, by sweeping the potential from -0.2 to 0.6 V vs Ag/AgCl at various scan rates.

Scan rate (V s^{-1})	Ip(Ox) (mA)	Ip(Re) (mA)	Ip(Ox)/Ip(Re)
0.02	0.16	0.15	1.07
0.04	0.22	0.21	1.05
0.08	0.30	0.29	1.03
0.10	0.34	0.33	1.03
0.12	0.36	0.36	1

5.3.7 DNA detection using TCpSi-THCpSi double layer-based voltammetric sensor

To demonstrate the suitability to use TCpSi-THCpSi double layer structures as electrochemical biosensing platforms, a label-free voltammetric DNA sensor was developed. The TCpSi top layer with large pores (27 ± 9 nm diameter) was selectively functionalized with a ssDNA probe while the THCpSi bottom layer with small pores (6 ± 3 nm diameter) acted as electrochemical transducer to convert the hybridization event confined in the top layer into an output current signal via DPV measurements. The sensing mechanism based on nanochannel blockage for label-free detection of ssDNA is shown in **Figure 5.13**.

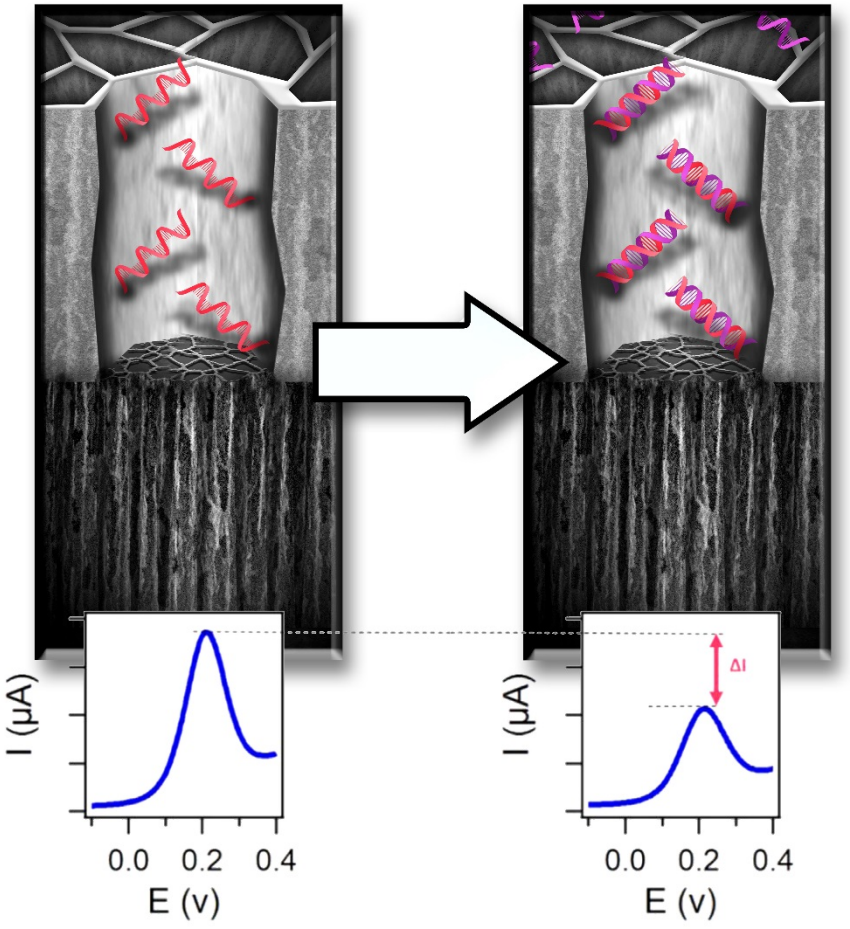

Figure 5.13 Schematic of the sensing mechanism of the designed voltammetric DNA sensor using a TCpSi-THCpSi double layer nanostructure.

When the target ssDNA hybridizes the ssDNA probe immobilized at the TCpSi top layer, partial blockage of the top layer nanochannels was induced. This partial nanochannel blockage hinders the diffusion of redox species such as $[Fe(CN)_6]^{3-/4-}$ towards the transducer surface, resulting in a decrease in the intensity of peak current monitored by DPV. Peak current changes obtained from differential pulse voltammograms acquired prior and after hybridization were normalized as follows:

$$\Delta i = (i° - i)/i° \qquad (5.2)$$

where t is the normalized current change, $i°$ is the peak current value after 15 min-incubation in buffer solution, and i is the peak current value after 15 min-incubation in ssDNA target solutions at different concentrations, both $i°$ and i extracted from the differential pulse voltammograms obtained in a 2 mM $[Fe(CN)_6]^{3-/4-}$ solution. A control sensor was also prepared using a random sequence of ssDNA as probe.

The normalized Δi is plotted as the function of Log [ssDNA] to determine the analytical performance of the DNA sensor (**Figure 5.14**). The Δi indeed exhibits a linear relationship over the target ssDNA concentration range from 1 to 1000 pM for the three tested structures. Control sensors (hollow symbols) show nearly no electrochemical response compared to the corresponding specific DNA sensors (solid symbols). As shown in **Figure 5.14**, the transducer thickness (i.e. THCpSi bottom layer) has an effect on the sensitivity of the designed DNA sensor. The structure with the thinnest THCpSi bottom layer tested (0.8 µm) shows the highest sensitivity.

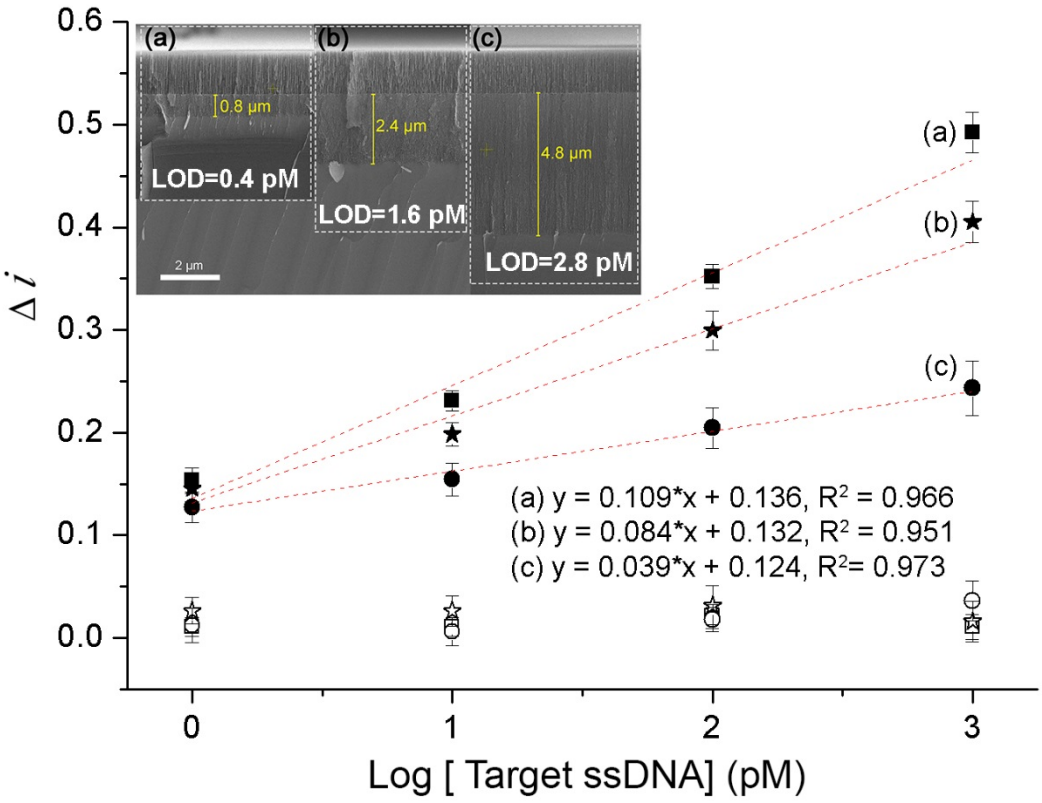

Figure 5.14 Dose response curves for the detection of a 28 base ssDNA in tris buffer using TCpSi-THCpSi double layer-based sensors prepared with either specific ssDNA probes (solid symbols) or non-specific ssDNA probes as controls (hollow symbols). Data are shown as mean of normalized current intensity ± standard deviation, n= 3. DPV measurements were performed in a 2 mM $[Fe(CN)_6]^{3-/4-}$ solution in 10 mM PBS, pH 7.4. Inset: Cross-sectional SEM images of the double layer; TCpSi top layer with an average pore size of 27 ± 9 nm, and 1.6 µm in depth; THCpSi bottom transducer layer with an average pore size of 6 ± 3 nm, and various depths (a) 0.8 µm, (b) 2.4 µm and (c) 4.8 µm.

The LOD is defined as the concentration corresponding to a signal equal to the average value of Δi plus three times of SD in blank buffer. A LOD was calculated using the equation y_b + 3*SD, where y_b is the value for the blank (normalized Δi in buffer) and SD is the associated standard deviation (n = 3). The LOD are 0.4, 1.6 and 2.8 pM for the TCpSi-THCpSi double layer nanostructured DNA sensors featuring 0.8, 2.4 and 4.8 µm transducer thickness, respectively. The developed pSi double layer-based DNA sensor demonstrates the sensitive detection of a 28 nucleotide DNA sequence, with a LOD as low as 0.4 pM, showing two orders of magnitude enhancement compared to the best LOD (50 pM)[74] achieved for a previously

reported pSi-based electrochemical DNA sensor that exploits pSi's semiconductor characteristics. The DNA sensor reported by Lugo et al. used oxidized pSi as the immobilization platform of a DNA capture probe complementary to the target DNA.[74] Taking advantage of pSi capability to modulate its electrical conductivity, DNA hybridization was monitored via the oxidation of guanine using ruthenium bipyridine $[Ru(bpy)_3]^{2+}$ as redox indicator.

5.4. Conclusion

In summary, this work demonstrates for the first time the design and fabrication of a carbon-stabilized pSi double layer nanostructure featuring fine-tuned hydrophilicity and layer-specific functionalization to facilitate further fit-for-purpose modification. Along with retaining the unique physical features derived from pSi, the carbon-stabilized TCpSi-THCpSi double layer nanostructures possess controllable surface functionalities and fast electron transfer kinetics suitable to harness them as both biointerface and electrochemical transducer. Their use to design novel highly performing biosensors is demonstrated by the developed TCpSi-THCpSi double layer-based voltammetric DNA sensor, showing a LOD of 0.4 pM in buffer, two orders of magnitude lower than the best performing previously reported pSi-based electrochemical DNA sensors. The user-definable controllability in nanostructural morphology and surface chemistry of this unique combination of carbon and pSi allows new applications of the pSi nanostructures as, but not limited to, sensing platforms.

5.5 References

1. Arshavsky-Graham, S.; Massad-Ivanir, N.; Segal, E.; Weiss, S., Porous Silicon-Based Photonic Biosensors: Current Status and Emerging Applications. *Anal. Chem.* **2019,** *91* (1), 441-467.

2. Mariani, S.; Robbiano, V.; Strambini, L. M.; Debrassi, A.; Egri, G.; Dähne, L.; Barillaro, G., Layer-by-Layer Biofunctionalization of Nanostructured Porous Silicon for High-Sensitivity and High-Selectivity Label-Free Affinity Biosensing. *Nat. Commun.* **2018,** *9* (1), 5256.

3. Kang, J.; Kim, D.; Wang, J.; Han, Y.; Zuidema, J. M.; Hariri, A.; Park, J. H.; Jokerst, J. V.; Sailor, M. J., Enhanced Performance of a Molecular Photoacoustic Imaging Agent by Encapsulation in Mesoporous Silicon Nanoparticles. *Adv. Mater.* **2018**, 1800512.

4. Li, W.; Liu, Z.; Fontana, F.; Ding, Y.; Liu, D.; Hirvonen, J. T.; Santos, H. A., Tailoring Porous Silicon for Biomedical Applications: From drug Delivery to Cancer Immunotherapy. *Adv. Mater.* **2018**, 1703740.

5. Kang, J. Y.; Joo, J.; Kwon, E. J.; Skalak, M.; Hussain, S.; She, Z. G.; Ruoslahti, E.; Bhatia, S. N.; Sailor, M. J., Self-Sealing Porous Silicon-Calcium Silicate Core-Shell Nanoparticles for Targeted Sirna Delivery to the Injured Brain. *Adv. Mater.* **2016,** *28* (36), 7962-7969.

6. Guan, P.; Li, J.; Lu, T.; Guan, T.; Ma, Z.; Peng, Z.; Zhu, X.; Zhang, L., Facile and Scalable Approach to Fabricate Granadilla-Like Porous-Structured Silicon-Based Anode for Lithium Ion Batteries. *ACS Appl. Mater. Interfaces* **2018,** *10* (40), 34283-34290.

7. Stead, S. O.; Kireta, S.; McInnes, S. J. P.; Kette, F. D.; Sivanathan, K. N.; Kim, J.; Cueto-Diaz, E. J.; Cunin, F.; Durand, J.-O.; drogemuller, C. J.; Carroll, R. P.; Voelcker, N. H.; Coates, P. T., Murine and Non-Human Primate Dendritic Cell Targeting Nanoparticles for in Vivo Generation of Regulatory T-Cells. *ACS Nano* **2018,** *12* (7), 6637-6647.

8. Tzur-Balter, A.; Shatsberg, Z.; Beckerman, M.; Segal, E.; Artzi, N., Mechanism of Erosion of Nanostructured Porous Silicon drug Carriers in Neoplastic Tissues. *Nat. Commun.* **2015,** *6*, 6208.

9. Mann, A. P.; Scodeller, P.; Hussain, S.; Joo, J.; Kwon, E.; Braun, G. B.; Mölder, T.; She, Z.-G.; Kotamraju, V. R.; Ranscht, B.; Krajewski, S.; Teesalu, T.; Bhatia, S.; Sailor, M. J.; Ruoslahti, E., A Peptide for Targeted, Systemic Delivery of Imaging and Therapeutic Compounds into Acute Brain Injuries. *Nat. Commun.* **2016,** *7*, 11980.

10. Kim, B.; Pang, H.-B.; Kang, J.; Park, J.-H.; Ruoslahti, E.; Sailor, M. J., Immunogene Therapy with Fusogenic Nanoparticles Modulates Macrophage Response to Staphylococcus Aureus. *Nat. Commun.* **2018,** *9* (1), 1969.

11. Gu, L.; Hall, D. J.; Qin, Z.; Anglin, E.; Joo, J.; Mooney, D. J.; Howell, S. B.; Sailor, M. J., In Vivo Time-Gated Fluorescence Imaging with Biodegradable Luminescent Porous Silicon Nanoparticles. *Nat. Commun.* **2013,** *4*, 2326.

12. Anglin, E. J.; Cheng, L. Y.; Freeman, W. R.; Sailor, M. J., Porous Silicon in drug Delivery Devices and Materials. *Adv. drug Deliv. Rev.* **2008,** *60* (11), 1266-1277.

13. Jane, A.; dronov, R.; Hodges, A.; Voelcker, N. H., Porous Silicon Biosensors on the Advance. *Trends Biotechnol.* **2009,** *27* (4), 230-239.

14. Sailor, M. J., *Porous Silicon in Practice: Preparation, Characterization and Applications*. John Wiley & Sons: **2012**.

15. Orosco, M. M.; Pacholski, C.; Sailor, M. J., Real-Time Monitoring of Enzyme Activity in a Mesoporous Silicon Double Layer. *Nat. Nanotechnol.* **2009,** *4* (4), 255-258.

16. Pacholski, C.; Sartor, M.; Sailor, M. J.; Cunin, F.; Miskelly, G. M., Biosensing Using Porous Silicon Double-Layer Interferometers: Reflective Interferometric Fourier Transform Spectroscopy. *J. Am. Chem. Soc.* **2005,** *127* (33), 11636-11645.

17. Jenison, R.; Yang, S.; Haeberli, A.; Polisky, B., Interference-Based Detection of Nucleic Acid Targets on Optically Coated Silicon. *Nat. Biotechnol.* **2001,** *19*, 62.

18. Zuidema, J. M.; Kumeria, T.; Kim, D.; Kang, J.; Wang, J.; Hollett, G.; Zhang, X.; Roberts, D. S.; Chan, N.; Dowling, C., Oriented Nanofibrous Polymer Scaffolds Containing Protein-Loaded Porous Silicon Generated by Spray Nebulization. *Adv. Mater.* **2018,** *30* (12), 1706785.

19. Urmann, K.; Walter, J.-G.; Scheper, T.; Segal, E., Label-Free Optical Biosensors Based on Aptamer-Functionalized Porous Silicon Scaffolds. *Anal. Chem.* **2015,** *87* (3), 1999-2006.

20. Janshoff, A.; Dancil, K.-P. S.; Steinem, C.; Greiner, D. P.; Lin, V. S. Y.; Gurtner, C.; Motesharei, K.; Sailor, M. J.; Ghadiri, M. R., Macroporous P-Type Silicon Fabry−Perot Layers. Fabrication, Characterization, and Applications in Biosensing. *J. Am. Chem. Soc.* **1998,** *120* (46), 12108-12116.

21. Urmann, K.; Arshavsky-Graham, S.; Walter, J.-G.; Scheper, T.; Segal, E., Whole-Cell Detection of Live Lactobacillus Acidophilus on Aptamer-Decorated Porous Silicon Biosensors. *Analyst* **2016,** *141* (18), 5432-5440.

22. Vilensky, R.; Bercovici, M.; Segal, E., Oxidized Porous Silicon Nanostructures Enabling Electrokinetic Transport for Enhanced DNA Detection. *Adv. Func. Mater.* **2015,** *25* (43), 6725-6732.

23. Islam, M. A.; Sinelnikov, R.; Howlader, M. A.; Faramus, A.; Veinot, J. G. C., Mixed Surface Chemistry: An Approach to Highly Luminescent Biocompatible Amphiphilic Silicon Nanocrystals. *Chem. Mater.* **2018,** *30* (24), 8925-8931.

24. Buriak, J. M., Illuminating Silicon Surface Hydrosilylation: An Unexpected Plurality of Mechanisms. *Chem. Mater.* **2014,** *26* (1), 763-772.

25. Buriak, J. M.; Stewart, M. P.; Geders, T. W.; Allen, M. J.; Choi, H. C.; Smith, J.; Raftery, D.; Canham, L. T., Lewis Acid Mediated Hydrosilylation on Porous Silicon Surfaces. *J. Am. Chem. Soc.* **1999,** *121* (49), 11491-11502.

26. Stewart, M. P.; Buriak, J. M., Exciton-Mediated Hydrosilylation on Photoluminescent Nanocrystalline Silicon. *J. Am. Chem. Soc.* **2001,** *123* (32), 7821-7830.

27. Sweetman, M. J.; McInnes, S. J. P.; Vasani, R. B.; Guinan, T.; Blencowe, A.; Voelcker, N. H., Rapid, Metal-Free Hydrosilanisation Chemistry for Porous Silicon Surface Modification. *Chem. Commun.* **2015,** *51* (53), 10640-10643.

28. Langner, A.; Panarello, A.; Rivillon, S.; Vassylyev, O.; Khinast, J. G.; Chabal, Y. J., Controlled Silicon Surface Functionalization by Alkene Hydrosilylation. *J. Am. Chem. Soc.* **2005,** *127* (37), 12798-12799.

29. Escorihuela, J.; Zuilhof, H., Rapid Surface Functionalization of Hydrogen-Terminated Silicon by Alkyl Silanols. *J. Am. Chem. Soc.* **2017,** *139* (16), 5870-5876.

30. Zhukhovitskiy, A. V.; Mavros, M. G.; Queeney, K. T.; Wu, T.; Voorhis, T. V.; Johnson, J. A., Reactions of Persistent Carbenes with Hydrogen-Terminated Silicon Surfaces. *J. Am. Chem. Soc.* **2016,** *138* (27), 8639-8652.

31. Kim, D.; Zuidema, J. M.; Kang, J.; Pan, Y.; Wu, L.; Warther, D.; Arkles, B.; Sailor, M. J., Facile Surface Modification of Hydroxylated Silicon Nanostructures Using Heterocyclic Silanes. *J. Am. Chem. Soc.* **2016,** *138* (46), 15106-15109.

32. Krueger, N. A.; Holsteen, A. L.; Kang, S.-K.; Ocier, C. R.; Zhou, W.; Mensing, G.; Rogers, J. A.; Brongersma, M. L.; Braun, P. V., Porous Silicon Gradient Refractive Index Micro-Optics. *Nano. Lett.* **2016,** *16* (12), 7402-7407.

33. Delalat, B.; Sheppard, V. C.; Rasi Ghaemi, S.; Rao, S.; Prestidge, C. A.; McPhee, G.; Rogers, M.-L.; Donoghue, J. F.; Pillay, V.; Johns, T. G.; Kröger, N.; Voelcker, N. H., Targeted drug Delivery Using Genetically Engineered Diatom Biosilica. *Nat. Commun.* **2015,** *6*, 8791.

34. Cunin, F.; Schmedake, T. A.; Link, J. R.; Li, Y. Y.; Koh, J.; Bhatia, S. N.; Sailor, M. J., Biomolecular Screening with Encoded Porous-Silicon Photonic Crystals. *Nat. Mater.* **2002,** *1*, 39.

35. Orosco, M. M.; Pacholski, C.; Sailor, M. J., Real-Time Monitoring of Enzyme Activity in a Mesoporous Silicon Double Layer. *Nat. Nanotechnol.* **2009,** *4*, 255.

36. Rémond, E.; Martin, C.; Martinez, J.; Cavelier, F., Silicon-Containing Amino Acids: Synthetic Aspects, Conformational Studies, and Applications to Bioactive Peptides. *Chem. Rev.* **2016,** *116* (19), 11654-11684.

37. Dhanekar, S.; Jain, S., Porous Silicon Biosensor: Current Status. *Biosens. Bioelectron.* **2013,** *41*, 54-64.

38. Lin, V. S.-Y.; Motesharei, K.; Dancil, K.-P. S.; Sailor, M. J.; Ghadiri, M. R., A Porous Silicon-Based Optical Interferometric Biosensor. *Science* **1997,** *278* (5339), 840-843.

39. Pujari, S. P.; Scheres, L.; Marcelis, A. T.; Zuilhof, H., Covalent Surface Modification of Oxide Surfaces. *Angew. Chem. Int. Ed.* **2014,** *53* (25), 6322-6356.

40. Tsang, C. K.; Kelly, T. L.; Sailor, M. J.; Li, Y. Y., Highly Stable Porous Silicon–Carbon Composites as Label-Free Optical Biosensors. *ACS Nano* **2012,** *6* (12), 10546-10554.

41. Scheres, L.; Giesbers, M.; Zuilhof, H., Organic Monolayers onto Oxide-Free Silicon with Improved Surface Coverage: Alkynes Versus Alkenes. *Langmuir* **2010,** *26* (7), 4790-4795.

42. Sweetman, M. J.; Shearer, C. J.; Shapter, J. G.; Voelcker, N. H., Dual Silane Surface Functionalization for the Selective Attachment of Human Neuronal Cells to Porous Silicon. *Langmuir* **2011,** *27* (15), 9497-9503.

43. Salonen, J.; Bjorkqvist, M.; Laine, E.; Niinisto, L., Stabilization of Porous Silicon Surface by Thermal Decomposition of Acetylene. *Appl. Surf. Sci.* **2004,** *225* (1-4), 389-394.

44. Torres-Costa, V.; Salonen, J.; Jalkanen, T.; Lehto, V. P.; Martín-Palma, R.; Martínez-Duart, J., Carbonization of Porous Silicon Optical Gas Sensors for Enhanced Stability and Sensitivity. *Phys. Satatus Solidi A* **2009,** *206* (6), 1306-1308.

45. Dhar, S.; Seitz, O.; Halls, M. D.; Choi, S.; Chabal, Y. J.; Feldman, L. C., Chemical Properties of Oxidized Silicon Carbide Surfaces Upon Etching in Hydrofluoric Acid. *J. Am. Chem. Soc.* **2009,** *131* (46), 16808-16813.

46. Makila, E.; Bimbo, L. M.; Kaasalainen, M.; Herranz, B.; Airaksinen, A. J.; Heinonen, M.; Kukk, E.; Hirvonen, J.; Santos, H. A.; Salonen, J., Amine Modification of Thermally Carbonized Porous Silicon with Silane Coupling Chemistry. *Langmuir* **2012,** *28* (39), 14045-14054.

47. Sciacca, B.; Alvarez, S. D.; Geobaldo, F.; Sailor, M. J., Bioconjugate Functionalization of Thermally Carbonized Porous Silicon Using a Radical Coupling Reaction. *Dalton Trans.* **2010,** *39* (45), 10847-10853.

48. Bimbo, L. M.; Sarparanta, M.; Santos, H. A.; Airaksinen, A. J.; Mäkilä, E.; Laaksonen, T.; Peltonen, L.; Lehto, V.-P.; Hirvonen, J.; Salonen, J., Biocompatibility of Thermally Hydrocarbonized Porous Silicon Nanoparticles and Their Biodistribution in Rats. *ACS Nano* **2010,** *4* (6), 3023-3032.

49. Schwartz, M. P.; Yu, C.; Alvarez, S. D.; Migliori, B.; Godin, D.; Chao, L.; Sailor, M. J., Using an Oxidized Porous Silicon Interferometer for Determination of Relative Protein Binding Affinity through Non-Covalent Capture Probe Immobilization. *Appl. Catal. B* **2007,** *204* (5), 1444-1448.

50. Dancil, K.-P. S.; Greiner, D. P.; Sailor, M. J., A Porous Silicon Optical Biosensor: Detection of Reversible Binding of Igg to a Protein a-Modified Surface. *J. Am. Chem. Soc.* **1999,** *121* (34), 7925-7930.

51. Cunin, F.; Schmedake, T. A.; Link, J. R.; Li, Y. Y.; Koh, J.; Bhatia, S. N.; Sailor, M. J., Biomolecular Screening with Encoded Porous-Silicon Photonic Crystals. *Nat. Mater.* **2002,** *1* (1), 39.

52. Orosco, M. M.; Pacholski, C.; Miskelly, G. M.; Sailor, M. J., Protein-Coated Porous-Silicon Photonic Crystals for Amplified Optical Detection of Protease Activity. *Adv. Mater.* **2006,** *18* (11), 1393-1396.

53. Reta, N.; Saint, C. P.; Michelmore, A.; Prieto-Simón, B.; Voelcker, N. H., Nanostructured Electrochemical Biosensors for Label-Free Detection of Water-and Food-Borne Pathogens. *ACS Appl. Mater. Interfaces* **2018,** *10* (7), 6055-6072.

54. Chen, M. Y.; Klunk, M. D.; Diep, V. M.; Sailor, M. J., Electric-Field-Assisted Protein Transport, Capture, and Interferometric Sensing in Carbonized Porous Silicon Films. *Adv. Mater.* **2011,** *23* (39), 4537-4542.

55. Díaz, D. J., Electrochemistry of Porous Materials. *J. Am. Chem. Soc.* **2010,** *132* (12), 4501-4502.

56. Reta, N.; Michelmore, A.; Saint, C.; Prieto-Simón, B.; Voelcker, N. H., Porous Silicon Membrane-Modified Electrodes for Label-Free Voltammetric Detection of Ms2 Bacteriophage. *Biosens. Bioelectron.* **2016,** *80*, 47-53.

57. Thakur, M.; Isaacson, M.; Sinsabaugh, S. L.; Wong, M. S.; Biswal, S. L., Gold-Coated Porous Silicon Films as Anodes for Lithium Ion Batteries. *J. Power Sources* **2012,** *205*, 426-432.

58. Yu, Y.; Gu, L.; Zhu, C.; Tsukimoto, S.; van Aken, P. A.; Maier, J., Reversible Storage of Lithium in Silver-Coated Three-Dimensional Macroporous Silicon. *Adv. Mater.* **2010,** *22* (20), 2247-2250.

59. Zhang, H.; Zhu, Y.; Qu, L.; Wu, H.; Kong, H.; Yang, Z.; Chen, D.; Mäkilä, E.; Salonen, J.; Santos, H. A.; Hai, M.; Weitz, D. A., Gold Nanorods Conjugated Porous Silicon

Nanoparticles Encapsulated in Calcium Alginate Nano Hydrogels Using Microemulsion Templates. *Nano. Lett.* **2018,** *18* (2), 1448-1453.

60. Lin, L.; Ma, Y.; Xie, Q.; Wang, L.; Zhang, Q.; Peng, D.-L., Copper-Nanoparticle-Induced Porous Si/Cu Composite Films as an Anode for Lithium Ion Batteries. *ACS Nano* **2017,** *11* (7), 6893-6903.

61. Yao, Y.; Liu, N.; McDowell, M. T.; Pasta, M.; Cui, Y., Improving the Cycling Stability of Silicon Nanowire Anodes with Conducting Polymer Coatings. *Energy Environ. Sci.* **2012,** *5* (7), 7927-7930.

62. Sciacca, B.; Secret, E.; Pace, S.; Gonzalez, P.; Geobaldo, F.; Quignard, F.; Cunin, F., Chitosan-Functionalized Porous Silicon Optical Transducer for the Detection of Carboxylic Acid-Containing drugs in Water. *J. Mater. Chem.* **2011,** *21* (7), 2294-2302.

63. Kaukonen, A. M.; Laitinen, L.; Salonen, J.; Tuura, J.; Heikkila, T.; Limnell, T.; Hirvonen, J.; Lehto, V. P., Enhanced in Vitro Permeation of Furosemide Loaded into Thermally Carbonized Mesoporous Silicon (Tcpsi) Microparticles. *Eur. J. Pharm. Biopharm.* **2007,** *66* (3), 348-356.

64. Salonen, J.; Björkqvist, M.; Paski, J., Temperature-Dependent Electrical Conductivity in Thermally Carbonized Porous Silicon. *Sens. Actuators A Phys.* **2004,** *116* (3), 438-441.

65. Salonen, J.; Mäkilä, E., Thermally Carbonized Porous Silicon and Its Recent Applications. *Adv. Mater*. **2018**, 1703819.

66. Kim, D.; Joo, J.; Pan, Y.; Boarino, A.; Jun, Y. W.; Ahn, K. H.; Arkles, B.; Sailor, M. J., Thermally Induced Silane Dehydrocoupling on Silicon Nanostructures. *Angew. Chem. Int. Ed.* **2016,** *55* (22), 6423-6427.

67. Ferrari, A. C., Raman Spectroscopy of Graphene and Graphite: Disorder, Electron–Phonon Coupling, Doping and Nonadiabatic Effects. *Solid State Commun.* **2007,** *143* (1), 47-57.

68. Hawaldar, R.; Merino, P.; Correia, M.; Bdikin, I.; Grácio, J.; Méndez, J.; Martín-Gago, J.; Singh, M. K., Large-Area High-Throughput Synthesis of Monolayer Graphene Sheet by Hot Filament Thermal Chemical Vapor Deposition. *Sci. Rep.* **2012,** *2*, 682.

69. Ferrari, A. C.; Basko, D. M., Raman Spectroscopy as a Versatile Tool for Studying the Properties of Graphene. *Nat. Nanotechnol.* **2013,** *8* (4), 235-246.

70. Tang, L.; Wang, Y.; Li, Y.; Feng, H.; Lu, J.; Li, J., Preparation, Structure, and Electrochemical Properties of Reduced Graphene Sheet Films. *Adv. Func. Mater.* **2009,** *19* (17), 2782-2789.

71. Elgrishi, N.; Rountree, K. J.; McCarthy, B. D.; Rountree, E. S.; Eisenhart, T. T.; Dempsey, J. L., A Practical Beginner's Guide to Cyclic Voltammetry. *J. Chem. Educ.* **2017,** *95* (2), 197-206.

72. Streeter, I.; Wildgoose, G. G.; Shao, L.; Compton, R. G., Cyclic Voltammetry on Electrode Surfaces Covered with Porous Layers: An Analysis of Electron Transfer Kinetics at Single-Walled Carbon Nanotube Modified Electrodes. *Sens. Actuators B Chem.* **2008,** *133* (2), 462-466.

73. Chang, K.; Chen, W., L-Cysteine-Assisted Synthesis of Layered Mos2/Graphene Composites with Excellent Electrochemical Performances for Lithium Ion Batteries. *ACS Nano* **2011,** *5* (6), 4720-4728.

74. Lugo, J.; Ocampo, M.; Kirk, A.; Plant, D.; Fauchet, P., Electrochemical Sensing of DNA with Porous Silicon Layers. *J. New. Mat. Electr. Sys.* **2007,** *10* (2), 113.

Chapter 6. Uniform gold-porous silicon composite nanochannel arrays controllably engineered by metal-assisted chemical etching (MACE) and their electrochemical properties

6.1 Introduction

Nowadays the emerging fields of nanoscience and nanotechnology are inextricably linked to chemistry, physics, materials science, electrical engineering and bionanotechnology. There is no doubt that nanoscience and nanotechnology have catalyzed a wide range of strongly interdisciplinary research interests in science. Especially, composite nanostructures combining the advantages from different nanomaterials have recently received increasing attention.

Vertically aligned pSi nanochannel arrays are a promising platform for biological applications (e.g. biosensing, drug delivery) that provides extensive tailoring of its structural properties (nanochannel diameter and depth), high surface area, biocompatibility, and potential integration with silicon technology.[1-5] However, not only the traditional pSi fabrication via electrochemical anodization, but also the method based on backside illumination of n-type silicon, are limited to the formation of branched nanochannels with diameters that can only be controlled below 100 nm.[6] As a powerful alternative, template-based MACE is a simple and low-cost way for the controllable fabrication of uniform ordered pSi nanostructures with adjustable nanochannel size, depth and density, and without the limitation of doping type and level of Si.[7-9] The final morphology of pSi nanostructures is defined by the pattern of the metal catalyst because the silicon underneath is etched much faster by HF than the non-coated Si.[10] Instead of electrical bias, the reduction of the oxidant (e.g. H_2O_2) catalyzed by the noble metal surface is the power supply action.[7] The holes generated from the reduction are injected into the silicon surface, which is specifically oxidized and then dissolved at the Si-metal interface by HF. The template can be easily produced by means of colloidal lithography, using readily available polymeric nano- or micro-particles (e.g. polystyrene spheres (PS)). Accurate control

of the initial template is key to define the features of the resulting pSi nanostructures such as nanochannel diameter and density. In this sense, oxygen plasma etching by deep reactive-ion etching (DRIE) is shown as a powerful tool to control these parameters by easily reducing the size of the colloidal spheres in a smooth, isotropic way without changing their spherical shape. Furthermore, argon inductively coupled plasma (ICP) DRIE can easily etch the gold layer in a few seconds.

Metallic gold nanostructures either as nanoparticles, nanorods or nanofilms, have also attracted growing attention due to their chemical stability, tunable surface chemistry and other unique properties in photonics, electronics and catalysis.[11-13] Apart from being one of the most electronegative noble metals, gold is also a very good conductor of heat and electricity.[14] The natural affinity between gold and sulfur allows self-assembling of ordered monolayers of a wide range of organic molecules containing thiol groups. Additionally, gold films less than 50 nm in thickness have nanoscale properties not present in bulk gold.[15] For instance, such thin films are moderately transparent to visible light, yet reasonably reflective in the near infra-red. All these properties make gold nanostructures ideally suited for a versatile platform in bionanotechnology, including either flexible electrodes with high transparency and metallic conductivity or optical probes for detection of pathogens or proteins, DNA analyses and targeted drug delivery.[15-18]

The only example of Au-pSi composite nanochannel arrays was reported by Brodoceanu and coworkers.[6] The method to etch the gold reported before relied on sputter etching, where the sample mounted onto a copper holder by means of carbon tape acted as the target. Therefore, the first limitation of the previously reported work is that the useful area of sample is only 5 mm in width due to the magnetic field of the magnetron sputtering system. Another limitation is related to the gradient of diameters of the gold disc arrays obtained after sputter etching. The

last limitation comes from the unavoidable contamination caused by the metallic holder used for sputter etching and the carbon tape used to fix the sample. Here, large areas (around 5 cm × 5 cm) of homogeneous and uniform Au-pSi composite nanochannel arrays, free from any contaminant that might be introduced during the fabrication process, were developed for the first time using MACE combined with colloidal lithography and controlled DRIE. This simple and low-cost fabrication process provides the ability to tune the dimensions and density of ordered Au-pSi composite nanochannel arrays. Straight and highly uniform silicon channel arrays, ranging from 100 nm to several μm in diameter, with flat gold discs at the bottom were produced. The diameter, depth and density of nanochannels were well controlled by selecting the proper template size and etching time. To improve the chemical stability, the nanochannel arrays were thermally hydrocarbonized, producing a thin carbon layer on their surface. Apart from passivating the surface against degradation, the carbon layer introduced via thermal hydrocarbonization of pSi (THCpSi) allowed further surface functionalisation to facilitate subsequent binding of specific recognition biomolecules (e.g. antibody).[19-22] The excellent control of the dimensions of the Au-THCpSi composite nanochannel arrays, and the high uniformity they feature, were exploited to use these platforms for electrochemical biosensing purposes.

6.2 Experimental section

Materials: P-type silicon wafers with different resistivity 0.01-0.02 Ω cm, 3-6 Ω cm and 10-20 Ω cm, n-type silicon wafers with 0.008-0.02 Ω cm resistivity (100)-oriented were purchased from Siltronix (France). Polystyrene spheres (PS) were purchased from Polysciences, Inc. Sulphuric acid (H_2SO_4) (98%, AR grade) and hydrogen peroxide (H_2O_2) (30%, AR grade) were purchased from J.T.Baker (Australia). Hydrofluoric acid (HF) (48%, AR grade) was purchased from Scharlau (Australia). Potassium ferrocyanide ($K_4[Fe(CN)_6]$), potassium ferricyanide ($K_3[Fe(CN)_6]$), undecylenic acid, N-hydroxysuccinimide (NHS), N(3-dimethylaminopropyl)

N-ethylcarbodiimide hydrochloride (EDC), phosphate buffered saline (PBS) tablets and 2-(N-morpholino)-ethanesulfonic acid (MES) were purchased from Sigma-Aldrich (Australia). Monoclonal antibody (produced in mouse) against MS2 bacteriophage was purchased from Tetracore (USA).

Apparatus: The gold layer was sputtered using an AC/DC sputtering system (Intlvac Nanochrome) in direct current power supplies. The process of oxygen plasma treatment to reduce the PS size and the argon etching were performed with a Plasmalab100 ICP380. Scanning electron microscopy (SEM) images were obtained with a FEI NovaNano SEM 430 at an accelerating voltage of 10 kV. Fourier transform infrared spectroscopy (FTIR) was performed with a Bruker Hyperion 100 microscope (Bruker Optics, Germany) coupled to a liquid nitrogen cooled mercury–cadmium-tellurite detector, in reflectance mode. Electrochemical measurements were carried out on an electrochemical analyzer (CH Instruments, model 600D series, USA) using a three-electrode Teflon cell containing the silicon chip on an aluminum film as the working electrode, Ag/AgCl reference electrode and a platinum wire counter electrode.

Fabrication of Au-pSi composite arrays: Firstly, the silicon substrates were cleaned with Piranha solution, a 3:1 mixture of H_2SO_4 and H_2O_2 (v:v), for 15 min at room temperature, followed by washing with MilliQ water and drying with N_2 gas stream. Secondly, a 30 nm gold layer was sputtered onto the surface of silicon using an AC/DC sputtering system in direct current power supplies at DC 100 W for 80 s. Thirdly, a monolayer of PS with diameters of 0.5 µm, 1 µm and 2 µm, was convectively assembled onto the gold-coated silicon surface using a setup described by Velev.[23] In order to have a hydrophilic surface for the convective assembly of PS monolayer, the gold-coated silicon was pretreated by oxygen plasma for 30 s. The size of PS was reduced properly by oxygen plasma (RF 10 W, ICP RF 500 W, oxygen flow 100

sccm) for a certain time using DRIE. Fourthly, the sputter etching process was conducted using DRIE with argon plasma (RF 100 W, ICP RF 1000 W, argon flow 50 sccm) for 40 s. Finally, the partially etched PS were removed by sonication in water, and the substrate was exposed to an aqueous etchant solution containing 4.8 M HF, 0.1 M H_2O_2 for a certain period of time. The Au-pSi composite nanochannel arrays were rinsed with MilliQ water then dried with a N_2 gas stream and stored in a desiccator.

Thermal hydrocarbonization of the silicon surface (Au-THCpSi): The silicon surface of the freshly etched Au-pSi composite substrates was thermally hydrocarbonized to improve its stability and conductivity using an acetylene-based process previously described by Salonen et al.[24-25] Briefly, the freshly etched pSi was placed into a quartz tube under N_2 flow at 2 L min^{-1} for 45 min at room temperature to remove oxygen and adsorbed moisture. A 1:1 N_2-acetylene mixture flow was introduced into the tube at room temperature for 15 min after the purging step, then the quartz tube was placed into a preheated tube furnace at 525 °C for another 15 min under the continuous mixture flow. Finally, the tube was allowed to cool down back to room temperature under N_2 flow.

Gold surface activation: The Au-THCpSi composite arrays were fitted into an electrochemical cell as the working electrode, while a Pt wire and Ag/AgCl electrodes were used as counter and reference. The gold surface of the discs at the bottom of the nanochannels was electrochemically activated by cycling the potential from -0.2 to 1.6 V at a scan rate of 0.1V/s in 0.5 M H_2SO_4.

Covalent immobilization of antibody onto THCpSi surface: Firstly, COOH groups were introduced on the THCpSi surface by hydrosilylation with undecylenic acid. The substrates were immersed in pure undecylenic acid at 150 °C for 10 h under inert atmosphere (N_2). After cooling down to room temperature, the samples were rinsed with absolute ethanol and were

dried at 80 °C for 1 h. Secondly, the COOH groups were activated by incubating the functionalised substrates in 10 mg/mL EDC and 15 mg/mL NHS in 0.1 M MES buffer, pH 5.5, at room temperature for 30 min, to produce a succinimidyl ester group. Thirdly, immediately after carbodiimide activation, 25 µg/mL monoclonal antibody anti-MS2 in 10 mM PBS was added and incubated overnight at 4°C.

6.3 Results and discussion

6.3.1 Fabrication process of Au-pSi composite nanochannels by MACE

Figure 6.1 presents the schematic of the four key fabrication steps to generate Au-pSi composite nanochannel arrays using MACE combined with colloidal lithography and controlled reactive ion etching. Firstly, the PS monolayer was convectively assembled onto the surface of a Au-coated silicon substrate (**Figure 6.1a**) and the size of the PS was reduced by oxygen plasma. Secondly, the exposed gold layer around the beads was removed by using DRIE with argon plasma for a certain period of time (**Figure 6.1b**). Thirdly, these partially etched PS were easily removed by sonication in a water bath. Dense arrays of gold discs with smooth edges and high uniformity were left on the silicon substrate (**Figure 6.1c**). Finally, straight and highly uniform Au-pSi composite nanochannel arrays were generated by using an aqueous etchant solution containing HF and H_2O_2 (**Figure 6.1d**). Each step of the fabrication process was assessed by SEM. **Figure 6.1e-h** show the corresponding SEM images.

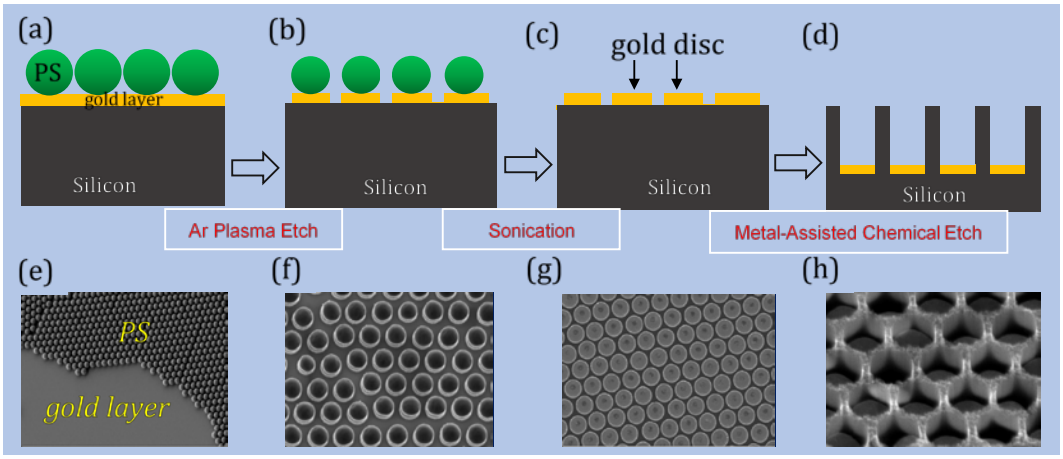

Figure 6.1 Schematic of the Au-pSi composite nanochannels fabrication process (a-d) and corresponding SEM images (e-h).

6.3.2 Control of the size of PS mask by O_2 plasma

Controlling the diameter of the gold discs is a key step in the fabrication process of Au-pSi composite nanochannel arrays, because it finally determines the diameter of the nanochannels. The application of oxygen plasma treatment during different periods of time, followed by a fixed gold etching process, was explored to reduce the size of PS in a smooth, isotropic way without changing their spherical shape. Three different sizes of PS were selected as the original mask: 0.5 µm, 1 µm and 2 µm, providing a range of nanochannel diameters summarized in **Table 6.1**. The diameter of the 0.5 µm PS was reduced to 410 nm, 380 nm, 200 nm and 120 nm after oxygen plasma treatment for 20 s, 28 s, 45 s and 55 s, respectively **(Figure 6.2)**. For an original mask prepared with 1 µm PS, the diameter of the PS was reduced to 800 nm and 350 nm after oxygen plasma treatment for 60 s and 195 s, respectively (**Figure 6.3**). Finally, 2 µm PS were reduced to 1.4 µm and 1.1 µm after 240 s and 360 s of oxygen plasma treatment, respectively (**Figure 6.4**).

Table 6.1 Final PS diameter depending on the time of oxygen plasma treatment followed by a fixed gold etching process.

Final Diameter (μm)	Original Mask (μm)	Oxygen Plasma Time (s)	Gold Etching (s)
0.41	0.5	20	40
0.38		28	
0.20		45	
0.12		55	
0.80	1.0	60	40
0.35		195	
1.40	2.0	240	40
1.10		360	

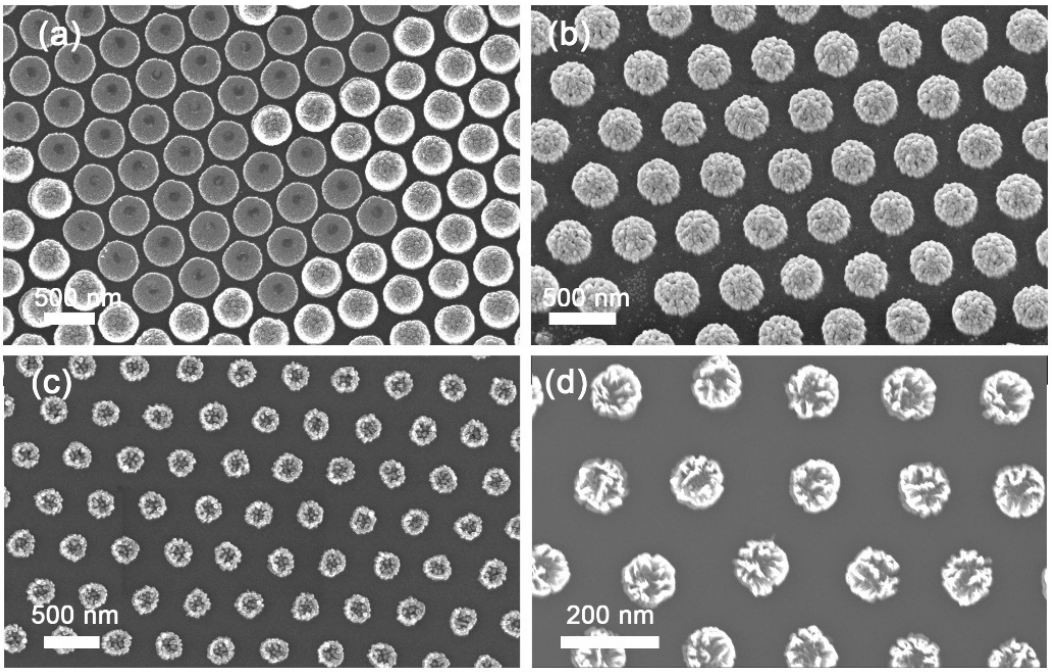

Figure 6.2 SEM images of oxygen plasma-treated 0.5 μm PS with subsequent gold etching process. PS diameter was reduced to (a) 410 nm, (b) 380 nm, (c) 200 nm and (d) 120 nm after oxygen plasma treatment for 20, 28, 45 and 55 s, respectively.

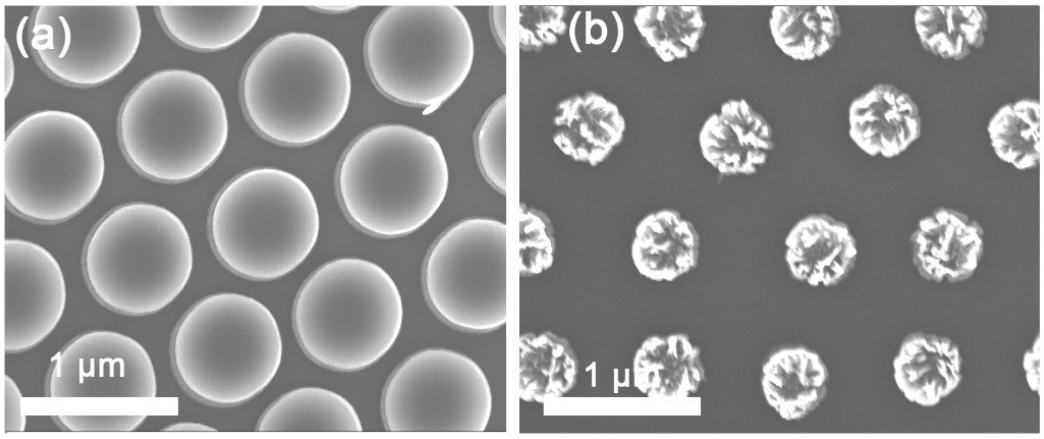

Figure 6.3 SEM images of oxygen plasma-treated 1 µm PS with subsequent gold etching process. PS diameter was reduced to (a) 800 nm and (b) 350 nm after oxygen plasma treatment for 60 and 195 s, respectively.

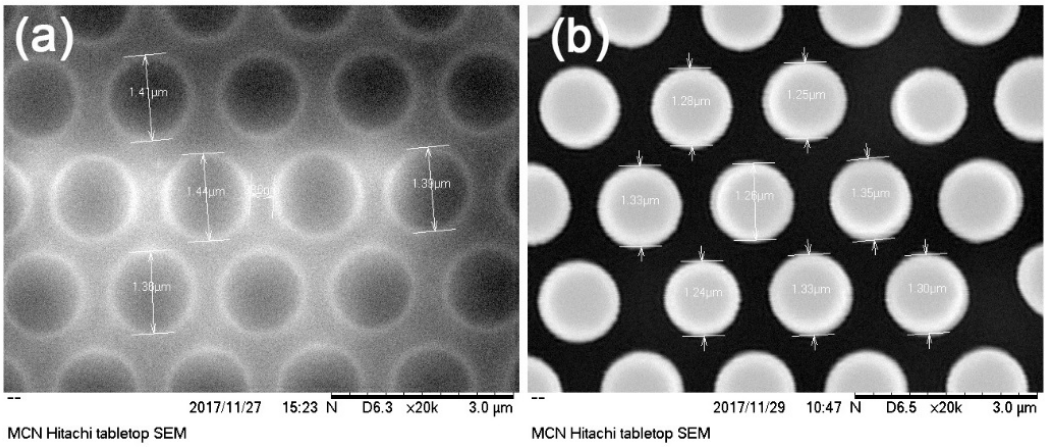

Figure 6.4 SEM images of oxygen plasma-treated 2 µm PS with subsequent gold etching process. PS diameter was reduced to (a) 1.4 µm and (b) 1.1 µm after oxygen plasma treatment for 240 and 360 s, respectively.

6.3.3 Argon plasma etching of exposed gold layer via DRIE

SEM was used to provide further details of the gold etching process. **Figure 6.5** presents each step of the fabrication process before wet etching using a 0.5 µm PS mask. The diameter of the

PS was reduced to approximately 410 nm by applying oxygen plasma treatment for 20 s (**Figure 6.5a**). The sputter etching process using argon plasma successfully removed the exposed gold around the PS mask as shown by the top and 45° titled SEM images in **Figure 6.5b-c**. These images clearly show the silicon substrate, gold discs and PS on top of the gold discs. The PS mask was removed by sonication in a water bath. Arrays of flat gold discs with smooth edges are depicted in the top view SEM image shown in **Figure 6.5d**.

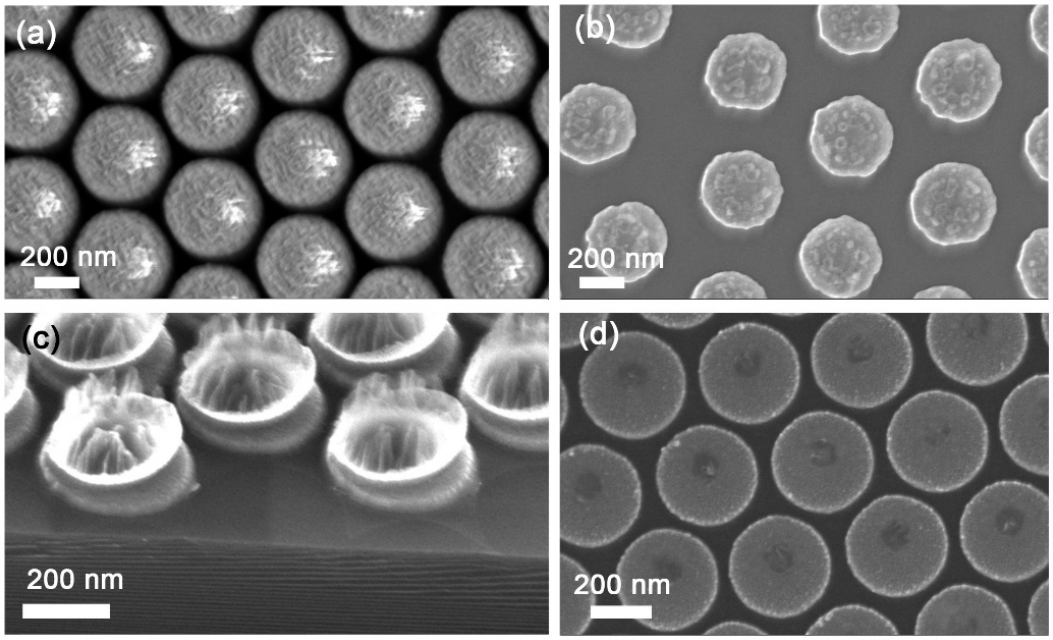

Figure 6.5 SEM images at each step of the fabrication process before wet etching using a 0.5 µm PS mask: (a) PS reduction after 20 s of oxygen plasma treatment; (b) top and (c) 45° titled view after the gold etching process; (d) array of flat gold discs on top of a silicon substrate.

6.3.4 Diameter, depth and density control of Au-pSi composite nanochannels

6.3.4.1 Diameter and depth control of Au-pSi composite nanochannels

On the one hand, by choosing a proper size of PS and shrinking them as required, both size and density of the Au-pSi composite nanochannels can easily be controlled. On the other hand, the depth of the Au-pSi nanochannels is controlled by the time of wet etching. **Figure 6.6a-c** show arrays of Au-pSi composite nanochannels with various diameters: 100 nm, 350 nm and 750 nm. The arrays with nanochannels of 100 nm and 350 nm in diameter were prepared by using the 0.5 µm PS mask. The nanochannels with a diameter of 750 nm were fabricated using the 1 µm PS mask. Prior to the argon inductively coupled plasma etching of the gold layer, oxygen plasma was applied for a certain period of time to reduce the size of the PS mask and thus achieve the desired nanochannel diameter as shown in **Table 6.1**. **Figure 6.6d-f** show the titled 45° SEM cross-sectional view of the Au-pSi composite nanochannels with a diameter of 350 nm but with different depths. The nanochannel depth can be easily controlled by the MACE processing time: 2 min, 6 min and 10 min produce nanochannels with a depth of 450 nm, 1.1 µm and 1.8 µm, respectively.

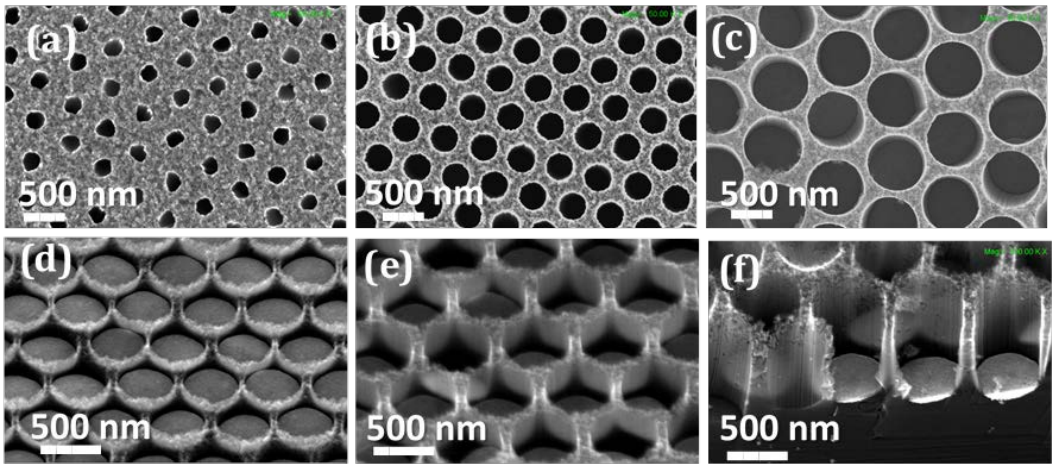

Figure 6.6 SEM images of Au-pSi composite nanochannel arrays: top view with various diameters (a) 100 nm, (b) 280 nm, (c) 750 nm; 45° titled view with various thicknesses (d) 450 nm, (e) 1.1 µm and (f) 1.8 µm.

6.3.4.2 Density control of Au-pSi composite nanochannels

Apart from the well-controlled diameter and depth, **Figure 6.7**. depicts the possibility to control the density of the Au-pSi composite nanochannels using 0.5 µm and 1 µm PS masks. Au-pSi composite nanochannels with similar diameter, around 350 nm, but with different nanochannel densities were characterised by SEM images of the top (**Figure 6.7a-b**) and 45° titled (**Figure 6.7c-d**) views. In order to fabricate arrays with a nanochannel diameter of 350 nm but with different nanochannel density, two PS sizes (0.5 µm and 1 µm) were used as the original mask. Prior to the etching process of the exposed gold, proper oxygen plasma treatment was applied to reduce the size of the mask features (spheres) and to increase the space between them. The 0.5 µm and 1 µm PS masks were oxygen plasma treated for 30 s and 2 min, respectively.

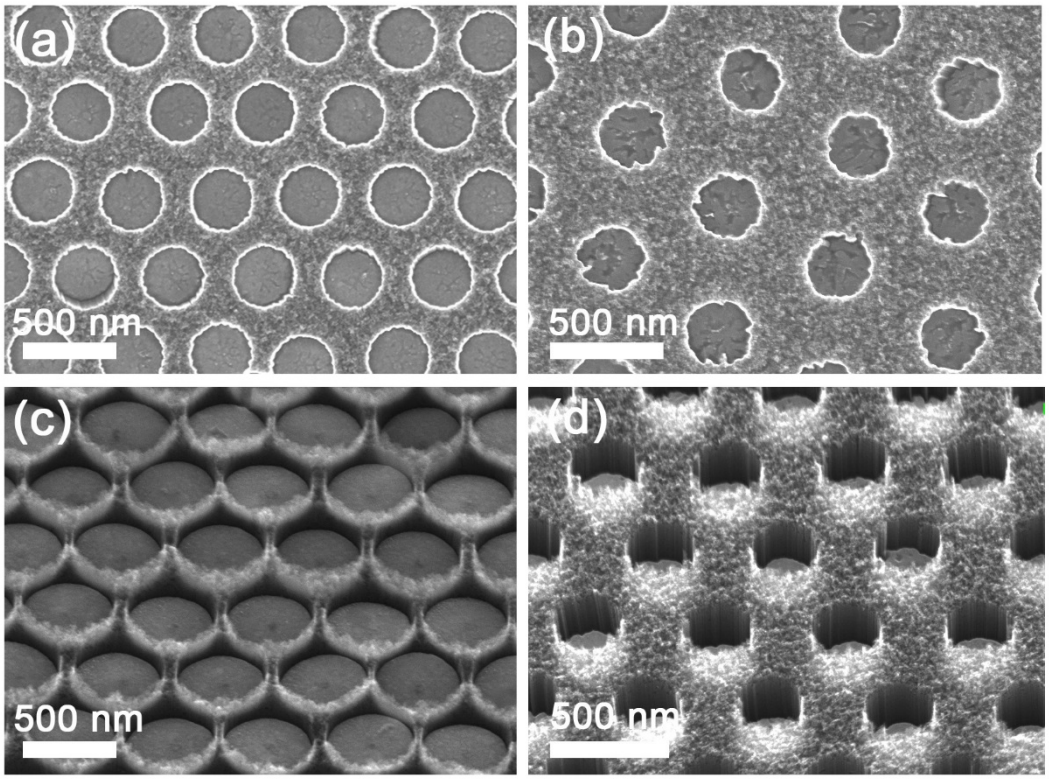

Figure 6.7 SEM images of Au-pSi composite nanochannel arrays with different nanochannel density. Top (a, b) and 45° titled (c, d) view of Au-pSi samples prepared using (a, c) a 0.5 µm and (b, d) a 1 µm PS mask.

6.3.5 Au-pSi composite nanochannels fabricated from different types of silicon wafer

Using this method to fabricate Au-pSi composite nanochannel arrays, there is no limitation in the doping levels and doping types of silicon wafers. p-type silicon wafers with a range of resistivity, including 0.01-0.02, 3-6 and 10-20 Ω cm, and n-type silicon wafers with a resistivity of 0.008-0.02 Ω cm were successfully used to fabricate Au-pSi nanochannel arrays (**Figure 6.8**). This pSi fabrication method outperforms the capabilities of the well-known and commonly used electrochemical etching. Unlike electrochemical etching, MACE allows fine tuning of the nanochannel diameter, in a wide range of sizes and density. Particularly, MACE allows us to fabricate pSi nanostructures using n-type silicon wafers without the additional backside illumination, which is necessary for n-type silicon electrochemical etching.

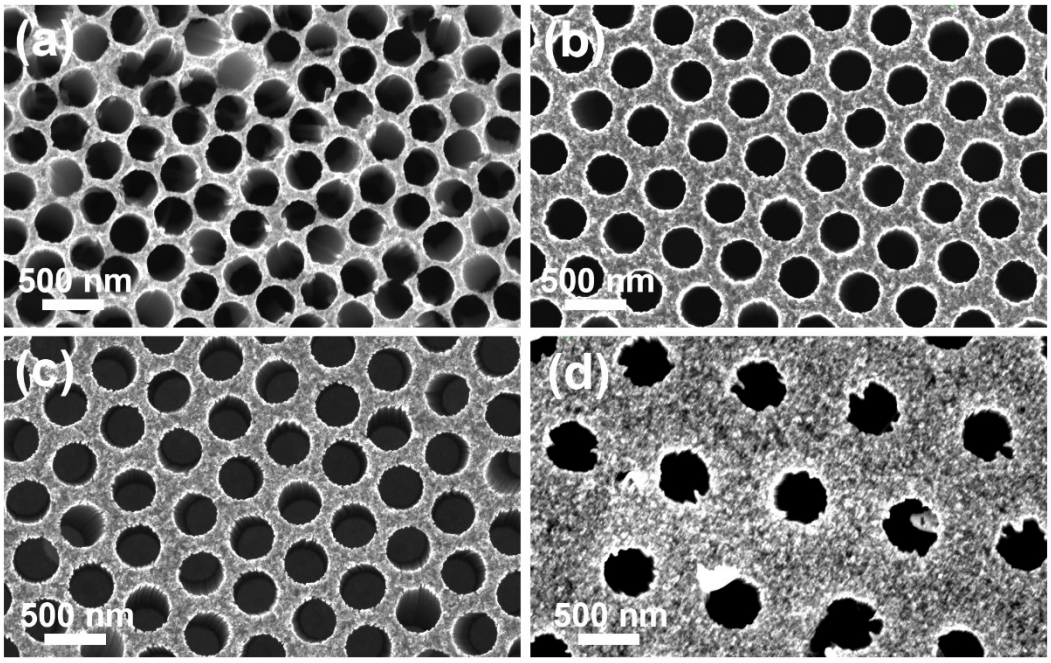

Figure 6.8 SEM images of Au-pSi composite nanochannel arrays derived from various types of silicon wafers: (a) p-type 0.01-0.02 Ω cm, (b) p-type 3-6 Ω cm, (c) p-type 10-20 Ω cm, and (d) n-type 0.008-0.02 Ω cm.

6.3.6 Carbon stabilization of the silicon surface of Au-pSi composite nanochannels

The freshly etched silicon surface of Au-pSi composite nanochannel arrays is terminated primarily with hydride species, which are highly reactive and prone to oxidation both in water and air.[26] To increase the arrays stability, thermal hydrocarbonization (THC) was used, providing in situ coating of the surface with a very thin carbon layer. The surface chemistry of THCpSi has been discussed in **Chapter 3**.

6.3.7 Electrochemical properties of Au-THCpSi composite nanochannels

The main novelty of this work comes from the feasibility to use the developed Au-THCpSi composite nanochannel arrays as electrochemical biosensing platforms. Once demonstrated the ability to modify the Au-THCpSi composite nanochannel arrays surface, the electrochemical properties of the arrays were assessed. Prior to their electrochemical characterization, the Au-THCpSi substrates were checked by 45° titled SEM (insert of **Figure 6.9a**). A thorough visual comparison of the Au-THCpSi and the non-carbonised Au-pSi, demonstrates no changes in their physical features. Of particular interest for the subsequent electrochemical characterization is the fact that the gold discs remain flat and kept the same circle shape. Prior to their electrochemical characterization, the surface of the gold discs was activated by cycling the potential between -0.2 V and 1.6 V vs Ag/AgCl at 0.1 V/s in 0.5 M H_2SO_4. After 20 cycles, a complete removal of the oxide layer is achieved, as shown by the stability reached by the specific peak at -0.9 V vs Ag/AgCl (**Figure 6.9a**). Then a systematic study of the electrochemical response of Au-THCpSi composite nanochannel arrays used as working electrode was performed in the presence of $[Fe(CN)_6]^{3-/4-}$. The $[Fe(CN)_6]^{3-/4-}$ redox system was selected because it is a quasi-reversible redox system commonly used for electrochemical characterization purposes.[27] **Figure 6.9b** presents the electrochemical performance of the Au-THCpSi composite nanochannel arrays electrode when undergoing cyclic voltammetry in

$[Fe(CN)_6]^{3-/4-}$, scanning the potential between -0.2 V and 0.6 V vs Ag/AgCl, at a scan rate of 0.1 V/s. The ratio of |Ip(Ox)|/|Ip(Re)|≈1 and the ΔEp= 170 mV suggest that the Au-THCpSi-based electrode possesses the required surface structure and electronic properties to allow efficient electron transfer. Moreover, CV measurements over a 60 h-period show 8 % changes in oxidation and reduction currents, proving the excellent stability of the platform. The CV response at different scan rates, ranging from -0.02 to 0.10 V/s, was recorded (**Figure 6.9c**). Both oxidation and reduction current values increase linearly with the square root of the scan rate (ν) (**Figure 6.9d**) suggesting that the reaction is controlled by the semi-infinite linear diffusion.[28] The linear regression equations are: $I(Ox) = 0.013 + 0.224 * \nu^{1/2}$ with correlation coefficient R^2=0.979, and $I(Re) = -0.014 - 0.225 * \nu^{1/2}$ with correlation coefficient R^2=0.979 (**Figure 6.9d**). The good linear fitting of the plots I vs $\nu^{1/2}$ indicates fast electron transfer on the electrode surface. The fast heterogeneous electron transfer kinetics between the electrolyte and the electrode is provided by the combination of the excellent electronic properties of the carbon layer, the good structural properties of the Au-THCpSi nanochannel arrays, featuring high surface area, and the excellent conductivity of gold.

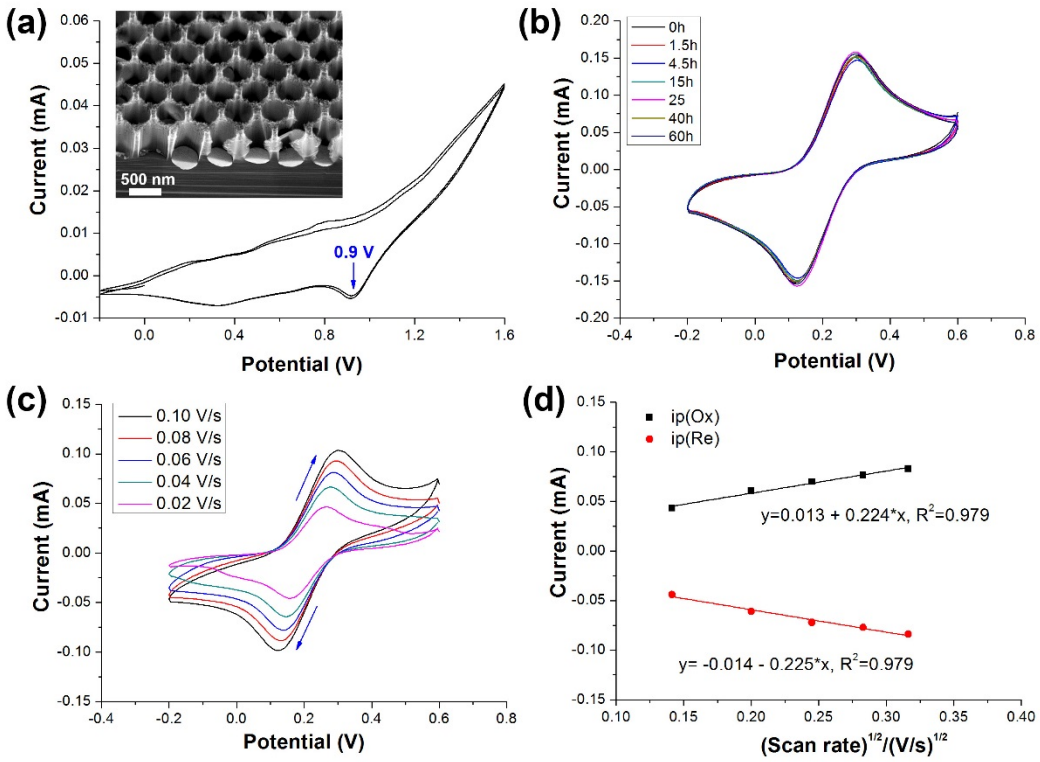

Figure 6.9 (a) Gold surface activation of the gold discs present at the bottom of the Au-THCpSi nanochannel arrays by running cyclic voltammetry in 0.5 M H_2SO_4; (insert) 45° titled SEM image of Au-THCpSi nanochannel array. (b) Cyclic voltammograms at 0.1 V/s scan rate, in 2 mM $[Fe(CN)_6]^{3-/4-}$ in 10 mM PBS, over a period of 60 h, using the Au-THCpSi composite array as working electrode. (c) Cyclic voltammograms at various scan rates ranging from 0.02 to 0.10 V/s, in 2 mM $[Fe(CN)_6]^{3-/4-}$ in 10 mM PBS, using the Au-THCpSi composite array as working electrode, and (d) corresponding plots of oxidation and reduction current vs the square root of the scan rate.

6.3.8 Surface functionalization of the silicon surface of Au-pSi composite nanochannels

The thermally hydrocarbonized pSi (THCpSi) surface of the Au-THCpSi composite nanochannel arrays was selectively modified with a monoclonal antibody against MS2 bacteriophage antibody. **Figure 6.10** presents the reflectance mode FTIR spectra of the Au-pSi surface at each step of modification: thermal hydrocarbonization (THC), thermal hydrosilylation with undecylenic acid, EDC/NHS activation of the carboxylic group and antibody immobilization. The freshly etched pSi displays bands characteristic of Si-H and Si-H_2 stretching vibrations at 2087 and 2114 cm^{-1}, and a band associated with Si-H deformation

mode at 905 cm^{-1}.[29] Compared to freshly etched pSi, Au-THCpSi does not show the featured bands of Si-H, while new bands are shown associated to stretching vibrations of saturated C-H at 1436, 2850 and 2920 cm^{-1}, CH_3 symmetric deformation mode of Si-CH_3 at 1250-1260 cm^{-1} and stretching vibrations of Si-C at 750-800 cm^{-1} (**Figure 6.10a**).[30-31] The FTIR spectrum of Au-THCpSi after thermal hydrosilylation with pure undecylenic acid is displayed in **Figure 6.10b)**. Apart from the feature bands of THCpSi, the C=O stretching vibrational mode at 1714 cm^{-1} suggests successful grafting of undecylenic acid to the THCpSi surface of the Au-THCpSi composite nanochannels arrays. Prior to the immobilization of the antibody, the COOH-terminated THCpSi surface was activated by EDC/NHS reaction to generate succinimidyl ester groups. Even though there is no obvious change after the activation step (**Figure 6.10c**), subsequent incubation with MS2 antibody, led to two new peaks, corresponding to peptide C=O stretching (amide I) at 1650 cm^{-1} and peptide N-H stretching (amide II) at 1550 cm^{-1}, indicating the successful immobilization of the antibody (**Figure 6.10d**).

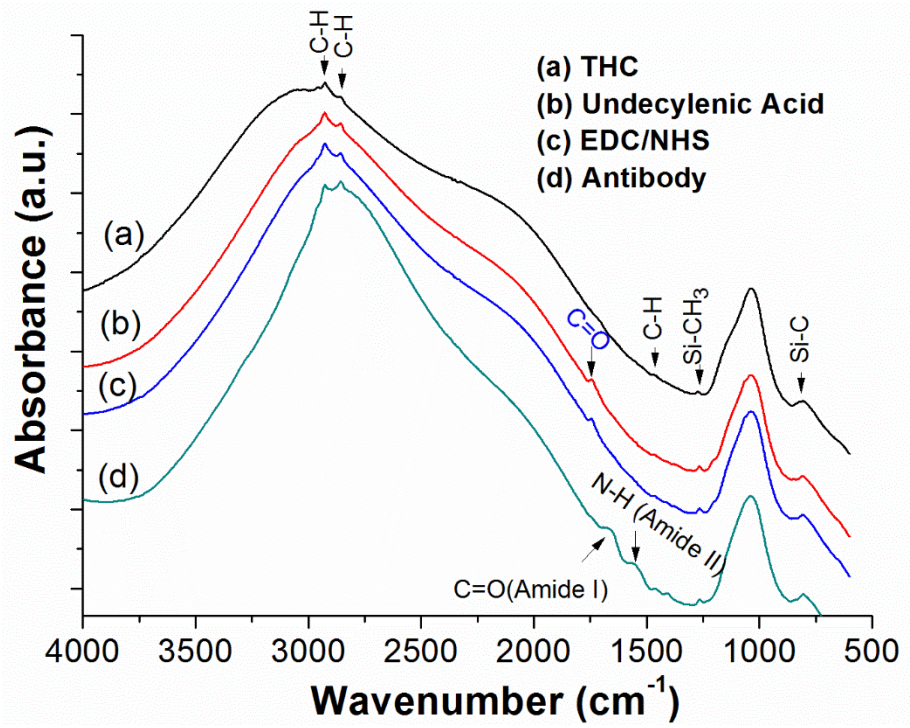

Figure 6.10 Reflectance mode FTIR spectra of the Au-pSi composite nanochannel arrays after (a) THC, (b) thermal hydrosilylation with undecylenic acid, (c) EDC/NHS activation, and (d) antibody immobilization.

6.4 Conclusion

Uniform Au-pSi composite nanochannel arrays were fabricated using MACE combined with colloidal lithography and controlled DRIE. This simple fabrication process provides the ability to tune the pore dimensions and density of ordered Au-pSi composite nanochannel arrays. Straight and highly uniform channel arrays in Si, ranging from 100 nm to several μm in diameter, with flat gold discs at the bottom were produced. The depth and density of nanochannel arrays were well controlled by selecting the proper template size and etching time. To improve the chemical stability of the nanochannel arrays, the pSi surface was carbon-stabilized via thermal decomposition of acetylene to form Au-THCpSi, introducing a thin carbon coating. Apart from the capability of surface passivation provided by the carbon layer, Au-THCpSi offered excellent electrochemical performance as shown by its fast electon-transfer kinetics. The successful covalent immobilization of an antibody on the carbon-stabilized pSi surface of Au-THCpSi supports its future application as novel electrochemical biosensing systems.

6.5 References

1. Reta, N.; Michelmore, A.; Saint, C.; Prieto-Simón, B.; Voelcker, N. H., Porous Silicon Membrane-Modified Electrodes for Label-Free Voltammetric Detection of MS2 Bacteriophage. *Biosens. Bioelectron.* **2016,** *80*, 47-53.

2. Jane, A.; Dronov, R.; Hodges, A.; Voelcker, N. H., Porous Silicon Biosensors on the Advance. *Trends Biotechnol.* **2009,** *27* (4), 230-239.

3. Anglin, E. J.; Cheng, L. Y.; Freeman, W. R.; Sailor, M. J., Porous Silicon in drug Delivery Devices and Materials. *Adv. Drug Deliv. Rev.* **2008,** *60* (11), 1266-1277.

4. Lin, V. S. Y.; Motesharei, K.; Dancil, K. P. S.; Sailor, M. J.; Ghadiri, M. R., A Porous Silicon-Based Optical Interferometric Biosensor. *Science* **1997,** *278* (5339), 840-843.

5. Guan, B.; Ciampi, S.; Le Saux, G.; Gaus, K.; Reece, P. J.; Gooding, J. J., Different Functionalization of the Internal and External Surfaces in Mesoporous Materials for Biosensing Applications Using “Click” Chemistry. *Langmuir* **2010,** *27* (1), 328-334.

6. Brodoceanu, D.; Elnathan, R.; Prieto-Simón, B.; Delalat, B.; Guinan, T.; Kroner, E.; Voelcker, N. H.; Kraus, T., Dense Arrays of Uniform Submicron Pores in Silicon and Their Applications. *ACS Appl. Mater. Interfaces* **2015,** *7* (2), 1160-1169.

7. Huang, Z.; Geyer, N.; Werner, P.; De Boor, J.; Gösele, U., Metal-Assisted Chemical Etching of Silicon: A Review. *Adv. Mater.* **2011,** *23* (2), 285-308.

8. Chen, Y.; Zhang, C.; Li, L.; Tuan, C.-C.; Wu, F.; Chen, X.; Gao, J.; Ding, Y.; Wong, C.-P., Fabricating and Controlling Silicon Zigzag Nanowires by Diffusion-Controlled Metal-Assisted Chemical Etching Method. *Nano. Lett.* **2017**.

9. Han, H.; Huang, Z.; Lee, W., Metal-Assisted Chemical Etching of Silicon and Nanotechnology Applications. *Nano Today* **2014,** *9* (3), 271-304.

10. Hochbaum, A. I.; Gargas, D.; Hwang, Y. J.; Yang, P., Single Crystalline Mesoporous Silicon Nanowires. *Nano. Lett.* **2009,** *9* (10), 3550-3554.

11. Pyykkö, P., Theoretical Chemistry of Gold. *Angew. Chem. Int. Ed.* **2004,** *43* (34), 4412-4456.

12. Daniel, M.-C.; Astruc, D., Gold Nanoparticles: Assembly, Supramolecular Chemistry, Quantum-Size-Related Properties, and Applications toward Biology, Catalysis, and Nanotechnology. *Chem. Rev.* **2004,** *104* (1), 293-346.

13. Cortie, M. B., The Weird World of Nanoscale Gold. *Gold Bulletin* **2004,** *37* (1), 12-19.

14. Glomm, W. R., Functionalized Gold Nanoparticles for Applications in Bionanotechnology. *J. Disper. Sci. Technol.* **2005,** *26* (3), 389-414.

15. Grabinski, C.; Schaeublin, N.; Wijaya, A.; D'Couto, H.; Baxamusa, S. H.; Hamad-Schifferli, K.; Hussain, S. M., Effect of Gold Nanorod Surface Chemistry on Cellular Response. *ACS Nano* **2011,** *5* (4), 2870-2879.

16. Takahata, R.; Yamazoe, S.; Koyasu, K.; Tsukuda, T., Surface Plasmon Resonance in Gold Ultrathin Nanorods and Nanowires. *J. Am. Chem. Soc* **2014,** *136* (24), 8489-8491.

17. Cobley, C. M.; Chen, J.; Cho, E. C.; Wang, L. V.; Xia, Y., Gold Nanostructures: A Class of Multifunctional Materials for Biomedical Applications. *Chem. Soc. Rev.* **2011,** *40* (1), 44-56.

18. Koo, K. M.; Sina, A. A. I.; Carrascosa, L. G.; Shiddiky, M. J. A.; Trau, M., DNA-Bare Gold Affinity Interactions: Mechanism and Applications in Biosensing. *Anal. Methods* **2015,** *7* (17), 7042-7054.

19. Buriak, J. M., Silicon-Carbon Bonds on Porous Silicon Surfaces. *Adv. Mater.* **1999,** *11* (3), 265-267.

20. Schwartz, M. P.; Cunin, F.; Cheung, R. W.; Sailor, M. J., Chemical Modification of Silicon Surfaces for Biological Applications. *Phys. Satatus Solidi A* **2005,** *202* (8), 1380-1384.

21. Sweetman, M. J.; Ronci, M.; Ghaemi, S. R.; Craig, J. E.; Voelcker, N. H., Porous Silicon Films Micropatterned with Bioelements as Supports for Mammalian Cells. *Adv. Func. Mater.* **2012,** *22* (6), 1158-1166.

22. Salonen, J.; Björkqvist, M.; Laine, E.; Niinistö, L., Stabilization of Porous Silicon Surface by Thermal Decomposition of Acetylene. *Appl. Surf. Sci.* **2004,** *225* (1), 389-394.

23. Prevo, B. G.; Velev, O. D., Controlled, Rapid Deposition of Structured Coatings from Micro-and Nanoparticle Suspensions. *Langmuir* **2004,** *20* (6), 2099-2107.

24. Torres-Costa, V.; Salonen, J.; Jalkanen, T. M.; Lehto, V. P.; Martin-Palma, R. J.; Martinez-Duart, J. M., Carbonization of Porous Silicon Optical Gas Sensors for Enhanced Stability and Sensitivity. *Phys. Status Solidi A* **2009,** *206* (6), 1306-1308.

25. Salonen, J.; Bjorkqvist, M.; Laine, E.; Niinisto, L., Stabilization of Porous Silicon Surface by Thermal Decomposition of Acetylene. *Appl. Surf. Sci.* **2004,** *225* (1-4), 389-394.

26. Sailor, M. J., *Porous Silicon in Practice*. John Wiley & Sons: **2012**.

27. Tang, L.; Wang, Y.; Li, Y.; Feng, H.; Lu, J.; Li, J., Preparation, Structure, and Electrochemical Properties of Reduced Graphene Sheet Films. *Adv. Func. Mater.* **2009,** *19* (17), 2782-2789.

28. Chang, K.; Chen, W., L-Cysteine-Assisted Synthesis of Layered Mos2/Graphene Composites with Excellent Electrochemical Performances for Lithium Ion Batteries. *ACS Nano* **2011,** *5* (6), 4720-4728.

29. Sciacca, B.; Alvarez, S. D.; Geobaldo, F.; Sailor, M. J., Bioconjugate Functionalization of Thermally Carbonized Porous Silicon Using a Radical Coupling Reaction. *Dalton Trans.* **2010,** *39* (45), 10847-10853.

30. Buriak, J. M.; Stewart, M. P.; Geders, T. W.; Allen, M. J.; Choi, H. C.; Smith, J.; Raftery, D.; Canham, L. T., Lewis Acid Mediated Hydrosilylation on Porous Silicon Surfaces. *J. Am. Chem. Soc.* **1999,** *121* (49), 11491-11502.

31. Socrates, G., *Infrared and Raman Characteristic Group Frequencies: Tables and Charts*. John Wiley & Sons: **2004**.

Chapter 7 Conclusions and future perspectives

7.1 Conclusions

In this thesis, the potential to use carbon-stabilized pSi nanostructures as electrochemical transducers to design simple, cost-effective, high sensitive and label-free electrochemical biosensors was explored. Various pSi nanostructures were fabricated via electrochemical anodization, and their pore morphological features (e.g. pore size, depth and porosity) were easily adjusted by simply varying the electrochemical anodization parameters (e.g. current density, etching time, HF and ethanol ratio). Uniform Au-pSi composite nanochannel arrays were also fabricated using MACE combined with colloidal lithography and controlled DRIE. The carbon-stabilization process via thermal decomposition of acetylene was employed to modify pSi nanostructures, not only rendering pSi suitable for electrochemical biosensing, but also providing pSi with high chemical stability, controllable hydrophilicity, and versatile surface chemistry. First, the electrochemical performance of carbonized pSi (both THCpSi and TCpSi) was systematically studied. The correlation between the chemical composition of the carbon layer formed onto the pSi nanostructures and the electrochemical behavior was explored. Second, a highly versatile nanostructured TCpSi-THCpSi double layer electrochemical biosensing platform was developed. This TCpSi-THCpSi double layer platform not only features remarkable geometrical properties such as open pore structure, tunable pore size, large available surface area and preserved Fabry-Pérot fringe pattern, but also versatile surface chemistry, dual surface functionality, and excellent electrochemical properties. Third, various impedimetric and voltammetric biosensors were developed using these carbon-stabilized pSi single and double layer nanostructures. These designed electrochemical biosensors, based on a nanochannel blockage sensing mechanism, were successfully employed for the label-free detection of analytes of interest including MS2 bacteriophage, ssDNA and *E. coli* 16S rRNA. With proper choice of the morphological features

(i.e. nanochannel diameter and depth) and functionalization strategy of such electrochemical sensing platforms, the designed label-free sensors show promising sensing performance with high sensitivity and selectivity.

7.1.1 Porous silicon nanostructures as effective Faradaic electrochemical sensing platforms

The promising electrochemical properties of THCpSi and TCpSi stabilized via thermal decomposition of acetylene at two temperatures (525 and 800 °C, respectively) were successfully demonstrated. The electrochemical performance of THCpSi and TCpSi was systematically studied by CV, CC and EIS, in the presence of three redox species, $[Fe(CN)_6]^{3-/4-}$, $[Ru(NH_3)_6]^{2+/3+}$ and HQ/Q. The results showed a correlation between the chemical composition of the carbon layer formed onto the pSi nanostructures and their electrochemical behavior. Compared to THCpSi, TCpSi not only presents a more effective charge transfer process due to its higher content percentage of Si-C species, but also shows better chemical stability to prevent self-oxidation thanks to its increased content percentage of Si-O species. The fast electron transfer kinetics and effective surface area of carbon-stabilized pSi are comparable to those shown by carbon-based commercial electrodes like SPEs and GCEs, without yielding significant double-layer capacitance effect. Apart from providing excellent electrochemical performance and stability, the novel electrochemical platform retains the unique physical and chemical features of pSi nanostructures such as large surface area, convenient surface chemistry and adjustable pore morphology. Proof of principle of applying these nanostructures as electrochemical platforms was demonstrated by developing a THCpSi-based immunosensor for impedimetric detection of MS2 bacteriophage. Changes in R_{ct} of the developed immunosensor enabled MS2 bacteriophage detection with a LOD of 4.9 pfu mL^{-1}, highlighting the future potential of carbon-stabilized pSi nanostructures as efficient biosensing systems.

7.1.2 Rapid and label-free detection of *Escherichia coli* 16S rRNA using a carbon-stabilized porous silicon-based voltammetric biosensor

A robust and highly sensitive voltammetric sensor for the detection of a specific bacterial biomarker, *E. coli* 16S rRNA, was developed. A simple, direct and label-free sensing mechanism based on nanochannel blockage was used. Taking advantage of the adjustable morphological features of pSi, the excellent electrochemical performance of THCpSi, and the enhanced hybridization event confinement into the nanochannels provided by an external Si_3N_4 insulating layer, the designed sensors detected the specific bacteria biomarker 16S rRNA with high sensitivity, a LOD down to 0.183 pM in buffer, and a short analysis time of 15 min. The sensing platform was firstly optimized by detecting a ssDNA sequence complementary to the immobilized ssDNA probe. The calculated LOD is 0.002 pM for its detection in buffer. The selectivity of the designed DNA sensor was also tested by exposing the sensor to solutions containing ssDNA sequences with 1 and 2 base mismatches. The label-free voltammetric biosensors prepared with carbon-stabilized pSi show great potential for their use as effective, affordable and portable diagnostic tools for infectious diseases. The LOD (0.183 pM) for 16 S rRNA detection is six orders of magnitude lower than the LOD (~330 nM) using a thermally oxidized pSi-based 16S rRNA sensor reported by Jia and coworkers (Sensors 2017, 17(5), 1078). The biosensing approach reported by Jia is to exploit fluorescence resonance energy transfer between quantum dots (QDs) and gold nanoparticles (AuNPs) through DNA hybridization within a pSi Bragg reflector host. This reported biosensor was applied for the detection of 16S rRNA based on quenching of the photoluminescence (PL) emission of QDs-conjugated onto the pSi layer by AuNPs-conjugated complementary 16S rRNA.

7.1.3 Designing versatile biosensing platforms using layered carbon-stabilized porous silicon nanostructures

The potential for biosensing purposes of a unique and versatile carbon-stabilized double layer nanostructure was further explored. We fabricated a unique and versatile carbon-stabilized pSi double layer nanostructure via a two-step electrochemical anodization process. The pore morphological features (e.g. pore size, depth and porosity) in each pSi layer were easily adjusted by simply varying the electrochemical anodization parameters (e.g. current density, etching time, hydrofluoric acid and ethanol ratio) used to fabricate pSi. Furthermore, different types of carbon with controllable hydrophilicity and surface chemistry were selectively formed in situ onto each porous layer via stepwise thermally decomposition of acetylene gas under controllable reaction temperature. Double layer structures with a top layer thermally carbonized pSi (TCpSi) @800 °C, and a bottom layer thermally hydrocarbonized pSi (THCpSi) @525 °C, were fabricated. The hydrophilic TCpSi top layer features -OH termination upon hydrofluoric acid pretreatment, suitable to generate functional surfaces via silanization. The hydrophobic THCpSi bottom layer enables further functionalization via hydrosilylation with alkenes and alkynes. This TCpSi-THCpSi double layer platform not only features remarkable geometrical properties such as open pore structure, tunable pore size, large available surface area and preserved Fabry-Pérot fringe pattern, but also versatile surface chemistry, dual surface functionality, and excellent electrochemical properties. Electrochemical characterization of the TCpSi-THCpSi double layer platforms using CV demonstrated they allow fast electron-transfer kinetics. The potential of such double layer structures as novel and highly performing biosensing platforms was demonstrated by the development of a TCpSi-THCpSi double layer-based voltammetric DNA sensor. The developed DNA sensor showed a LOD of 0.4 pM in buffer, being two orders of magnitude lower than that achieved by previously reported pSi-based electrochemical DNA sensors. This LOD is four orders of magnitude lower than the best

sensing performance for DNA detection reported by Segal's group (1 nM) using a thermally oxidized pSi-based interferometric DNA sensor (Adv. Funct. Mater. 2015, 25: 6725-6732). This work reported by Segal and coworkers integrates an oxidized pSi optical biosensor with electrokinetic focusing for a highly sensitive label-free detection of nucleic acids. Under proper oxidation conditions, the delicate nanostructure of pSi was preserved, while providing sufficient dielectric insulation for application of high voltages. Isotachophoresis (ITP), which is an electrokinetic technique for concentration and separation of charged analytes, was applied on a thermal oxidized pSi Fabry-Pérot interferometer for real-time and on-chip preconcentration of a DNA target, allowing for the delivery of a highly concentrated zone of ssDNA molecules to the biosensor surface, with a 10000-fold enhancement in local concentration. While most ITP assays are labeled, in this work DNA hybridization was realized in a label-free format using reflective interferometric Fourier transform spectroscopy (RIFTS), and a measured LOD value of 1 nM was demonstrated.

7.1.4 Uniform gold-porous silicon composite nanochannel arrays controllably engineered by metal-assisted chemical etching (MACE) and their electrochemical properties

Added to the electrochemical anodization method used to fabricate pSi nanostructures, MACE was also explored to engineer pSi nanostructures with uniform channel arrays. Uniform Au-pSi composite nanochannel arrays were developed using MACE combined with colloidal lithography and controlled DRIE. Straight and highly uniform pSi channel arrays, ranging from 100 nm to several µm in diameter, with flat gold discs at the bottom were produced. This fabrication process provides the ability to tune the pore dimensions and density of ordered Au-pSi composite nanochannel arrays. The depth and density of nanochannel arrays were well controlled by selecting the proper template size and etching time. Additionally, the silicon surface of these Au-pSi composite nanochannels was selectively carbon-stabilized via thermal decomposition of acetylene at 525 °C to form Au-THCpSi. Electrochemical characterization of these Au-THCpSi platforms using CV demonstrated their excellent electrochemical performance, shown by their fast electron-transfer kinetics. Further covalent immobilization of bioreceptors (e.g. antibody) on the carbonized pSi surface of Au-THCpSi demonstrated the possibility to use these platforms to design novel electrochemical biosensors.

7.2 Future perspectives

The work presented in this thesis opens up multiple avenues of research on pSi-based electrochemical biosensors. As discussed in detail, carbon-stabilized pSi nanostructures working as electrochemical transducers have shown many advantages for electrochemical biosensor design. Their adjustable morphological features, excellent electrochemical performance, high chemical stability, versatile surface chemistry and capability to be modified with suitable bioreceptors, have been well demonstrated. Various electrochemical biosensors including an impedimetric MS2 sensor, and a voltammetric DNA/RNA sensor with promising

sensing performance have been developed for the detection of analytes of interest in water quality control and medical diagnostics.

Achieving a clinically relevant detection using such carbon-stabilized pSi as electrochemical transducer is possible but challenging. Even though as an area that was previously unexplored in the field of electrochemical biosensors, further research activities involved with miniaturization and portability for such pSi-based electrochemical biosensors can be easily and effectively achieved by combining well-established silicon technology. Taking advantage of the biocompatibility of carbon-stabilized pSi, there is also a possibility to design wearable or implantable integrated devices that are able to monitor biological activities in real time. A challenge to tackle in the design of carbon-stabilized pSi platforms for point-of-care medical applications is the ability to handle real samples and achieve a clinically relevant level of sensitivity. Particularly in complex biological samples, minimization of cross reactivity and non-specific binding, enhancement of biosensor and signal stability, and methods for sensitivity improvement should continue to be studied.

.